The University Of Sheffield.

Conditioning of Legacy Radioactive Wastes Requiring Additional Treatment

By:

Jack Samuel Clarke

A thesis submitted in partial fulfilment of the requirements for the degree of Doctor of Philosophy

The University of Sheffield
Faculty of .Engineering
Department of Materials Science and Engineering

December 2018

Abstract

This thesis explores the thermal conditioning of three different legacy nuclear wastes requiring additional treatment. For the first waste stream (encapsulated Magnox drums showing evidence of internal corrosion) it was found that thermal conditioning passivates the reactants responsible for the underlying corrosion reactions, by oxidising both Magnox and uranium. At high waste loadings, the main constraint is forsterite crystallisation, which occurs at high Mg concentrations in the glass. Thermal conditioning offers a slight volume reduction compared to cementation. The resulting thermally conditioned waste form has a high short-term chemical durability with an increased durability observed when leached in saturated $Ca(OH)_2$ solution (this result was also observed for the other two waste streams). For the second waste stream, clinoptilolite, thermal conditioning at low melting temperatures, as low as 900 ^{o}C, was demonstrated. The main benefit of these low melting glass formulations is the retention of Cs during processing (between 92% and 99%). Increasing the molar ratio of Na_2O to B_2O_3 has a significant impact on glass structure and glass dissolution, depolymerising the network, decreasing NL_{Na} and NL_B slightly, but significantly increasing NL_{Si}, due to the higher pH of the leachate. However chemical durability of these glasses was low, performing worse than HLW glass. For the third waste stream, co-conditioning of sand / clinoptilolite from SIXEP, with sludge waste, was found to significantly decrease waste volumes (by a factor of 6 compared to cementation). Similar to the encapsulated Magnox drums, the main constraint on glass formulation is Mg concentration, with forsterite crystallising at ~29 mol% of MgO. It was demonstrated that, for this compositional range, Mg behaves as a modifier and in the short-term forsterite serves to significantly increase the durability of the overall waste form. Overall, it was demonstrated that thermal conditioning offers many benefits and should be given strong consideration as a conditioning strategy for some of the U.K.'s legacy nuclear wastes.

Acknowledgements

My thesis is the culmination of four years of academic research, to get to this point it would not have been possible without the support of colleagues, family and friends. Firstly thank-you to my supervisor Prof. Neil Hyatt for his support and guidance throughout my PhD. Thank-you to my second supervisor Prof. Russell Hand and my industrial supervisor Dr. Ewan Maddrell for their contributions. Many thanks to other members of academic staff for supporting my research including Dr. Claire Corkhill and, in particular, the perpetually working Dr. Martin Stennett, without whom this research would not have been possible. On that vein I'd like to recognise the technical staff who also made this research possible- Ben Parkinson (for thermal analysis), Dr. Lisa Hollands (for glass melting), Dr. Cheryl Shaw (for electron microscopy), and Dr. Nik Reeves-McClaren (for all things X-ray). Massive thanks to my fellow PhD students for their support and friendship during the PhD including (but not limited to) Dr. Colleen Mann, Dr. Laura Gardiner and Dr. Steph Thornber and in general the whole ISL team. I would like to thank the EPSRC and the NDA for funding this research and the award of the Arnold J Holland scholarship, by the Department of Materials Science and Engineering, which enabled me to travel to the USA to do research. On that note special thanks to Professor John McCloy and his awesome research group for hosting me during my time at Washington State University. You were a great mentor and I learnt a lot during my time with you there. The Americans certainly do hospitality best. My deepest gratitude is reserved to my parents for their constant encouragement and unwavering support for everything that I do. I really can't thank them enough and am really blessed to have such a loving Mum and Dad. Unfortunately my lovely grandparents (Norman and Anne) passed away suddenly before I got to submit. To them I dedicate this thesis. Also thank-you to Meg the dog and my beautiful niece Rayah for being a welcome distraction for dog and baby sitting at weekends. Sheffield is a great city and a wonderful place to study and I made some great friends and memories during my time here. Last, but not least, lots of love to my beautiful fiancé Lily for putting up with me these last few years and being a wonderful partner. Can't wait to see what you put in your acknowledgments about a year from now!

Table of Contents

Abbreviations

AGR	Advanced Gas Reactor
ASTM	American Society for Testing and Materials
a.u.	Atomic Units
AVM	Atelier de Vitrification de Marcoule
BFS	Blast Furnace Slag
BSE	Back Scattered Electron
BST	Bulk Storage Tank
C4AF	Tetracalcium Aluminoferrite (Ferrite)
C3A	Tricalcium Aluminate (Aluminate)
C3S	Tricalcium Silicate (Alite)
C2S	Dicalcium Silicate (Belite)
CCM	Cold Crucible Melter
CEC	Cation Exchange Capacity
C-S-H	Calcium Silicate Hydrate
DTA	Differential Thermal Analysis
d.p	Decimal Point
DWPF	Defence Waste Processing Facility
EDS	Energy Dispersive Spectroscopy
EDX	Energy Dispersive X-ray
FHP	Fuel Handling Plant
FINGAL	Fixation IN Glass of Active Liquors
GDF	Geological Disposal Facility
GGBS	Ground Granulated Blast Furnace Slag
HARVEST	Highly Active Residue Vitrification Experimental Studies
HLW	High Level Waste
HTXRD	High Temperature X-ray Diffraction
HWFM	Half Width at Full Maximum
HWHM	Half Width at Half Maximum
ICP-MS	Inductively-Coupled Plasma – Mass Spectroscopy
ICP-OES	Inductively-Coupled Plasma – Optical Emission Spectroscopy
ICV	In-Container Vitrification

ILW	Intermediate Level Waste
I.S.	Isomer Shift
JHCM	Joule Heated Ceramic Melter
LLW	Low Level Waste
LLWR	Low Level Waste Repository
MCC	Materials Characterisation Centre
MEP	Magnox Encapsulation Plant
NDA	Nuclear Decommissioning Authority
NNL	National Nuclear Laboratory
NIST	National Institute of Standards and Technology
NMR	Nuclear Magnetic Resonance
PC	Portland Cement
PCM	Plutonium Contaminated Material
PCT	Product Consistency Test
PIVER	PIlot VERre
PUREX	Plutonium Uranium Redox EXtraction
PWR	Pressurised Water Reactor
Q.S.	Quadrupolar Shift
S.A./V.	Surface Area to Volume ratio
SEM	Scanning Electron Microscopy
SIXEP	Site Ion eXchangE Plant
STA-MS	Simultaneous Thermal Analysis – Mass Spectroscopy
TGA	Thermal Gravimetric Analysis
W/C	Water-to-Cement
XANES	X-ray Absorption Near Edge Spectroscopy
XAS	X-ray Absorption Spectroscopy
XRD	X-ray Diffraction
XRF	X-ray Fluorescence
VLLW	Very Low Level Wast

1. Introduction

This PhD thesis examines the conditioning of nuclear waste produced from UK civil energy production, which accounts for 95% of all nuclear waste generated [1]. In particular, this thesis examines the vitrification of Intermediate Level nuclear Waste (ILW). In Europe, historically, 35% of electricity is generated from nuclear power, however, of the waste generated from all electricity production, from all sources, nuclear waste only accounts for 0.05% of the total waste volume [2]. An estimate of the average carbon dioxide production per day, per person, due to fossil fuel consumption, in the U.K., is 30 kg, if all of this fossil fuel consumption was replaced with energy from nuclear power the average person would generate 0.25 g of nuclear waste per day [3]. These statistics highlight the point that nuclear waste forms a small fraction of the total waste produced during energy production. However nuclear waste poses unique challenges, and with cost of construction, nuclear waste is still considered the biggest draw-back of nuclear power. Therefore, it is crucial that we deal with the legacy of nuclear waste from this and previous generations to present a stronger argument to the wider society of the benefits of nuclear.

The aim of this thesis is explore the possibility of thermal conditioning of ILW requiring additional treatment and to examine whether thermal conditioning of legacy wastes can provide benefits that can be utilised in the clean-up of UK nuclear sites. ILW is defined as having a specific activity of $\alpha > 4$ MBq kg^{-1} or $\beta/\gamma > 12$ MBq kg^{-1} but having a specific power of < 2 kW m^{-3}. ILW forms the greatest volume of nuclear waste requiring disposal in a dedicated facility; thermal conditioning could be utilised to condition waste streams incompatible with current conditioning methods and provide decreases in transport, storage and disposal costs. To explore this possibility, laboratory scale studies were undertaken and a common methodology used for the different ILW streams studied. This common methodology can be seen in Figure 1-1.

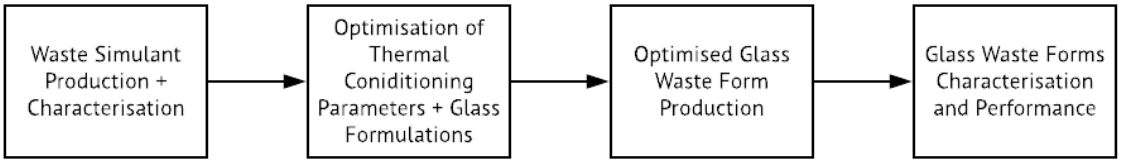

Figure 1-1. Flow chart outlining the common methodology used throughout this work.

Waste simulant production was either from raw starting reagents as in Chapter 4 or sourced from suppliers as in Chapter 5 and 6. Optimisation of thermal conditioning parameters and glass formulations was performed to maximise waste loading, whilst keeping the processing parameters within reasonable limits. This was then used to produce optimised glass formulations and these were characterised using common analytical techniques. These were density, thermal analysis, Scanning Electron Microscopy (SEM), X-ray Diffraction (XRD), compositional analysis (Inductively Coupled Plasma- Mass Spectroscopy (ICP-MS) and the Product Consistency Test (PCT-B). An explanation of these analytical techniques is provided in Chapter 3.

This thesis is structured with each ILW stream studied forming its own separate chapter, (chapters 4, 5 and 6) with an introduction, results, discussion and conclusion. It has been structured this way due to the common methodology adopted and because the study of each ILW stream itself forms a stand-alone piece of work. The separation of the results and discussion from one another is to allow the discussion to draw from different parts of the results section and form a coherent, uninterrupted discourse. Chapter 7 is a summary discussion drawing on common themes between the different results chapters to highlight some of the key findings from the whole thesis and conclusions from the work are given in chapter 8.

The next sections in this chapter, and in chapter 2, provide some background to the nuclear industry to give some context for this thesis.

1.1 Background on Civil Nuclear Power

1.1.1 Reactor Types

Most of the nuclear waste produced, that this thesis is concerned with, has been generated from Magnox reactors. These reactors used uranium metal fuel, clad in a magnesium-based alloy, called Magnox (originating from the acronym Magnesium non-oxidising.) This alloy was selected for the fuel cladding primarily due to its low neutron capture cross-section. Magnox fuel elements evolved as more Magnox reactors were constructed, learning from operational experience, particularly of bowing of the fuel elements during service. This led to many different designs, particularly of the heat-exchange fins and of the threaded end caps [4]. A comparison of Magnox and other types of reactors can be found in Table 1-1. The journey of a Magnox fuel element from when it first leaves the reactor core and becomes waste, to the point that it becomes packaged waste is shown in Figure 1-2.

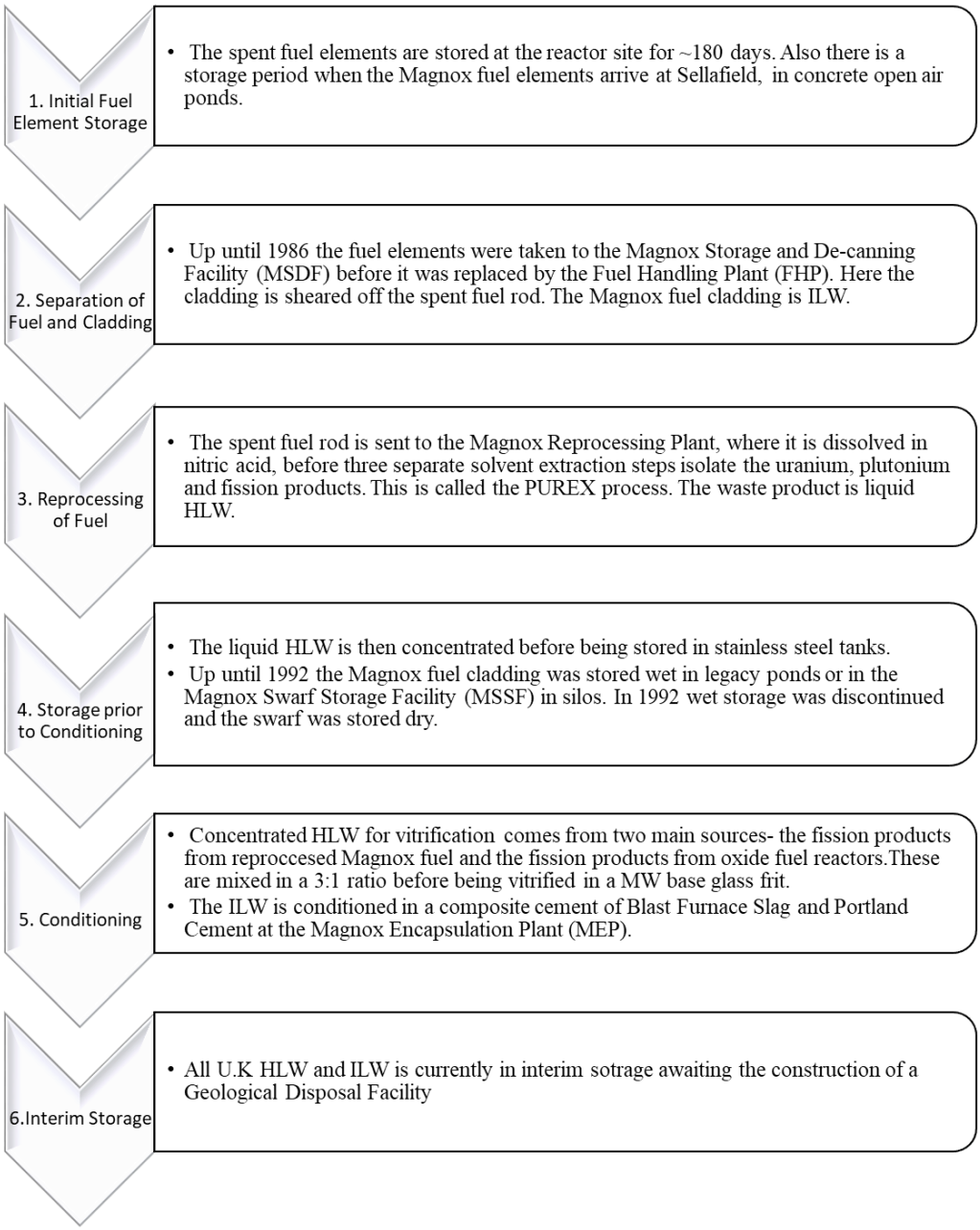

Figure 1-2. Flow chart that outlines the process from when a Magnox fuel element leaves the reactor, to the point at which the waste is conditioned and in interim storage [5],[6].

Table 1-1.
Examples of different types of reactors used around the world. Adapted from [7].

Reactor Type	Fuel Type	Cladding	Moderator	Coolant	Typical number of fuel rods per fuel assembly	Typical number of fuel assemblies
Magnox Reactor	Natural U Metal	Magnox	Graphite	CO_2	1	49,000
Advanced Gas Cool Reactor (AGR)	Enriched UO_2	Stainless Steel (20% Cr, 25% Ni, 0.5% Nb)	Graphite	CO_2	36	2,500
Light Water Reactors (e.g. PWR, BWR and VVER)	Enriched UO_2	Zircaloy	H_2O	H_2O	96-264	193-732
CANDU	Natural UO_2	Zircaloy	D_2O	D_2O	37	5,760
RBMK	Enriched UO_2	Zircaloy-Niobium	Graphite	H_2O	18	3,400

1.1.2 Waste Handling

Nuclear waste, in the United Kingdom, is classified based on both its specific activity and also the specific power. See Figure *1-3*. The main categories being very low level waste (VLLW), low level waste (LLW), intermediate level waste (ILW) and high level waste (HLW). VLLW can be disposed of with regular waste at permitted landfill sites. LLW is permitted for disposal at the low level waste repository (LLWR) in Cumbria. On the other hand ILW and HLW will be disposed of in a deep level geological disposal facility (GDF)[8], [9].

HLW has the lowest volume, but the highest concentration of radioactivity with sources including fission products (which generally have short half-lifes with some exceptions) together with actinides, which generally have long half-lifes. ILW originates from varied different sources- materials from within a reactor (e.g. reactor cores and pressure vessels), materials associated with spent fuel (e.g. fuel cladding), materials from waste storage (e.g. sludges), materials from effluent treatment (e.g. ion exchange material) and conditioned ILW itself (e.g. cemented waste) [1],[8]. In the United Kingdom there are three ways of recording nuclear waste volumes.

- The first is reported volume, which is just the volume of the waste.

- The second is conditioned volume, which is the volume of the waste form, i.e. the waste and the immobilising medium. The term conditioning refers to a process that produces a waste package suitable for handling, transport, storage and disposal. This may include the conversion of the waste to a solid waste form, enclosure of the waste in containers, and, if necessary, providing an overpack [10].

- Thirdly the packaged volume (the volume of the waste, immobilising medium and waste container). The packaged volumes of each category of waste are shown in Figure 1-3, as well as the criteria by which different forms of waste are categorised [1],[11].

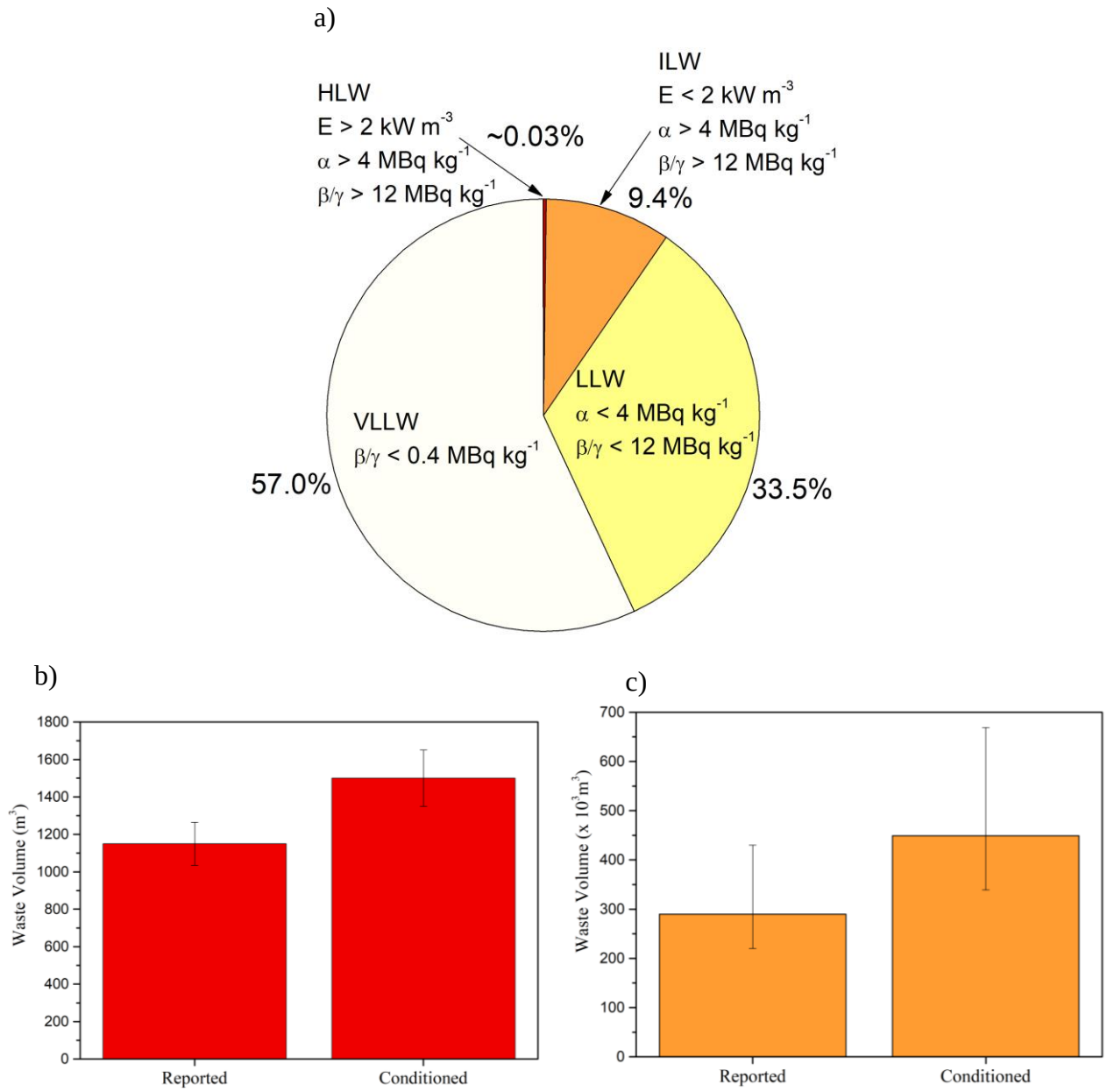

Figure 1-3 a) Pie chart showing the percentages of the total packaged volumes of different categories of waste, as well as the criteria of those categories, b) + c) Bar charts displaying both reported and conditioned volumes for HLW and ILW respectively (note the different scales on the vertical axis for b) and c)) [9].

Frequent sources of radioactivity associated with ILW are U-238, Cs-137, Sr-90, Pu-241, Cs-134 and Ce-144. As can be seen in Table 1-2, apart from U-238, these are short-lived. The radioactive hazard associated with ILW decreases with time, however, the waste must still be isolated from the environment for a period up to 100,000 y for the activity, due to longer-lived radioisotopes, such as ^{99}Tc, ^{239}Pu, ^{243}Am and ^{129}I to reach background level [1].

Table 1-2.
The main radioisotopes associated with ILW, their half-lifes, mode of decay and decay energy.

Isotope	$t_{1/2}$ / y	Radiation Type	Decay Energy / MeV
U-238[12]	4.47×10^9	α	4.269
Cs-137[13]	30.08	β	1.176
Sr-90[14]	28.79	β	0.546
Pu-241[15]	14.33	β	0.028
Ce-144[16]	0.78	β	0.320
Cs-134[17]	2.06	β	2.058
Tc-99 [18]	2.11×10^5	β	0.297
Pu-239 [19]	2.41×10^4	α	5.24
Am-243 [20]	7.37×10^3	α	5.44
I-129 [21]	1.57×10^7	β	0.189

1.1.3 Waste Disposal

The UK's preferred disposal route for conditioned radioactive waste, both ILW and HLW, is a geological disposal facility (GDF) between 200 m to 1 km below the surface [22],[23]. The central principle underpinning a GDF is termed the multi-barrier concept. This is where multiple layers of protection of the environment from the radioactivity is envisioned. These include: the waste form itself, the waste container (or overpack material), the backfill material and finally the host rock [1].

As of writing a preferred site and, therefore, a preferred geology, has yet to be identified. Potential host rocks are distinguished based upon their mechanical strength and include higher strength rocks (such as granite), lower strength sedimentary rocks (such as clays) and evaporites (e.g. calcium sulfate or sodium chloride), the advantage of evaporite formations is the lack of deep ground waters [23]. For the backfill, clay, as clays are impervious to water, could be used as well as cement grout (proposed as a

backfill for ILW). These will be placed around the waste packages [2]. As a buffer material cement is permeable and it is expected that ground waters would dissolve significant $Ca(OH)_2$. As such, one purpose of a backfill could be to alter the composition of the ground water to decrease corrosion of the waste container and waste package [23].

In such a facility, packaged HLW and ILW would be contained in separate areas. Deposition holes would be drilled in the host rock where the packaged waste forms will be placed; either holes bored down into the rock or through horizontal emplacement into the host rock. The most common waste forms are glass and cement-based systems. For waste containers the most prevalent are metal containers that are not particularly corrosion-resistant, such as steels (both carbon and stainless), whereas other concepts (such as in salt-based rock formations) use copper and titanium (such as titanium-palladium alloy (Ti-99.8- Pd), in particular for spent nuclear fuel [2].

1.2 References

[1] I. W. Donald, “Waste Immobilisation in Glass and Ceramic Based Hosts- Radioactive, Toxic and Hazardous Wastes,” 1st ed., Chichester: Wiley, 2010, pp. 1–31, 57–177, 275–334, 465–490.

[2] E. U. Director-General For Research, “Geological Disposal of Radioactive Wastes Produced by Nuclear Power... from concept to implementation,” 2004, pp. 4–43.

[3] D. J. Mackay, “Sustainable Energy- Without The Hot Air,” 2008, pp. 161–173.

[4] G. Marsh and H. Eccles, “Fuel Fabrication,” in *The Nuclear Fuel Cycle From Ore To Waste*, Oxford: Oxford University Press, 1996, p. 43,48-50.

[5] Sellafield, “Information on Sellafield Storage.” [Online]. Available: http://www.sellafieldsites.com/solution/risk-hazard-reduction/. [Accessed: 14-Mar-2015].

[6] Sellafield, “Information on Sellafield Reprocessing.” [Online]. Available: http://www.sellafieldsites.com/solution/spent-fuel-management/. [Accessed: 14-Mar-2015].

[7] K. W. Hesketh, “Power Reactors,” in *The Nuclear Fuel Cycle From Ore To Waste*, Oxford: Oxford University Press, 1996, pp. 84–96.

[8] S. Richardson, P. Curd, and E. J. Kelly, “Disposal of Fuel or Solid Wastes,” in *The Nuclear Fuel Cycle From Ore To Waste*, Oxford, 1996, pp. 184–197.

[9] M. L. Ojovan and W. E. Lee, “An Introduction To Nuclear Waste Immobilisation,” 2nd ed., Oxford: Elsevier, 2005, pp. 81–85, 187, 213–248, 259–268.

[10] IAEA, “IAEA, Design And Operation Of High Level Waste Vitrification And Storage Facilities,” *Tech. Rep. Ser. No. 339*, 1992.

[11] NDA, “NDA radioactive waste inventory,” 2013. [Online]. Available: https://www.nda.gov.uk/ukinventory/the-2013-inventory/2013-uk-data/. [Accessed: 10-Sep-2016].

[12] E. Browne and J. K. Tuli, “Nuclear Data Sheets for A=238,” *Nucl. Data Sheets*, vol. 127, pp. 191–332, 2015.

[13] E. Browne and J. K. Tuli, “Nuclear Data Sheets for A=137,” *Nucl. Data Sheets*, vol. 108, no. 10, pp. 2173–2318, 2007.

[14] E. Browne, “Nuclear Data Sheets for A=90,” *Nucl. Data Sheets*, vol. 82, pp. 379–546, 1997.

[15] C. D. Nesaraja, “Nuclear Data Sheets for A=241,” *Nucl. Data Sheets*, vol. 130, pp. 183–252, 2015.

[16] A. A. Sonzogni, “Nuclear Data Sheets for A=144,” *Nucl. Data Sheets*, vol. 93, no. 3, pp. 599–762, 2001.

[17] A. A. Sonzogni, “Nuclear Data Sheets for A=134,” *Nucl. Data Sheets*, vol. 103, no. 1, pp. 1–182, 2004.

[18] E. Browne and J. K. Tuli, “Nuclear Data Sheets for A=99,” *Nucl. Data Sheets*, vol. 145, pp. 25–340, 2017.

[19] E. Browne and J. K. Tuli, “Nuclear Data Sheets for A=239,” *Nucl. Data Sheets*, vol. 122, pp. 293–376, 2014.

[20] Y. A. Akovali, “Nuclear Data Sheets for A=243,” *Nucl. Data Sheets*, vol. 103, pp. 515–564, 2004.

[21] J. Timar and Z. Elekes, “Nuclear Data Sheets for A=129,” *Nucl. Data Sheets*, vol. 121, pp. 143–194, 2014.

[22] N. C. Hyatt and M. James, “Thermal Treatment of ILW,” *Nuclear Engineering International*, pp. 10–14, 2013.

[23] NDA/RWMD/013, “Geological Disposal: Steps Towards Implementation. Nuclear Decommisioning Authority Report,” 2010.#

2. Literature Review

The current state of the art of glass science and vitrification of nuclear wastes is reviewed in this chapter. Material covered will include glass theories, glass chemistry, vitrification technologies, secondary phases, glass dissolution and more detail on the waste streams subject to thermal conditioning in this thesis. As the literature on ILW thermal conditioning is less mature than that of HLW vitrification, sections of this literature review will focus on HLW vitrification due to certain similarities. ILW glass product performance is still affected by the same factors and secondary phases in observed in HLW glass are observed to form in ILW glasses too. However, the differences between the HLW and ILW streams leads to differences particularly in vitrification technologies, processing parameters and redox chemistry and these differences are discussed.

All materials will form glasses if the cooling rate from a liquid is sufficiently fast and the final ambient temperature is below the material's glass transition temperature, T_g. Generally, the glass-transition temperature, T_g, is defined as the temperature at which the material has a viscosity of 10^{12} Pa s. This temperature separates solid-like behaviour from liquid-like behaviour [1], [2]. It can be detected *via* thermal analysis and is demarcated by sharp changes in thermal properties [2]. Glass, historically, has been utilised for immobilisation of radioactive isotopes, as effectively it acts as a solvent and, therefore, is capable of dissolving many different radionuclides *via* chemical incorporation into the glass structure.

2.1 Structural Theories of Glasses

Three main theories have been proposed to explain the structure of glasses- the crystallite theory, the random network theory and the cybotactic theory, which essentially is a reconciliation of the previous two theories [3].

The earliest model, the crystallite theory, was that of Lebedev. This theory stated that the basic unit of a glass is a "crystallite", which is a deformed version of a crystal. These units are highly dispersed and are connected to one another by amorphous regions, analogous to grain boundaries (but on a much smaller scale). A typical

"crystallite" will be on the order of 15 Å [4],[5]. The random network model was first postulated by Rosehain, this theory states that varying inter-atomic distances and bond angles are necessary, throughout the structure, to produce the random network of glasses [6]. Oxygen has a maximum coordination number of two, whereas cations in the structure are in a triangular or a tetrahedral arrangement. These triangular or tetrahedral structural arrangements dominate the structure of the glass [4]. The cybotactic theory states that the "crystallite" regions, defined by Lebedev, are actually regularly stretched or compressed molecular groups with surrounding areas that are strongly disordered [7]. There are essentially areas within the glass that are more ordered than others, with the most ordered regions approaching the degree of order of a crystalline phase, but on a much smaller scale (<10 Å). However, it is impossible to delineate these more ordered regions from the less ordered as there is no distinct transition between the two. The cybotactic theory states that glasses are essentially nanoheterogenous [3].

2.1.1 Role of Glass Constituents by Field Strength

The structural role of an element in a glass can be predicted by its field strength, (i.e. Z / a^2), where Z is the valence and a is the sum of the ionic radii of the cation and the oxide ion. Those with a high field strength become network formers (> 1.3 $Å^{-2}$), whereas those with low field strengths become modifiers (approximately < 0.45 $Å^{-2}$). Those in between typically adopt an intermediate role [1]. Table 2-1 shows typical elements found in glass structures and the role that they adopt.

2.2 Glass Melting and Glass Formation

During the initial melting of a glass batch, early melt phases are formed and there is a release of gas, such as from carbonates, sulfates and nitrates creating a mixing and stirring action. As the temperature increases further- liquid phases are formed by the melting of either decomposition products or eutectic mixtures. An example of a eutectic mixture is $Na_2O.2SiO_2$ and SiO_2. This stage of the melt is characterised by the release of lots of gas and high mixing of liquid and solid phases. At higher temperatures the rates of dissolution of more refractory components, such as silica and

alumina increase dramatically. This is also coupled with an increase in the viscosity of the melt due to the higher silica content, along with the further release of gases, particularly CO_2, the solubility of which is vastly decreased by the increase in silica content of the liquid [2].

Table 2-1.
The structural role and properties of various cations within a glass structure [1], [8].

Element	Coordination number	a (Å)	Field Strength of oxide ions ($Å^{-2}$)
Former			
P +5	4	1.54	2.1
Si +4	4	1.60	1.57
B +3	3	1.36	1.62
B +3	4	1.73	1.34
U +6	6	2.08	1.39
Intermediate			
U +6	8	2.21	1.23
U +5	6	2.11	1.12
U +4	8	2.35	0.72
Ti +4	4	1.79	1.25
Ti +4	6	1.96	1.04
Al +3	4	1.77	0.96
Al +3	6	1.89	0.84
Fe +3	4	1.88	0.85
	6	1.99	0.76
Mg +2	4	1.94	0.53
Modifier			
Fe +2	6	2.16	0.43
Mg +2	6	2.11	0.45
Ca +2	8	2.46	0.33
Sr +2	8	2.69	0.28
Li +1	6	2.09	0.23
Na +1	6	2.29	0.19
K +1	8	2.77	0.13
Cs +1	12	3.16	0.10

The thermodynamically most favourable product from a glass melt, on cooling, is a crystalline phase; it is the rapid quenching of the melt that allows the glass to form. Figure 2-1 shows the relationship between the material's volume (or enthalpy) as a function of temperature in terms of glass formation. To form a glass the liquid is

cooled rapidly past the now liquid's melting temperature, T_m, to form a super-cooled liquid. A lower cooling rate will mean the super-cooled liquid will follow the equilibrium line for longer, but at some point the super-cooled liquid deviates from the equilibrium line (drawn as a red curve in Figure 2-1.). This is the glass transformation, which occurs over a distinct temperature range, rather than at a distinct temperature [9]. The viscosity during this transformation increases, in such a way that the atoms can no longer re-arrange to the equilibrium structure. An important factor in glass formation is viscosity- less viscous melts are prone to crystallisation on cooling and require much faster cooling rates. For example, an increase of 40 ^{o}C for a glass, in specific circumstances, increases the critical cooling rate (the minimum cooling rate needed to yield a glass) by a factor of 10^4 ^{o}C s^{-1} [4]. Generally the glass transition temperature is defined as the onset temperature of the glass transformation. Another quantity, the fictive temperature, T_f, is given by the intersection of the extrapolated lines of the glass and super-cooled liquid curves [10]. Both the glass transition and fictive temperatures are dependent on cooling rate and thermal history. Eventually the volume (or enthalpy) again varies linearly with temperature and the structure of the super-cooled liquid becomes fixed: a glass is formed [2], [11].

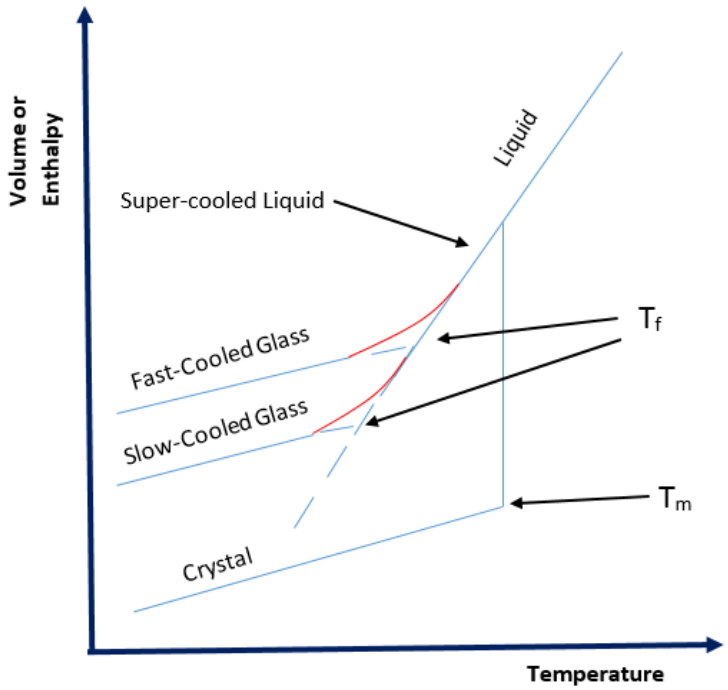

Figure 2-1. Graph of volume/enthalpy versus temperature, containing equilibrium lines for liquids, crystals and glasses.

2.3 Chemistry of Alkali Borosilicate Glasses

Glasses in this thesis are essentially based around the alkali borosilicate system. The structure of silicate glasses can be described by the degree of polymerisation of the silica tetrahedra, denoted by Q_x, where x denotes the number of oxygen atoms bonded to other network formers. In the Na_2O- B_2O_3- SiO_2 ternary the structure of the glass is composed of silica tetrahedra, borate tetrahedra and borate trigonal arrangements [1],[12]. Figure 2-2 shows some of the structural units present in a borosilicate glasses [13],[14]. In this section the nomenclature for describing borosilicate glasses is discussed.

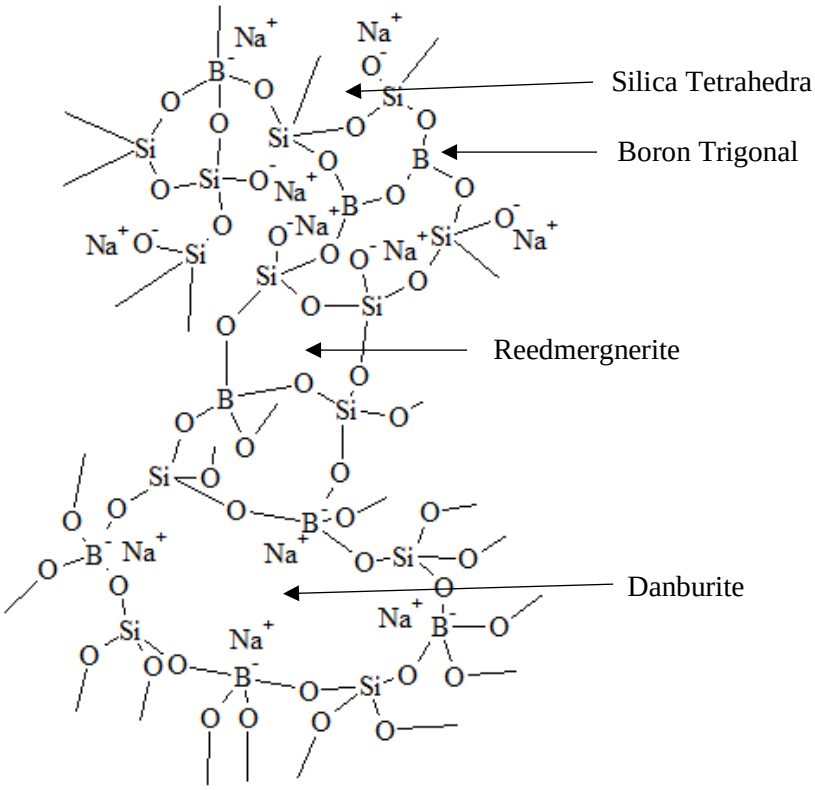

Figure 2-2. Schematic stick diagram showing some of the structural and super-structural units present in a typical sodium borosilicate glass.

The most important molar ratio for describing borate and borosilicate glasses is R, given by Equation 2-1 [13], [15].

$$R = \frac{Na_2O}{B_2O_3} \qquad \text{Equation 2-1}$$

The trigonal arrangement of boron occurs exclusively when R= 0, between 0 and 0.5 the tetrahedral and trigonal units co-exist up to a maximum of 50% each at R = 0.5 (called the diborate composition), tetrahedral units are then consumed at R ? 0.5 forming non-bridging oxygen atoms. Trigonal units and associated modifiers, are far less durable than their tetrahedral BO_4 counterparts. Borate tetrahedra avoid connecting to adjacent borate tetrahedra and instead bond to trigonal units [1],[16].

In addition to R, borosilicate glasses are dependent upon another molar ratio K, given by Equation 2-2 [15].

$$K = \frac{SiO_2}{B_2O_3} \qquad \text{Equation 2-2}$$

Borosilicate glasses can be characterised by four structural regimes [13], [17], [18], [19]. These are outlined below:

1. $R < 0.5$ In this range all the modifier is bonded to boron tetrahedra, charge compensating these units. As R approaches 0.5, the coordination number of boron has increased from 3 to 4. Amorphous phase separation is present with modified borate and silicate phases forming. However, there is evidence that at $R > 0.33$, some of the modifier will enter the silicate network.
2. $R > 0.5$ and $R < 0.5 + \frac{K}{16}$ In this range the sodium in excess of the diborate composition now enters the silicate network, along with boron to form structures analogous to reedmergnerite $Q_4(1B)$ and/or danburite $Q_4(2B)$. The additional sodium and boron continue to enter the silicate network until the boron content is of such a concentration that coordination to surrounding silica tetrahedra is impossible. The silicate network has become saturated with boron.
3. $R > 0.5 + \frac{K}{16}$ and $R < 0.5 + \frac{K}{4}$ In this range the excess sodium now associates with non-bridging oxygens on silica tetrahedra. The preference is for Q_4 species (in the silicate network) to depolymerise first compared to $Q_4(1B)$ and $Q_4(2B)$ units in reedmergnerite and danburite.
4. $R > 0.5 + \frac{K}{4}$ and $R < 2 + K$ In this range the silicate network has been extensively depolymerised and any additional sodium is assumed to be charge

compensated by the formation of asymmetric trigonal boron sites where the average coordination number of boron now begins to decrease from 4 to 3 [13], [15].

Aluminium is a common component of the glasses examined in this thesis due to its occurrence in the waste streams, therefore, it is important to understand its structural role. Aluminium preferentially forms negatively charged alumina tetrahedra. There is evidence that alkali ions have a preference for bonding to alumina tetrahedra as opposed to silica tetrahedra and borate tetrahedra, which remain in a three-fold coordination, until all of the alumina has been coordinated to by modifier. Alkali metals bonded to aluminium and boron oxide tetrahedra, i.e. BO_4^- and AlO_4^- are more strongly bonded than to the non-bridging oxygens of silica [1]. For example, ^{11}B NMR shows that 29% of the boron is 4 coordinated for $9.4Na_2O$-$25.4B_2O_3$-$65.2SiO_2$, it decreases to 21% with the addition of 3% Al_2O_3 [20]. However there is experimental evidence which contradicts this showing that borate coordination for a given alkali ion concentration is unchanged, irrespective of alumina content [2].

Keeping the total molar content of alkali constant, but varying the relative molar ratios of alkalis, e.g. Li_2O and Na_2O, affects viscosities, ionic conductivity and diffusion in a non-linear way. This phenomena is called the common ion effect. A similar effect is observed for alkaline earth metals where Vickers micro hardness, glass transition temperatures and viscosities vary, non-linearly, for different MgO_{1-x} CaO_x ratios in sodium aluminosilicate glasses, where $0 < x < 1$. This is explained by a weakening of the bonds around the network modifiers [21].

2.4 Vitrification of Nuclear Waste

There is a growing interest in the vitrification of ILW, previous studies have researched the vitrification of plutonium-contaminated material (PCM) [22]–[24] and wet ILW from Magnox decommissioning, namely- organic ion exchange resins, sludges and sand filter waste [25]–[27]. It has been demonstrated that the benefit of vitrifying these waste streams include large reductions in the volume of waste, producing durable waste forms and the immobilisation of key radionuclides in the glass structure (e.g. Pu (by studying Ce as a surrogate)).

In the following sections aspects of the vitrification of ILW are reviewed along with the more developed and extensive literature of HLW vitrification to provide the context for the studies in this work. Borosilicate glasses are the glass compositions selected by most HLW producing or handling nuclear sites as the immobilising matrix, as these glasses offer relatively high waste-loading, can incorporate many different waste elements into the network, have relatively low melting temperatures and have good chemical durability [11], [28]. A selection of borosilicate glasses used throughout the world is shown in Table 2-2. UK HLW glass can accommodate waste loadings of 25-30 wt%. Higher melting temperatures often results in the possibility of higher waste loadings being achieved [29].

One of the initial choices to be made when vitrifying nuclear waste is whether to calcine or not. This can be in a separate step or *in-situ* with glass additives already present. The reasons for calcination may be to dry the waste, to condition redox properties or to generally help with the vitrification process. For example, lithium nitrate is added during the calcination of wet HLW, at Sellafield, in an attempt to prevent refractory spinels from forming during glass processing [11]. During glass processing another choice is whether to anneal or not. A glass that is not annealed, will likely crack on cooling, resulting in a larger surface area available for leaching. Despite this, radionuclide retention is sufficiently high in un-annealed glasses, when compared to other waste forms, such as cement encapsulation [1]. However, even when performing dissolution experiments on powdered glass samples (with the same S.A./V. ratio) there can be differences between annealed and un-annealed glass. One study showed that slow-cooled glasses have slightly lower mass losses compared to quenched glasses [30].

Table 2-2.
Compositions of some silicate glasses either used to vitrify HLW or simulate HLW glass. Adapted from [11].

	Glass Designation and Origin										
Oxide (wt%)	209	MW	M7	AVM	SON 68	PNL 76-68	SRL 131	Tokai	GG WAK1	Canada 1	ISG
	U.K.		France			U.S.A.		Japan	Germany	Canada	Inter-National
SiO_2	68.5	61.7	52.1	56.1	54.9	59.4	57.9	61.0	60.0	51.2	56.2
B_2O_3	15.0	21.9	16.0	25.3	16.9	14.3	14.7	19.8	17.6	0	17.3
Al_2O_3	0	0	5.6	0	5.9	0	0	5.0	3.1	20.4	6.1
Fe_2O_3	0	0	3.3	0	0	0	0	0	0	0.1	0
MgO	0	0	0	0	0	0	2.0	0	2.2	0	0
CaO	0	0	4.6	0	4.9	2.9	0	2.8	5.3	15.0	5.0
BaO	0	0	0	0	0	0	0	0	0	0	0
Li_2O	5.4	5.3	0	0	2.4	0	0	0	3.5	0	0
Na_2O	11.2	11.1	14.1	18.6	11.9	11.3	17.7	11.4	7.1	11.4	12.2
ZnO	0	0	0	0	3.0	7.6	0	0	0	0	0
TiO_2	0	0	0	0	0	4.5	0	0	1.2	0	0
ZrO_2	0	0	0	0	0	0	0	0	0	0	3.3

2.5 Vitrification Technologies

The four main technologies available for ILW vitrification are:

1) Induction melters,
2) Joule heated ceramic melters (JHCMs),
3) In-container vitrification (ICV) melters, and
4) Plasma melters.

Induction melters and JHCMs are more widely-used, than ICV and plasma melters, in the conditioning of HLW. Induction melters use a metallic melting vessel. Heat is provided, *via* induction heating, from the application of an external radiofrequency field [11], [31]. The cold crucible melter (CCM) is a variant of the induction melter, where a layer of batch material, at the melt line, is purposely maintained at a low temperature (*via* water-cooled stainless steel or copper tubes). The cooling can also be

extended to the entire outer surface of the melt, using the same means, generating a protective "skull" [25]. The cooling water in the tubes is < 100 ^{o}C, this typically keeps the outside of the molten glass at < 200 ^{o}C. A disadvantage of induction melters is that the heating is provided externally, via heating of the metal chamber; this limits the temperature to ~1100 ^{o}C and generally can only produce glass at a rate of 25 kg/h [11]. Induction melters can also be operated as in-container vitrification, where the melting vessel acts as the final disposal container.

Joule-heated ceramic melters (JHCMs) melt glass in a ceramic melting vessel, in which heat is generated by passing current between electrodes submerged in the glass melt. These submerged electrodes are typically made of Inconel 690 alloy or molybdenum silicide based heating elements. Current is applied to the electrodes through stainless steel tubes [11]. By heating waste directly, JHCMs are much more efficient than induction melters. JHCMs typically offer less loss of volatile radionuclides than induction melters and can produce 40-120 kg/h of glass [11]. Cold crucible melter technology can also be applied with JHCMs. It is also possible to bubble gases through the glass melts allowing good mixing and manipulation of redox conditions, which can be beneficial for high metallic containing ILW.

In-container vitrification (ICV) uses an insulated ceramic vessel as both the melter and the final disposal container. This is often lined with silica (~6 cm thick), which is in contact with the melt and often results in increased SiO_2 within the final waste form. This increase can change the local chemistry of the glass at the interface (e.g. baddeleyite crystals can form at the interface (in relatively high ZrO_2 glass melts) due to the change in local composition of the glass, causing a decrease in the solubility of ZrO_2. The melt penetrates into the silica lining to various depths, this in effect forms a passivating interfacial layer between the glass and melting vessel. The material is Joule-heated by sacrificial, submerged graphite electrodes, within the melt [30]. One of the main advantages of ICV is that higher temperatures can be used, thereby avoiding the accumulation of molten salts that limits waste loadings of higher sulfate container wastes. ICV shows particular promise for immobilising mixed waste- a study found a vitrified waste form (40 kg) could be formed from immobilising a high metallic waste stream with significant quantities of organic waste [32]. An advantage

of ICV is that less secondary waste is generated and some of the problems associated with continuous melters are avoided or mitigated such as settling of high density phases.

Plasma technology for vitrification is also feasible for certain waste forms, but in general due to its expense there must be a clear benefit for using it over other technologies. This technology employs a metallic melter, such as copper, with refractory lined walls above the melter; both are water-cooled at their exterior. The electrodes are positioned at the top of the melter above the melt line of the glass and a plasma arc is created between the electrodes by introducing a gas (typically $Ar_{(g)}$) through the electrodes [11]. Simulant PCM (plutonium-contaminated material) was vitrified using this technology achieving a waste loading of 54 wt%, and observing that 98% of the CeO_2, studied as a surrogate for PuO_2, partitions into the glass. The main benefit of plasma technology is due to the very high temperatures generated: 1500-5000 ^oC (250-500 kW), the waste can be treated without any pre-treatment steps and conditioned in a single process [23], [33], [34] ,[35].

A selection of HLW melters found around the world can be seen in Table 2-3, technologies implemented in one place but developed elsewhere have been omitted. For example, the UK adopted a continuous vitrification line, adapted from the French AVM process. ILW streams tend to widely vary in composition and volume and can require higher temperatures in order to facilitate a more fluid melt. These constraints mean that in-container vitrification (ICV) melters or plasma melters may be more suitable for the task [36]. These are relatively newer technologies that have not been constructed on an industrial scale for conditioning of nuclear waste. A potential drawback with ICV is that the continuous melters have much higher throughputs, which may be problematic as longer melt campaigns will be required to condition the higher volume of ILW. A potential drawback of plasma melting is crucible corrosion and the much higher energy use of this process.

Table 2-3.
Nuclear waste vitrification plants in operation, or that were operated, from around the world [11], [37-38].

Name	**Melter Technology**	**Calcination step**	**Glass additive**	**Location**	**Process**	**Stage of Development**
Highly Active Residue Vitrification Experimental Studies (HARVEST)	Resistive external heating furnace	*In-situ*	Raw batch	Harwell, U.K.	In-container	Pilot
Pilot Verre (PIVER)	Induction-heated	*In-situ*	Frit	Marcoule, France	In-container	Pilot
Atelier de Vitrification de Marcoule (AVM)	Induction-heated	Separate	Frit	Marcoule, France	Continuous	Industrial
GeoMelt	JHCM	Separate	Raw Batch	Hanford, U.S.A	Continuous	Pilot
PAMELA	JHCM	*In-situ*	Frit	Mol, Belgium	Continuous	Industrial
EP-500	JHCM	*In-situ*	Frit/Raw Batch	Mayak, Russia	Continuous	Industrial
Defence Waste Processing Facility (DWPF)	JHCM	*In-situ*	Frit	Savannah River Site, U.S.A.	Continuous	Industrial

2.6 Refractory Materials and Corrosion

The material to be used in contact with the glass during processing is an important consideration for waste vitrification. Refractory metals are used, in induction melters and plasma melters, but can be problematic for ILW vitrification due to the very high temperatures and often reducing conditions in the melt. On the other hand, oxide refractories can withstand very high temperatures- originally common oxide refractory materials were fireclay, silica and sandstone. The next development was the introduction of sillimanite and mullite, followed by the development of fusion cast refractories such as alumina-zirconia-silica (AZS) based refractories, including Monofrax. These are far more durable than standard sintered ceramics due to their

lower porosity and high zirconia content. Pure alumina is rarely used in industrial melters as it is less resistant to attack than AZS compositions [36].

One of the most effective ways of limiting refractory corrosion is to lower the melt temperature, which negates the stronger transport properties of more fluid melts [26]. A common corrosion mechanism is drilling, this occurs when a thin film of melt (such as that surrounding a bubble or metal) meets an interface. Upward drilling occurs when a downward facing refractory surface is in contact with gas bubbles trapped against it. Downward drilling is generally when metals are present (the higher density of metals and also sulfides means that they settle) causing a solid-solid state reaction to proceed at the base of the furnace [36]. Dissolution of the refractory proceeds with a fast initial stage, followed by a longer secondary stage where the layer of the refractory has been passivated with an altered layer rich in spinel phases [39].

2.7 Processing Parameters and Waste Form Performance

Producing a waste glass formulation is a balance between waste form performance and melt processing parameters. Key waste form performance parameters include durability and waste form homogeneity. For example, having more than one phase in a waste form can be undesirable as activity may partition into a lower durability phase. This highlights the point that a waste form is only as effective as the least durable phase at immobilising radionuclides [40]. Key melt processing parameters include the melting temperature and the waste loading. Melting temperature, T_M, can be selected based on the temperature at which the glass has a viscosity of 5 Pa s [29]. In any case it is important to maintain viscosities below 10 Pa s to enable good casting and allow the glass to be homogeneous, particularly for continuous operations. Glasses with viscosities greater than 50 Pa s at the melting temperature cannot be cast easily [25]. To ensure problem-free melting it has been suggested that T_M - T_L must be substantially positive (>100 ^{o}C), to greatly reduce the chances of spinel formation [29]. High waste loadings are very important to minimise the volume of waste that has to be ultimately disposed of, both to reduce the size of a GDF, and to minimise the length of the campaign for the melter technology. This is particularly important for ILW because of the high volume of this category of waste [1], [24], [40].

2.8 Redox Chemistry in the Glass Melt

The redox environment in a glass melt is a function of temperature, time, oxygen fugacity and concentration of multivalent ions in the batch. For typical HLW glass processing at 1150 ^{o}C, to prevent foaming, a pO_2 range of 10^{-2} to 10^{-9} atm is desirable [36]. Glasses which contain sulfates can affect the redox environment. For example, sodium sulfate can act as an oxidising agent, as can nitrates; they are reduced to sulfites and nitrites respectively [26]. Waste streams with high levels of carbonaceous and metallic material lead to a reducing environment. Multivalent species act as redox buffers and from this can used to determine whether the melt is reducing or oxidising. For example, iron has two oxidation states, Fe(II) and Fe(III) and the ratio $\frac{Fe^{2+}}{\sum Fe}$ is often used to determine how oxidising or reducing a melt is [41]. The redox couple can be observed in Equation 2-3.

$$2\ Fe^{3+}_{(melt)} + O^{2-}_{(melt)} \rightarrow 2\ Fe^{2+}_{(melt)} + \frac{1}{2} O_{2(g)} \qquad \text{Equation 2-3}$$

It's suggested that $\frac{Fe^{2+}}{\sum Fe}$ of < 33% is desirable to limit the reduction of metal oxides to metals and also to prevent the formation of metal sulfides (which are both problematic due to refractory corrosion and also they can cause spontaneous mechanical fracture of the glass if in high enough concentration). Higher concentrations of iron(III) oxide in the starting batch is beneficial for vitrification of wastes with high carbon or metallic content, as it promotes oxidation [25], [26], [41], [42].

2.9 Volatilisation

Volatile loss of radionuclides is a major issue with nuclear waste glass processing. Volatile losses proceed through either volatilisation or entrainment. Above the solidus temperature, where the larger, more refractory particles have not yet fully melted, volatilisation can occur from the initial melt phases. Diffusion through the melt and along pore surfaces is likely to be the mechanism of loss in these cases. Volatilisation from the glass melt will be controlled by diffusion through the liquid [43], see Equation 2-4.

$$M = \left(\frac{4}{\pi}\right)^{\frac{1}{2}} C_0 (Dt)^{1/2}$$ Equation 2-4

where M = mass loss per unit area (kg m^{-2}).
C_0 = initial concentration of volatile material (kg m^{-3}).
D = effective diffusion coefficient of the species (m^2 s^{-1}).
t = time (s) [43].

Some elements within a glass melt promote volatilisation, for example, chlorine significantly volatilises and can increase the volatilisation of other components such as Cs. The volatility of the halides, similarly to the alkali metals, increases as the atomic weight increases. Losses proportional to $t^{1/2}$ indicate diffusion-based loss whereas a linear mass loss with t indicates loss from the surface [44],[45].

2.10 Glass Homogeneity

Amorphous phase separation and inhomogeneity in glassy waste forms are two different phenomena. Amorphous phase separation is a thermodynamic phenomenon explained by the Gibbs energy of mixing of the glass batch, see Equation 2-5. A positive Gibbs energy will lead to amorphous phase separation.

$$\Delta G_{mix} = \Delta H_{mix} - T_{critical} \Delta S_{mix}$$ Equation 2-5

where ΔG_{mix} = Gibbs energy of mixing.
ΔH_{mix} = enthalpy of mixing.
$T_{critical}$ = the critical temperature.
ΔS_{mix} = entropy of mixing [2].

The enthalpy of mixing can be positive or negative depending on bond enthalpies in the batch material, whereas entropy is always a positive term that encourages mixing. A given glass composition will have a critical temperature, $T_{critical}$, below which amorphous phase separation will occur and above which a single amorphous phase will exist [2], [12]. Alkali borosilicate glasses display large regions of immiscibility. The addition of alumina to borosilicate glasses act to supress phase separation, by

lowering the critical temperature. Regions of phase separation in alkali borosilicate glasses are 5 to 20 nm in diameter [2].

Glass inhomogeneities typically occur on a larger scale. Increased glass homogeneity can be obtained through thorough mixing of batch components, low melt viscosity and agitation of melt through bubbling and mechanical stirring. A glass heterogeneity may be a different localised glass composition, (called a striation, and evident as glassy layers of a composition different to that from the bulk), a secondary crystalline phase, bubbles or undissolved batch material. Striae and cords can be also formed at the melt interface and due to the interaction of the glass melt with refractories [2]. Secondary crystalline phases are encountered relatively often in nuclear waste vitrification, either due to low solubility of a waste constituent within the glass melt, or crystallisation during cooling, not prevented by kinetic barriers. Examples of some common secondary phases are highlighted below. "Yellow phase" is a common secondary phase in HLW and even though it is not expected to be a common occurrence in ILW thermal conditioning it is a useful secondary phase to discuss as it highlights some of the problems that secondary phases lead to. Spinels and sulfates are also introduced and as discussed these form both in HLW and ILW.

2.10.1 "Yellow phase"

A common secondary phase in HLW melters, including U.K. HLW, is so-called "yellow phase", these are molybdate-rich phases, but can also contain sulfate and chromate [46]. Mo has a low solubility in typical borosilicate glasses (< 1 wt%), usually has a coordination number of 4 and a typical Mo-O distance of 1.76-1.78 Å. Yellow phase has a low chemical durability and therefore is problematic as it may partition radionuclides [46-47]. An example of an actual phase formed in "yellow phase" is $Na_3Li(MoO_6)_2$, and due to its low density it settles on the surface, forming a separate layer, and can preferentially partition ^{137}Cs and ^{135}Cs, ^{90}Sr, ^{36}Cl and ^{99}Tc, thus enhancing both volatile and leaching losses [42], [48]. Alkali-rich yellow phase will form at the top of the melter whereas alkaline earth-rich yellow phases tend to settle out at the bottom of the melter [42]. Changing the glass chemistry can be used to increase molybdenum incorporation. For example, magnesium aluminosilicates show good promise for incorporation of MoO_3 into the glass structure with a solubility up to

(12 wt%) possible [47]. For HLW vitrification at present waste loadings are less than 25 wt% for alkali borosilicate glasses although studies have found 45 wt% is possible with melting temperatures less than 1100^{o}C if the MoO_3 in the waste feed is kept below 2.5 wt% [49].

2.10.2 Spinels

Another common phase found in glass melts are spinel crystalline phases, AB_2O_4. In general, glasses high in iron tend to form spinel crystalline phases and they usually incorporate Cr, Fe, Ni and Ru if present in the waste [25]. Due to frequent occurrence of spinels in HLW glass melts, an empirical equation has been formulated to predict the final concentration of spinel, as a function of cooling rate and equilibrium kinetic data, for spinel crystallization. Components that are part of the spinel structure typically have high $T_{L,i}$ such as Cr_2O_3 and NiO, where $T_{L,i}$ is the partial specific liquidus temperature of oxide *i* [29], [50]. Spinels have a low impact on waste form performance as they have high aqueous durability and do not incorporate glass-formers. However, due to the high density, sedimentation occurs and spinels settle at the base of a melter, thus causing problems, in the long-term, with continuous glass melting technologies [42]. Cr has low solubility in borosilicate glasses (<2 wt%), and in the presence of Fe, chromium will preferentially partition into spinel phases [51],[52]. In the absence of transition metal ions, if the atmosphere is reducing, eskolaite (Cr_2O_3) will form. In more oxidising atmospheres chromium(VI) will form as a separate liquid chromate phase. Eskolaite is believed to have minimal impact on glass properties (at least in non-continuous melter operations) whereas the liquid chromate phase is undesirable (for the same reason as “yellow phase”[53].

2.10.3 Sulfates

Sulfates in glass melts are problematic as they have high solubility in water and that alkali and alkaline earths readily partition into these salts. The reason for this phase separation is that sulfur has a low solubility limit in glass melts, leading to a molten sulfate layer forming on top of the melt [54]. Sulfide forms under reducing conditions in the melt, however, with time, sulfides will convert to sulfate due to prolonged contact with O_2 during melting [26]. However, some sulfides persist, namely Fe, Cd,

Zn, Sn and Ni, without oxidising. The solubility of SO_3 in typical alkali borosilicate glasses is usually stated as <1 wt% [55], with solubility limits of 0.53- 1.60 wt% [56], and 0.37-2.05 wt% [57] also quoted. One approach to enhance the solubility limit of SO_3 is through the addition of high ionic radii, low field strength cations- such as BaO. There exists a positive linear relationship between increasing total cation field strength and increasing sulfate solubility [25], [26], [55], [58].

2.11 Radioactivity in the Resulting Glass

Initially waste forms will be subjected to β and γ radiation from immobilised radionuclides; irradiation from these types will continue for a few hundred years with the main sources being ^{137}Cs and ^{90}Sr for HLW glass. Gamma radiation in borosilicate glasses results in the formation of boron-oxygen hole centres, which are detectable by electron paramagnetic resonance (EPR). There is evidence that the presence of transition metals such as Fe, Cr, Zr and some actinides, such as U, may inhibit formation of defects by these elements effectively trapping the electrons and hole pairs by redox reactions [27]. In the longer-term α radiation comes to dominate with actinides being the main source- a concern with α radiation is the associated recoil of the daughter nucleus post-emission. As an example, when ^{239}Pu decays to ^{235}U, the uranium nucleus recoils causing damage to the structure of the waste form, with cracking possible [11], [27].

2.11.1 Uranium

In borosilicate glasses, the dominant oxidation state for uranium is 6+, with U(VI) existing as the uranyl species, UO_2^{2+}. This has a coordination number of six or seven oxygen atoms in an octahedral or pentagonal bipyramidal coordination environment [59]. Using the field strength of uranium(VI) it is predicted that it will be an intermediate in the glass. However, EXAFS data suggests that the uranyl group exists in channels, similar to other modifiers, due to evidence of clustering of uranium atoms (demonstrated by short U-U bond distances). The axial uranyl oxygen atoms have a U-O bond distance of approximately 1.8 Å whereas the 4 or 5 equatorial oxygen atoms have longer distances at 2.2 Å [60]. In contrast ^{11}B MAS-NMR data showed that the fraction of four-coordinated B decreases with increasing U(VI) content, indicating that U(VI) acts as an intermediate. In an intermediate role the uranyl species is required to

be charge balanced by around 4 alkali cations with two non-bridging uranyl oxygen ions and 6 equatorial oxygen ions bonding to Si(IV) or B(III), as the coordination number of the U(VI) is now 8 [61].

The +4 and +5 oxidation states of uranium can also exist in glasses. A highly polymerised glass network decreases the solubility of uranium and under reducing conditions only 9 wt% of U(IV) can be dissolved, whereas under oxidising conditions upto 40 wt% of U(VI) will dissolve in the melt [62],[63]. Uranium (V) has a coordination number of six with slight tetragonal, i.e. axial distortion (compression along the z-axis) and uranium(IV) has a coordination number of 8. The redox state of uranium in the glass appears to have a little effect on the durability with uranium leaching at equal rates irrespective of its oxidation state [64].

2.12 Durability Studies

There can be no durability test that fully replicates the conditions that a vitreous waste form would experience in a GDF, should it ever be exposed to ground water. Neither can tests be conducted on a vitreous waste forms (at the same Surface Area to Volume (S.A./V.) and time scale) that can be used to study rates of glass alteration in a GDF. However standards have been developed by ASTM to measure the durability of a waste form under controlled conditions, for example, tests on powdered samples (PCT (product consistency test)) and tests on monolithic samples (MCC-1) [65], [66]. There are certain elements that have a positive influence on glass durability and certain elements that have a negative influence. In general network formers and intermediates such as silica, alumina and iron increase durability, whereas network modifiers, in particular, alkali metals, give the greatest leach rates [1], [67].

2.12.1 Dissolution Mechanisms

The GRAAL (glass reactivity with allowance for the alteration layer) is a computational model that describes the important regimes of glass dissolution [68]. It states that there are three main regimes of glass dissolution (initial rate, rate drop and residual rate) with a possible fourth (rate resumption), see Figure 2-3. A key aspect of

the GRAAL model is that once the solution is saturated, an alteration layer is formed at the surface of the glass [68]. It is diffusion of water, through this gel layer, which is the rate-limiting step for glass dissolution. The stability of the gel, is dependent upon the precipitation of any secondary phases in the leachate and the nature of how the leachate renews itself [68].

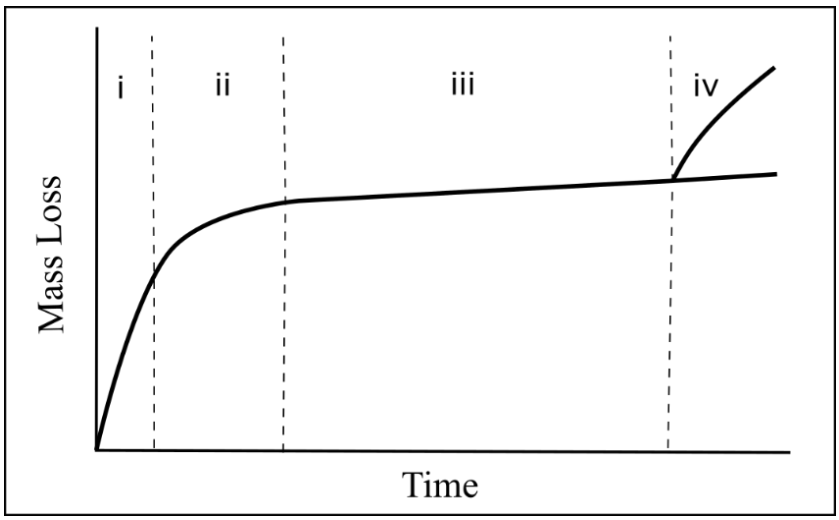

Figure 2-3. Figure showing the different stages of glass dissolution, i) initial rate, ii) rate drop, iii) residual rate and iv) rate resumption.

In the initial rate regime, hydrolysis of the glass network and inter-diffusion (i.e. ions from the glass and protons from solution) occur simultaneously. The initial rate is observed, whilst the leachate is sufficiently dilute, to prevent any effects from leached elements, such as the formation of alteration products. In the initial rate regime, all elements are leached at the same rate, initial dissolution rate is dependent on temperature, pH, and glass composition and also on concentration of ions in solution, [68] see Equation 2-6.

$$r_0 = k^+ [H^+]^n e^{\frac{-E_a}{RT}}$$ Equation 2-6

where k^+ is the forward rate constant.

$[H+]^n$ is a pH dependent factor.

E_a is the activation energy for hydrolysis of the glass [68].

A key concept with the GRAAL model is that the rate that elements are leached into solution depends upon the transport properties of the alteration layer. This alteration layer is described as a "dynamically restructured hydrated glass that with time becomes dense and restricts the corrosion rate" [68].

Other authors have suggested modifications to the GRAAL model, they argue that congruent glass dissolution occurs in the initial rate regime, but that it continues through the residual rate regime. In effect, glass dissolution occurs locally at the pristine glass surface with glass dissolution, and precipitation and growth of the gel layer, occurring simultaneously, from inside to out [69]. It is essentially a reprecipitation process- solutions undersaturated in silica results in the dissolution of glass until saturation of monomeric silica in solution occurs. The solution at the surface is now supersaturated triggering silica nucleation at hydroxylated glass surface sites. The silica reaction rim reaches a critical thickness, where transport of water and solute species through the silica corrosion rim is slower than glass dissolution and contemporaneous silica deposition [69]. It is known that, at high ionic strengths, aggregation of silica particles can take place, even in alkaline solutions, although a homogeneous gel may not form owing to partial silica precipitation before gel formation [70].

2.12.2 HLW Glass Dissolution

Many studies on HLW glass dissolution have been conducted to qualify them for final disposal, it is worth reviewing some of the key literature on HLW dissolution to enable to comparison of ILW glass performance given the relatively underdeveloped ILW glass literature. At a S.A./V. ratio of 2000 m^{-1}, at 25 wt% waste loading (75 wt% from reprocessed AGR and PWR fuel and 25 wt% from reprocessed Magnox fuel), over 7 days, the normalised release rates of waste loaded MW glass are as follows: NL_B of 0.79 g $m^{-2}d^{-1}$, NL_{Na} of 0.59 g $m^{-2}d^{-1}$ and NL_{Si} of 0.08 g m^{-2} d^{-1} [71]. MW glass, modified to incorporate 1.8 wt% CaO and 5.6 wt% ZnO, and waste loaded (75 wt% oxide fuel / 25 wt% Magnox fuel) to 20 wt%, were leached for 28 days at 90 ^{o}C in deionised water and at a S.A./V. ratio of 1200 m^{-1}. The effect of the addition of CaO and ZnO was to increase durability, with NL_B of 0.37 g m^{-2} d^{-1} and NL_{Na} of 0.23 g m^{-2} d^{-1} [72]. The leachates typically buffer to pH 9.5-10.0 for waste loaded MW glasses

altered using the PCT-B protocol. In another study, a simulant of waste loaded MW glass was corroded using both the PCT and MCC-1 methodologies at 90 ^{o}C with S.A./V. ratios of 1200 m^{-1} and 10 m^{-1} respectively using MCC-1. A NL_B of 1.2 g m^{-2} d^{-1} was obtained after 90 days. It was found that increasing the temperature incrementally from 70, 90 and 110 ^{o}C increased the initial rate but had minimal effect on the residual rate. Hectorite, $Mg_{5.33}Li_{0.67}Si_8O_{20}(OH)_4$ (a clay mineral) was found to be the main precipitate on the surface of the glass [73].

SON 68 frit, see Table 2-2 for composition, was altered at buffered pHs of 7, 8.5, 9.5, 10, 10.5, 11 and 11.5, at a S.A./V ratio of 5000 m^{-1} and at 90 ^{o}C. At pH 11, and higher, the precipitation of aluminium and sodium aluminosilicates led to the resumption of glass dissolution and rapid rate resumption. This was driven by the solubility of Al which is higher at high pH, below pH 10, there is insufficient Al in solution to induce this type of secondary phase precipitation and the passivating effect of the layer is retained [74]. Another study using PCT on SON68 and MW glasses, at 90 ^{o}C and a S.A./V. ratio of 1200 m^{-1} were performed. The dissolution of the MW glass was found to be almost an order of magnitude greater than for the SON68 base glass, based on B and Li as dissolution tracers. Alteration of MW glass produced Mg-containing clay mineral precipitates, whereas SON68 glass produced a smaller quantity of Ca-Zn-Fe-Ni-containing clay minerals in the alteration layer. It was suggested in this study that Mg in solution, after dissolution from the glass, promotes corrosion due to this precipitate [75]. A mechanism suggested for this is due to the silica and alumina in the alteration layer being taken up in the secondary clay mineral structure, thus accelerating dissolution due to a thinner alteration layer and Si under-saturation in solution [76]. Longer term dissolution rates were calculated using linear regression, on samples leached for longer than 500 days, giving $9.6 \pm 5.0 \times 10^{-4}$ g m^{-2} d^{-1} for MW and $1.3 \pm 0.2 \times 10^{-4}$ g m^{-2} d^{-1} for SON68 [75].

ISG glass was altered for 511 days at 50 ^{o}C and a S.A/V. ratio of 20,000 m^{-1}, with additions of Zn, Mg, Ni and Co to solution at regular monthly intervals. All additions led to the formation of secondary phases, identified to be tri-ocathedral smectite clays, with molecular formula $Mg_3Si_4O_{10}(OH)_2$, but where Al can substitute into the Si site up to 0.45 and where Al, Zn, Ni and Co can substitute into the Mg site. A pH > 8 is needed for Mg smectite phases to crystallise. In all cases, the addition of Zn, Mg, Ni

and Co lead to an increase in NL_B compared to no additions [77]. Dissolution rate increases from neutral to higher pHs. For example, at pH > 9, at 90 ^{o}C, the dissolution rate was reported to be 2.38-3.06 g m^{-2} d^{-1} for SON68 and a novel Li_2O-MgO-Na_2O-Al_2O_3-Fe_2O_3-B_2O_3-SiO_2 glass, significantly higher than when in neutral conditions [74],[78]. These studies used alkali metal hydroxides which do not interact with the dissolved glass components during the early stages of dissolution, whereas, the calcium ion interacts with dissolved leached species, in particular Si. An important point for glass dissolution is that radionuclides may be retained in the alteration layer, or form as secondary precipitates on the surface of the glass, therefore, glass dissolution rates are not sufficient to predict their release, only an upper limit on the release rate [75].

2.12.3 Calcium in Glasses and in Solution

The large amount of cement envisioned to be in the U.K.'s GDF, originating from both cemented ILW and the use of cement as a backfill, means that in the event of groundwater infiltrating the facility it will likely become saturated with Ca, creating hyperalkaline leachates, due to the formation of concentrated $Ca(OH)_{2(aq)}$. It has been observed, in various studies, that dissolution in Ca-rich leachates, hinders glass dissolution, both in the initial rate regime and during the residual rate regime, due to the formation of a calcium silicate hydrate (C-S-H) gel on the surface of borosilicate glasses [79].

In one study blended waste loaded MW glass was leached using the PCT-B (S.A/V. of 10 000 m^{-1}) and MCC-1 (S.A/V. of 10 m^{-1}) protocols in both de-aerated water and de-aerated saturated $Ca(OH)_2$ solution, at 50 ^{o}C. For PCT-B the normalised mass loss, NL_B, in water, was rapid for the initial 28 day period, followed by a slower rate from day 28 to the end of the experiment. This trend is also shown by Na, Si and Li. In $Ca(OH)_2$ solutions lower normalised mass losses were observed, as well as three main dissolution periods (0-28, 28-84 and 84-168 days) in contrast to two main dissolution periods when in water (initial and residual rate).The reason for the lower rates in $Ca(OH)_2$ solution, compared to in water, is suggested to be because of the quasi-equilibrium is reached between the aqueous phase rich in Ca and Si and the C-S-H phase [80].

Pilot scale and laboratory scale vitrified ILW (clinoptilolite/ Magnox sludge and PCM waste) have also been leached in saturated $Ca(OH)_2$ solutions at S.A./V. ratios from 1200 to 1350 m^{-1}. For the full scale clinoptilolite/Magnox sludge and PCM glass, the usual regimes of initial, rate drop and residual regimes are observed whereas the laboratory scale glass showed an "incubation period." This incubation period was hypothesised to be due to an interaction between boron (present in much higher concentrations in the lab scale melt) and Ca, in solution, forming dissolution-inhibiting calcium borates on the surface of the glass [33], [80]. These persist until C-S-H phases begin to precipitate at which point the calcium borates dissolve and dissolution of the pristine glass continues. The authors found that the dissolution was much lower than that expected when in high pH, due to formation of Ca-rich phases on the surface of the glass [33]. A further study on similar vitrified ILW at a much higher S.A./V. ratio of 10,000 m^{-1}, reached the residual rate as well as rate resumption being observed after 56 days. It was concluded this this was due to the precipitation of Mg-rich saponite clays (in addition to C-S-H phases), thereby stimulating rate resumption [81]. A dissolution study at pH 9 (a lower pH than saturated $Ca(OH)_2$ solution, which is ~12.5), at 90 ^oC, on a novel Na_2O-CaO-ZrO_2-B_2O_3-Al_2O_3-SiO_2 glass found a Ca-rich alteration layer was again observed but not C-S-H, believed to be due lower pH that prevented precipitation of the C-S-H phase [82]. This study indicates Ca will incorporate into the alteration layer regardless of whether it originates from the solution or from the glass and that this incorporation acts to lower glass dissolution.

2.12.4 Magnesium in Glasses and in Solution

The precipitation of Mg-containing secondary phases from solution and the glass alteration layer accelerates glass corrosion. This rate resumption is attributed to consumption of Si from the alteration layer into Mg-containing clays, the removal of this alteration layer causes rate resumption at a rate equal to or less than the initial rate [83].

Further studies have examined the effect of Mg in solution on the dissolution of HLW. In one experiment, with a high S.A/ V. ratio of 20,000 m^{-1}, SON68 was dissolved over 114 days at 50 ^oC. After 29 days, Mg was added to the leachate to trigger precipitation of Mg-silicate. A time lag is observed (~7 days) between the addition of Mg and the

resumption of glass alteration because silicon is first provided by partial dissolution of the previously formed alteration gel. A pH > 8 is necessary for the phase to precipitate [83]. Two sets of novel AVM glasses (Na_2O-ZrO_2-Al_2O_3-B_2O_3-SiO_2), batched with and without MgO, were altered with and without addition of Mg to solution at 50 ^oC. The S.A./V. ratio was 5500 and 20,000 m^{-1} and the experiment ran for 2500 days. It was found that glasses containing MgO were less altered than those without, as the MgO from the glass incorporates into the alteration layer as a charge compensator, thus inhibiting dissolution. Smectite clay precipitation, and subsequent rate increase, was only observed when both the Mg originated from solution only and where Mg could not be incorporated into the alteration layer as a charge compensator [84]. The conclusion is that Mg in solution, with time, becomes incorporated into the alteration layer increasing its passivating properties; however, when there is already Mg in the alteration layer secondary phases form, which increase the dissolution rate. The affinity of the gel is highest for Ca, Mg and Na in that order, therefore magnesium will get taken up by the gel if the gel is Na-rich but will not if it is Ca-rich [84]. With Ca in solution it will form part of the alteration layer and Mg remained in solution. If the pH is > 8.5 the magnesium will precipitate leading to rate resumption as silica is taken from the gel however if the pH < 8 the magnesium silicate will not precipitate and the alteration layer decreases the rate [84].

2.13 Waste Streams

As first introduced in section 1 this thesis is structured with each ILW stream forming its own separate results chapter (forming chapters 4, 5 and 6). In this sub-section background information on the three different waste streams studied is provided. In chapter 4 encapsulated Magnox swarf waste drums, showing evidence of expansion, are reworked utilising thermal conditioning. For this reason some background information on Portland cement blends in provided. The purpose of reworking these drums using thermal conditioning is to remove the underlying reactants causing the underlying corrosion by oxidising the Magnox and driving off the water. In chapter 5 spent clinoptilolite produced from ion exchanging fission products from waste effluent is thermally condition with the aim of producing low melting glass formulations to maximise Cs retentions. For this reason background information on zeolites in

provided. In chapter 6 the thermal co-conditioning of Magnox sludge and clinoptilolite / sand waste is explored with the aim of waste loadings to produce low final waste volumes, therefore an introduction to Magnox sludges is also provided.

2.13.1 Cement

Materials classified as ILW, in the U.K., are usually encapsulated in Portland based cement blends, the different encapsulation plants found at the Sellafield site are shown in Table 2-4. Portland cement is a powder consisting of the phases alite (denoted C_3S), belite (C_2S), tricalcium aluminate (C_3A) and tetracalcium aluminoferrite (C_4AF), with a small amount of gypsum to prevent flash setting of the tetracalcium aluminate phase [85]. The products, when water is added to Portland cement, are Portlandite ($Ca(OH)_2$) and an amorphous, or partially crystalline, calcium silicate hydrate (C-S-H) gel, covering a wide molar ratios of Ca and Si and capable of incorporating other elements. These are the products formed from the reaction of C_3S and, the much slower reaction of C_2S with water. The reaction of C_3A and C_4AF produces ettringite (AFt) with molecular formula $3CaO.\ Al_2O_3.\ 3CaSO_4.32H_2O$ as well as monosulfate (AFm) with molecular formula $3CaO.\ Al_2O_3.\ CaSO_4.12H_2O$ [85].

The primary phase in hydrated cement is calcium silicate hydrate (C-S-H) with setting and hardening behaviour dependent on this gel. It has a very high surface area, which can be beneficial for nuclear waste encapsulation as radionuclides can be potentially sorbed onto the gel. Pores in hydrated Portland Cement (PC) based systems are 95-98% hydrated after 12 months and contain pores about one micron in diameter [1]. PC is often used with modifiers to improve the properties of the resulting waste form. Examples of modifiers, often used to form 30 wt% to 90 wt% of the cement blend, are BFS (blast furnace slag) and PFA (pulverised fuel ash). One of the primary uses of modifier additions is to lower the heat output during the hydration reactions [1].

Table 2-4.
Current operating cementation plants for ILW in the U.K. [86].

Encapsulation Plant	Year of First Operation	Waste Stream	Method of Encapsulation
MEP (Magnox encapsulation plant)	1992	Magnox cladding	Grout infilling
WEP (waste encapsulation plant)	1994	Fuel cladding sludge	Grout infilling and in-drum mixing
WPEP (waste packaging encapsulation plant)	1994	Effluents and flocs	In-drum mixing
WTC (waste treatment complex)	1996	Plutonium-contaminated materials (PCM)	Super compaction and annulus grouting

2.13.2 Clinoptilolite

Zeolites are layered aluminosilicate minerals, which are often used in ion exchange processes, as they have the ability to ion exchange different cations based on size and also shape. They are formed by corner-sharing SiO_2 and Al_2O_3 tetrahedra with fixed bond angles at 109.5^o, however, the bond length between bridging tetrahedral units varies [87]. The pore sizes of zeolites range from 3-30 Å. Clinoptilolite is nominally given the formula $(Na,K)_6Si_{30}Al_6O_{72}.nH_2O$. Its structure is very similar to heulandite, and is distinguished from it by having a minimum molar ratio of Si/Al > 4 and is also generally more enriched in potassium. In clinoptilolite the molar ratio of SiO_2 to Al_2O_3 is 5.18:1.

An important parameter for zeolites is the distribution coefficient, K_d, (L g^{-1}), a pH dependent quantity, which is a measure of the ratio of concentration of a species between two immiscible phases at equilibrium, see Equation 2-7.

$$K_d = \frac{[C]_s}{[C]_l} \times \frac{V}{m}$$ Equation 2-7

where $[C]_s$ is the concentration of the species in the solid phase.
$[C]_l$ is the concentration of the species in the liquid phase.
V is the volume of solution, m is the mass of exchange material.

It is known that the presence of other cations of similar size affects the capacity for sorption of caesium, for example the presence of 0.02 M $KCl_{(aq)}$ solution decreased the distribution coefficient from 3.9 to 1.9 L g^{-1} for a naturally occurring clinoptilolite sample [88],[89]. Clinoptilolite used at the Sellafield site is from a deposit near Barstow, California [90].

2.13.3 Sludges

Spent Magnox fuel has historically been stored wet in ponds and silos. Corrosion in storage ponds is limited by maintaining the pH at least above 10.5 with sodium hydroxide, however, corrosion still occurs. Magnox fuel cladding initially corrodes to the mineral brucite ($Mg(OH)_2$) due to hydration of the magnesium oxide layer present on the surface of the alloy [91], [92]. This can release Cs radioisotopes into the ponds as well as Sr-90. Wet storage strategies have led to a range of heterogeneous and, as of yet, poorly characterised sludges, with various solids to water ratios. Brucite has a low solubility (~10 ppm) in water and is fairly unreactive, causing it readily to form sludges. Cementation of Magnox sludge in typical nuclear cement blends results in encapsulation of brucite crystals by hydrated cement phases. There is no incorporation of Mg into the C-S-H phases, the only possible reaction between the sludge and the hydrating cement is to produce a small quantity of hydrotalcite phase [92].

On occasion, the water in the storage ponds are pumped through the SIXEP plant before discharge to the sea and the water is replenished. A typical composition of sludge water is shown in Table 2-5. Prior to 1985 the pond water was discharged without any treatment directly into the Irish sea [90]. Initially, effluent from the fuel

storage ponds was allowed to settle in the Bulk Storage Tanks (BSTs) for periods ranging from 10 h to a week before being processed through SIXEP [91]. This resulted in the formation of sludge at the base of the BSTs, an estimated composition of which is shown in Table 2-5 [93]. At SIXEP there are two ion exchange columns filled with the ion exchange material clinoptilolite. Prior to this there are sand pressure filters (to remove fine particles of Magnox sludge taken up by the pumps) and carbonating towers (to reduce the pH to about 7). Storage tanks (nominally 1000 m^3) are used to store spent ion exchange material and any materials that the sand pressure filters have collected after backwashing [90]. As can be observed most of the elements in the effluent settle and concentrate in the sludge, particular Mg and U.

Table 2-5.
Typical concentration of ions in SIXEP effluent in BST wet sludge [93], [94].

Oxide	Concentration in SIXEP input effluent (ppm)	Concentration in wet sludge (ppm)
Mg	0.7	97000
U	No data	100000
Ca	1.5	8000
Cl	5	8200
Na	100	5600
K	No data	6000
Al	No data	2900
Fe	No data	3100
SO_3	5	900
Cs	2	< 1
Sr	0.1	< 1
Si	10	< 1
NO_3	5	< 1

Activities of the three ILW streams studied in this thesis are shown in Table 2-6. The U-238 wt% values are from the given references with the specific activity calculated from the wt% data, whereas the specific activities of Cs-137, Sr-90, Pu-241 and Cs-134 are from the given references with the wt% calculated from the given activities.

2.13.4 Waste Conditioning

The prospect of thermal conditioning of the ILW streams discussed in this chapter, i.e. corroding cement encapsulated Magnox swarf drums, ion-exchanged clinoptilolite, sand filters and Bulk Storage Tank sludges is attractive for many reasons. These reasons vary from each waste stream from passivating a waste stream that is evolving

with time to conditioning of wastes that are incompatible with current cementation conditioning. Ultimately the main benefits are significant reductions in waste volumes, improved passive safety and the production of waste forms with high chemical durability. The rest of this thesis will explore this prospect by producing simulant waste streams, thermal conditioning on a laboratory scale and analysis of the resulting waste forms using the experimental techniques detailed in the next chapter.

Table 2-6.
Some of the radioisotopes present in selected ILW streams. Data collected from [93], [95], [96], [97] and [98].

Isotope	Cemented Magnox Fuel Cladding from MEP				Clinoptilolite/ Sand from SIXEP				Magnox Sludge from Bulk Storage Tanks			
	Higher Specific Activity Estimate / TBq m^{-3}	Lower Specific Activity Estimate / TBq m^{-3}	Higher Mass Content in Waste / wt%	Lower Mass Content in Waste / wt%	Higher Specific Activity Estimate / TBq m^{-3}	Lower Specific Activity Estimate / TBq m^{-3}	Higher Mass Content in Waste / wt%	Lower Mass Content in Waste / wt%	Higher Specific Activity Estimate / TBq m^{-3}	Lower Specific Activity Estimate / TBq m^{-3}	Higher Mass Content in Waste / wt%	Lower Mass Content in Waste / wt%
U-238	1.5×10^{-4}	1.2×10^{-4}	0.64	0.52	4.0×10^{-5}	3.3×10^{-5}	0.23	0.19	6.2×10^{-3}	5.1×10^{-3}	33.0	27.3
Cs-137	21.5	9.5	3.6×10^{-4}	1.6×10^{-4}	180.0	6.0	4.0×10^{-3}	1.3×10^{-4}	21.3	0.7	4.4×10^{-4}	1.5×10^{-5}
Sr-90	28.5	3.2	3.0×10^{-4}	3.3×10^{-5}	18.9	0.6	2.6×10^{-6}	8.8×10^{-8}	90.0	0.3	1.2×10^{-3}	3.9×10^{-6}
Pu-241	46.5	5.2	6.6×10^{-4}	7.3×10^{-5}	1.0	0.1	1.8×10^{-7}	2.1×10^{-8}	81.0	9.0	1.4×10^{-3}	1.6×10^{-4}
Ce-144	86.7	38.5	4.0×10^{-5}	1.8×10^{-5}	/	/	/	/	0.5	0.1	2.5×10^{-7}	2.8×10^{-8}
Cs-134	8.0	3.6	9.0×10^{-6}	4.0×10^{-6}	2.2	0.1	3.2×10^{-8}	1.1×10^{-9}	0.4	0.01	5.01×10^{-7}	1.7×10^{-8}
Volume of waste (m^3)	12780				2460				1250			

2.14 References

[1] M. L. Ojovan and W. E. Lee, “An Introduction To Nuclear Waste Immobilisation,” 2nd ed., Oxford: Elsevier, 2005, pp. 81–85, 187, 213–248, 259–268.

[2] J. E. Shelby, “Introduction to Glass Science and Technology,” 2005, pp. 3–6, 26–48, 93–100, 154–159, 198–200.

[3] A. C. Wright, “The great crystallite versus random network controversy: A personal perspective,” *Int. J. Appl. Glas. Sci.*, vol. 5, no. 1, pp. 31–56, 2014.

[4] A. Paul, “Chemistry of Glasses,” 2nd ed., London: Chapman and Hall, 1990, pp. 1–15.

[5] J. Randall, H. Rooksby, and B. Cooper, “X-ray Diffraction and the Strcuture of Vitreous Solids - I,” *Z. Krist.*, vol. 75, pp. 196–214, 1930.

[6] W. Rosenhain, “The Structure and Constitution of Glass,” *J. Soc. Glas. Technol. Trans.*, vol. 11, pp. 77–97, 1927.

[7] N. Valenkov and E. Poray-Koshitz, “X-Ray Investigation of the Glassy State,” *Z. Krist.*, vol. 95, pp. 195–229, 1936.

[8] A. Dietzel, “Die Kationenfeldstarken und ihre Beziehungen zu Entglasungsvorgangen, zur Verbindungsbildung und zu den Schmelzpunkten von Silikaten,” *Z. Elektrochem.*, vol. 48, pp. 9–23, 1942.

[9] R. H. Doremus, “Glass Science,” 2nd ed., New York: John Wiley & Sons, 1994, pp. 113–121.

[10] C. T. Moynihan, A. J. Easteal, M. A. De Bolt, and J. Tucker, “Dependence of the Fictive Temperature of Glass on Cooling Rate,” *J. Am. Ceram. Soc.*, vol. 59, no. 1–2, pp. 12–16, 1976.

[11] I. W. Donald, “Waste Immobilisation in Glass and Ceramic Based Hosts-Radioactive, Toxic and Hazardous Wastes,” 1st ed., Chichester: Wiley, 2010, pp. 1–31, 57–177, 275–334, 465–490.

[12] W. Vogel, “Glass Chemistry,” 2nd ed., Berlin: Springer-Verlag, 1994, pp. 123–157.

[13] B. C. Bunker, D. R. Tallant, R. J. Kirkpatrick, and G. L. Turner, “Multinuclear nuclear magnetic resonance and Raman investigation of sodium borosilicate glass structures,” *Phys. Chem. Glas.*, vol. 31, pp. 30–41, 1990.

[14] M. W. Phillips, G. V. Gibbs, and P. H. Ribbe, “The Crystal Structure of Danburite: A Comparison with Anorthite, Albite and Reedmergnerite,” *Am.*

Mineral., vol. 59, pp. 79–85, 1974.

[15] D. Manara, A. Grandjean, and D. R. Neuville, "Advances in Understanding the Structure of Borosilicate Glasses: A Raman Spectroscopy Study," *Am. Mineral.*, vol. 94, pp. 777–784, 2009.

[16] U. Selvaraj and K. J. Rao, "Infrared spectroscopic study of mixed-alkali effect in borate glasses," *Spectrochim. Acta Part A Mol. Spectrosc.*, vol. 40, no. 11–12, pp. 1081–1085, 1984.

[17] W. J. Dell, P. J. Bray, and S. Z. Xiao, "^{11}B NMR Studies and Structural Modelling of Na_2O-B_2O_3-SiO_2 glasses of high soda content," *J. Non. Cryst. Solids*, vol. 58, pp. 1–16, 1983.

[18] Y. H. Yun and P. J. Bray, "Nuclear Magnetic Resonance Studies of Glasses in the System Na_2O- B_2O_3- SiO_2," *J. Non. Cryst. Solids*, vol. 27, pp. 363–380, 1978.

[19] Y. H. Yun, S. A. Feller, and P. J. Bray, "Correction and Addendum to 'Nuclear Magnetic Resonance Studies of the Glasses in the system Na_2O-B_2O_3-SiO_2,'" *J. Non. Cryst. Solids*, vol. 33, pp. 273–277, 1979.

[20] W. F. Du, K. Kuraoka, T. Akai, and T. Yazawa, "Study of Al_2O_3 effect on structural change and phase separation in Na_2O-B_2O_3-SiO_2 glass by NMR," *J. Mater. Sci.*, vol. 35, pp. 4865–4871, 2000.

[21] J. Kjeldsen, M. M. Smedskjaer, J. C. Mauro, R. E. Youngman, L. Huang, and Y. Yue, "Mixed alkaline earth effect in sodium aluminosilicate glasses," *J. Non. Cryst. Solids*, vol. 369, pp. 61–68, 2013.

[22] P. A. Bingham, R. J. Hand, and C. R. Scales, "Immobilization of simulated plutonium-contaminated material in phosphate glass: an initial scoping study," *Mater. Res. Soc. Symp. Proc.*, vol. 932, pp. 345–352, 2006.

[23] N. C. Hyatt, S. Morgan, M. C. Stennett, C. R. Scales, and D. Deegan, "Plasma vitrification of waste plutonium contaminated materials," *Mater. Res. Soc. Proc.*, vol. 985, pp. 393–398, 2007.

[24] N. C. Hyatt, R. R. Schwarz, P. A. Bingham, M. C. Stennett, C. L. Corkhill, P. G. Heath, R. J. Hand, M. James, A. Pearson, and S. Morgan, "Thermal Treatment of Simulant Plutonium Contaminated Materials From The Sellafield Site By Vitrification In A Blast-Furnace Slag," *J. Nucl. Mater.*, vol. 444, pp. 186–199, 2014.

[25] P. A. Bingham, N. C. Hyatt, and R. J. Hand, "Vitrification of UK intermediate level radioactive wastes arising from site decommissioning: property modelling and selection of candidate host glass compositions," *Glas. Technol. Eur. J. Glas. Sci. Technol. A*, vol. 53, pp. 83–100, 2012.

[26] P. A. Bingham, N. C. Hyatt, and R. J. Hand, “Vitrification of UK intermediate level radioactive wastes arising from site decommissioning. Initial laboratory trials,” *Glas. Technol Eur. J. Glas. Sci. Technol. A.*, vol. 54, no. 1, pp. 1–19, 2013.

[27] O. J. McGann, P. . Bingham, R. J. Hand, A. S. Gandy, M. Kavčič, M. Žitnik, K. Bučar, R. Edge, and N. C. Hyatt, “The effects of gamma radiation on model vitreous wasteforms intended for the disposal of intermediate and high level radioactive wastes in the UK,” *J. Nucl. Mater.*, vol. 429, pp. 353–367, 2012.

[28] I. W. Donald, “Immobilisation Of Radioactive And Non-Radioactive Wastes In Glass-Based Systems: An Overview,” *Glas. Technol Eur. J. Glas. Sci. Technol. A.*, vol. 48, pp. 155–163, 2007.

[29] P. Hrma, J. D. Vienna, and M. J. Schweiger, “Liquidus Temperature Limited Waste Loading Maximisation For Vitrified HLW,” *Ceram. Trans.*, vol. 72, pp. 449–56, 1996.

[30] P. R. Hrma, D. S. Kim, J. D. Vienna, J. Matyas, D. E. Smith, M. J. Schweiger, and J. D. Yeager, “Testing of Large-Scale ICV Glasses with Hanford LAW Simulant,” 2005.

[31] D. A. McQuarrie and J. D. Simon, “Physical Chemistry: A Molecular Approach,” in *Physical Chemistry: A Molecular Approach*, 1st edn., San Francisco: University Science Books, 1997, pp. 118–124, 257–260, 292–302.

[32] K. Witwer, S. Woosley, B. Campbell, M. Wong, and J. Hill, “GeoMelt ICV Treatment of Sellafield Pond Solids Waste,” *Proc. Waste Manag. Symp.*, 2013.

[33] C. A. Utton, R. J. Hand, P. A. Bingham, N. C. Hyatt, S. W. Swanton, and S. J. Williams, “Dissolution of vitrified wastes in a high-pH calcium-rich solution,” *J. Nucl. Mater.*, vol. 435, pp. 112–122, 2013.

[34] J. Deckers, “The innovative plasma tilting furnace for treatment of radioactive and problematic chemical waste,” in *Thermal treatment of radioactive wastes: research, development and demonstration*, 2013, p. http://www.sheffield.ac.uk/polopoly_fs/1.384714!/f.

[35] D. Deegan and C. Scales, “The role of Tectronics plasma vitrification technology in the management and conditioning of nuclear waste,” *Proc. Int. Conf. Environ. Remediat. Radioact. Waste Manag.*, pp. 1179–1189, 2009.

[36] P. Bingham, a J. Connelly, N. C. Hyatt, and R. J. Hand, “Corrosion of glass contact refractories for the vitrification of radioactive wastes: a review,” *Int. Mater. Rev.*, vol. 56, no. 4, pp. 226–242, 2011.

[37] M. N. Elliot, R. Gayler, J. R. Grover, and W. H. Hardwick, “Fixation of radioactive waste in glass. Part I. Pilot-Plant Experience at Harwell,” *Treat.*

Storage High-Level Radioact. Wastes, pp. 465–487, 1962.

[38] É. Vernaz and J. Bruezière, "History of Nuclear Waste Glass in France," *Procedia Mater. Sci.*, vol. 7, no. December 2014, pp. 3–9, 2014.

[39] X. D. Lu, H. Gan, A. C. Buechele, and I. L. Pegg, "Corrosion of K-3 glass-contact refractory in sodium-rich aluminosilicate melts," *Mater. Res. Soc. Symp. Proc.*, vol. 556, pp. 279–286, 1999.

[40] N. C. Hyatt and M. James, "Thermal Treatment of ILW," *Nuclear Engineering International*, pp. 10–14, 2013.

[41] F. Farges, Y. Lefrere, S. Rossano, A. Berthereua, G. Calas, and G. E. Brown Jr., "The effect of redox state on the local structural environment of iron in silicate glasses: a combined XAFS spectroscopy, molecular dynamics and bond valence study," *J. Non. Cryst. Solids*, vol. 334, p. 176, 2004.

[42] P. B. Rose, D. I. Woodward, M. I. Ojovan, N. C. Hyatt, and W. E. Lee, "Crystallisation of a simulated borosilicate high-level waste glass produced on a full-scale vitrification line," *J. Non. Cryst. Solids*, vol. 357, pp. 2989–3001, 2011.

[43] M. Cable and M. A. Chaudry, "Volatisation from soda-lime-silica melts at one atmosphere and reduced pressures," *Glas. Technol*, vol. 16, pp. 125–134, 1975.

[44] B. P. Spalding, "Volatilisation of caesium-137 from soil with chloride amendments during heating and vitrification," *Environ. Sci. Technol.*, vol. 28, pp. 1116–1123, 1994.

[45] R. W. Goles and G. J. Sevigny, "Off-Gas Characteristics of Defence Waste Vitrification Using Liquid-Fed Joule Heated Ceramic Melters, PNNL-4819-UC70, Pacific Northwest National Laboratory, Richland, Washington," 1983.

[46] D. Caurant, O. Majerus, E. Fadel, M. Lenoir, C. Gervais, and O. Pinet, "Effect of Molybdenum on the structure and on the crystallisation of SiO_2-Na_2O-CaO-B_2O_3 glasses," *J. Am. Ceram. Soc.*, vol. 90, pp. 774–783, 2007.

[47] S. Tan, M. I. Ojovan, N. . Hyatt, and R. J. Hand, "MoO3 incorporation in magnesium aluminosilicate glasses," *J. Nucl. Mater.*, vol. 458, pp. 335–342, 2015.

[48] W. E. Morgan , S. , Hand , R. J. , Hyatt , N. C. , and Lee, "Interactions of simulated high level waste (HLW) calcine with alkali borosilicate glass," *Mater. Res. Soc. Symp. Proc.*, vol. 807, pp. 151–156, 2004.

[49] K. Kawamura and J. Ohuchi, "Characterisation of highly waste loaded glass for HLW," *Mater. Res. Soc. Symp. Proc.*, vol. 353, pp. 87–93, 1995.

[50] D. G. Casler and P. Hrma, "Nonisothermal kinetics of spinel crystallization in a

HLW glass," *Mater. Res. Soc. Symp. Proc.*, vol. 556, pp. 255–262, 1999.

[51] M. Mika, M. J. Schweiger, J. D. Vienna, and P. Hrma, "Liquidus temperature of spinel precipitating high-level waste glasses," *Sci. Basis Nucl. Waste Manag. XXX*, p. 71, 1997.

[52] P. Hrma, G. F. Piepel, P. E. Redgate, D. E. Smith, M. J. Schweiger, J. D. Vienna, and D. S. Kim, "Prediction of Processing Properties for Nuclear Waste Glass," *Ceram. Trans.*, p. 505, 1995.

[53] P. Hrma, J. D. Vienna, B. K. Wilson, T. J. Plaistead, and S. M. Heald, "Chromium phase behaviour in a multi-component borosilicate glass melt," *J. Non. Cryst. Solids*, vol. 352, p. 2114, 2006.

[54] P. A. Bingham and R. J. Hand, "Sulphate incorporation and glass formation in phosphate systems for nuclear and toxic waste immboilisation," *Mater. Res. Bull.*, vol. 43, pp. 1679–1693, 2008.

[55] P. A. Bingham, S. Vaishnav, S. D. Forder, A. Scrimshire, B. Jaganathan, J. Rohini, J. C. Mana, K. M. Fox, E. M. Pierce, P. Workman, and J. D. Vienna, "Modelling the sulfate capacity of simulated radioactive waste borosilicate glasses," *J. Alloys Compd.*, vol. 695, pp. 656–667, 2017.

[56] A. A. Kruger, H. Gan, I. L. Pegg, W. K. Kot, and Z. Feng, "Final Report - Sulfate Solubility in RPP-WTP HLW Glasses, VSL-06R6780-1," 2006.

[57] J. D. Vienna, D.-S. Kim, I. S. Muller, G. F. Piepel, and A. A. Kruger, "Toward Understanding the Effect of Low-Activity Waste Glass Composition on Sulfur Solubility," *J. Am. Ceram. Soc.*, vol. 97, no. 10, pp. 3135–3142, 2014.

[58] C. M. Jantzen, M. E. Smith, and D. K. Peeler, "Dependency of Sulfate Solubility on Melt Composition and Melt Polymerisation," *Ceram. Trans.*, vol. 168, pp. 141–152, 2005.

[59] G. N. Greaves, N. T. Barrett, G. M. Antonini, F. R. Thornley, B. T. M. Willis, and A. Steel, "Glancing Angle X-ray Absorption Spectroscopy of Corroded Borosilicate Glass Surfaces Containing Uranium," *J. Am. Chem. Soc.*, vol. 111, p. 4313, 1989.

[60] F. Farges, C. W. Ponader, G. Calas, and G. E. Brown, "Structural environments of incompatible elements in silicate glass/melt systems: U(IV), U(V), U(VI)," *Geochim. Cosmochim. Acta*, vol. 56, pp. 4205–4220, 1992.

[61] A. J. Connelly, N. C. Hyatt, K. P. Travis, R. J. Hand, M. C. Stennett, A. S. Gandy, A. P. Brown, and D. C. Apperley, "The effect of uranium oxide additions on the structure of alkali borosilicate glasses," *J. Non. Cryst. Solids*, vol. 378, pp. 282–289, 2013.

[62] H. D. Schreiber and G. B. Balazs, “The Chemistry of Uranium in Borosilicate Glasses. Part 1. Simple Base Compositions Relevant to the Immobilisation of Nuclear Waste,” *Phys. Chem. Glas.*, vol. 23, p. 139, 1982.

[63] H. D. Schreiber, G. B. Balazs, P. L. Jamison, and A. P. Shaffer, “The Chemistry of Uranium in Borosilicate Glasses. Part 2. Base Compositions Containing Titanium Relevant to the Immobilisation of Nuclear Waste,” *Phys. Chem. Glas.*, vol. 23, p. 147, 1982.

[64] H. D. Schreiber, G. B. Balazs, and T. N. Solberg, “Chemistry of Uranium in Borosilicate Glasses. Part 6. The Leaching of Uranium from Glass,” *Phys. Chem. Glas.*, vol. 26, p. 35.

[65] ASTM, “C1285 - 14. Standard Test Methods for Determining Chemical Durability of Nuclear, Hazardous, and Mixed Waste Glasses and Multiphase Glass Ceramics: The Product Consistency Test (PCT),” West Conshohocken, PA, 2014.

[66] ASTM, “C1220 - 17. Standard Test Method for Static Leaching of Monolithic Waste Forms for Disposal of Radioactive Waste,” West Conshohocken, PA, 2017.

[67] J. . Vienna, P. Hrma, D. Jiricka, D. E. Smith, T. H. Lorier, A. Reamer, and R. L. Schulz, “Hanford Immobilised LAW Product Acceptance Testing: Tank Focus Area Results, PNNL-13744, Pacific Northwest National Laboratory, Richland, Washington,” 2001.

[68] P. Frugier, S. Gin, Y. Minet, T. Chave, B. Bonin, N. Godon, J. E. Lartigue, P. Jollivet, A. Ayral, L. De Windt, and G. Santarini, “SON68 nuclear glass dissolution kinetics: Current state of knowledge and basis of the new GRAAL model,” *J. Nucl. Mater.*, vol. 380, pp. 8–21, 2008.

[69] T. Geisler, T. Nagel, M. R. Kilburn, A. Janssen, J. P. Icenhower, R. O. C. Fonseca, M. Grange, and A. A. Nemchin, “The mechanism of borosilicate glass corrosion revisited,” *Geochim. Cosmochim. Acta*, vol. 158, pp. 112–129, 2015.

[70] R. K. Iller, *The Chemistry of Silica. Solubility, Polymerisation, Colloid and Surface Properties and Biochemistry*. Wiley.

[71] M. T. Harrison, “The Effect of Composition on short- and long-term durability of UK HLW glass,” *Procedia Mater. Sci.*, vol. 7, pp. 186–192, 2014.

[72] H. Zhang, C. L. Corkhill, P. G. Heath, R. J. Hand, M. C. Stennett, and N. C. Hyatt, “Effect of Zn- and Ca- oxides on the structure and chemical durability of simulant alkali borosilicate glasses for immobilisation of UK high level wastes,” *J. Nucl. Mater.*, vol. 462, pp. 321–328, 2015.

[73] H. U. Zwicky, B. Grambow, C. Magrabi, and E. T. Aerne, “Corrosion

behaviour of British Magnox Waste Glass in Pure Water," *MRS Online Proc. Libr.*, vol. 127, p. 129, 1988.

[74] S. Gin and J. P. Mestre, "SON 68 nuclear glass alteration kinetics between pH 7 and pH 11.5," *J. Nucl. Mater.*, vol. 295, pp. 83–96, 2001.

[75] E. Curti, J. L. Crovisier, G. Morvan, and A. M. Karpoff, "Long-term corrosion of two nuclear waste reference glasses (MW and SON68): A kinetic and mineral alteration study," *Appl. Geochemistry*, vol. 21, pp. 1152–1168, 2006.

[76] S. Gin, I. Robert, and M. Couillard, "Role and properties of the gel formed during nuclear glass alteration: importance of gel formation conditions," *J. Nucl. Mater.*, vol. 298, pp. 1–10, 2001.

[77] H. Aréna, N. Godon, D. Rébiscoul, R. Podor, E. Garcès, M. Cabie, and J. P. Mestre, "Impact of Zn, Mg, Ni and Co elements on glass alteration: Additive effects," *J. Nucl. Mater.*, vol. 470, pp. 55–67, 2016.

[78] P. K. Abraitis, B. P. McGrail, D. P. Trivedi, F. R. Livens, and D. J. Vaughan, "Single-pass flow-through experiments on a simulated waste glass in alkaline media at 40°C.: I. Experiments conducted at variable solution flow rate to glass surface area ratio," *J. Nucl. Mater.*, vol. 280, pp. 196–205, 2000.

[79] Z. Andriambololona, N. Godon, and E. Vernaz, "Glass Alteration in the Presence of Mortar: Effect of the Cement Grade," *Proc. Mat. Sci. Symp.*, vol. 257, pp. 151–158, 1992.

[80] C. L. Corkhill, N. J. Cassingham, P. G. Heath, and N. C. Hyatt, "Dissolution of UK High-Level Waste Glass Under Simulated Hyperalkaline Conditions of a Colocated Geological Disposal Facility," *Int. J. Appl. Glas. Sci.*, vol. 4, pp. 341–356, 2013.

[81] C. A. Utton, R. J. Hand, N. C. Hyatt, S. W. Swanton, and S. J. Williams, "Formation of alteration products during dissolution of vitrified ILW in a high-pH calcium-rich solution," *J. Nucl. Mater.*, vol. 442, no. 1–3, pp. 33–45, 2013.

[82] T. Chave, P. Frugier, S. Gin, and A. Ayral, "Glass-water interphase reactivity with calcium rich solutions," *Geochim. Cosmochim. Acta*, vol. 75, pp. 4125–4139, 2011.

[83] B. Fleury, N. Godon, A. Ayral, and S. Gin, "Son68 glass dissolution driven by magnesium silicate precipitation," *J. Nucl. Mater.*, vol. 442, pp. 17–28, 2013.

[84] B. M. J. Thien, N. Godon, A. Ballestro, S. Gin, and A. Ayral, "The dual effect of Mg on the long-term alteration rate of AVM nuclear waste glasses," *J. Nucl. Mater.*, vol. 427, pp. 297–310, 2012.

[85] H. F. W. Taylor, "Cement Chemistry," 1st ed., London: Academic Press, 1990,

pp. 1–28.

[86] Nirex Solutions, “Work Package Part 1. The Wastes and cementation processes employed at Sellafield for treatment of ILW.”

[87] F. A. Mumpton, “La Roca Magica: Uses of Natural Zeolites in Agriculture and Industry,” *Proc. Nat. Acad. Sci. USA*, vol. 96, no. 7, pp. 3463–3470, 1999.

[88] P. Rajec, F. Macasek, M. Feder, P. Misaelides, and E. Samajova, “Sorption of caesium and strontium on clinoptilolite- and modernite-containing sedimentary rocks,” *J. Radioanal. Nucl. Chem.*, vol. 229, pp. 49–55, 1998.

[89] R. Rodriguez-Trejo, P. Bosch, and S. Bulbulian, “Combustion treatment of Co2+ and Cs+ exchanged zeolites,” *J. Nucl. Mater.*, vol. 354, pp. 110–122, 2006.

[90] S. G. Baxtor and D. C. Berghauser, “The Selection and Performance of the Natural Zeolite Clinoptilolite in British Nuclear Fuels’ Site Ion Exchange Plant (SIXEP).”

[91] Z. Maher, P. Ivanov, L. O’Brien, H. Sims, R. J. Taylor, S. L. Heath, F. R. Livens, D. Goddard, S. Kellet, P. Rand, and N. D. Bryan, “Americium and plutonium association with magnesium hydroxide colloids in alkaline nuclear industry process environments,” *J. Nucl. Mater.*, vol. 468, pp. 84–96, 2016.

[92] N. C. Collier and N. B. Milestone, “The encapsulation of Mg(OH)2sludge in composite cement,” *Cem. Concr. Res.*, vol. 40, no. 3, pp. 452–459, 2010.

[93] K. S. Matlack, W. K. Kot, H. Gan, I. L. Pegg, G. A. Diener, and B. W. Bowan, “Sellafield Thermal Treatment Trials Using Advanced Joule Heated Ceramic Melter Technology,” *Waste Manag.*, pp. 1–13, 2010.

[94] S. G. Baxter and D. C. Berghauser, “The selection and performance of the natural zeolite clinoptilolite in British Nuclear Fuels’ site ion exchange effluent plant, SIXEP,” *Waste management*, vol. 2, no. 86. pp. 347–358, 1986.

[95] NDA, “Waste Stream 2D26 Ion Exchange Material (Clinoptilolite) and Sand,” 2013. [Online]. Available: http://ukinventory.nda.gov.uk/wp-content/uploads/sites/18/2014/04/2D26.pdf. [Accessed: 15-Nov-2014].

[96] NDA, “Waste Stream 2D35/C Encapsulated Retrieved Magnox Cladding,” *2013*. [Online]. Available: http://ukinventory.nda.gov.uk/wp-content/uploads/sites/18/2014/05/2D35_C.pdf. [Accessed: 15-Nov-2014].

[97] NDA, “Waste Stream 2D38/C Encapsulated Magnox Cladding,” *2013*. [Online]. Available: http://ukinventory.nda.gov.uk/wp-content/uploads/sites/18/2014/05/2D38_C.pdf. [Accessed: 15-Nov-2014].

[98] NDA, “Waste Stream 2D34 Sludge from Sand Filters and Transfers,” 2016.

[Online]. Available: http://ukinventory.nda.gov.uk/wp-content/uploads/sites/18/2014/04/2D34.pdf. [Accessed: 14-Mar-2017].

3. Characterisation Techniques

This thesis examines three different ILW streams: Magnox-cemented drums showing evidence of internal corrosion, clinoptilolite and mixed clinoptilolite / sand waste with Bulk Storage Tank (BST) sludge. The conditioning of each simulant ILW, through vitrification, forms the basis of chapters 4, 5 and 6, therefore, the simulant waste characterisation, the glass formulations and glass-making are detailed at the beginning of the respective chapters. This chapter details sample preparation for characterisation and describes the characterisation and analytical techniques used.

3.1 Density

Density was measured using gas pycnometry where volume displacement is calculated in a known volume containing a known mass of sample, allowing density to be calculated. Helium gas is pumped into the sample chamber and equilibrium reached, once this is achieved the outlet valve is opened and the helium gas vented into a second chamber of known volume. The pressure differential between the sample chamber and secondary chamber allows the volume of sample in the sample chamber to be calculated. From this, and the mass of the sample in the sample chamber, the density can be calculated [1].

For Chapter 4, 5 and 6 density measurements were made using a Micromeritics AccuPyc 1340 helium gas pycnometer on glass samples. Chapter 4 used ~0.5 g of powders (<63 μm) with 25 measurements made. Chapter 5 used ~0.6 g of powders (<63 μm) with 25 measurements made. Chapter 6 used ~0.5g of powders (<75 μm) with 20 measurements made.

3.2 Thermal Analysis

3.2.1 Differential Thermal Analysis

Differential Thermal Analysis (DTA) was used to determine phase transitions within a sample, specifically the glass transition temperatures, crystallisation temperatures and melting temperatures. Powdered samples are placed into a small crucible and heated simultaneously in the same furnace with a reference material (usually an empty

crucible) see Figure 3-1. The temperature differential between the sample and reference material is monitored throughout as both are heated [2]. By convention endothermic thermal events are troughs and exothermic thermal events are peaks.

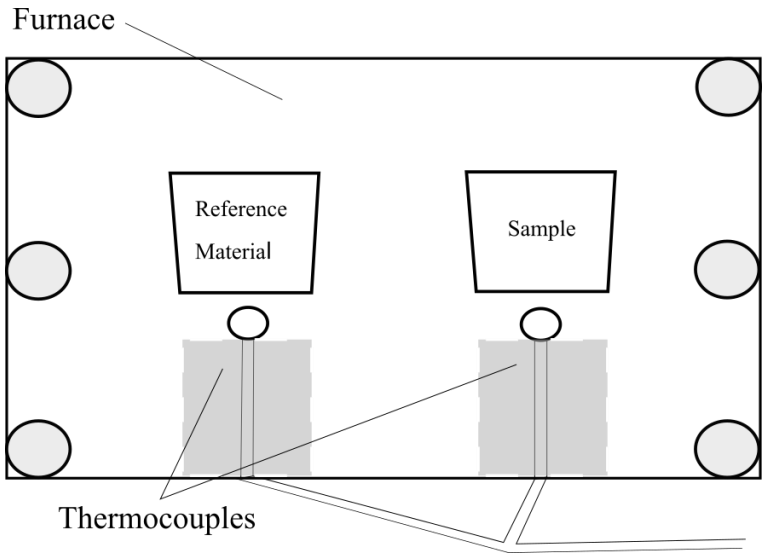

Figure 3-1. The experimental set-up of a DTA instrument, which measures the temperature difference between a reference material and a sample.

3.2.2 Thermogravimetric Analysis

Thermal analysis was performed simultaneously with a Thermogravimetric Analysis (TGA) module to monitor mass loss, whilst also monitoring the temperature differential between the sample and reference material. This allows the vaporisation or decomposition of any substances to be monitored as a function of temperature, in addition to this a mass spectrometer can be used, in conjunction with the TGA apparatus, to measure the atomic or molecular mass of any volatile species.

For chapters 4 and 5, DTA data were collected on a TA instruments Q600 SDT instrument, on 20 mg of powder, in alumina sample pans. The samples were heated at 10 ^{o}C min^{-1}, in air, up to 1300 ^{o}C for chapter 4, and 900 ^{o}C for chapter 5. For chapter 6, DTA data was collected on a Netzsch STA 449 F3 Jupiter instrument, on ~250 mg of powder, in alumina sample pans. The samples were heated at 10 ^{o}C min^{-1}, under $N_{2(g)}$, up to 1200 ^{o}C.

For chapter 5, simultaneous thermal analysis data was collected on a Netzsch TG 449 F3 Jupiter Instrument with a QMS 403 D Aeolos Mass Spectrometer. Mixtures of ground Cs clinoptilolite and borax/sodium carbonate were dried at 90 ^{o}C ± 5 ^{o}C for 16 h prior to analysis to remove any weakly-bound water. 35-40 mg was added to an alumina crucible (except for Cs clinoptilolite where 100 mg was added to the crucible). The acquisition rate was 10 points K^{-1} and 200 points min^{-1}, with a heating rate of 20 ^{o}C min^{-1}. The mass spectrometer scanned for volatile species between 10 and 300 atomic units.

3.3 Photography and Optical Microscopy

Optical microscopy was used to resolve features of interest on the order of 10^2 microns. In optical microscopy a sample is illuminated with visible light focussed on the surface of the sample, the scattered light, in reflection mode, is reflected back and an image captured using a digital camera. Samples for optical microscopy were prepared using the same method for electron microscopy, see section 3.4, except no carbon-coating was used. In chapter 5 a Veho Discovery VMS-004 Deluxe digital microscope was used.

Photography was used to capture features of interest within a sample that were visible to the naked eye. For chapters 4, 5 and 6 photographs were taken using a 16 Mega Pixel Sony Exmor sensor digital camera.

3.4 Scanning Electron Microscopy and Electron Dispersive Spectroscopy

Scanning electron microscopy (SEM) was used to resolve features of interest on the order of 0.1-10 µm in samples, particularly crystalline phases and alteration layers present. Scanning electron microscopy is used to generate high magnification images of samples by focusing an electron beam, with a series of electromagnetic lenses, onto the surface of a sample, see Figure 3-2. Topographical and microstructural information is obtained by observing the corresponding electrons and X-rays that are emitted. A typical energy of the incident electrons is between 5 and 30 keV [3], [4]. Emitted electrons and X-rays are as follows:

- Auger electrons- formed when an inner electron is ionised and an outer electron transitions down to fill the gap; the excess energy is now dissipated as the ionisation of outer electrons.
- Secondary electrons- these are formed from inelastic scattering interactions with the incident beam and are emitted from close to the surface of the sample. They have quite low energies (>50 eV), but relatively high intensity and allow topological imaging of the surface.
- Backscattered electrons- these are incident electrons on the sample that interact with nuclei, then reflected back to the detector. They have a lower intensity than secondary electrons, but have a higher energy. The number of electrons backscattered is proportional to the atomic mass of the element with high atomic number elements appearing brighter.
- Characteristic X-rays- core electrons from the K, L and, for heavier elements, M shell can be ionised by the incident electrons. This generates X-rays, as electrons transition from the higher energy core shells to fill the gaps in the core shells. These are characteristic of the elements from which they were produced and can be used to identify the element. This is the basis of EDX measurements. See Figure 3-2 [3].

Measuring characteristic X-rays has to account for certain effects: the characteristic X-rays are produced beneath generated backscattered electrons, secondary electrons and Auger electrons at the surface, therefore their signals can be attenuated. Detector software usually overcomes the issue with the atomic number (Z), absorption factor (A) and fluorescence factor (F) correction i.e. the ZAF correction, given by Equation 3-1.

$$N_i^{char} = \frac{\Omega}{4\pi} I_0 \, t \, \omega_i \, \varepsilon_i q_i \, c_i \, (ZAF)_i^{char} \qquad \text{Equation 3.1}$$

where N_i^{char} = intensity of X-rays of the characteristic energy of certain element I.

Ω = solid angle covered by the detector.

I_0 = electron beam current.

t = acquisition time.

ω_i = fluorescence yield.

ε_i = detector efficiency.

q_i = relative emission rate.

c_i = concentration of element i in mass fraction.

Z = atomic number factor.

A= absorption factor.

F = fluorescence factor.

EDX is a semi-quantitative technique for a number of reasons: one is the significantly larger interaction volume of the X-rays than the area covered by the incident beam, see Figure 3-2, another is the peak to background ratio is the starting point for analysis, with the background originating from bremsstrahlung radiation, furthermore the technique is standardless and coating thicknesses is not routinely accounted for. It

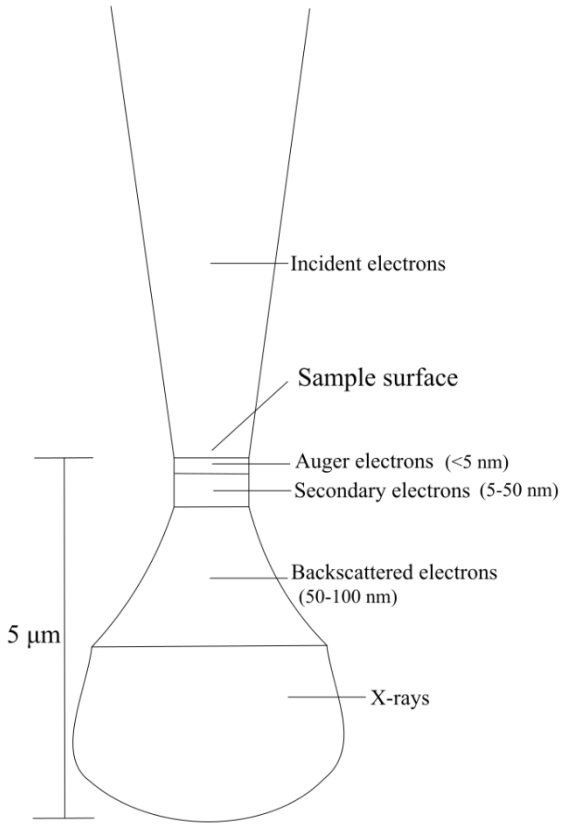

Figure 3-2. Figure showing the interactions of an incident electron beam, with a sample, that occurs in a typical SEM.

must be noted boron and lithium cannot be detected, reliably, using SEM-EDS or XRF due to the low energy X-rays and low fluorescence yield of these elements.

For chapters 4, 5 and 6 Scanning Electron Microscopy (SEM) back-scattered electron micrographs and Energy Dispersive X-ray (EDX) spectra were collected on a Hitachi TM3030 and Oxford Instruments Quantax 70 EDX detector, respectively. For chapters 5 and 6, SEM back-scattered electron micrographs and EDX spectra of leached powders were collected on a FEI Inspect F SEM and Oxford Instruments EDX detector. Samples were sectioned and mounted in epoxy resin. The resin was ground flat with 50 μm SiC grit paper, and the samples ground with 16 μm and 5 μm SiC paper and polished with 3 μm and 1 μm diamond paste suspension (water-based). The samples were then carbon-coated. For the leached powders a small volume of epoxy resin was added to the powders to suspend them and the slurry poured into small plastic sleeves, which were placed into a larger mould. The leached powders were then ground, polished and carbon-coated as described above.

3.5 X-ray Diffraction

X-ray diffraction was used to identify crystalline phases within the starting materials and slag-like waste forms, and to confirm the lack of long range order in glass waste forms. X-ray diffraction is caused by the interaction of X-rays with the atoms in repeating planes within a crystalline structure. The X-ray source is at a fixed energy (or wavelength λ), with the angle that diffraction occurs, θ, dependent upon the distance between crystalline planes, d. This can be summarised using Bragg's equation [5]. See Equation 3-2.

$$n\lambda = 2d\sin\theta \qquad \text{Equation 3.2}$$

XRD experiments here utilised the Bragg-Brentano arrangement where the X-ray source and detector are moved through an angle 2θ to bring successive {hkl} planes into a position to diffract (Figure 3-3). Divergence slits define the footprint of the beam on the sample ensuring that, particularly important at low angles, the beam does not overspill onto the specimen holder. The relationship between *d*, the lattice parameters *a*, *b* and *c*, the planes denoted by Miller indices {hkl} for a cubic unit cell is given by Equation 3-3.

$$d = \left(\frac{a^2}{h^2+k^2+l^2}\right)^{\frac{1}{2}}$$ Equation 3.3

For lower symmetry unit cells the equation has more terms. The diffracted X-rays converge and focus at a point on the diffraction circle, and then diverge once more onto the secondary beam monochromator. This bent crystal (often graphite) diffracts the X-rays once more according to Bragg's law and can be used to remove the K_β radiation and any fluorescence.

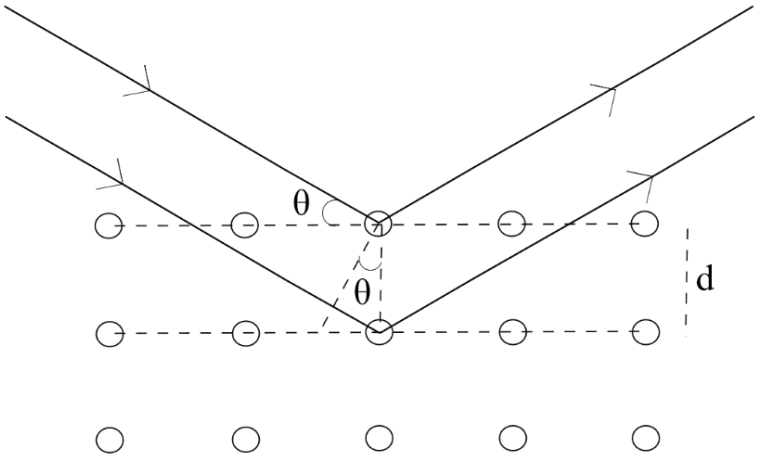

Figure 3-3. Figure showing the diffraction of X-rays by atoms, within a lattice structure, and the parameters of inter-planar spacing, d, and the scattering angle, θ.

For chapters 4, 5 and 6, X-ray diffraction data were collected on a Bruker D2-phaser diffractometer with a Cu Kα source (1.5418 Å). Diffraction patterns were collected in reflection mode between $10^o < 2\theta < 70^o$ with an increment of 0.02^o. A solid-state, position sensitive, LYNXEYE 1D Si strip detector was used and a Ni foil filter was used to remove K_β radiation. For chapters 4 and 5 X-ray energy discrimination was used to remove sample fluorescence. For chapter 6 this was unnecessary as there was no appreciable Fe in these samples. For chapter 4, 5 and 6 powders (<75 μm) were placed into a depressed zero-background Si sample holder. In chapter 4, uranium containing samples were stuck with petroleum jelly onto a flat, zero-background Si sample holder. In chapter 6, uranium containing samples were placed into a depressed zero-background Si sample holder and then covered with acetate film.

3.5.1 High Temperature X-ray Diffraction

To study the phase evolution of Cs clinoptilolite, with temperature, High Temperature X-ray Diffraction (HTXRD) was used. HTXRD data is collected utilising the same principles as room temperature XRD, but the sample in inserted into a hot stage and allow to equilibrate at the required temperatures before and after each XRD scan is taken. For chapter 5, HTXRD was collected on a Panalytical X'pert 3 diffractometer with a Cu Kα source (1.5418 Å) and fitted with an Anton Paar high temperature stage. Powders (<75 μm) were placed onto a flat Al_2O_3 sample holder attached to an automatic sample height adjuster. Diffraction patterns were collected at 15, 250, 500, 750, 800, 850 and 900 ^oC with a final XRD pattern collected at room temperature after cooling. The sample was heated at 60 $^oC\ min^{-1}$ from 15 ^oC to 50^o with a step size of 0.013^o. The detector was a PIXcel 1D solid-state, hybrid detector.

3.5.2 Rietveld Analysis

The Rietveld method was used to estimate the quantity of crystalline phase and amorphous phase in a heat-treated glass. Powdered sample (<75 μm) was mixed wet with isopropanol in a mortar and pestle with 10 wt% of NIST SRM Si 640d standard. The Rietveld method uses a least-squares approach to fit a theoretical profile to an actual XRD scan, the weight fraction from each crystalline component is a function of the refined scale factor, unit cell mass and unit cell volume. Rietveld refinement was conducted using Bruker's TOPAS software. Refinement of the XRD scan was as follows- a shifted Chebyshev function was fitted to the background and starting Pseudo-Voigt profiles fit to the XRD scan, variables refined were peak shapes, peak width, lattice parameters and a spherical harmonic term (to model preferred orientation).

3.6 X-Ray Fluorescence

X-Ray Fluorescence (XRF) was used to quantify the chemical composition of samples by irradiating with X-rays, causing ionisation of inner electrons. As outer electrons de-excite to fill the lower energy shells, X-ray photons fluoresce. These X-rays are characteristic to each element and their intensity is proportional to the quantity of that element within the sample.

For Chapters 4, 5 and 6 samples were ground to a fine powder (< 75 μm) and mixed with a Li_2B_4O7 or a $Li_2B_4O_7$ (50 wt%):$LiBO_2$ (50 wt%) mix fluxing agents. Samples were mixed with the flux using the following proportions: (90-95% flux: 5-10% sample) and heated in a Pt crucible within a Claisse LeNeo Fusion instrument to 1065 ^oC for ~15 mins. These fused beads were then run on a Panalytical Zetium instrument using a 4 kW rhodium x-ray source and EDX detectors.

3.7 X-Ray Absorption Spectroscopy (XAS)

XAS was used to study the oxidation state and coordination number of multivalent ions within the glass. Producing high intensity and high energy (5-25 keV) X-rays is possible by accelerating electrons around in a circular track with the use of magnets. As the path of the electrons is modified, broadband X-ray radiation is created.

The absorption of X-rays by individual atoms in a sample is dependent upon the energy of the X-ray and if the energy of the X-rays is equal to or greater than the ionisation energy of core electrons. By studying the XANES region of an X-ray absorption spectrum, and comparing to standards, it is possible to determine the oxidation state of atoms in a sample. As the oxidation state increases, the absorption energy increases, to higher energies, as the excited electron becomes progressively more tightly bound. Features of the absorption edges of atoms are due to the scattering of ionised electrons by the electron shells of surrounding atoms. X-ray Absorption Near Edge Spectroscopy (XANES) is typically taken to be the region 20 eV above and below the edge position whereas Extended X-ray Absorption Fine edge Spectroscopy (EXAFS) is typically taken to be 20-100 eV above the edge position. The EXAFS region results from interference between the ionised electron and neighbouring atoms- the wavelength of the ionised electron being comparable to interatomic distances [6].

A typical x-ray absorption experiment consists of the X-ray source, which is incident on a double, single crystal monochromator, see Figure 3-5, for an example of a single crystal monochromator. This tunes the energy of the X-rays to the particular absorption edge of interest, these then irradiate the sample and are followed by ion chambers used to detect the transmitted beam intensity, (I_t), followed by the reference beam intensity (I_t). The reference is generally a metal foil of the element of interest and is used as it has a known absorption energy. This allows the data to be calibrated.

If measuring in transmission the detector is parallel to the incident beams whereas if the measuring fluorescence the detector is perpendicular to the incident beam. See Figure 3-4. One reason for measuring the fluorescence is due to a low concentration of the element of interest within the sample, prohibiting measurement in transmission.

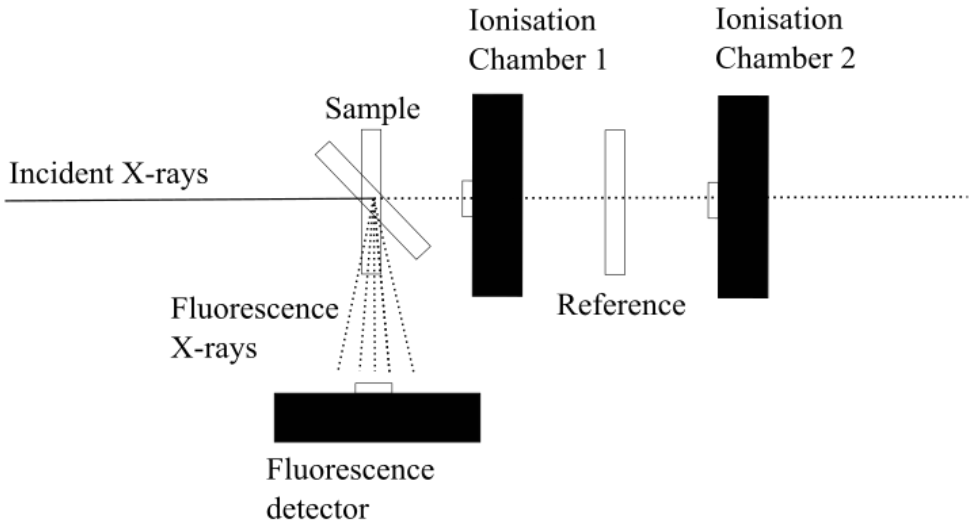

Figure 3-4. Schematic of the set-up an XAS experiment, from the incident X-rays on the left, its interaction with the sample and the various detectors.

For chapter 4 XANES were collected on a monolithic sample at the Swiss Light Source synchrotron at Paul Scherrer Institut (PSI) on beamline X05LA. Uranium L_{III} edge (i.e. 2p J = 3/2 to d orbitals) XANES spectra were recorded by detecting the U Lα edge fluorescent intensity (13.614 keV) and tuning the photon intensity from 16.9 to 17.5 keV, with the incident beam intensity I_0 measured by an ionisation chamber. Energy calibration was performed with respect to the K edge of Y_2O_3 ceramic (17.038 keV). Powdered standards of UTi_2O_6 (uranium(IV)), $Y_{0.5}U_{0.5}Ti_2O_6$ (uranium(V)) and $CaUO_4$ (uranium(VI)) were prepared and synthesised using methods described in the literature [7].

For chapter 5, XANES were collected on a monolithic sample at the European Synchrotron Research Facility (ESRF) at the DUBBLE beamline on bending magnet 26A. Iron K edge XANES spectra were recorded by detecting the Fe Kα edge fluorescent intensity (6.404 keV) and tuning the photon intensity, with a Si(111) monochromator, from 6.96 to 7.30 keV, with the incident beam intensity I_0 measured

by an ionisation chamber and the fluorescence measured using a Ge detector. Powdered standards of $NaFeSi_2O_6$ (iron(III)) and Fe_2SiO_4 (iron(II)) were used.

For chapter 6, XANES were collected, in transmission mode, on pressed pellets at the photon factory light source at the High Energy Accelerator Research Organisation (KEK) in Japan. Glass samples (< 75 μm) were mixed and pressed with polyethylene glycol (PEG). Uranium L_{III} edge (i.e. 2p J = 3/2 to d orbitals) XANES spectra were recorded by tuning the photon intensity from 17.0 to 18.0 keV, with the incident beam intensity I_0 and transmitted beam intensity I_t measured by ionisation chambers. Energy calibration was performed with respect to the K edge of Y_2O_3 ceramic (17.038 keV). Powdered standards of UTi_2O_6 (uranium(IV)), $Yb_{0.5}U_{0.5}Ti_2O_6$ (uranium(V)) and $CaUO_4$ (uranium(VI)) were prepared and synthesised using methods described in the literature [7]. In all three chapterS sample preparation, data reduction and data analysis were performed using the Hephaestus and Athena Software packages [8].

3.8 Mössbauer Spectroscopy

In this technique a radioactive source, ^{57}Co, decays via electron capture, to ^{57}Fe, with the release of gamma photons. As ^{57}Fe de-excites, the emission of the gamma photon is accompanied by a recoil of the nucleus as per the conservation of linear momentum. The energy of the photon no longer corresponds to the energy of the I = 1/2 to I = 3/2 transition of ^{57}Fe. To account for this the source nuclide is vibrated at a few mm s^{-1}. This movement of the source increases the linewidth, by giving the source more translational energy, meaning that some of the photons now have the required energies to excite the Fe atoms. These photons (14.4 keV) are collimated to the sample where the ^{57}Fe isotope therein absorb the radiation via the I = 1/2 to I = 3/2 nuclear transition. The width of a spectral line, Γ, is determined by the uncertainty principle [9], see Equation 3.4.

$$\Gamma\tau = \hbar \qquad \text{Equation 3.4}$$

where τ is the mean lifetime of the excited state (in Mössbauer this can be ~10 s).
$\hbar$ is the reduced Planck's constant [9].

The velocity at which the source must be moved to provide the required excitation energy varies depending upon the environments of the iron atoms in the sample. This manifests itself as the *isomer shift*, I.S. Another parameter which is of significance is the *quadrupole slitting,* Q.S., which occurs for those nuclei with a nuclear spin quantum number of half integer and $I > ½$ (^{57}Fe I = 3/2 state is quadrupolar). This results in the absorbance line splitting into $I + 1/2$ degenerate states. The physical basis of this is due to incompletely filled electron shells and charges on surrounding atoms interacting with the quadrupolar moment of the nuclei, causes the splitting of nuclear energy levels. An important parameter in Mössbauer spectroscopy is the recoil-free fraction, *f*. Atoms when they interact with gamma electrons will recoil. However in a solid the atoms are bound within a lattice and therefore the recoil energy is negligible compared to the mass of the whole lattice; instead of individual atoms recoiling the energy can be taken up by the entire lattice through vibrations (these are quantised as phonons). Only when a decay occurs involving no recoil is the Mössbauer effect observable, this has a finite probability of occurring and is called the recoil-free fraction [10].

For chapters 4 and 5 Mössbauer spectra were collected on ~75 mg of powders (<63 μm) using a Wissel MRG-500 spectrometer at room temperature, with a ^{57}Co source. All parameters are quoted in mm s^{-1} relative to alpha iron foil. A quartz sample holder was used and measurements collected for one week. A cubic spline interpolation was used to correct the spectra for transducer nonlinearities. The raw data was then folded using the corresponding calibration file, before the data normalised to intensity.

3.9 Raman Spectroscopy

Raman spectroscopy was be used to study SiO_2 polymerisation and B_2O_3 ring structures in glasses by studying the relevant vibrational degrees of freedom in the sample. In Raman spectroscopy samples are irradiated with a laser (in the UV to visible region) and certain vibrational modes in the sample cause absorption of the light. These include stretching modes (where the bond lengths between atoms change) and bending modes (where the bond angle between atoms change). A Raman spectrometer typically consists of the following components- a laser, a series of lenses before and after the sample to focus the laser and scattered radiation, a sample holder,

a monochromator and a detector. Most of the radiation is scattered without a change in energy (termed Rayleigh scattering), however, some of the radiation will be absorbed due to excitations of the vibrational modes of the material (this is called Raman scattering). This absorbance of energy can be attributed to specific bonds or structural units in a material. Stokes lines i.e. $v_0 - v$ (where v_0 is the frequency of the incident radiation and v is the frequency of the scattered radiation) have higher intensities than anti-Stokes lines $v_0 + v$ so these are usually the lines observed for Raman spectra. Not all vibrational modes can be observed via Raman spectroscopy- in order for a change in energy to occur the vibrational mode must lead to a change in the polarizability of the structural unit [11], [12]. The monochromator removes Rayleigh scattering (which is 10^2 to 10^4 more times intense than Raman scattering.) The concave mirrors are used to collimate the scattered radiation, and the diffraction grating is slowly rotated to resolve different Raman bands. See Figure 3-5 [11], [13].

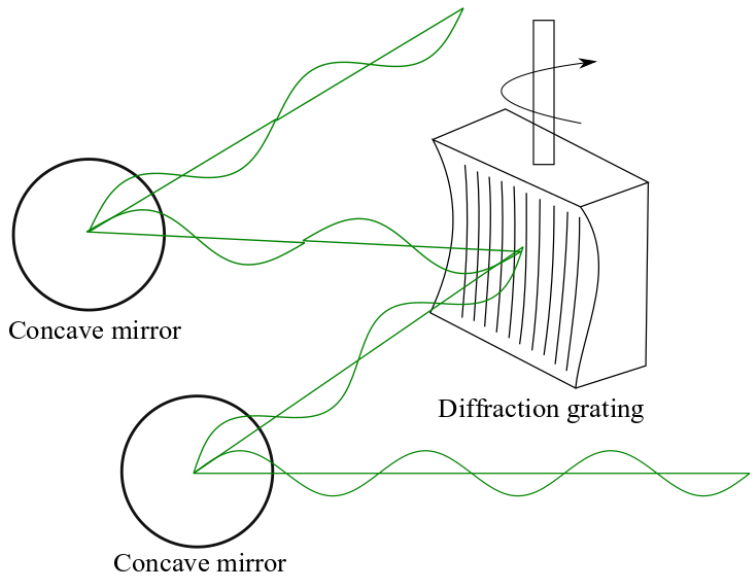

Figure 3-5. Diagram of a typical single monochromator set-up used for the dispersion of Raman scattering.

For chapters 5 and 6 Raman spectra were measured at room temperature on a Horiba XploRA PLUS confocal Raman spectrometer equipped with a CCD detector. The system operated a 532 nm laser, which was operated at full power (25 mW). The collection time was 180 s recorded 8 times between 200 and 1600 cm^{-1} with a precision of ± 1.4 cm^{-1} and at an objective of x100. Sample homogeneity and variation in Raman bands was checked by measuring at different points on the surface.

Automatic calibration with a silicon reference was undertaken each time the spectrometer was used. An initial baseline was fitted to the data using cubic spline interpolation and subtracted to give a linear baseline. The data was then normalised to the total area under the curve to enable features across the entire spectral range to be evaluated.

3.10 Inductively Coupled Plasma- Optical Emission Spectroscopy

Inductively Couple Plasma Optical Emission Spectroscopy (ICP-OES) was used to quantify the chemical composition of glasses using an acid digestion method as well as to determine the concentration of leached species in solution from glass dissolution experiments. This technique pumps liquid samples into a nebuliser, which produces a fine spray (larger drops are removed in a spray chamber). The fine liquid droplets are then atomised, (i.e. the solvent is evaporated off and dissolved species are decomposed to atoms and ionised), with the application of a plasma torch. As the ions are ionised in the plasma, outer electrons de-excite releasing photons, in the optical range, which the detector observes. The intensity of the observed photons is proportional to the concentration in the sample. Caesium cannot be detected using ICP-OES as the thermal energy of the plasma is sufficient to ionise the atoms, therefore a significant amount of the metal is in the ionised form in the instrument. The sensitivity of the emission lines from the caesium ion is far less than from the atom, thus detection of caesium using this technique is very difficult. Chlorine cannot be detected in glass compositions using the acid digest method due to the use of $HCl_{(aq)}$ in the digestion procedure.

For chapters 4, 5 and 6 chemical composition of samples (except Cs + Cl) were determined by ICP-OES, via a full chemical digest, on a Spectro Ciros Vision ICP-OES. Powdered glass samples (<75 micron) were dissolved in duplicate (~30 mg) and (~60 mg) in aqua regia with a few drops of hydrofluoric acid before dilution. The two duplicate measurements were taken to ensure reproducibility and that the digestion method was fit for purpose. For chapters 4, 5 and 6 the concentration of a given ion in leachates was determined by ICP-OES on a Thermo-Fisher 6000iCAP spectrometer. An internal gold standard was used to correct for the attenuation of the measured

intensities for solutions in saturated $Ca(OH)_2$ solution.

3.11 Inductively Coupled Plasma- Mass Spectroscopy

Inductively Coupled Plasma Mass Spectroscopy (ICP-MS) was used to quantify the concentration of caesium in the glass samples using the same acid digestion period as outlined above. The ICP part of an ICP-MS operates in the same way as an ICP-OES. ICP-MS typically offers a greater detection limit than ICP-OES and therefore can be used to detect low concentration of leachates. Ions from the ICP-OES are drawn by vacuum through two, small diameter, apertures to a series of electromagnetic lenses, which focus the ions through to the mass spectrometer. The mass spectrometer separates ions based upon their mass-to-charge ratio using a quadrupolar mass filter and the application of current and an alternating radiofrequency field. The result is a spectrum of mass-to-charge ratio versus intensity, with intensity of each ions being proportional to its concentration. For chapter 5 caesium concentration was determined by ICP-MS, via a full chemical digest, on an Agilent 4500 ICP-MS instrument.

3.12 Ion Chromatography

Ion chromatography pumps eluent through columns filled with resin and separates dissolved ions, *in-situ*, based upon their affinity to the resin. Those with high affinity move through the columns more slowly, those with low affinity move more quickly. The electrical conductivity of the dissolved species is measured with the intensity proportional to ion concentration. In this thesis, cation chromatography was used to quantify caesium in leachates. Ion chromatography was performed on a Thermo-Fisher DIONEX ICS-1100 instrument with a 20 mM methylsulfamic acid eluent, a flow rate of 0.25 mL min^{-1}, 15 mA current at 30 ^{o}C.

3.13 Durability Studies

The durability of glass waste forms, in aqueous media, was assessed to study the effect of glass and leachate composition on the durability of the waste forms [14]. For chapters 4, 5 and 6 studies were performed based on the PCT-B protocol [15], using a S.A./V. ratio of 1200 m^{-1}. Samples were size reduced using a percussion mortar and

sieved to a particle size range of 75-150 μm. The powders were washed according to ASTM standard C1285–14 [15]. Fine glass particles were removed by forcing cold isopropanol over the sieved glass, placing in an ultrasonic bath, and then decanting off the supernatant. This was continued until the supernatant was no longer cloudy. The sieved glass was left to dry. This dry, sieved glass was then weighed and placed into either clean PTFE vessels (for chapters 4 and 6) or clean HDPE vessels (for chapter 5) with 10 mL deionised water (18 Ω cm^{-1}) or with saturated $Ca(OH)_{2(aq)}$ solution. Saturated $Ca(OH)_{2(aq)}$ solution was prepared in a glove box, under $N_{2(g)}$, at room temperature, with excess $Ca(OH)_2$ added to deaerated, deionised water (18 Ω cm^{-1}). The solution was left stirring for 3 days for the solution to equilibrate and the solution filtered twice. The solution was oversaturated and buffered with $Ca(OH)_2$, as the solution was prepared at room temperature and the solubility of $Ca(OH)_2$ decreases with increasing temperature.

Dry, washed, sieved glasses were weighed to four d.p. with the following masses:

- For chapter 4, 0.5951 g of glass composition UNBS-46% was placed into the vessels. Vessels were placed in ovens at the desired temperatures (50 and 90 ± 2 ^{o}C). The vessels containing saturated $Ca(OH)_{2(aq)}$ were placed in an air-tight stainless steel container with $N_{2(g)}$ flowing through and vessels were removed at time points- day 1, 3, 7, 14, 21 and 28. Duplicate experiments at each point were performed.

- For chapter 5, 0.5752 g of glass composition NBS-56.0% and 0.5894 g of glass composition N15NBS-53.5% were placed into the vessels. Vessels were placed in ovens at the desired temperature (90 ± 2 ^{o}C). The vessels containing saturated $Ca(OH)_{2(aq)}$ were placed in an air-tight stainless steel container with $N_{2(g)}$ flowing through and vessels removed at time points- day 1, 2, 4, 7, 14, 21 and 28. Duplicate experiments at each time point were performed.

- For chapter 6, 0.5797 g of glass composition Mg22.5NL7.5BS-67.5% and 0.6152 g of glass composition crysMg22.5NL7.5BS-67.5% were placed into the vessels. Vessels were placed in ovens at the desired temperature (50 ± 2

^{o}C). Vessels were removed at time points- day 1, 2, 4, 7, 14, 21 and 28. Triplicate experiments at each time point were performed.

Each vessel (containing glass and leachate) was weighed before the start and at the conclusion of each experiment, to determine any mass loss of leachate. At the conclusion of each experiment leachates were removed from the vessels and filtered (through 0.2 µm filters) and the pH measured. Leachates were then acidified with 20 µL of concentrated nitric acid. From the pH data, and in some cases preliminary ICP-OES data (chapters 4 and 5), a dilution factor was chosen and each leachate diluted, according to this dilution factor, using deionised water (18 Ω cm^{-1}). For chapter 4, leachates were diluted in a 1 to 5 ratio, for chapter 5, NBS-56.0% was diluted in a 1 to 10 ratio and N15NBS-53.5% was diluted in a 1 to 33 ratio and for chapter 6 no dilution of leachates was undertaken.

Concentrations in the leachates were determined using ICP-OES or ion chromatography (for Cs) as described in Sections 3.10 and 3.12. These concentrations were converted to give normalised mass losses, NL_i, for a given element i, at each time point. This value was calculated using Equation 3.5.

$$NL_i(g\,m^{-2}) = \frac{\text{mass loss}_i\ (g)}{\text{mass fraction}_i \text{ x surface area of glass}(m^2)} \qquad \text{Equation 3.5}$$

where mass loss is given by: ([leachate]$_i$ x volume of blank) – ([blank]$_i$ x volume of blank),
mass fraction$_i$ was determined using the procedure outlined in Section 3.10.
surface area of glass (m^2) was determined using the density of the glasses (Section 3.1) and the size fraction of the sieves.

A closely related quantity, the normalised release rate was calculated using Equation 3.6.

$$\text{normalised release rate}_i\ (g\,m^{-2}d^{-1}) = \frac{NL_i\ (g\,m^{-2})}{\text{time (d)}} \qquad \text{Equation 3.6}$$

3.14 References

[1] Micromeritics, “AccuPyc II 1340 Pycnometer Gas Displacement Pycnometry System.” [Online]. Available: http://www.micromeritics.com/Product-Showcase/AccuPyc-II-1340.aspx. [Accessed: 02-Oct-2018].

[2] S. Gaisford, V. Kett, and P. Haines, “Principles of Thermal Analysis and Calorimetry,” 2nd ed., London: Royal Society of Chemistry, 2016, pp. 18–43, 67–103, 214–228.

[3] P. J. Goodhew, J. Humphreys, and R. Beanland, *Electron Microscopy and Analysis*, 3rd ed. London: Taylor and Francis, 2001.

[4] L. Reimer, *Scanning Electron Microscopy Physics of Image Formation and Microanalysis*, 2nd ed. Berlin: Springer, 1998.

[5] B. E. Warren, *X-Ray Diffraction*, 1st ed. New York: Dover, 2003.

[6] J. E. Penner-Hahn, “X-ray Absorption Spectroscopy,” in *Comprehensive Coordination Chemistry*, 2nd ed., Oxford: Pergamon, 2004, pp. 159–186.

[7] I. Grenthe, J. Drozdynski, T. Fujino, E. C. Buck, T. E. Ablrecht-Schmitt, and S. F. Wolf, *Uranium in The Chemistry of the Actinide and Transactinide Elements*, 3rd ed. Dordrecht: Springer, 2010.

[8] B. Ravel and M. Newville, “ATHENA, ARTEMIS, HEPHAESTUS: Data analysis for X-ray absorption spectroscopy using IFEFFIT,” *J. Synchrotron Radiat.*, vol. 12, no. 4, pp. 537–541, 2005.

[9] R. H. Herber, “Introduction to Mössbauer Spectroscopy,” *J. Chem. Educ.*, vol. 42, no. 4, pp. 180–188, 1965.

[10] G. M. Bancroft, *Mössbauer Spectroscopy: an introduction for inorganic chemists and geochemists*. 1973.

[11] J. R. Ferraro and K. Nakamoto, *Introductory Raman Spectroscopy*. 1994.

[12] C. Housecroft and A. Sharpe, “Inorganic Chemistry,” in *Inorganic Chemistry*, 3rd ed., Harlow, 2008, pp. 100–102.

[13] D. A. Long, *Raman Spectroscopy*, 1st ed. London: McGraw Hill, 1977.

[14] C. . Jantzen and N. E. Bibler, “The Product Consistency Test (PCT): How and Why It Was Developed,” in *Environmental Issues and Waste Management Technologies*, John Wiley & Sons, 2009, pp. 155–167.

[15] ASTM, “C1285 - 14. Standard Test Methods for Determining Chemical Durability of Nuclear, Hazardous, and Mixed Waste Glasses and Multiphase Glass Ceramics: The Product Consistency Test (PCT),” West Conshohocken, PA, 2014.

4. Vitrification as a Means of Reworking Problematic Cemented Waste Forms

4.1 Introduction

Encapsulation in cement is the UK's baseline conditioning method for intermediate level waste (ILW) [1]. Encapsulation of reactive metals, such as from fuel cladding, can lead to corrosion within the grout, challenging the passive safety of the waste form. One such waste stream is Magnox fuel cladding, which is encapsulated in a Ground Granulated Blast Furnace Slag (GGBS) and Portland Cement (PC) blend of 3.44:1 wt%, with a water to cement (W/C) ratio of 0.35. At the Magnox Encapsulation Plant (MEP), Magnox swarf (a few centimetres in size) and cement grout are placed in 500 L stainless steel (grade 316L) containers [1]–[3]. Within the grout corrosion occurs, as can be observed in Equation 4-1.

$$Mg + 2H_2O \rightarrow Mg(OH)_2 + H_2 \qquad \text{Equation 4.1}$$

This is problematic as the magnesium hydroxide produced has a volume x 1.8 greater than the original Magnox metal. Another reactive metal within the grout is uranium, which has adhered to the cladding after decanning [4]. Uranium metal also corrodes in cementitious matrices, reacting with water in a highly exothermic reaction to give uranium dioxide and hydrogen. See Equation 4-2.

$$U + 2H_2O \rightarrow UO_2 + 2H_2 \qquad \text{Equation 4.2}$$

Once hydrogen is generated it reacts further with any remaining uranium metal to form uranium hydride (UH_3) see Equation 4-3, generally found in high concentrations along cracks and grain boundaries. In turn, this reacts further to produce more uranium dioxide, Equation 4-4 [5].

$$2U + 3H_2 \rightarrow 2UH_3 \qquad \text{Equation 4.3}$$

$$2UH_3 + 4H_2O \rightarrow 2UO_2 + 7H_2 \qquad \text{Equation 4.4}$$

The reactions occurring within the cement grout can cause cracking of the grout and the subsequent manifestation of protuberances on the surface of the container. See Figure 4-1.

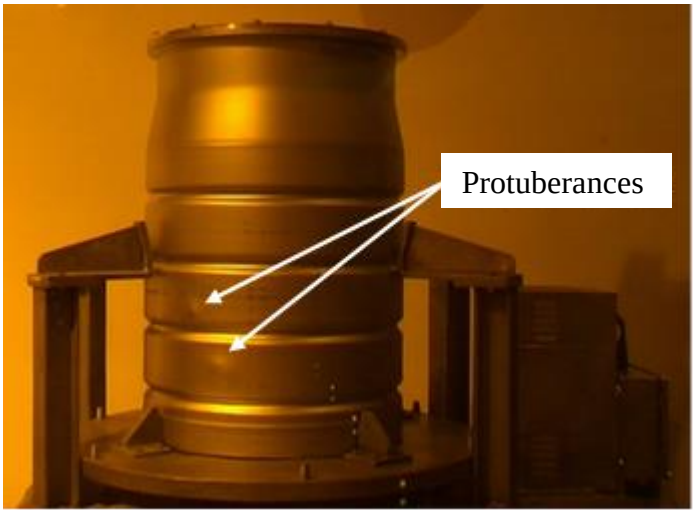

Figure 4-1. Picture illustrating visible blistering of encapsulated Magnox swarf waste container. W.E. Lee, Personal Communication.

It is believed there is an acute corrosion rate lasting several days, followed by a longer chronic rate as the ability of the cement to provide water diminishes. For example, corrosion rates of Magnox swarf in cement, in 2 L containers, determined from hydrogen gas evolution, was in the range of 0.7-2 wt% corrosion per year in the first three days. After three months the corrosion rate drops to < 0.2 wt% per year, in the even longer term, this decreases to < 0.01wt% per year [4]. In another study, it was estimated that amount of Magnox swarf corroded, after 900 days (2.5 years), is between 10 wt% and 25 wt% [6]. A certain proportion of encapsulated Magnox swarf drums are thought to have significantly degraded such that they *may* not meet waste acceptance criteria for geological disposal.

4.1.1 Reworking of Problematic Waste Forms

Several strategies for conditioning such corroded waste forms exist [7]. The term for this is reworking, which covers the following processes:

- *repair* of the waste container. Overpacking around the waste container with cementitious material is recommended for conditioning waste forms with

serious structural problems and to reduce surface dose rates. However, this method does not solve the underlying problems with the waste form.

- *stabilisation* of the waste form. Examples include drilling through the waste package and injecting a stabilising compound- either to fill voids through addition of grout or polymers, or removal of fluids through the addition of absorbents for example.
- *repackaging* of the waste. This includes retrieving the waste and reconstitution into a new waste form; its advantage is that the underlying problem affecting the waste form is resolved. Vitrification, the subject of the current investigation, falls under the category of repackaging [7].

The attraction of vitrifying this waste is that the magnesium is passivated, by oxidising in the melt and the water content evaporated.

4.2 Results

4.2.1 Waste Simulant Production

Representative lab-scale simulants for encapsulated Magnox swarf were produced according to the chemical composition provided on the UK Radioactive Waste Inventory (RWI) website [2], [3] Cement was encapsulation-grade Ribblesdale Portland Cement (PC) from Hanson Heidelberg. BFS was encapsulation-grade Ground Granulated Blast furnace Slag (GGBS) from the Scunthorpe steel works. The chemical composition of the PC and BFS can be seen in Table 4-1. Magnesium was used as magnesium turnings (< 2 mm in length) from Acros Chemicals (99.9% purity). Stainless steel was grade 316L powdered stainless steel from Goodfellow. Iron was used as iron filings (< 0.1 mm in length) produced in-house. Sand was high-purity glass making sand from Glassworks Services Ltd. (99% purity) from Loch Aline, Tilcon, U.K.. Boron oxide was from Acros Chemicals (99% purity) and sodium carbonate was from Alfa Aesar (98% purity).

The following assumptions were made when producing the lab-scale, Magnox-cemented waste: the Magnox was 100% magnesium and that the additional metallic

waste (such as the anti-flotation plate and flow splitter found in the grout) were accounted for as iron filings. Later experiments used actual Magnox, instead of magnesium, and uranium metal to account for the spent fuel.

Table 4-1.
XRF of Portland Cement and Blast Furnace Slag.

Oxide	PC	BFS
CaO	66.10 ± 2.30	39.62 ± 1.19
SiO_2	19.91 ± 0.60	35.62 ± 1.07
Al_2O_3	5.30 ± 0.16	12.23 ± 0.37
MgO	1.34 ± 0.07	8.37 ± 0.25
Na_2O	0.29 ± 0.02	0.38 ± 0.02
K_2O	0.60 ± 0.04	0.61 ± 0.02
SO_3	3.49 ± 0.10	1.14 ± 0.03
P_2O_5	0.16 ± 0.01	0.02 ± 0.00
Fe_2O_3	2.20 ± 0.07	0.48 ± 0.01
TiO_2	0.29 ± 0.02	0.87 ± 0.03
Mn_3O_4	0.03 ± 0.01	0.47 ± 0.01
Others	0.29 ± 0.02	0.21 ± 0.02

Table 4-2 contains the reagents used to produce the cement encapsulated Mg and were weighed on a 2 decimal point balance. The water was added to a beaker, the PC was added and the slurry mixed for 3 min. BFS was added and the paste stirred for 1 min. The magnesium turnings were added gradually in batches and the resulting product mixed for 1 min. The mixture was then poured into 50 mL centrifuge tubes. Air bubbles were agitated to the surface and removed using a vortex whirlimixer. The density was found to be 1.86 ± 0.1 g mL^{-1}, calculated by measuring the mass and then the volume, using Vernier calipers, of five cement samples. The cement samples were left to cure for 28 days at a temperature of 20.1 ± 0.5 ^{o}C and a humidity of 1%.

Table 4-2.
Reagents used to produce encapsulated Mg.

Reagent	wt%
BFS	47.78
PC	13.90
Water	21.56
Mg	16.74

4.2.2 Waste Simulant Analysis

Cross-sections of cured encapsulated Mg were prepared and an XRD pattern collected, see Figure 4-2. Reflections from magnesium, portlandite, a C-S-H phase, a monosulfoaluminate phase and gehlenite can be observed as well as some diffuse scatter from an amorphous phase. The highest intensity reflections are from magnesium, due to it forming a large mass fraction of the waste. The highest intensity cement phases are portlandite and C-S-H formed from hydration reactions with the PC, with monosulfoaluminate also forming from reaction with the cement [8]. The origin of the diffuse scatter (at 29° 2θ) and gehlenite (at 31° 2θ) are from BFS, as BFS is largely amorphous with small mass fraction of gehlenite present [6]

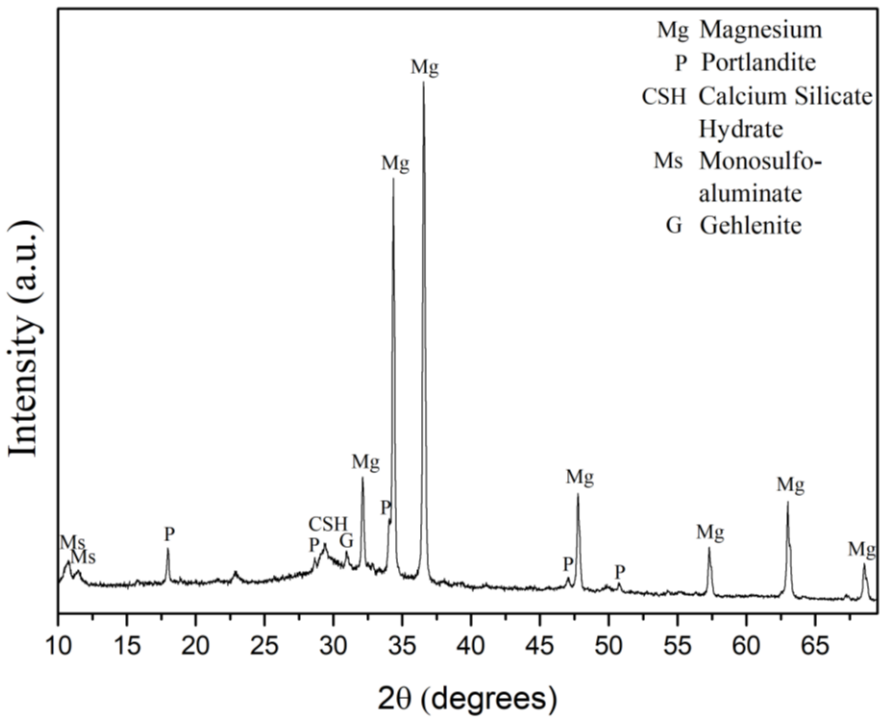

Figure 4-2. XRD of a cross-section of a cured cement encapsulated Mg sample.

Figure 4-3 shows a SEM-BSE image of a encapsulated Mg sample. A particle of Mg swarf on the right of the image is labelled, as is a large unreacted BFS particle on the left of the image. Particles of BFS can be seen dispersed within the hydrated cement microstructure; they are irregularly shaped and have a wide size distribution. Figure 4-4 shows EDX maps of the same sample. Some of the finer BFS particles have begun to hydrate at their surfaces, which can be observed due to the change in contrast. Ca and Si can be seen to be distributed within the binding C-S-H phase, with strong Ca counts identifying the portlandite phase. Al is strongly associated, as is Si, with the unreacted BFS. Monosulfoaluminate, from the reaction of C3A with water and gypsum, can be identified from the high sulfur concentrations and the dark thin needles that can be seen to run through this phase in the BSE image. Fe doesn't appear to concentrate in any particular phase.

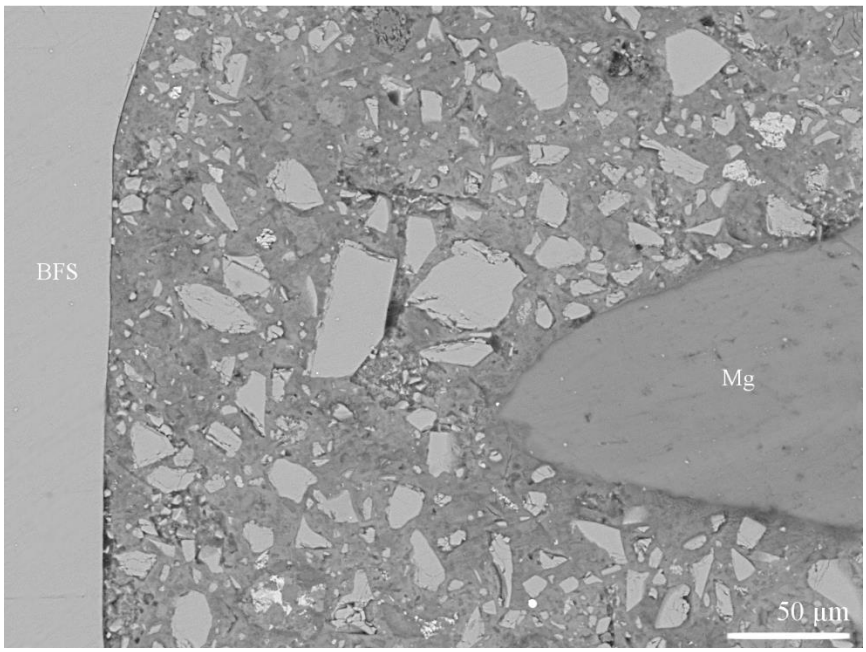

Figure 4-3. SEM-BSE image of an encapsulated Mg cement sample. A large BFS particle is labelled on the left of the image and large particle of Mg is labelled on the right.

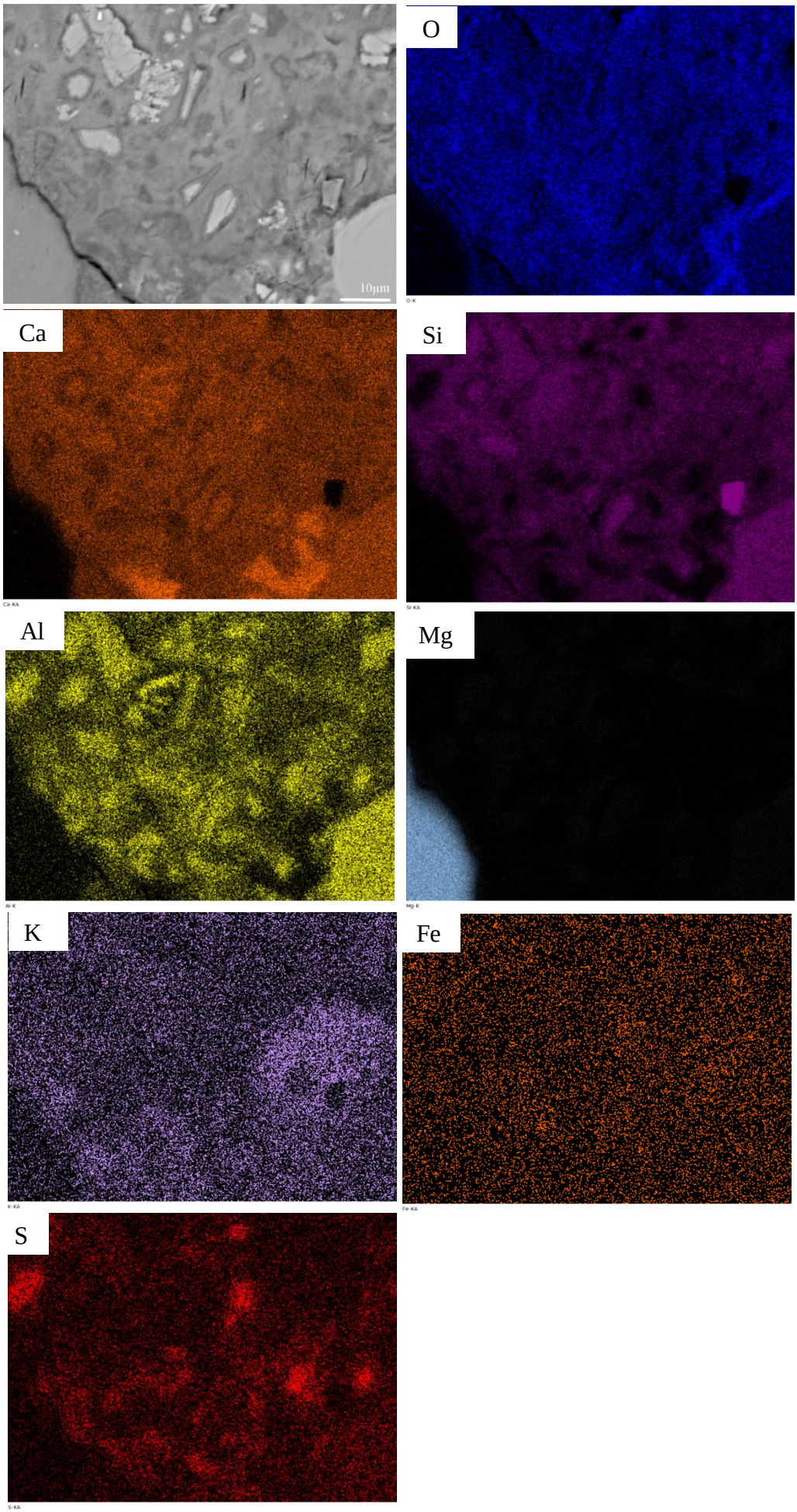

Figure 4-4. EDX maps of an encapsulated Mg sample displaying the chemical incorporation of elements within the different phases.

4.2.3 Glass Formulations

To repackage cement encapsulated Mg drums, suitable glass formulations were developed. The melting temperature of the cement drums is >1400 ^{o}C (this was determined by attempting to melt ground-up encapsulated Mg at temperatures up to 1400 ^{o}C). The high melting temperature is due to the high alkaline-earth content of the cement; indeed alkaline-earth rich glasses, such as calcium aluminosilicate glasses, have been discounted for vitrifying HLW because of too high a melting temperature [9]. Therefore, the addition of glass additives (Na_2O and B_2O_3 to decrease melting temperatures and SiO_2 to increase concentration of network formers) was used to minimise the melt temperature with the objective of maximising the waste loading as far as possible. Before taking into account the ferrous metallic waste, initial formulation work demonstrated that this was possible with the use of glass additives. Later further preliminary work demonstrated that melting, with the ferrous metal taken into account, for prolonged periods (8 h and 1400 ^{o}C) led to severe crucible corrosion. An example of this is illustrated in Figure 4-5. Therefore, melting times of ≤ 4 h and melting temperatures of ≤ 1400 ^{o}C were selected.

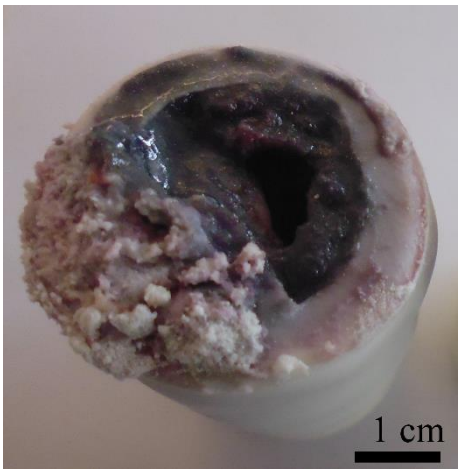

Figure 4-5. Photograph of corroded crucible base.

Two different formulations of glass compositions were investigated: the first formulation was with the addition of a source of B_2O_3 and SiO_2 (termed BS) and the second formulation was with the addition of Na_2O, B_2O_3 and SiO_2 (termed NBS). Additionally, two classes of waste loadings were utilised: high waste loading (89 wt%

and 72 wt%); and low waste loading (46 wt% and 36 wt%). Therefore, a waste form with ~72% waste loading and a source of Na_2O, B_2O_3 and SiO_2 totalling 28% is denoted NBS-72% and so on. Melt temperatures of 1200 ^oC, 1300 ^oC and 1400 ^oC were used.

BS glass formulations were produced only at 72 and 46 wt% waste loading. BS glass formulations contain more SiO_2 and no Na_2O so are more refractory; as the NBS-89% composition produced a poor waste form it was clear that BS-89% composition would produce an ever poorer waste form so it was not produced and studied. NBS-36%, NBS-46% and BS-46% all produced candidate waste forms, however after these three were produced it was clear that waste forms at 46% waste loading performed well and it was therefore unnecessary to produce BS-36% as it had undesirably 10% less waste loading.

To produce laboratory-scale re-packaged encapsulated Mg swarf drums the following procedure was used: encapsulated Mg samples were ground to a powder using a percussion mortar and passed through a 2 mm sieve. All grinding was performed, at most, two days before the melt to limit accelerated carbonation of portlandite phases in the powder. Not all of the Magnox swarf would pass through a 2 mm sieve, but these fragments were also included. The batched glass samples, see Table 4-3, were weighed out on a four decimal point balance for the different compositions (note the totals are not equal to 100%) due to the batch conversion factor for sodium carbonate to give the desired wt% of Na_2O. These samples were produced on a 20 g batch scale. Batched glass samples were mixed by hand, in a plastic bag, for 15 minutes, and heated at 3^o min^{-1} to the temperatures specified in Table 4-3 and dwelled at that temperature for 4 h. Samples were air-quenched in the crucible and not annealed. Cylindrical recrystallised alumina crucibles were used (S.A./V. ratio of 0.25 cm^{-1}).

Table 4-3.
Formulations of the different glass compositions used in this study.

	NBS-36%	BS-46%	NBS-46%	BS-72%	NBS-72%	NBS-89%
Waste Simulant (wt%)						
Cement Encapsulated Mg	31.19	39.80	39.80	61.58	61.58	76.38
Iron	0.47	0.60	0.60	0.93	0.93	1.16
Stainless steel	4.56	5.82	5.82	9.01	9.01	11.18
Glass Additive (wt%)						
Sand	37.61	36.83	31.71	19.51	16.79	0.00
Boron oxide	17.33	16.94	14.61	8.97	7.74	7.48
Sodium carbonate	15.09	0.00	12.74	0.00	6.75	6.52
Melting Temperature (^{o}C)						
	1200 + 1300	1200 + 1300	1200 + 1300	1200 + 1300	1200 + 1300	1400

In all cases the repackaged Mg-encapsulated waste form formed an opaque black vitrified product. At 89% waste loading the melt does not appear to have reached the liquidus, is partially sintered and is easily crumbled with light pressure. At 72% waste loading the waste product is partially melted and sintered, with porosity present at both 1200 ^{o}C and 1300 ^{o}C (with proportionally less porosity for NBS-72% compared to BS-72% composition), see Figure 4-6. At lower waste loadings (46% and 36%) there was negligible porosity in the glass, and all glasses were capable of being cast, except for BS-46% 1200 ^{o}C, which had white crystalline deposits running through the sample (later identified as quartz). For these 20 g scale melts, no significant separate metallic phase was observed.

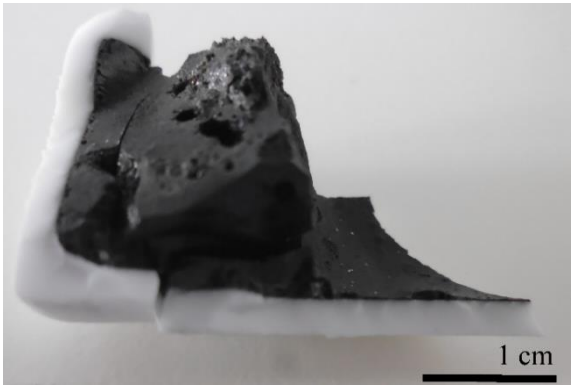

Figure 4-6. Photograph of NBS-72% 1300 ºC.

In addition to visual observation of the reworked glass product a mass balance calculation was performed to provide a measure of the oxidation of metallic waste within the melt using Equation 4.5.

$$\text{mass balance} = \frac{m_{metal} + m_{waste\ form} - (m_{batch} - m_{volatile})}{m_{metal}} \times 100 \qquad \text{Equation 4.5}$$

where

m_{metal} = mass of metallic waste (i.e. mass of magnesium, stainless steel and iron).

$m_{waste\ form}$ = mass of crucible and reworked waste – mass of empty crucible.

m_{batch} = mass of batch added to crucible.

$m_{volatile}$ = mass of water (from cured encapsulated Mg) and mass of carbon dioxide (from Na_2CO_3).

An example of performing a simple calculation using Equation 4.5 can be demonstrated using the oxidation of Mg, which gives a value of 166% from $\frac{m_{MgO}}{m_{Mg}} \times 100$, however the total mass increase associated with the oxidation of metallic waste will be less, as not all of the metallic waste is magnesium. Iron, chromium and molybdenum mass increase with oxidation is less as these elements have greater atomic weights. Therefore the value of 166% should be the theoretical maximum. The mass balances calculated here are likely to be an over-estimate as we have not accounted for loss for all of the volatiles such as B_2O_3. This data comes from a single

measurement from the glass melts, therefore, it was not possible to include confidence limits of these measurements. Figure 4-7 illustrates mass balance calculations for high waste loading glasses.

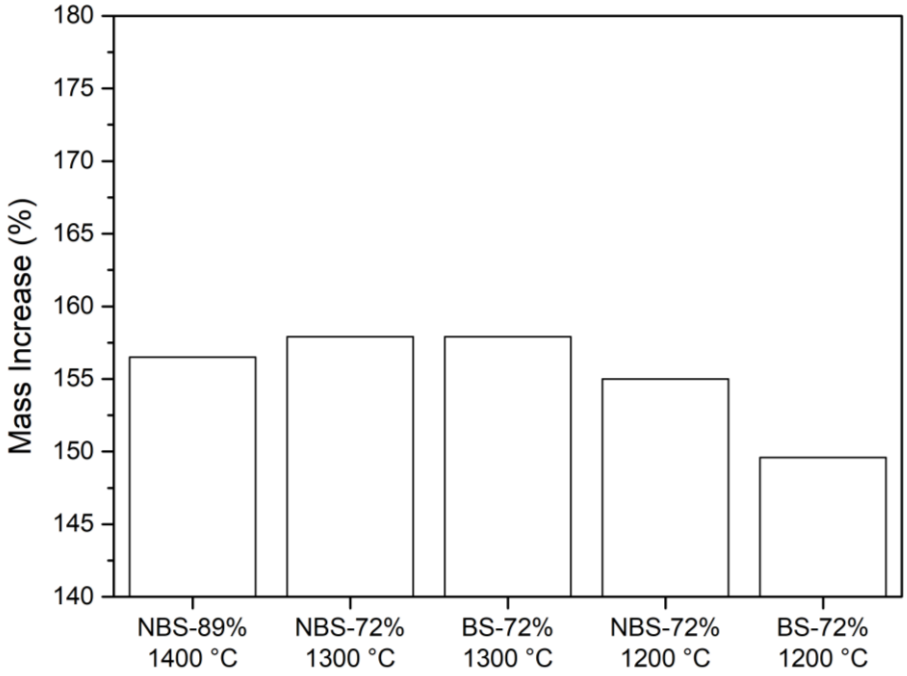

Figure 4-7. Bar chart showing mass balance data for high waste loading glasses performed on a 20 g scale.

For high waste loading glasses the mass increase associated with repackaging encapsulated Mg was between 150% and 158% with no definite trend between mass increase and temperature, or mass increase and glass formulation. Figure 4-8 illustrates mass balance calculations for low waste loading glasses. For the low waste loading glasses there are clear differences between the mass increase and glass formulation and between the mass increase and temperature. At 1300 ºC NBS-46% had the greatest mass increase at 178%, followed by BS-46% at 167%. For all glass formulations the increase in temperature from 1200 ºC to 1300 ºC led to an increase in metallic oxidation. For NBS-46% this was an increase of 14%, for BS-46% an increase of 12% and for NBS-36% an increase of 15%. For the low waste loading glasses it is clear a relationship between mass gain and glass composition exists.

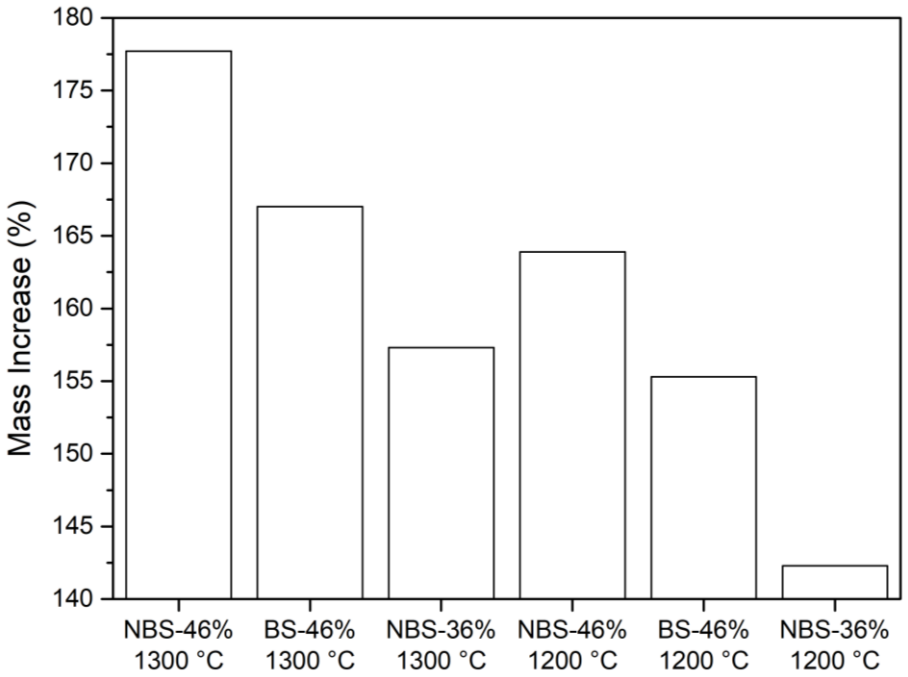

Figure 4-8. Bar chart showing mass balance data for low waste loading glasses performed on a 20 g scale.

4.2.4 Phase Assemblage

The phase assemblages for the reworked cement encapsulated Mg were examined using XRD and SEM-EDS.

4.2.4.1 XRD

Figure 4-9 shows the powder XRD for the high waste loading glasses. For all glass compositions there is present some diffuse scatter. Periclase (MgO) is the major crystalline phase for NBS-89% and forsterite (Mg_2SiO_6) at 72% waste loading (NBS-72% and BS-72%). The composition NBS-89% was very heterogeneous and only partially sintered, for these reasons it was difficult to obtain a sample that was representative. The SiO_2-CaO-MgO ternary phase diagram predicts at equilibrium that these crystalline phases (forsterite and periclase) will be present for the given compositions, showing good agreement with the respective XRD. At 1200 ^oC, for NBS-72% and BS-72%, there is another crystalline phase present: monticellite ($MgCaSiO_4$) . However, at 1300 ^oC the phase is not present for both compositions. The spinel phase is observable in all high waste loading reworked glasses.

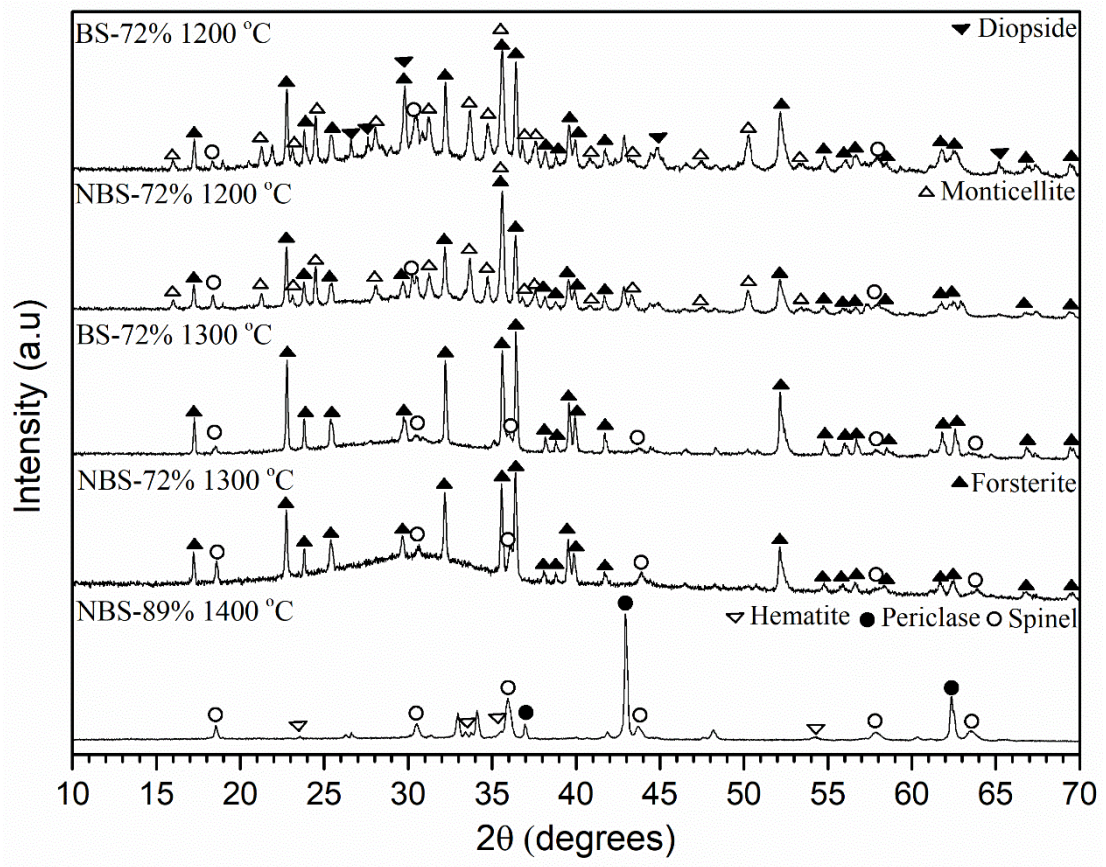

Figure 4-9. Powder XRD of high waste loading glasses on a 20 g scale.

Figure 4-10 shows the powder XRD for low waste loading glasses. In all traces, except BS-46% 1200 °C (where quartz is the major phase), there is broad diffuse scattering consistent with the major phase being amorphous. NBS-46% 1300 °C and 1200 °C and NBS-36% 1300 °C display reflections attributed to the spinel crystalline phase. Quartz (PDF 00-85-0335) was identified in BS-46% 1300 °C and 1200 °C and NBS-46% 1200 °C XRD traces, indicative of unreacted batch material.

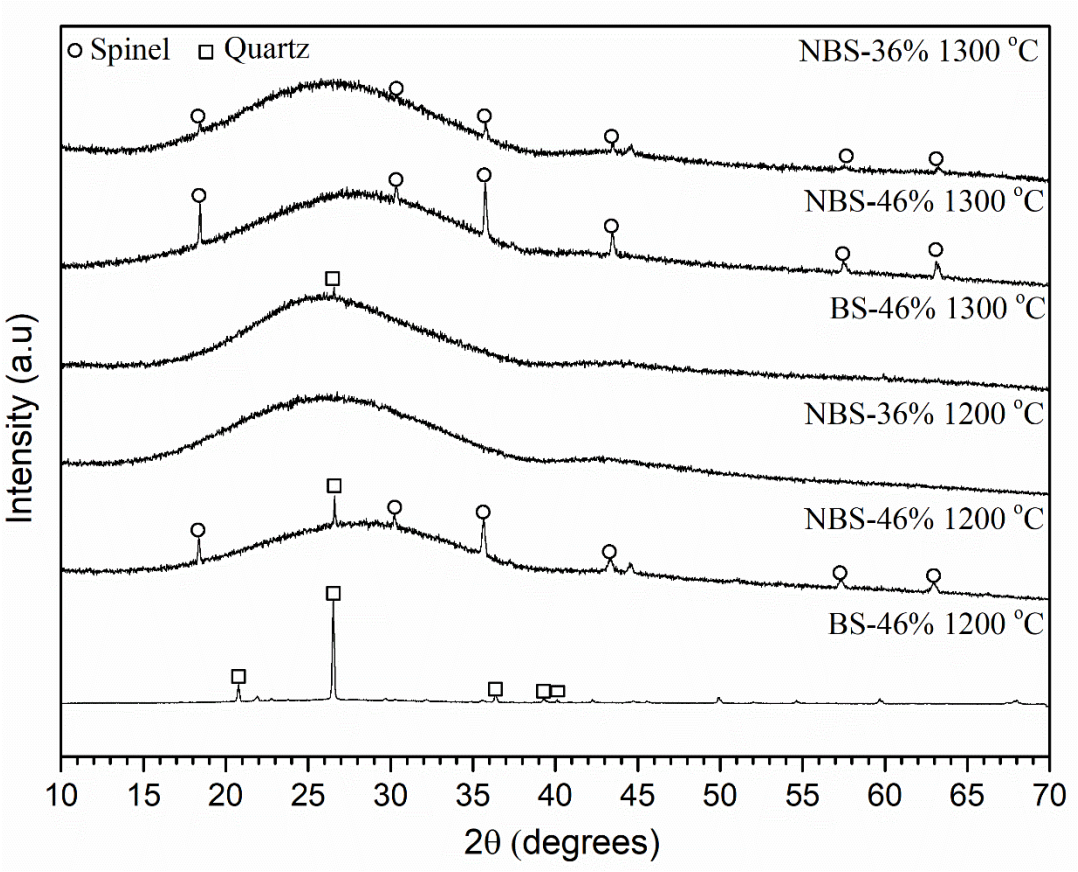

Figure 4-10. Powder XRD of low waste loading glasses on a 20 g scale.

4.2.4.2 SEM-EDX

Figure 4-11 contains SEM-BSE images and EDX spectra of the high waste loading glasses- NBS-72% and BS-72% at 1300 °C. SEM-BSE images of NBS-89%, NBS-72% 1200 °C and BS-72% 1200 °C were not collected as it was not possible to cross-section these samples without them crumbing. This is due to them being composed of a highly porous, partially sintered, slag-like waste form, see Figure 4-9. For NBS-72% 1300 °C and BS-72% 1300 °C the microstructure of both samples consist of a residual glassy phase (grey) with crystals of forsterite (dark grey) homogeneously distributed throughout the glass and clusters of spinel crystals (light grey) localised in certain areas. The EDX spectra demonstrated the glass matrix of NBS-72% 1300 °C was composed of Na_2O-MgO- CaO- Fe_2O_3- Al_2O_3- SiO_2 and the glass matrix of BS-72% 1300 °C consisted of the same oxides minus the Na_2O. B_2O_3 cannot be detected using EDS as described in Section 3.4. MgO partitions between the glass, forsterite and spinel phase and SiO_2 is partitioned between the glass and forsterite phase.

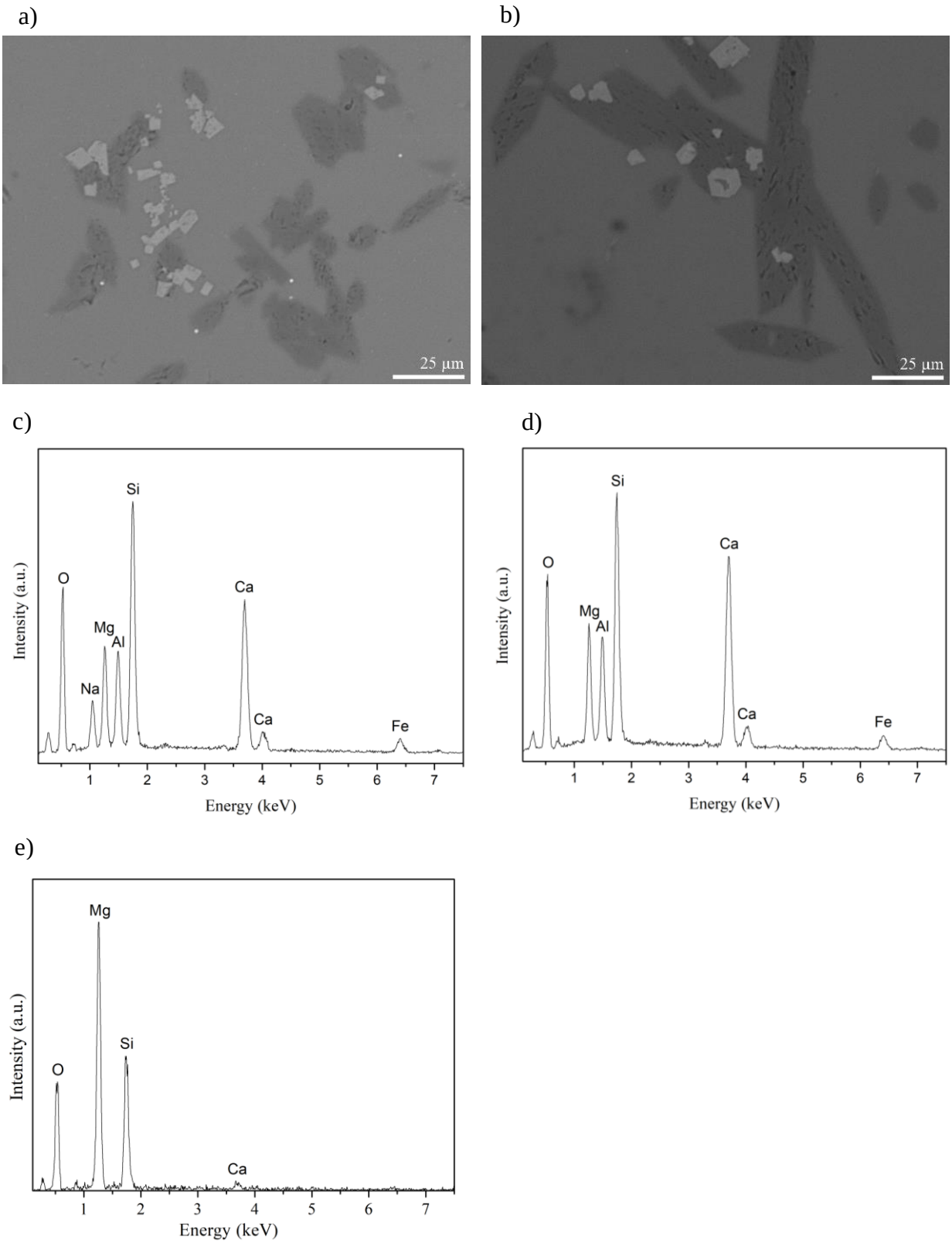

Figure 4-11 a) SEM-BSE image of NBS-72% 1300 ºC on a 20 g scale, b) SEM-BSE image of BS-72% 1300 ºC on a 20 g scale, c) EDS of the glass matrix from NBS-72% 1300 ºC, d) EDS of glass matrix from BS-72% 1300 ºC and e) representative EDS of forsterite.

Figure 4-12 shows SEM-BSE images for the low waste loading glasses. All low waste loading glasses have a microstructure consisting of a predominant amorphous phase with small areas of contrast due to the presence of secondary phases. The small (<4 μm), light circular inclusions evident in NBS-36% 1200 ºC, NBS-36% 1300 ºC, NBS-46% 1200 ºC and BS-46% 1200 ºC are suspended stainless steel particles. The slightly larger bright phases in NBS-46% 1200 ºC, NBS-46% 1300 ºC and BS-46% 1300 ºC, with a hexagonal habit, were identified as spinel phases. In BS-46% 1200 ºC the relatively large bright phase is a sintered metallic particle and the dark spots in the glass particle are undigested quartz particles.

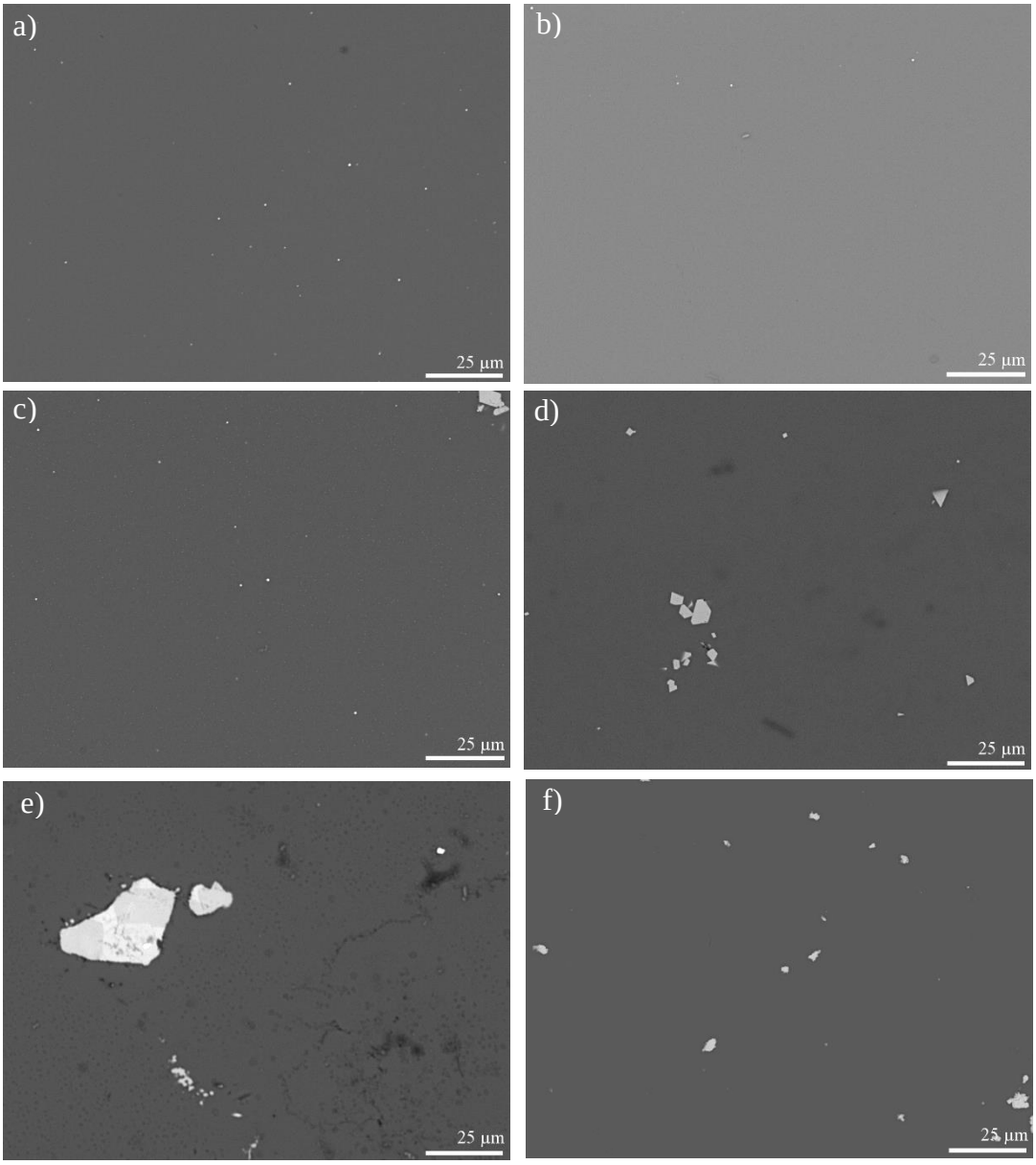

Figure 4-12. SEM-BSE images of low waste loading glasses on a 20 g scale, a) NBS-36% 1200 ºC, b) NBS-36% 1300 ºC, c) NBS-46% 1200 ºC, d) NBS-46% 1300 ºC, e) BS-46% 1200 ºC, and f) BS-46% 1300 ºC.

4.2.5 Glass Properties (Density and DTA)

Further characterisation of the repackaged cement encapsulated Mg were density measurements and DTA of the glass samples. Table 4-4 shows the density measurements. NBS-89% had the highest density at 3.50 ± 0.02 kg dm^{-3}. At 72% waste loading the densities were between 3.01 and 3.12 ± 0.02 kg dm^{-3}. These densities are higher than typical borosilicate glass formulations due to the presence of the relatively higher density forsterite, and also monticellite at 1200 ^{o}C. For the lower waste loading glasses, the densities were between 2.78 and 2.60 ± 0.02 kg dm^{-3}. BS-46% 1200 ^{o}C has the highest density due to the large mass fraction of undigested quartz, see Figure 4-10. Similarly NBS-46% 1300 and NBS-46% 1200 ^{o}C both have relatively high densities (2.76 and 2.74 ± 0.02 kg dm^{-3}) due to the presence of spinel phase, see Figure 4-10 and Figure 4-12.

Table 4-4.
Melting temperatures and measured densities (± 0.02 kg dm^{-3}) of samples produced on a 20 g scale.

	NBS-89%	NBS-72%	NBS-72%	BS-72%	BS-72%	
Temperature (^{o}C)	1400	1300	1200	1300	1200	
Density (kg dm^{-3})	3.50	3.01	3.09	3.12	3.07	
	NBS-46%	NBS-46%	BS-46%	BS-46%	NBS-36%	NBS-36%
Temperature (^{o}C)	1300	1200	1300	1200	1300	1200
Density (kg dm^{-3})	2.76	2.74	2.68	2.78	2.61	2.60

Figure 4-13 shows the DTA traces for the high waste loading glasses and Table 4-5 shows the temperature of thermal events identified from the DTA. Glass transitions can be observed for the glasses produced at 72% waste loading, followed by a crystallisation event, T_x, and then at least one, but up to two, high temperature melting events, T_{m1} and T_{m2}. T_{m1} only occurs for those glasses produced at 1200 ^{o}C. Only one discernible thermal event could be observed for the NBS-89% composition (T_x). The glass transition temperatures are within error of one another for the same compositions

processed at 1200 and 1300 ºC, however, T_x, occurs at a higher temperature when processed at 1300 ºC. The effect of Na_2O in the NBS-72% compositions, compared to the BS-72% compositions is to significantly lower the temperature at which the T_g, T_x and T_{m2} events occur. For instance the T_g of the NBS-72% composition is between 25 and 40 ºC lower than the BS-72% compositions.

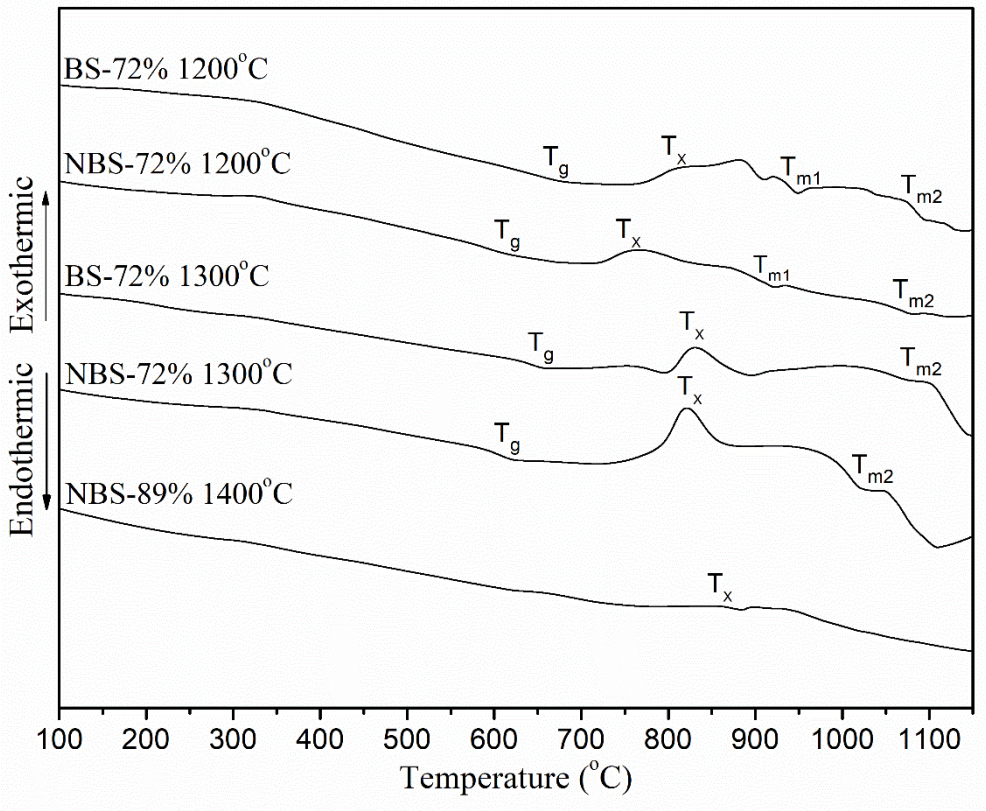

Figure 4-13. Stacked DTA traces for the high waste loading glasses, displaying four distinct thermal events.

Table 4-5.
Thermal events identified from the DTA for the high waste loading glasses.

	NBS-89%	NBS-72% 1300 ºC	NBS-72% 1200 ºC	BS-72% 1300 ºC	BS-72% 1200 ºC
T_g / ±5 ºC	/	624	624	652	660
T_x / ±5 ºC	856	823	769	831	819
T_{m1} / ±5 ºC	/	/	927	/	958
T_{m2} / ±5 ºC	/	1024	1084	1086	1100

Figure 4-14 shows the DTA traces for the low waste loading glasses and Table 4-6 shows the temperature of events identified from the DTA. At 1300 °C all three glass compositions show a glass transition (T_g), two crystallisation events (T_{x1} and T_{x2}) and a melting event (T_m). At 1200 °C the two crystallisation events cannot be conclusively identified from the DTA traces but T_g and T_m can, although a T_m cannot be identified from the traces. The glass transition temperatures are within error of one another for the same compositions processed at 1200 °C and 1300 °C, except for NBS-46% 1300 °C and 1200 °C, which have a difference of 21°C. Similar to the high waste loading glasses, the effect of Na_2O is to significantly lower the temperature at which T_g and T_m occur.

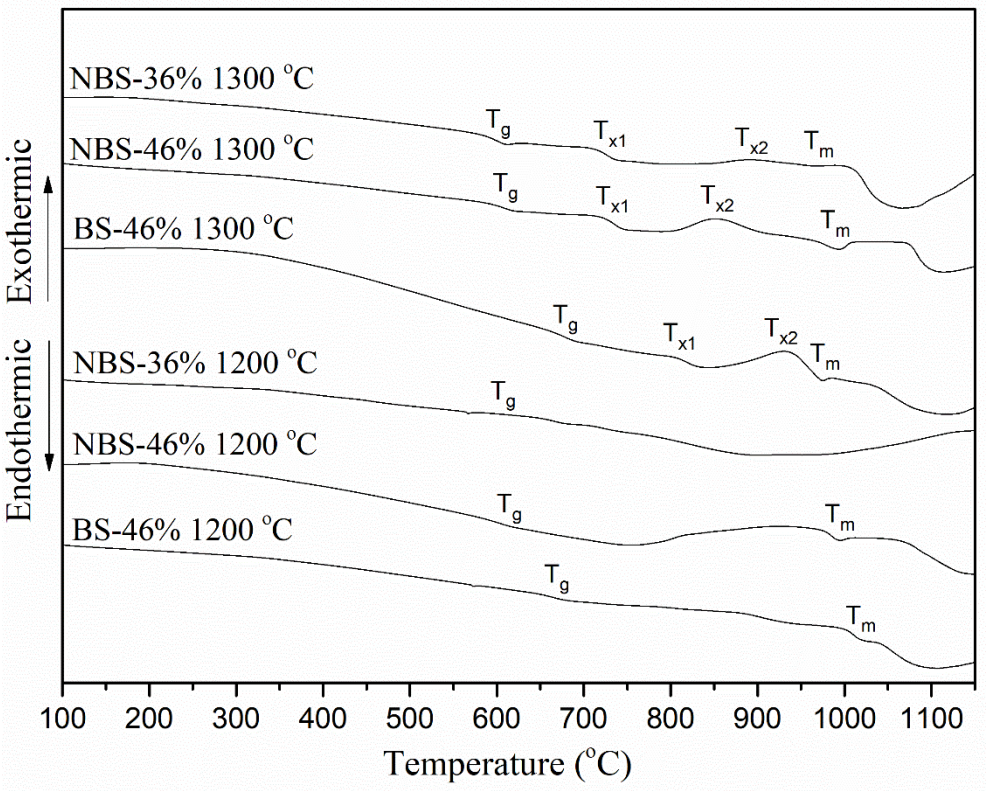

Figure 4-14. Stacked DTA traces for the low waste loading glasses.

Table 4-6.
Thermal events identified from the DTA for the low waste loading glasses.

	NBS-46% 1300 °C	NBS-46% 1200 °C	BS-46% 1300 °C	BS-46% 1200 °C	NBS-36% 1300 °C	NBS-36% 1200 °C
T_g / ±5 °C	591	612	700	691	580	582
T_{x1} / ±5 °C	718	/	806	/	713	/
T_{x2} / ±5 °C	822	/	935	/	897	/
T_m / ±5 °C	983	1000	972	1016	963	/

4.2.6 Effect of Scale on Low Waste Loading Glasses

The lower waste loading glass compositions (BS-46%, NBS-46% and NBS-36%) produced a castable glass with minimal porosity, therefore these were reproduced at a larger scale (~70 g). The higher waste loading glasses (BS-72%, NBS-72% and NBS-89%) were partially reacted and sintered slag-like waste forms so were not taken further. This was to observe whether scale had an effect on the waste form produced. The glasses were batched, as in Table 4-3, at 1300 ^{o}C, in a tapered wall recrystallised alumina crucible (S.A./V ratio of 0.18 cm^{-1}) and cast onto a pre-heated steel plate. In addition to the three glass compositions mentioned above, an additional glass sample of NBS-46% was prepared, but with an additional processing step. This sample was calcined, *in-situ*, at 750 ^{o}C, for 4 h (these parameters chosen to accelerate oxidation but mindful of not causing excessive volatilisation of batch). This was to attempt to oxidise as much of the metallic waste as possible. The sample is denoted NBS-46% with calcination.

For these larger scale melts, in addition to the dark black glass produced, there was a separate metallic phase produced. Figure 4-15 shows the glass phase in addition to sintered metallic phases recovered from NBS-46%, BS-46% and NBS-36%. As can be seen the stainless steel forms small balls, approximately 1 cm in diameter. The processing temperature (1300 ^{o}C) is less than the melt temperature of the stainless steel; grade 316L stainless steel has a solidus temperature of 1405 ^{o}C and a liquidus temperature of 1445 ^{o}C [10]. However, the oxidation of Mg will generate a large amount of localised heat [11], therefore temperature gradients may exist in the melt. Potentially in regions of the glass melt the localised temperature may be high enough to cause melting of the stainless steel and produce a low S.A./V. ratio spherical shape. Nevertheless, at 1300 ^{o}C two processes will occur: sintering and oxidation. As sintering occurs and the metallic particle size increases, oxidation occurs at a progressively lower rate, due to the lower surface area. The calcination step at 750 ^{o}C oxidised more of the stainless steel for the NBS-46% with calcination composition, with no small metallic particles suspended in the glass, but a small amount left in the base.

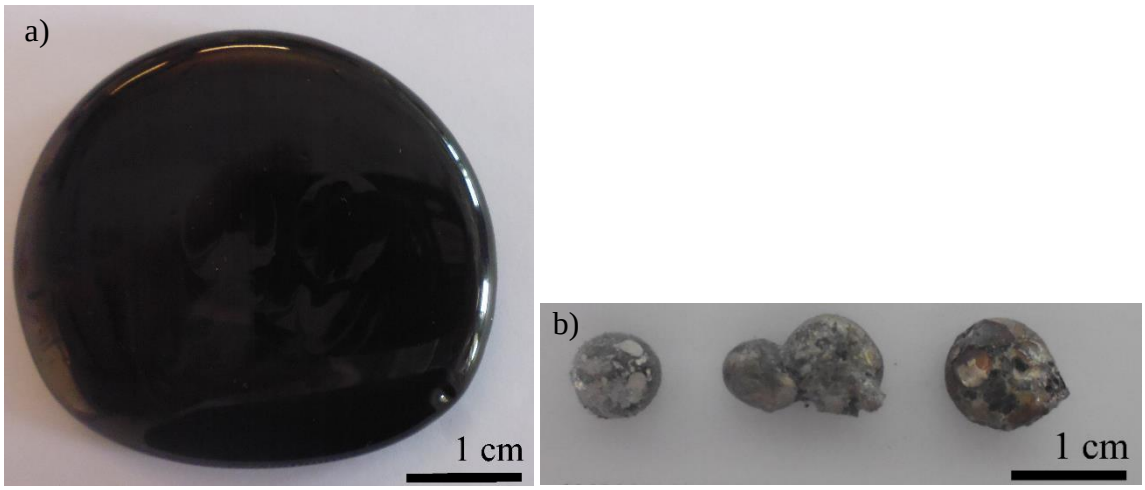

Figure 4-15. a) Photograph of NBS-46% with calcination and b) sintered steel balls recovered from the base of the crucible of the scaled-up low waste loading melts (NBS-46%. NBS-46% with calcination and BS-46%).

Analysed compositions can be found in Table 4-7, as can be seen the glasses contain a large variety of oxides with the glass matrix composed predominantly (> 98.3 mol%) of Na_2O- (for NBS compositions only) MgO- CaO- B_2O_3- Al_2O_3- SiO_2. All these oxides are at concentrations expected from batching, except for Al_2O_3, which contains a higher concentration due to corrosion of the alumina crucible. NBS-46% with calcination contains the higher concentration of Fe_2O_3 (0.97 mol%), followed by NBS-46% (0.79 mol%), BS-46% (0.25 mol%) and NBS-36% (0.12 mol%). The compositions with greater Fe_2O_3 content suggest greater metallic waste oxidation.

Table 4-7.
Analysed compositions of the four glasses produced on a 70 g scale using chemical digestion and ICP-OES.

	NBS-46% with calcination		NBS-46%		BS-46%		NBS-36%	
	Wt%	Mol%	Wt%	Mol%	Wt%	Mol%	Wt%	Mol%
Na_2O	6.40 ± 0.19	6.26 ± 0.19	6.97 ± 0.21	6.77 ± 0.20	0.79 ± 0.02	0.75 ± 0.02	8.71 ± 0.26	8.52 ± 0.26
MgO	13.35 ± 0.40	20.06 ± 0.60	14.26 ± 0.43	21.29 ± 0.64	15.07 ± 0.45	22.17 ± 0.67	10.30 ± 0.31	15.50 ± 0.46
CaO	11.21 ± 0.34	12.11 ± 0.36	11.60 ± 0.35	12.45 ± 0.37	12.22 ± 0.37	12.92 ± 0.39	9.67 ± 0.29	10.46 ± 0.31
B_2O_3	15.80 ± 0.47	13.76 ± 0.41	15.32 ± 0.46	13.24 ± 0.40	16.84 ± 0.51	14.34 ± 0.43	16.40 ± 0.49	14.28 ± 0.43
Al_2O_3	8.94 ± 0.27	5.32 ± 0.16	9.51 ± 0.29	5.62 ± 0.17	8.85 ± 0.27	5.15 ± 0.15	8.90 ± 0.27	5.29 ± 0.16
SiO_2	40.45 ± 1.21	40.79 ± 1.22	39.06 ± 1.18	39.13 ± 1.17	44.27 ± 1.33	43.69 ± 1.31	44.89 ± 1.35	45.30 ± 1.36
Fe_2O_3	2.57 ± 0.13	0.97 ± 0.05	2.08 ± 0.11	0.79 ± 0.04	0.66 ± 0.03	0.25 ± 0.01	0.32 ± 0.02	0.12 ± 0.01
Cr_2O_3	0.55 ± 0.03	0.22 ± 0.01	0.45 ± 0.02	0.18 ± 0.01	0.54 ± 0.03	0.21 ± 0.01	0.18 ± 0.01	0.07 ± 0.01
SO_3	0.17 ± 0.01	0.13 ± 0.01	0.18 ± 0.01	0.13 ± 0.01	0.11 ± 0.01	0.08 ± 0.01	0.15 ± 0.01	0.11 ± 0.01
TiO_2	0.15 ± 0.01	0.12 ± 0.01	0.17 ± 0.01	0.13 ± 0.01	0.19 ± 0.01	0.14 ± 0.01	0.15 ± 0.01	0.11 ± 0.01
K_2O	0.14 ± 0.01	0.09 ± 0.01	0.15 ± 0.01	0.10 ± 0.01	0.17 ± 0.01	0.11 ± 0.01	0.14 ± 0.01	0.09 ± 0.01
Others	0.27 ± 0.02	0.17 ± 0.01	0.26 ± 0.02	0.17 ± 0.01	0.29 ± 0.02	0.19 ± 0.01	0.19 ± 0.01	0.15 ± 0.01

Figure 4-16 shows the relationship between mass gain and density, with Table 4-8 containing the mass gain and density values, for the glass compositions produced on a 70 g scale. The graph demonstrates that with higher mass gains, glass samples have higher densities. This is due to the higher mass gains originating from greater metallic oxidation and causing a higher concentration of spinel crystals suspended in the glass. These spinel crystals have a greater density (4.5-4.8 kg dm^{-3}) than the glass phase and therefore the density of the overall glass waste form is increased.

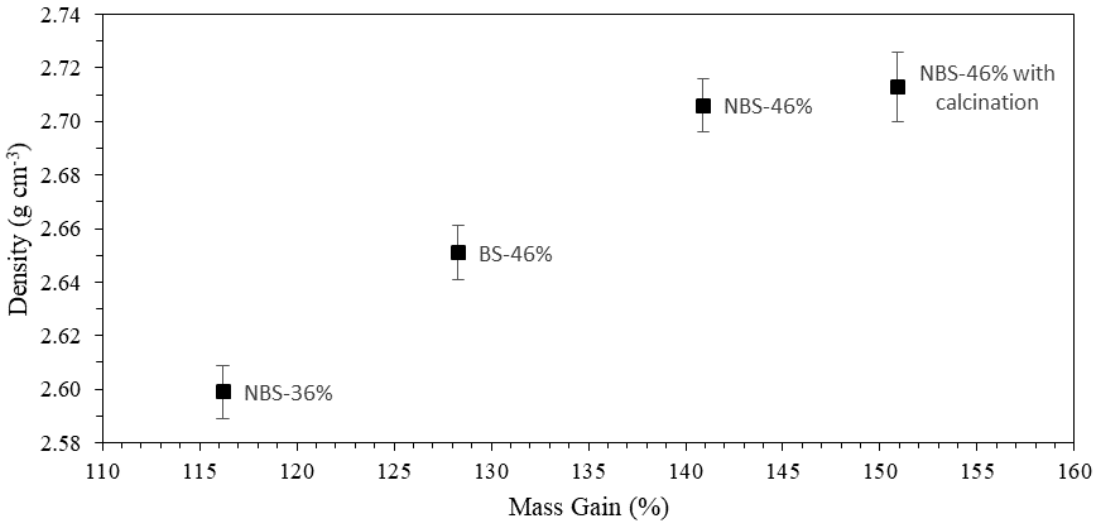

Figure 4-16. Graph demonstrating the relationship between mass gain and density for the four glasses produced on a 70 g scale.

Table 4-8.
Measured densities (± 0.02 kg dm^{-3}) and mass gains for the four compositions produced on a 70 g scale.

	NBS-46% with calcination	NBS-46%	BS-46%	NBS-36%
Density (kg dm^{-3})	2.71	2.71	2.65	2.60
Mass Gain %	151	141	128	116

Figure 4-17 shows the powder XRD patterns for the four glass compositions produced on a 70 g scale. All four glasses give broad diffuse scattering consistent with a major amorphous phase. NBS-46% and NBS-46% with calcination have minor reflections attributed to a spinel crystalline phase; the same as the spinel phase identified in glasses produced on a 20 g scale, see Figure 4-10. This presence of the spinel phase in the XRD patterns is linked to mass gain, with higher mass gains observed for NBS-46% with calcination and NBS-46%, than the other two glasses.

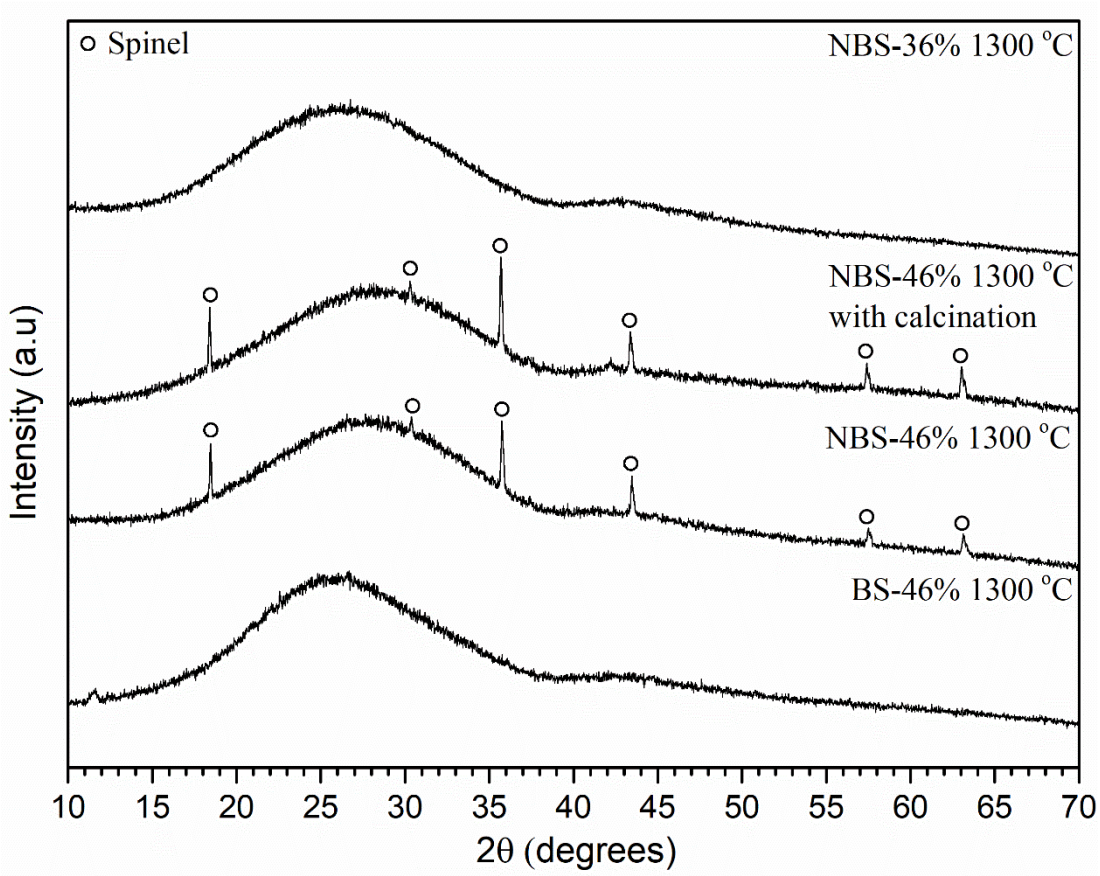

Figure 4-17. Powder XRD for the four glass compositions produced on a 70 g scale.

4.2.6.1 Characterisation of Metallic Waste Fraction and of Iron in Glass

In all the glasses produced, on a 70 g scale, there was a significant fraction of the reworked encapsulated Mg samples that remained metallic, however, glass compositions with higher mass gains had a lower mass fraction of metal remaining. Most of the metallic waste was found at the base of crucible where it had settled due to its increased density, but some remained suspended in the glass. Similarly spinel crystals could be observed at the base of the crucible with a higher fraction suspended in the glass. These suspended spinel crystals are not dispersed evenly throughout the glass matrix but tend to be in clusters, covering an average area of 625 $\mu m^2 \pm 375\ \mu m^2$ determined from 10 clusters of spinel crystals across the four glass compositions produced at 70 g scale. Figure 4-18 a is a SEM image of a cross-section of the metallic phase/ glass phase interface at the base of the crucible, Figure 4-18b is a SEM image of spinel crystals suspended in the glass, as can be observed they have a trapezium or square shape. Figure 4-18c and d show the chemical composition of the metallic phase, away from the glass phase, and close to the glass phase, respectively, and Figure 4-18e shows the EDX spectra of the spinel phase. Figure 4-18a shows the high density of spinel phases close to the metallic particle, with also a few crystals of forsterite present; in contrast to this Figure 4-18b shows a few spinel crystals suspended within the bulk glass. This demonstrates the heterogeneity of the waste form as a function of depth in the crucible. Figures 4-18c and d, demonstrate the differences in metallic waste composition depending on the distance from the glass interface. Those particles in contact with the glass are completely depleted in chromium with no signal detected in the EDX spectrum, whereas chromium is present in those particles further from the glass. This can be explained by the chromium in the stainless steel oxidising, forming a thin film, which is subsequently digested by the glass. This localised high concentration of chromium precipitates out as spinel phases of composition shown in Figure 4-18e.

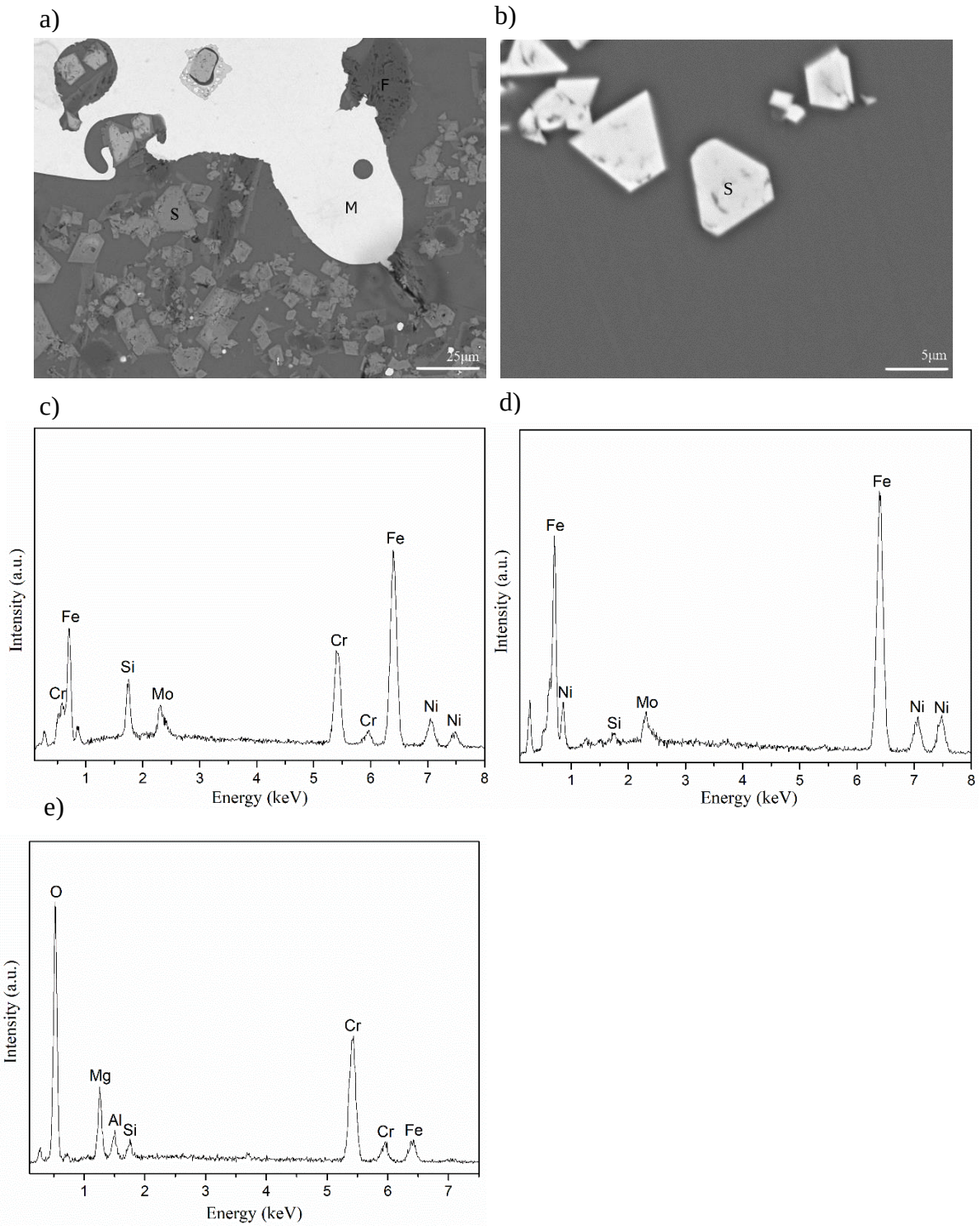

Figure 4-18a) SEM-BSE image of the interface of the metallic waste and the glass phase at the base of the crucible, from NBS-46% 1300 ºC 20 g scale, b) SEM-BSE image of spinel crystals, still suspended in the glass, from NBS-46% 1300 ºC 20 g scale. Label S denotes spinel phase, label M metallic phase and label F forsterite, c) EDX of metallic waste away from glass interface, d) EDX of metallic waste close to glass interface and e) EDX of spinel phase.

4.2.6.2 Spinel Composition and Oxidation of Metal

Semi-quantitative EDX was used to quantify the chemical composition of the spinel phase in the lower waste loading glasses, i.e. NBS-46%, NBS-46% with calcination, BS-46% and NBS-36%. The EDX spectra were obtained from one relatively large spinel crystal (to achieve a good S/N ratio) from each of the four low waste loading glasses. An average composition was then calculated; the results are shown in Table 4-9. Si is present in the EDX spectra of the spinel crystals, however this was omitted from the analysis, as Si is not known to routinely partition into spinel. The presence of Si is due to the interaction volume of the electron beam impinging on the glass, as the small size of the spinel crystal (typically on the ~5 μm size range) is insufficient to cover the entire beam. It should be noted that the interaction volume of electrons will lead to significant uncertainties for other elements also present in the glass, i.e. Mg, Fe and Al. The cation with the strongest count in the EDX spectra of the spinel is Cr, followed by Mg, Fe and Al.

Table 4-9.
Results from quantitative EDX of spinel phase.

Element	Atomic%	Proportion in formula	Error in formula
Oxygen	60.15 ± 2.15	4.00	± 0.00
Magnesium	8.80 ± 0.20	0.59	± 0.02
Iron	5.60 ± 0.40	0.37	± 0.03
Chromium	20.95 ± 0.25	1.39	± 0.02
Aluminium	1.85 ± 0.45	0.12	± 0.03

4.2.6.3 Mössbauer Spectroscopy

Mössbauer spectroscopy was utilised to provide information on the redox environment within the glass matrix, see Figure 4-19. EDS showed that iron was present in two different phases- the glass and the spinel phase. The best fit was with two Voigt based sites to fit to the glass- iron(II) and iron(III) and one Voigt based site to account for the spinel phase- iron(II). Fitting just two sites one for iron(II) and one for iron(III) gave a much poorer fit, this can be observed in Table 4-10. The recoil-free fraction for the Fe^{2+} and Fe^{3+} site were assumed to be equal [12]. The order of refinement for site

fitting was- areas (using the initial peak parameters); Lorentzian HWHM (and thereafter constrained); isomer shift of both sites; Q.S. of the Fe^{2+} site; both isomer shifts again; Q.S. of the Fe^{3+} site; finally both isomer shifts again. In spinels, often the iron(II) occupies the tetrahedral site and iron(III) occupies the octahedral site, although disordered spinels exist where iron(III) occupies the tetrahedral site and iron(II) the octahedral site [13],[14]. Redox ratios ($\frac{Fe^{2+}}{\sum Fe}$) can be calculated from the fitted values in Table 4-10 and are between 73.8 and 75.3%.

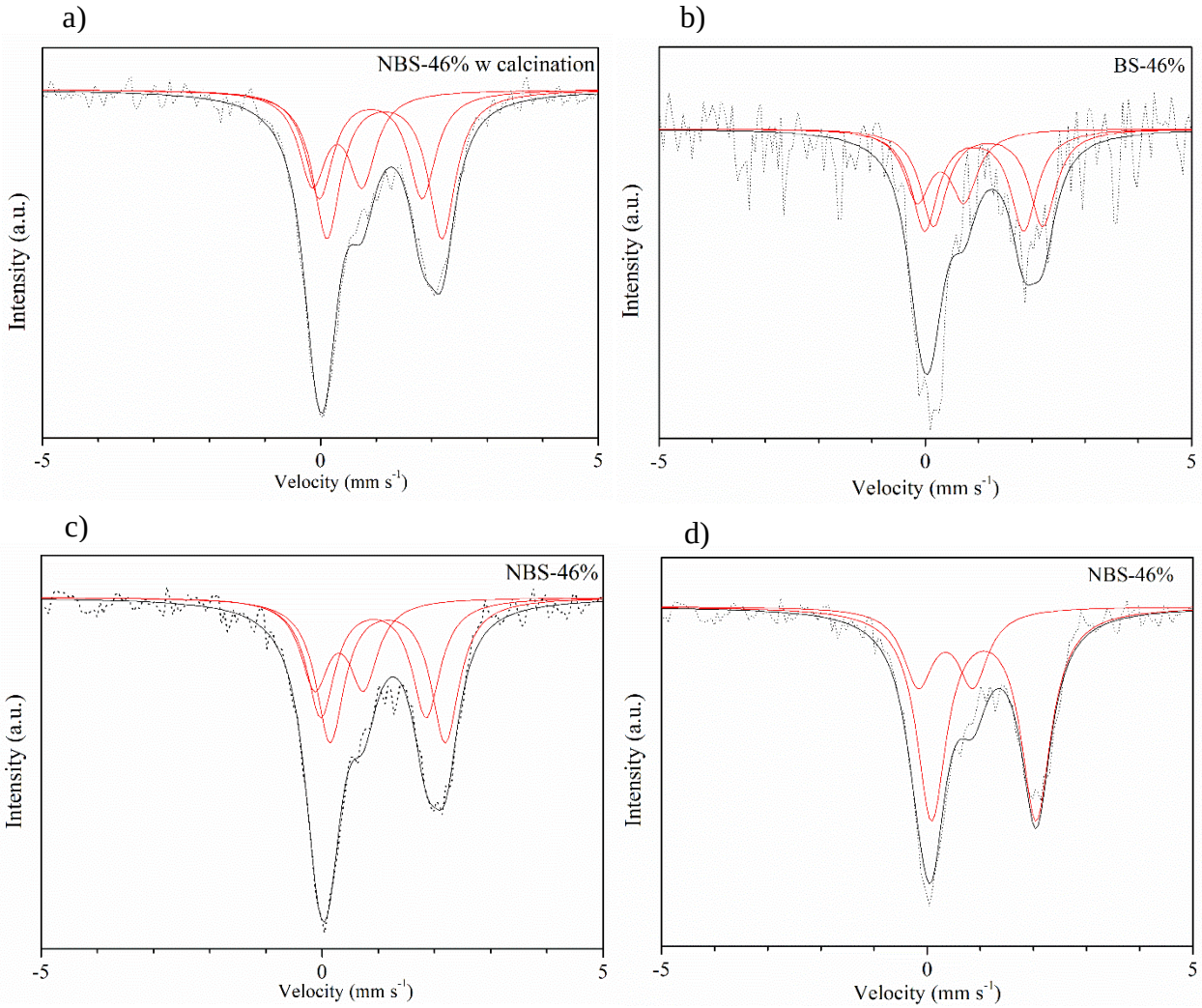

Figure 4-19. Mössbauer spectra with superimposed fitted profiles, derived from fitting of Voigt-based doublet sites, a) NBS-46% with calcination, b) BS-46%, c) NBS-46% and d) NBS-46% fitted with two sites, instead of three.

Table 4-10.
Parameters used to fit the Mössbauer spectra.

Sample	Isomer Shift (mm s^{-1})	Quadrupolar Splitting (mm s^{-1})	FWHM (mm s^{-1})	Area (%)	Assigned Phase	Reduced χ^2
NBS-46% with calcination	0.30	0.90	0.30	26.2%	Fe^{3+} glass	1.01
	1.15	2.07	0.30	42.7%	Fe^{2+} glass	
	0.91	1.85	0.30	31.1%	Fe^{2+} spinel	
BS-46%	0.29	0.88	0.30	25.8%	Fe^{3+} glass	0.87
	1.18	2.05	0.30	36.3%	Fe^{2+} glass	
	0.92	1.86	0.30	37.8%	Fe^{2+} spinel	
NBS-46%	0.30	0.87	0.30	24.7%	Fe^{3+} glass	0.95
	1.17	2.05	0.30	41.2%	Fe^{2+} glass	
	0.92	1.88	0.30	34.1%	Fe^{2+} spinel	
NBS-46%	0.30	0.92	0.30	26.4%	Fe^{3+} glass	1.40
	1.06	1.96	0.30	73.6%	Fe^{2+}	

4.2.7 Analysis of Uranium-Containing Low Waste Loading Glass

In the previous sections reworked glass products were produced from encapsulated Mg. In this section, Mg was substituted for Magnox alloy, and uranium included, to provide a more representative simulant waste form. Magnox was size reduced to swarf (< 5 mm in length) from a larger element provided by the National Nuclear Laboratory (NNL). Uranium metal was from Goodfellow and was size reduced from a piece of foil to small fragments (~1 cm x 1 cm). Uranium dioxide powder was from BDH Pharmaceuticals. The reagents were weighed according to Table 4-11 on a 2 decimal point balance. The cement samples were prepared using the same method as in section 4.1, with the mixture added to 50 mL centrifuge tubes in three batches, with uranium fragments added between the first and second batch. The cement samples were left to cure for a minimum of 28 days.

Table 4-11.
Reagents used to produce encapsulated Magnox swarf and uranium.

Reagent	wt%
BFS	47.78
PC	13.90
Water	21.56
Magnox Swarf	16.16
Uranium Metal	0.59

From the results of sections 4.3 and 4.4, the NBS-46% composition with calcination was selected as the most suitable formulation to repackage the encapsulated Magnox swarf with uranium. This was because of the low viscosity at the processing temperature, high metallic waste oxidation, low volume fraction of secondary phases and relatively high waste loading. The reagents were weighed according to Table 4-12 to 2 d.p. Most of the glass batch (iron, stainless steel, sand, boron oxide and sodium carbonate) was mixed, by hand, for 15 mins, however, the encapsulated Magnox swarf and uranium was not mixed due to the sharp edges of the Magnox and uranium shards, and due to the uranium being handled in a glovebox. The batch was doped with UO_2 powder (0.29 wt%) with the intention of giving double the uranium content of that quoted in the UK RWI specification for the drum [2],[3]. The glass was prepared as previously, but using a calcination step (at 750 ^{o}C for 8.5 h) and on a 150 g scale. A tapered wall recrystallised alumina crucible (S.A./V. ratio of 0.20 cm^{-1}) was used. The glass was then quenched into a mild steel rectangular annealing block, annealed close to the glass transition temperature for 1 h, and cooled at 1 ^{o}C min^{-1}. This glass is termed UNBS-46%.

Table 4-12.
Table showing the glass formulation used to vitrify the encapsulated Magnox swarf and uranium (UNBS-46%).

Precursor /wt%	
Magnox-encapsulated cement with uranium	39.51
UO_2	0.29
Iron	0.60
Stainless Steel	5.82
Sand	31.71
Boron Oxide	14.61
Sodium Carbonate	12.74

The reworked encapsulated Magnox swarf and uranium formed a dark black vitrified product, similar to the other glass compositions in this study. A large mass fraction of unreacted stainless steel remained at the base of the crucible with a ball of unreacted steel, similar to in Figure 4-15, recovered from the cast glass. The analysed composition of the UNBS-46% glass is given in Table 4-13. The glass contains are large range of oxides, but is composed predominantly (> 98.9 mol%) of a Na_2O- MgO- CaO- B_2O_3- Al_2O_3- SiO_2. The concentration of Fe in the glass is much lower than glasses produced on a smaller scale, due to less of the stainless steel oxidising at this larger scale. The glass composition was batched to have a final concentration of UO_2 of 0.52 wt%, as can be seen in Table 4-13, the value is close to the error of the measured value.

Table 4-13.
Analysed composition of UNBS-46% using the acid digestion method described in section 3.10.

Oxide	Wt%	Mol%
Na_2O	7.08 ± 0.21	6.90 ± 0.21
MgO	13.24 ± 0.40	19.84 ± 0.60
CaO	11.81 ± 0.35	12.72 ± 0.38
B_2O_3	16.77 ± 0.50	14.55 ± 0.44
Al_2O_3	9.64 ± 0.29	5.71 ± 0.17
SiO_2	39.01 ± 1.17	39.18 ± 1.18
UO_2	0.60 ± 0.04	0.14 ± 0.01
Fe_2O_3	0.58 ± 0.04	0.22 ± 0.02
Cr_2O_3	0.47 ± 0.03	0.19 ± 0.02
SO_3	0.21 ± 0.02	0.16 ± 0.01
TiO_2	0.18 ± 0.01	0.14 ± 0.01
K_2O	0.16 ± 0.01	0.10 ± 0.01
MnO	0.11 ± 0.01	0.10 ± 0.01
Others	0.14 ± 0.01	0.05 ± 0.01

Figure 4-20 shows the XRD spectrum for UNBS-46% with no crystalline phases observable and broad diffuse scattering present confirming that the major phase is amorphous.

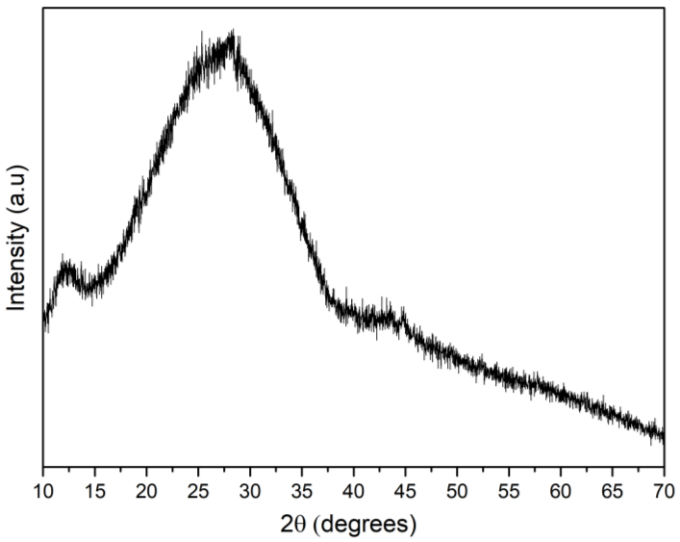

Figure 4-20. Powder XRD spectra of UNBS-46%.

Figure 4-21 shows the SEM-BSE image of UNBS-46% and the EDX spectrum of the glass. No secondary phases were found suspended in the glass and the EDX confirmed the glass was composed primarily of Na_2O- MgO- CaO- Al_2O_3 and SiO_2. Uranium was found to form part of the glass, see Figure 4-21b and no uranium was detected in the metal fraction found in the base of the glass.

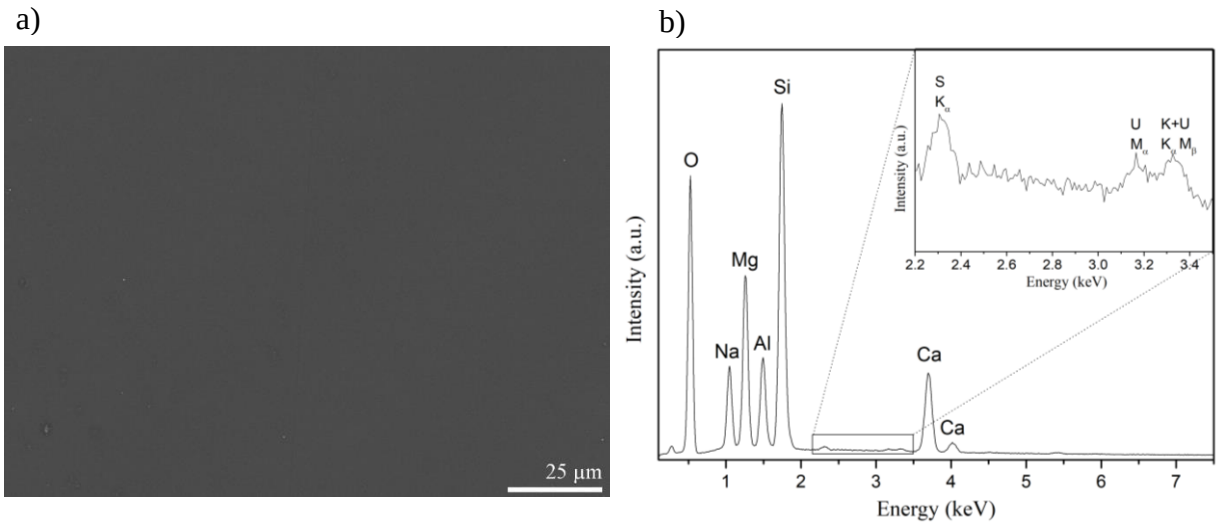

Figure 4-21. a) SEM-BSE image of UNBS-46%, b) EDX spectrum of the glass, with an inset between 2.2 and 3.5 keV, showing the characteristic M_α and M_β X-rays of uranium.

4.2.7.1 Uranium XANES Data

XANES spectra of the uranium L_{III}-edge were collected for UNBS-46% to determine the valency of uranium within the glass, along with standards of uranium(IV) (UTi_2O_6), uranium(V) ($Y_{0.5}U_{0.5}Ti_2O_6$) and uranium(VI) ($CaUO_4$), see Figure 4-22. The XANES spectrum for UNBS-46% closely resembles that of the uranium(IV) standard- the white line being narrower compared to the uranium(V) and (VI) standards and also lacking the flat edge feature of the white line of the uranium(V) standard. Also the UNBS-46% sample has a similar post-edge oscillation of the white line at around 17.21 keV, similar to the uranium(IV) standard.

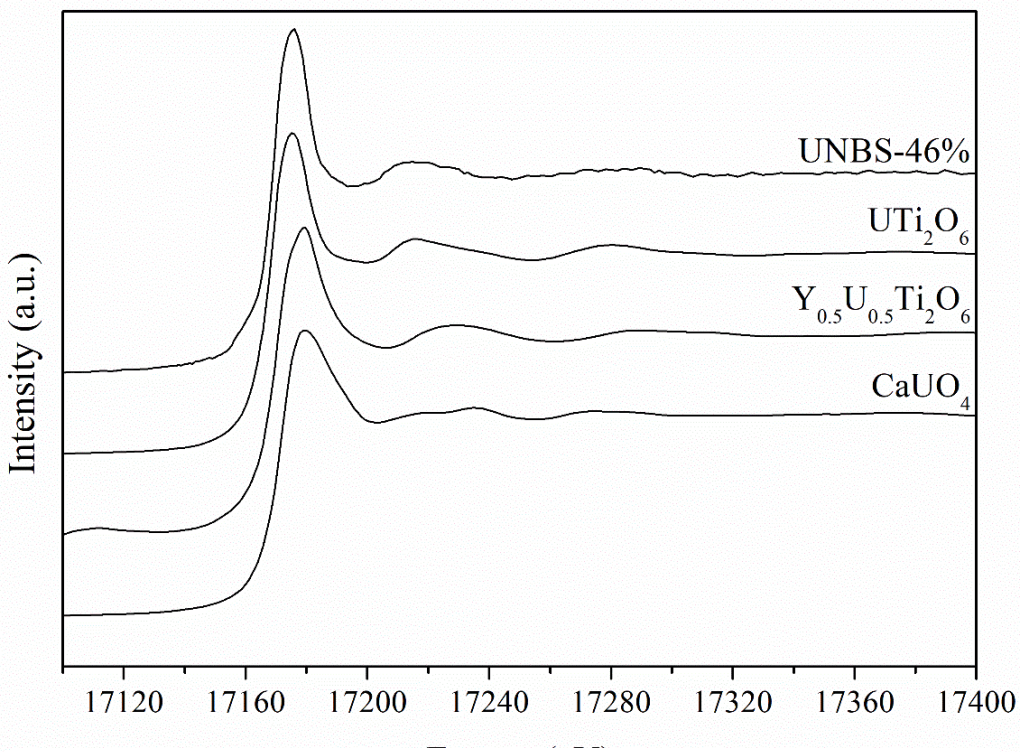

Figure 4-22. Stacked uranium XANES data of UNBS-46% showing the white line and post-edge features.

To determine the average oxidation state of uranium within the glass structure, linear regression lines were plotted of the energies of:

a) half the normalised absorption energy,
b) peak of the first derivative of the absorption energy, and
c) peak position of the white line.

These can be observed in Figure 4-23. The average oxidation state obtained from: a) half the normalised absorption energy was 4.5 ± 0.2, b) the peak of the first derivative of the absorption energy was 4.7 ± 0.2 and, c) the peak of white line was 4.1 ± 0.2. The best regression line of oxidation state versus energy of a particular feature, for the standards, was a) with R^2 of 1.00, followed by b) with R^2 of 0.97. The poorest linear relationship was for c) with R^2 of 0.77.

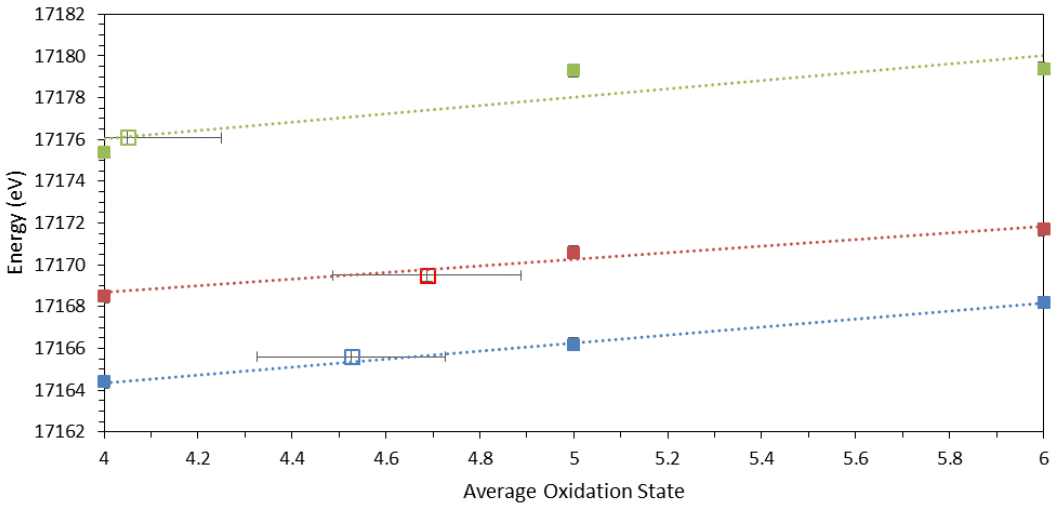

Figure 4-23. Linear regression plots of oxidation state and the energy of three different features of the XANES data, see above. Blue corresponds to a), red corresponds to b) and green corresponds to c). Filled squares are standards, open squares correspond to data obtained from UNBS-46% XANES.

4.2.7.2 Glass Dissolution

The short-term chemical durability of UNBS-46% was investigated using PCT-B dissolution experiments. Figure 4-24 shows the results from subjecting UNBS-46% to the PCT-B test protocol for 28 days at either 50 or 90 ^{o}C. B, Na, and Si and were used to monitor glass dissolution, whereas Cr, which EDX analysis shows is present in the spinel phase only, could be used to monitor spinel dissolution. Ca, Mg, Al, U and Fe were also measured in solution using ICP-OES, but Mg, U and Fe were below the detection limit of the instrument and Al and Ca were close to the detection limit and, therefore, the data was very noisy with significant variation in the measurements for a given time point. Glasses dissolved incongruently with $NL_{Na} > NL_{B} > NL_{Si}$. Na and B dissolution is rapid during the initial 7 days before decreasing for the final 21 days. However, dissolution during the later stages of the experiment continues with the concentration of Na and B in solution steadily increasing, as the residual rate regime is reached. For UNBS-46%, at 50 ^{o}C, the final data point at 28 days shows a large increase in NL_{B} and NL_{Na} suggesting that rate resumption may have occurred. However, this was not observed for UNBS-46% at 90 ^{o}C. NL_{Si} is constant throughout the experiment after rapidly dissolving at the first time point. NL_{Cr} is significantly less than the NL_{Na} and NL_{B} suggesting that the spinel phase is more durable than the glass phase, however, it is possible that Cr precipitates or forms part of the alteration layer. The experiments show that the effect of higher temperature (90 ^{o}C versus 50 ^{o}C) is to increase the dissolution during the first 7 days. After which the dissolution rate decreases and NL_{B}, NL_{Cr} and NL_{Si} are in error of another; NL_{Na} are also in error of one another for the two temperatures, but after 21 days rather than 7. Throughout the experiment the pH is between 9.7 and 10.4 and the pH of the leachates are, largely, within error of one another at the two different temperatures. Over 7 days the normalised release rates (g m^{-2} d^{-1}) at 50 ^{o}C for Na is 0.18, for B is 0.063, for Si is 0.0081 and for Cr is 0.015. The normalised release rates (g m^{-2} d^{-1}) at 90 ^{o}C for Na is 0.23, for B is 0.069, for Si is 0.0079 and for Cr is 0.0017.

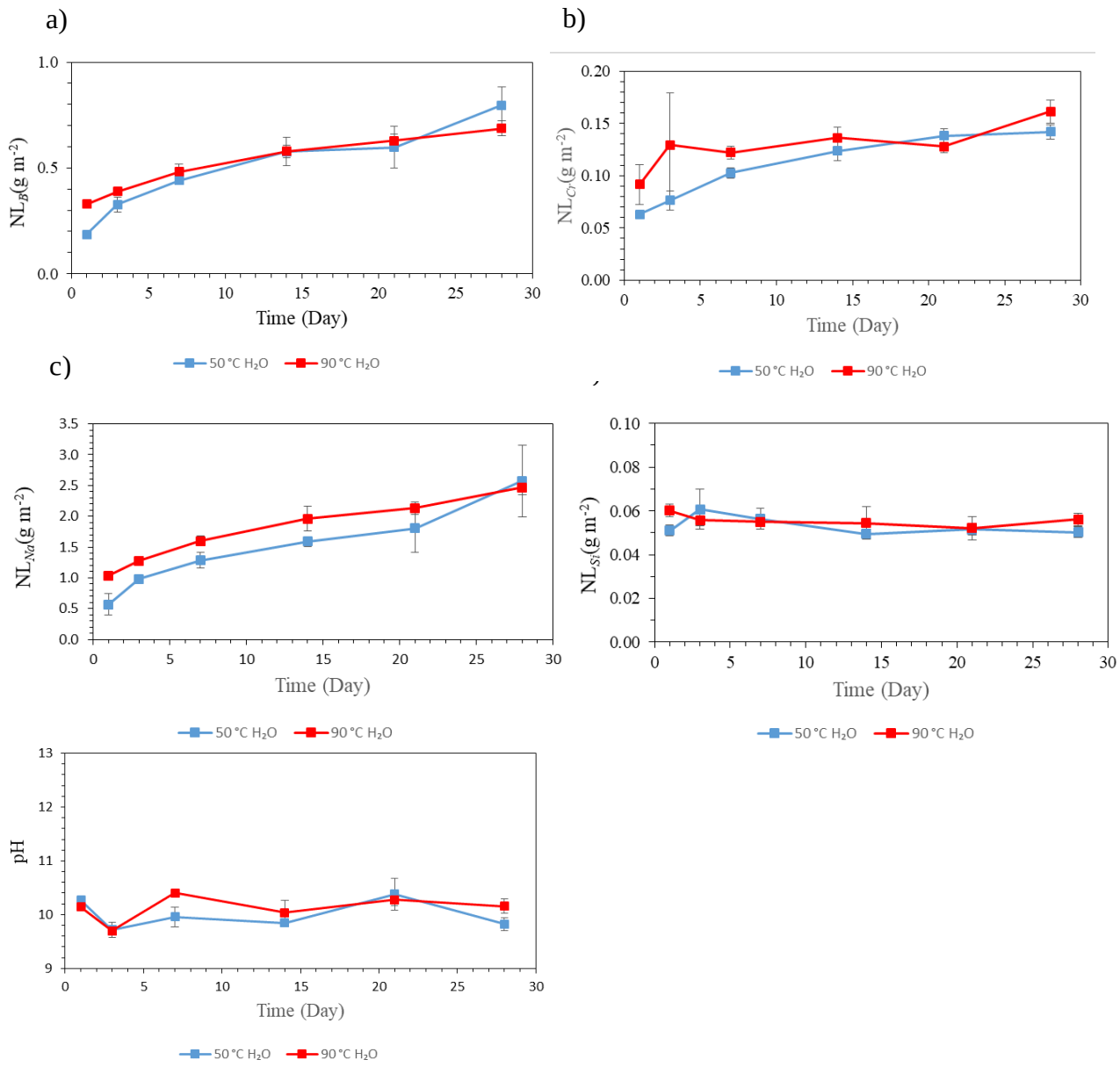

Figure 4-24. PCT-B dissolutions results at 50 °C (blue markers) and 90 °C (red markers), in deionised water, for a) NL_B, b) NL_{Cr}, c) NL_{Na}, d) NL_{Si} and e) pH.

Figure 4-25 shows the results from short-term dissolution experiments for UNBS-46% at 50 °C in deionised water and saturated $Ca(OH)_{2(aq)}$ solution. Note the results from the dissolution experiment for UNBS-46%, at 50 °C, in deionised water are the same as in Figure 4-24, but are presented again to allow comparisons between the different leachates to be made. B, Na, and Si and were used to monitor glass dissolution whereas Cr, which EDX analysis shows is present in the spinel phase only, could be used to monitor spinel dissolution. Ca was also measured in solution to monitor the interaction of the glass with $Ca(OH)_{2(aq)}$ from the leachate. As in the experiments at 50

and 90 ºC in deionised water, UNBS-46% in saturated $Ca(OH)_{2(aq)}$ dissolves incongruently with $NL_{Na} > NL_B > NL_{Si}$. Na and B dissolution is rapid during the initial 7- 14 days in saturated $Ca(OH)_{2(aq)}$ before decreasing for the rest of the experiment as the residual rate regime is reached. The concentration of Si in solution is negligible due to its precipitation. In saturated $Ca(OH)_{2(aq)}$, NL_{Na}, NL_B and NL_{Si} are significantly lower than in deionised water, for all of the initial rate regime, rate drop and residual rate regimes. NL_{Cr} is initially very high before decreasing throughout the rest of the experiment. At the start of the experiment $Ca(OH)_2$ is saturated in solution (806 ppm), over the course of the experiment this steadily drops, before reaching a final value at the end of 28 days at 222 ppm. The blank solutions of saturated $Ca(OH)_{2(aq)}$ remains saturated throughout the 28 days proving that the experimental set-up is sufficient to exclude CO_2, preventing carbonation. The pH at 50 ºC in deionised water is between 9.7 and 10.4, in contrast the pH in saturated $Ca(OH)_2$ solution is much higher starting at 12.8 and then decreasing linearly with time to a pH of 12.1 at the end of the experiment. Over 7 days the normalised release rates (g m^{-2} day^{-1}) at 50 ºC in saturated $Ca(OH)_{2(aq)}$ for Na is 0.098, for B is 0.037, for Si is 0.00027.

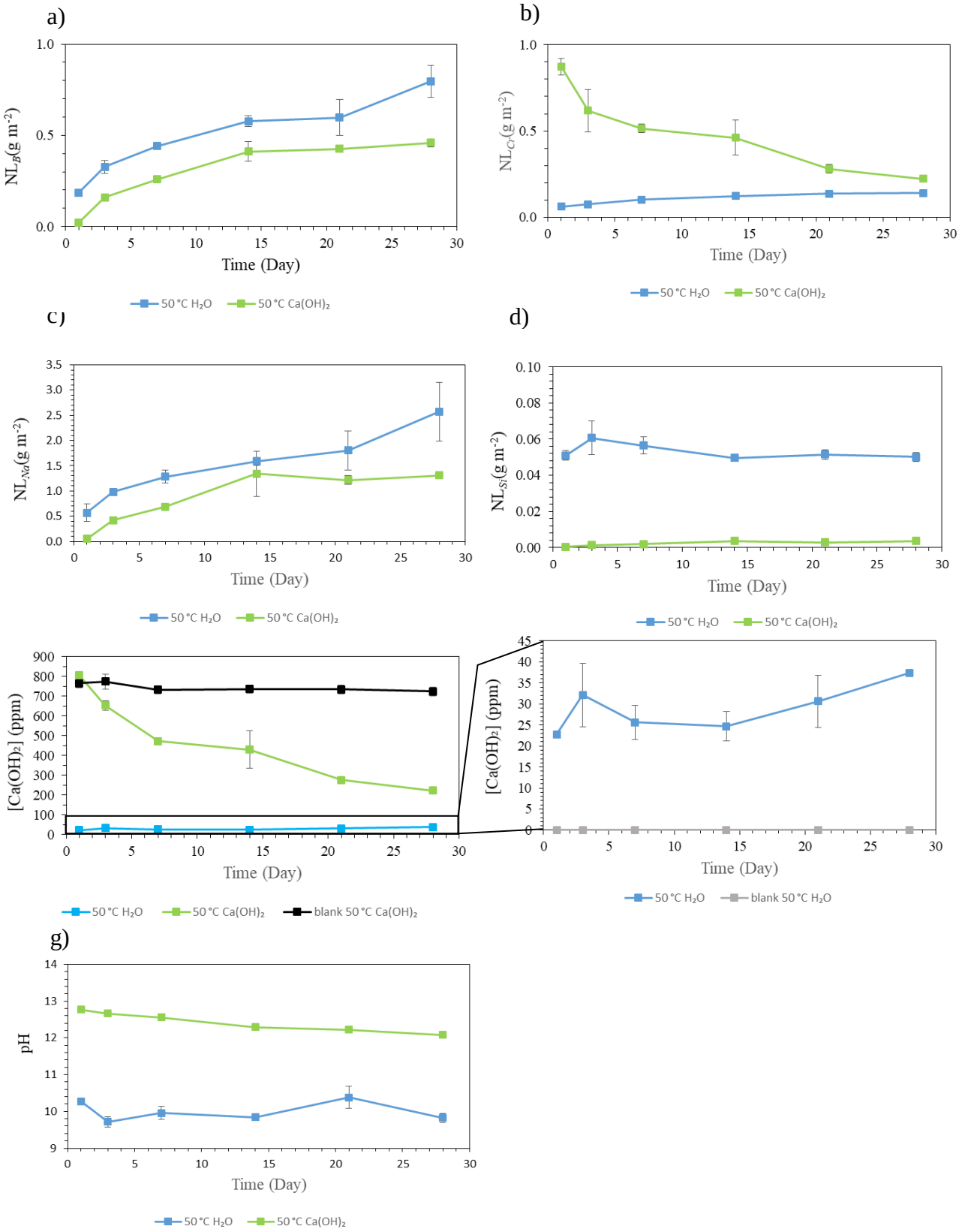

Figure 4-25. PCT-B dissolution results at 50 °C (blue markers) in deionised water and saturated $Ca(OH)_{2(aq)}$ solution (green markers) for a) NL_B, b) $NL_{Cr,}$ c) NL_{Na}, d) NL_{Si} and e) $Ca(OH)_2$ concentration, f) inset of $Ca(OH)_2$ concentration for 50 °C deionised water and g) pH.

Figure 4-26 displays altered glass particles from glass dissolution experiments using SEM-BSE as well as EDX line scans starting at the pristine glass, across the altered layer and into resin used to mount the powders. The altered layer is thin, with its thickness varying between particles, but typical thickness was between 2 and 10 μm. It was observed that the alteration layers tend to be thicker at 90 ^{o}C in water, than at 50 ^{o}C in water, but due to the variability in alteration layer thickness this is uncertain, without further analysis. The chemical composition of the alteration layer of UNBS-46%, in deionised water, is enriched in Si and Mg, with Al and Ca also detectable. The chemical composition is the same for UNBS-46% altered at 50 and 90 ^{o}C in deionised water. However the chemical composition of the altered layer is significantly different when dissolved in saturated $Ca(OH)_{2(aq)}$, the layer is enriched in Si and Ca with no other elements detected.

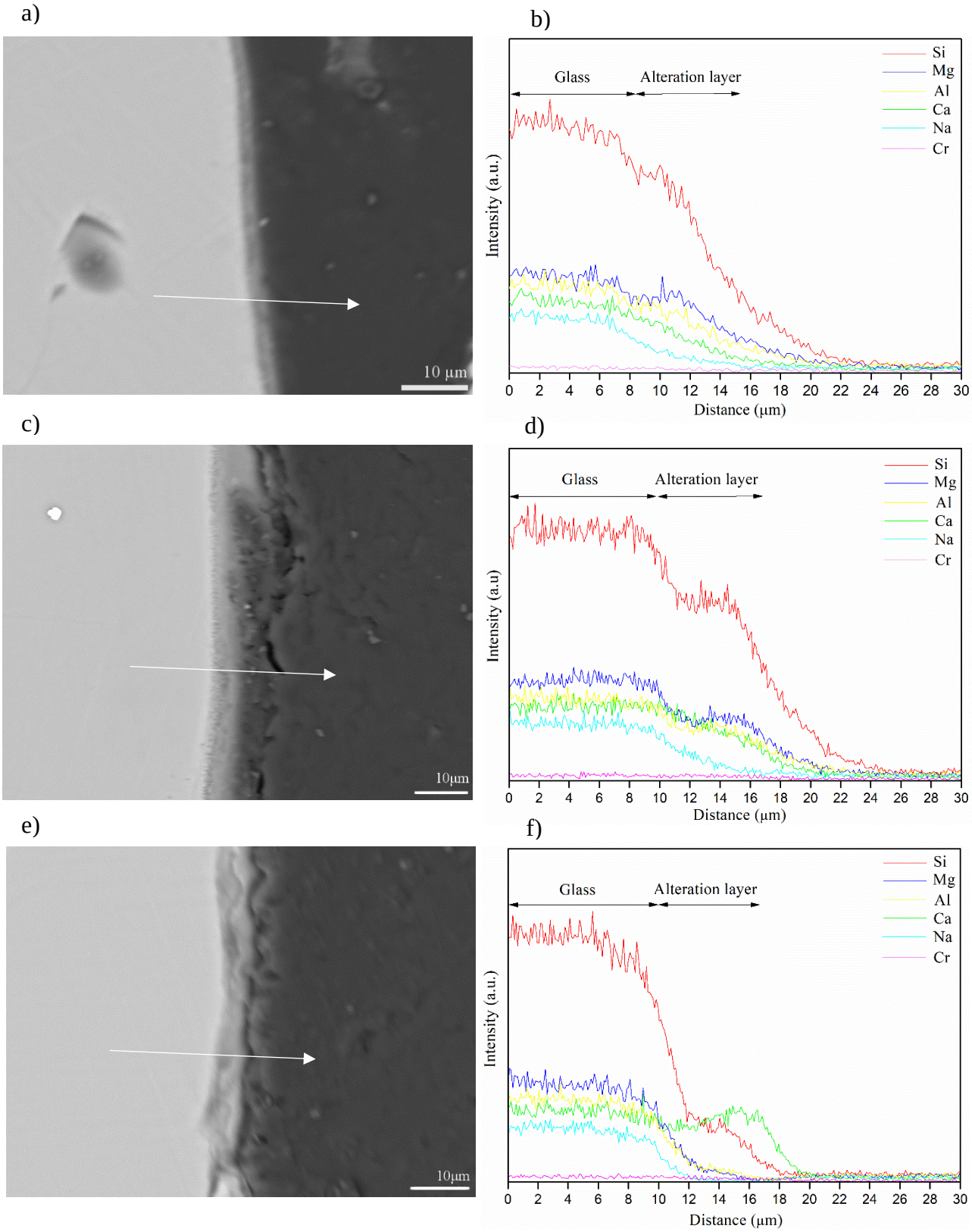

Figure 4-26. SEM-BSE images of alteration layers from leached glass powders (UNBS-46%) and EDX line scans across the alteration layers with lines indicating where the scans were collected, a) and b) from 50 ºC in water, c and d) from 90 ºC in water and d) and e) from 50 ºC in saturated $Ca(OH)_{2(aq)}$ solution.

4.3 Discussion

4.3.1 Glass Compositions and Phase Assemblage

The purpose of this chapter was to study the possibility of repackaging cement encapsulated Magnox swarf drums showing evidence of internal corrosion. It was found that thermal conditioning of cemented Magnox waste forms decomposes the cement phases and oxidises the metallic content (all of the Mg / Magnox and most of the stainless steel). The extent of stainless steel oxidation is dependent on temperature, glass composition and, most significantly, scale. The evaporation of all water and oxidation of Magnox removes the reactants in the main corrosion reaction, see Equation 4.1. There is diffuse scattering in the XRD patterns of glasses produced at higher waste loadings, which is more prominent at lower waste loadings, indicating the presence of a major amorphous phase. Higher waste loading glasses (72% and 89%) crystallised Mg-containing secondary phases. Low waste loading glasses could incorporate at least 22 mol% MgO before forsterite (Mg_2SiO_4) or any other Mg-containing secondary phases crystallised. For the higher waste loading glasses, the MgO was estimated to be 29 mol% at 72% waste loading and 36 mol% at 89% waste loading. At 1200 ^oC, monticellite ($CaMgSiO_4$) is present, but at 1300 ^oC this phase melts during processing and is incorporated into the glass phase (for both BS-72% and NBS-72% compositions). These higher waste loading glasses produced high viscosity glass melts and partially crystalline waste forms with high porosity. It was demonstrated that the porosity could be reduced by increasing the processing temperature (from 1200 to 1300 ^oC), however, during initial trial melts it was observed that crucible corrosion was more aggressive at higher temperatures. This severe crucible corrosion is due to the high metallic content leading to the corrosion process of downward drilling [15]. All lower waste loading glasses showed broad diffuse scattering in XRD patterns, except BS-46% 1200 ^oC, which had a significant quantity of undigested quartz present, due to unreacted batch. Two minor phases were identified in the other low waste loading glass batches- spinel, formed from oxidation of metallic waste (in particular stainless steel) and quartz (from unreacted batch).

There are positive mass gains due to oxidation of metallic waste during thermal conditioning. For the higher waste loading glasses at small scales (~20 g), where there was little metallic phase separation, the mass gains were between 158 to 150% and temperature and glass composition had little effect on the mass gains. On the other hand, for the lower waste loading glasses temperature and glass composition did have an effect on mass gain. This may be due to the low waste loading glasses being more fluid, with the higher temperature and different glass composition increasing this fluidity and promoting $O_{2(g)}$ diffusion through the glass melt.

It was found that the higher the mass gains, the greater the intensities of the reflections from the spinel phase in the XRD. Spinel phases were observed, from powder XRD, in every sample at high waste loading and in NBS-46% 1300 ^{o}C and 1200 ^{o}C and NBS-36% 1300 ^{o}C. They are typically <5 μm in size. The only source of chromium is from the stainless steel and the spinel is rich in chromium, whereas, there is no chromium present in the glass. Therefore, a proposed mechanism for the spinel crystallisation is that the glass corrodes the stainless steel creating high local concentration of Fe and Cr, which precipitate forming spinel phases. These, with the undigested metallic waste, settle with time but the natural mixing of the glass melt leaves some suspended. DTA of the small scale (~20 g) glass melts showed three main events- the glass transition, crystallisation temperature(s) and melting temperature(s). The presence of Na_2O, in the NBS glass compositions, leads to a decrease in the glass transition temperature compared to BS compositions, due to a weakening of the glass structure. The crystallisation event that occurs upon heating is due to the formation of diopside ($CaMgSi_2O_6$), which was determined from XRD of the heated glasses. This occurs between 770 and 940 ^{o}C. For a given glass composition, processing at 1300 ^{o}C, rather than 1200 ^{o}C, gave more intense crystallisation peaks. For the high waste loading glasses there is a melting event for the glasses processed at 1200 ^{o}C (NBS-72% and BS-72%) not present for those processed at 1300 ^{o}C. This occurs between 927 and 958 ^{o}C and may be due to the melting of monticellite as it gets digested into the glass on re-heating. The final thermal event is hypothesised to be due to re-melting of the diopside phase; for the low waste loading glasses this occurs between 960 and 1020 ^{o}C and for the high waste loading glasses this occurs between 1020 and 1100 ^{o}C.

4.3.2 Effect of Scale on Glass Melt

Increasing the batch size from 20 g to 70 g oxidised all of the Mg and the majority of the stainless steel, however, for some compositions it led to the formation of balls of sintered stainless steel in the glass melt, as the conditions were insufficient to oxidise all of the metal. Although the melt temperature is below the melting point of 316L stainless steel, localised temperatures in the glass, originating from the heat released when Mg oxidises, could be sufficient to melt the stainless steel and therefore explain the spherical shape of undigested metallic waste, as seen in Figure 4-15. Mass gains for those glasses produced at 20 g scale, at 1300 ºC, were between 157 and 178%; at the 70 g scale they had dropped to between 116 and 151%. The trend in mass gains with glass composition is corroborated with that at 20 g scale with NBS-36% having the lowest mass gain at 116%. Even though NBS-36% has a higher concentration of Na_2O than NBS-46%, which causes a decrease in viscosity, it has less MgO (between 4.6 and 6.7 mol%) and more SiO_2 (between 1.6 and 6.2 mol%), which both contribute to increasing viscosity. It was observed that there was a linear relationship between mass gains and density. Those compositions of higher mass gains oxidise more of the metallic waste, producing relatively high density spinel phases, some of which stay suspended in the glass and increase the overall density of the reworked waste form.

4.3.3 Redox Environment in the Glass Melt

Information on the redox environment of the glass melts is possible from data extracted from Mössbauer spectra. This is possible as redox ratios ($\frac{Fe^{2+}}{\sum Fe}$) can be calculated from the areas of the fitted spectral features. Observed redox ratios for low waste loading glasses are 73.8% for NBS-46% with calcination, 75.3% for NBS-46% and 74.1% for BS-46%, and are all in error of one another. The best fit was obtained by using three sites to model the data giving reduced χ^2 values between 0.87 and 1.01. An attempt at fitting two sites for the NBS-46% composition, one to account for the Fe^{2+} and one for the Fe^{3+}, gave a poor fit (reduced χ^2 of 1.40), indicating that the model was not accounting for a site. Fe^{3+} in the glasses have isomer shifts of ~0.3 mm s^{-1} indicating that they are octahedrally coordinated. Fe^{2+} in the glasses have isomer shifts between 1.15-1.18 and Q.S. between 2.05-2.07 indicating that they are also octahedrally coordinated [16]. For the Fe^{2+} spinel site, the I.S. of ~0.92 mm s^{-1}

suggests that it is tetrahedrally coordinated, consistent with the A site of the spinel. Semi-quantitative EDX of the spinel phase demonstrated that its composition is essentially composed of Cr, Mg and Fe, with Cr in the B site, Mg in the A site and, from the Mössbauer data, Fe^{2+} also in the A site. There is also evidence of some of the Al incorporating too. Most of these elements (in the case of Cr all of it) originates from the metallic waste present in the cemented Magnox waste form.

4.3.4 Characterisation of Encapsulated Magnox Swarf and Uranium

The glass composition, UNBS-46%, was produced on a 150 g scale, and included Magnox, uranium metal and UO_2, with the uranium added as 67 wt% U metal and 33 wt% UO_2. Thermal conditioning, using the UNBS-46% composition, causes oxidation of the Magnox and uranium, thermal decomposition of the hydrated phases and removal of free water from the cement. This removes the reactants from the corrosion reactions, shown in Equation 4-1 and Equation 4-2, thereby removing the underlying issue with the cemented waste. By studying the uranium L_{III}-edge it was determined that the average oxidation state of uranium in the glass was 4.5 ± 0.2, indicating that the uranium had close to an equal distribution of the +4 and +5 oxidation states in the glass (assuming no +6). This highlights how reducing the glass melt is, as, in oxidising atmospheres uranium will form the +6 oxidation state as a uranyl species acting as a modifier [17]. The low oxidation state of uranium in the glass is attributed to the highly reducing nature of the melt (due to the high metallic waste content). Despite this, the uranium is still oxidised from an average starting oxidation state of 1.3 (if we take uranium metal's oxidation state as 0) to 4.5. In the +4 and +5 oxidation state, uranium will behave as an intermediate in the glass [18]. It was found that half the normalised absorption energy of uranium gave the best fit for determining average oxidation state with the peak energy of the first derivative giving good agreement. However, the peak position of the white line significantly underestimates the average oxidation state.

For the short-term glass dissolution studies, it was found that NL_{Si} was an order of magnitude less than both NL_{Na} and NL_B under all three different test conditions. The Si saturates by 24 h and remains constant throughout the experiment, with a small decrease from day 1 to day 7. In deionised water, NL_{Na} and NL_B are within

experimental error of one another at both 50 and 90 ºC. This could be due to the high initial dissolution rates, which lead to a plateau in mass loss after approximately 7 days when the residual rate regime is reached. NL_{Si} is similar for the 50 and 90 ºC experiments, in deionised water, but is an order of magnitude less when conducted at 50 ºC in saturated $Ca(OH)_2$ solution. This is due to the precipitation of C-S-H phases onto the surface of the glass. The effect of $Ca(OH)_{2(aq)}$ in solution is to decrease the rate with NL_B, NL_{Na} and NL_{Si} significantly lower than in water. Compared with the NL_B (0.79 g m^{-2} d^{-1}) and NL_{Na} (0.59 g m^{-2} d^{-1}) for waste-loaded MW-25% HLW glass (90 ºC in H_2O), the UNBS-46% composition has increased durability with NL_B (0.07 g m^{-2} d^{-1}) and NL_{Na} (0.23 g m^{-2} d^{-1}), (i.e. approximately by a factor of 11 for B and 3 for Na). The concentration of SiO_2, B_2O_3 and Na_2O in UNBS-46% are similar to that found in waste-loaded (25 wt%) MW glass, so the increased durability is attributed to the high levels of Al_2O_3, but also the presence of CaO and MgO, which are known to increase durability in the short-term [19],[20]. The initial rate, over 7 days, at 50 ºC in saturated $Ca(OH)_{2(aq)}$, based on NL_{Na}, was 0.10 g m^{-2} d^{-1}. Previously reported simulant ILW glasses (from PCM vitrification) (in saturated $Ca(OH)_{2(aq)}$ at 50 ºC) had initial dissolution rates between 0.04-0.18 g m^{-2} d^{-1}, dependent upon the particular PCM waste stream [15]. This demonstrates similarly durable waste form performance compared to other ILW glasses. Cr (a marker for spinel dissolution) has an increased initial leach rate in $Ca(OH)_2$ compared to that in water, this may be due to the elevated pH, however in the later part of the experiment Cr concentrations decrease, indicating precipitation from solution. This decrease of Cr in solution could be due to the decrease in pH (from 12.8 to 12.1) caused by C-S-H precipitation. The reason for the lower rates in $Ca(OH_2)$ could be explained by precipitation of calcium onto the surface of the glass forming a C-S-H phase. Over the 28 day period the normalised release rates (g m^{-2} d^{-1}) for NBS-46% are, for B 0.027, for Na 0.083 and for Si 0.0024. The incubation period observed for other ILW glasses leached in saturated $Ca(OH)_2$ was not observed for UNBS-46%, with dissolution following the usual regimes of initial rate followed by the residual rate. The incubation period in previous studies was hypothesised to be to the formation of dissolution-inhibiting calcium borates on the surface of the glass (with calcium originating from solution only) [21], the absence of the incubation period here may be because of the high concentration of Ca already present in the glass. For UNBS-46% the concentration of $Ca(OH)_{2(aq)}$ decreases from

800 ppm (after 24 h) to 655 ppm (after 3 days). When conducted in water it was found that after 24 h, 25ppm of Ca had dissolved from the glass, which may explain the small increase from 770 ppm (at day 0) to 800 ppm (after 24 h) followed by the decrease in concentration as C-S-H formation occurs.

4.3.5 Applicability to Industrial Scale Conditioning

In order for the packaged waste form to be vitrified it is suggested the best approach would involve size reduction, in an industrial shredder, prior to thermal conditioning. Shredders typically recirculate material internally, crushing and piercing the feed material, whilst passing over a large sieve at the base, which only allows through material on the order of a few centimetres [22], [23]. This preliminary step would enable good contact between the glass additives and the cement grains in the glass melter. It would also encourage oxidation of the metallic waste due to the greater surface area of metal available. It is likely on an industrial scale the repackaged waste form will consist of a main vitreous phase with a large fraction of undigested metallic waste, comprising mainly of stainless steel at the base of the melting vessel. A metallic phase is not a major issue as a separate phase forming in a vitreous waste form, but its oxidation is preferred. One potential issue is radioisotopes partitioning into the stainless steel; for example Ce-144 forms a significant of the radiological inventory looked at in this study, and could alloy into the steel. However, if you are below the melting point of steel it is unlikely radioactive isotopes will dissolve into the steel. A second issue is the method of vitrification- direct heating of waste (as occurs in JHCMs and in-container vitrification) could lead to a low conductive path forming between the electrodes, and thus shorting the melter. For repackaging of encapsulated Magnox swarf, plasma melters may be more suitable; another advantage of plasma technology would be the potential to condition the waste without the use of a shredder beforehand.

One of the main advantages of thermal conditioning of ILW, in general, is volume reduction, leading to significant cost savings during interim storage and final disposal. The total volume of a cemented Magnox drum is ~500 L. For the UNBS-46% composition, assuming all metallic waste has oxidised, the repackaged waste form takes up 575 L. An alternative rework strategy could be to repair, for example,

encapsulating 4x 500 L drums in a $3m^3$ box, this would lead to an equivalent of 750 L per drum. It must be noted that glass composition development could increase the waste loading from the UNBS-46% composition, however, a $3m^3$ box is the smallest volume container that could possibly accommodate 4 x 500 L drums and at that would only provide a thin overpack. The NBS-46% composition results in a waste volume x 1.2 ± 0.1 greater than the original drum, whereas repair would result in x 1.5 + 0.3 greater volume than the original drum.

4.4 Conclusions

Thermal conditioning as a rework strategy for encapsulated Magnox swarf, showing evidence of internal corrosion, is advantageous. Glass compositions that successfully rework the cemented waste at 1200 ºC and 1300 ºC at 46 wt% waste loading have been demonstrated. Higher waste loadings (>72 wt% waste loading) produce a slag-like waste form with high concentration of the Mg-containing phases (forsterite, monticellite and periclase). Temperatures > 1400 ºC can lead to severe crucible corrosion. The main advantage of reworking, versus repair, is that the reactants in the corrosion reactions, i.e. Magnox and uranium, are oxidised within the glass melt, with Mg forming both part of the glass and other crystalline secondary phases, and uranium forming part of the glass only. The ferrous metal fraction, of the encapsulated Magnox swarf drums, oxidises, to an extent, dependent upon glass composition, temperature and scale. The stainless steel either oxidises and precipitates as a spinel phase or remains unreacted. The high metallic fraction of this waste (~13 wt% for the UNBS-46% composition) results in a highly reducing glass melt, with $(\frac{Fe^{2+}}{\sum Fe})$ from 73%-76%, and an average oxidation state of uranium of 4.5 ± 0.2. The durability of the reworked waste (UNBS-46%) is significantly better than HLW glass, and similar to other ILW glasses. Using measured densities it was calculated that there is the potential for significant waste volume reductions using reworking rather than repair, with reworking giving a waste volume x1.2 ± 0.1 greater than the original encapsulated Magnox swarf and repair giving a volume x1.5 + 0.3 greater. Overall, should any cement encapsulated Magnox swarf drums require reworking, it has been demonstrated that vitrification offers several advantages over other reworking strategies, in particular repair, with demonstration on an industrial scale as a priority.

4.5 References

[1] Nirex Solutions, “Work Package Part 1. The Wastes and cementation processes employed at Sellafield for treatment of ILW.”

[2] NDA, “Waste Stream 2D38/C Encapsulated Magnox Cladding,” *2013*. [Online]. Available: http://ukinventory.nda.gov.uk/wp-content/uploads/sites/18/2014/05/2D38_C.pdf. [Accessed: 15-Nov-2014].

[3] NDA, “Waste Stream 2D35/C Encapsulated Retrieved Magnox Cladding,” *2013*. [Online]. Available: http://ukinventory.nda.gov.uk/wp-content/uploads/sites/18/2014/05/2D35_C.pdf. [Accessed: 15-Nov-2014].

[4] G. A. Fairhall and J. D. Palmer, “The Encapsulation of Magnox Swarf in Cement in the United Kingdom,” *Cem. Concr. Res.*, vol. 22, pp. 293–298, 1992.

[5] H. I. Godfrey and M. Brogden, “Minimisation of Uranium Corrosion when Treating Hanford KE and KW Basin Wastes using Cementation, NSTS(04) 4993,” 2004.

[6] J. Cronin and N. Collier, “Corrosion And Expansion Of Grouted Magnox,” *Miner. Mag.*, vol. 76, no. 8, pp. 2901–2909, 2012.

[7] Environment Agency, “Reworking intermediate level radioactive waste. Science report: SC040047,” Bristol, 2005.

[8] L. G. Baquerizo, T. Matschei, K. L. Scrivener, M. Saeidpour, and L. Wadsö, “Hydration states of AFm cement phases,” *Cem. Concr. Res.*, vol. 73, pp. 143–157, 2015.

[9] P. A. Bingham, R. J. Hand, and C. R. Scales, “Immobilization of simulated plutonium-contaminated material in phosphate glass: an initial scoping study,” *Mater. Res. Soc. Symp. Proc.*, vol. 932, pp. 345–352, 2006.

[10] S. . Henry, F. Reidenbach, G. M. Davidson, W. W. S. Jr., and J. . Davis, “Physical Properties,” in *ASM Speciality Handbook: Stainless Steels*, 1994, p. 489.

[11] M. W. J. Chase, “NIST-JANAF Thermochemical Tables,” *J. Phys.Chem. Ref. Data*, vol. Monograph, pp. 1–1951, 1998.

[12] O. J. McGann, P. . Bingham, R. J. Hand, A. S. Gandy, M. Kavčič, M. Žitnik, K. Bučar, R. Edge, and N. C. Hyatt, “The effects of gamma radiation on model vitreous wasteforms intended for the disposal of intermediate and high level radioactive wastes in the UK,” *J. Nucl. Mater.*, vol. 429, pp. 353–367, 2012.

[13] M. D. Osborne, M. E. Fleet, and G. M. Bancroft, “Fe(II)-Fe(III) ordering in chromite and Cr-bearing spinels,” *Contrib. to Mineral. Petrol.*, vol. 77, no. 3,

pp. 251–255, 1981.

[14] G. A. Sawatazky, “Recoiless-fraction ratios for 57Fe in octahedral and terahedral sites of a spinel and a garnet,” *Phys. Rev.*, vol. 183, pp. 383–386, 1969.

[15] N. C. Hyatt, R. R. Schwarz, P. A. Bingham, M. C. Stennett, C. L. Corkhill, P. G. Heath, R. J. Hand, M. James, A. Pearson, and S. Morgan, “Thermal Treatment of Simulant Plutonium Contaminated Materials From The Sellafield Site By Vitrification In A Blast-Furnace Slag,” *J. Nucl. Mater.*, vol. 444, pp. 186–199, 2014.

[16] M. D. Dyar, D. G. Agresti, M. W. Schaefer, C. A. Grant, and E. C. Sklute, “Mössbauer Spectroscopy of Earth and Planetary Materials,” *Annu. Rev. Earth Planet. Sci.*, vol. 34, pp. 83–125, 2006.

[17] A. J. Connelly, N. C. Hyatt, K. P. Travis, R. J. Hand, M. C. Stennett, A. S. Gandy, A. P. Brown, and D. C. Apperley, “The effect of uranium oxide additions on the structure of alkali borosilicate glasses,” *J. Non. Cryst. Solids*, vol. 378, pp. 282–289, 2013.

[18] H. D. Schreiber and G. B. Balazs, “The Chemistry of Uranium in Borosilicate Glasses. Part 1. Simple Base Compositions Relevant to the Immobilisation of Nuclear Waste,” *Phys. Chem. Glas.*, vol. 23, p. 139, 1982.

[19] I. W. Donald, “Waste Immobilisation in Glass and Ceramic Based Hosts-Radioactive, Toxic and Hazardous Wastes,” 1st ed., Chichester: Wiley, 2010, pp. 1–31, 57–177, 275–334, 465–490.

[20] B. M. J. Thien, N. Godon, A. Ballestro, S. Gin, and A. Ayral, “The dual effect of Mg on the long-term alteration rate of AVM nuclear waste glasses,” *J. Nucl. Mater.*, vol. 427, pp. 297–310, 2012.

[21] C. A. Utton, R. J. Hand, P. A. Bingham, N. C. Hyatt, S. W. Swanton, and S. J. Williams, “Dissolution of vitrified wastes in a high-pH calcium-rich solution,” *J. Nucl. Mater.*, vol. 435, pp. 112–122, 2013.

[22] S. S. I. INC, “SSI Shredding Systems, Four-Shaft Shredders,” 2015. [Online]. Available: https://www.ssiworld.com/en/products/four_shaft_shredders/. [Accessed: 15-Nov-2015].

[23] J. Deckers, “The innovative plasma tilting furnace for treatment of radioactive and problematic chemical waste,” in *Thermal treatment of radioactive wastes: research, development and demonstration*, 2013, p. http://www.sheffield.ac.uk/polopoly_fs/1.384714!/f.

5 Thermal Conditioning of Clinoptilolite Using Low Melting Borosilicate Glass Formulations

5.1 Introduction

Clinoptilolite is a zeolite mineral that is used in the nuclear industry to treat waste effluent by ion exchanging alkali and alkaline earth fission products. In one such application clinoptilolite is used in the Site Ion eXchangE Plant (SIXEP), at the Sellafield site, to remove radioactive Cs and Sr isotopes from aqueous effluent prior to discharge. Clinoptilolite ($Na_4K_2Al_6Si_{30}O_{72}$) is highly selective for cations with large atomic radii such as: Rb^+, K^+, NH_4^+ and Cs^+. The major source of radioactivity in clinoptilolite, from SIXEP, is Cs-137 which form 89% of the specific activity associated with this waste [1].

Vitrification is an attractive conditioning method for ILW as it can result in significant waste volume reductions, as well as producing a monolithic waste form, which is both passively-safe and chemically durable. Additionally cementation poses problems for conditioning of clinoptilolite ILW, as zeolites exhibit pozzolanic behaviour, reacting with $Ca(OH)_{2(aq)}$, to form hydration products possessing cementitious properties [2]. In typical cement blends used in the nuclear industry, $Ca(OH)_{2(aq)}$ preferentially reacts with clinoptilolite grains rather than the BFS or PFA particles[3]. This reaction results in any ions originally bonded within the clinoptilolite structure being more easily leached from the cement. However some may sorb to C-S-H phases, with more fission products bonding to the C-S-H phases when the Ca/Si ratio decreases [4]. A typical waste loading for cementation of waste clinoptilolite from the nuclear industry is between 10-20 wt% [3]. Static dissolution experiments demonstrated that the amount of Cs lost is between 7.5 wt% to 25 wt% for in-pot leaching (5 g, <63 μm) for various composite PC cement blends with BFS and PFA [3]. This test was conducted in 40 mL distilled water for a duration of 24 h at room temperature. The estimated S.A./ V. ratio corresponds to ~14200 cm^{-1} if we assume a density of 1.65 g cm^{-3} for the cement [5].

A challenge with vitrification is volatilisation of radionuclides during glass melting. In borosilicate glasses, Cs is typically volatilised either as $CsBO_{2(g)}$ or gaseous $Cs_{(g)}$ at a

temperature range of 800-1150 ^{o}C [6]. In the temperature range 572-877 ^{o}C, volatile species identified were, again, $CsBO_{2(g)}$, $Cs_2(BO_2)_{2(g)}$ and $NaCs(BO_2)_{2(g)}$ was also observed. Additionally, when the molar ratio of Na_2O / [Cs_2O and B_2O_3] is >1, $Na_{(g)}$ has been observed, however, $Na_{(g)}$ is not observed when the molar ratio is ≤ 1 [7]. Other borate species are often lost at glass melting temperatures, such as $2K_2O.B_2O_3$ [8]. Chlorine (itself very volatile) is found to significantly increase caesium volatility: addition of 5 wt% NaCl led to a loss of >99% Cs at 1000 ^{o}C [9]. Moisture can increase the loss of Cs, x 3.5 more is lost in a wet atmosphere compared to a dry one [8],[10] . Usually off-gas systems are used to deal with volatile radioactive species, to prevent them from being released to the environment. However volatilisation should be minimised to prevent melter/ off-gas corrosion and minimise the risk of radionuclide release during processing, transport and storage [11].

Initially vitrification of UK HLW was conducted at Harwell and differs from the process used at Sellafield today. Instead of using a glass frit, silica and borax were used as glass-formers [12]. The melting temperatures examined were between 1050-1150 ^{o}C and glasses were processed in furnaces; this process was designed to vitrify HLW at 25-30 wt% waste loading, with borax added between 23-40 wt%, the balance being made up of silica. The silica/borax slurry and fission product waste were fed into stainless steel cylinders 15 cm in diameter and ~150 cm long. Off-gas was passed through pipes to the next stainless steel melting vessel, with a small particulate filter in, and maintained at 250 ^{o}C, this was then moved into the furnace and more waste and glass additives are fed in to be vitrified again [12]. The experimental study described here was planned with a view to utilising the pilot studies conducted at Harwell as a route to scale up the process.

5.2 Results

5.2.1 Waste Simulant Analysis

The clinoptilolite in this study was provided by the National Nuclear Laboratory (NNL). The clinoptilolite was ion exchanged with concentrated $CsCl_{(aq)}$ solution according to the following procedure: the clinoptilolite (240 g) was washed 3 times with deionised water, the water decanted and the clinoptilolite dried for 4 h at 90 ^{o}C.

This was then added to a 0.25 M CsCl solution (667 mL) and left overnight, with stirring, for 18 h. The Cs clinoptilolite was then filtered and dried for 24 h at 90 ^{o}C. The quantity of Cs added was with the aim of achieving a Cs loading of 100 mg g^{-1}, which is near to the cation exchange capacity (CEC) of the clinoptilolite, if all Cs was exchanged onto the zeolite. A CEC of 84.5 mg g^{-1} was achieved. Five samples were dried for 24 h at 600 ^{o}C with an average loss of 14.0 ± 2.0 wt% (the value gives the total H_2O content of the Cs clinoptilolite). Figure 5-1 contains a picture and a SEM-BSE image of the Cs clinoptilolite grains. The analysed composition, of the Cs clinoptilolite, was determined *via* a total acid digest and ICP-OES / ICP-MS analysis. The results are shown in Table 5.1. An average particle size of ~900 μm, as determined from measuring particles in SEM images, was obtained for the Cs clinoptilolite, excluding the finer material adhering to the larger grains.

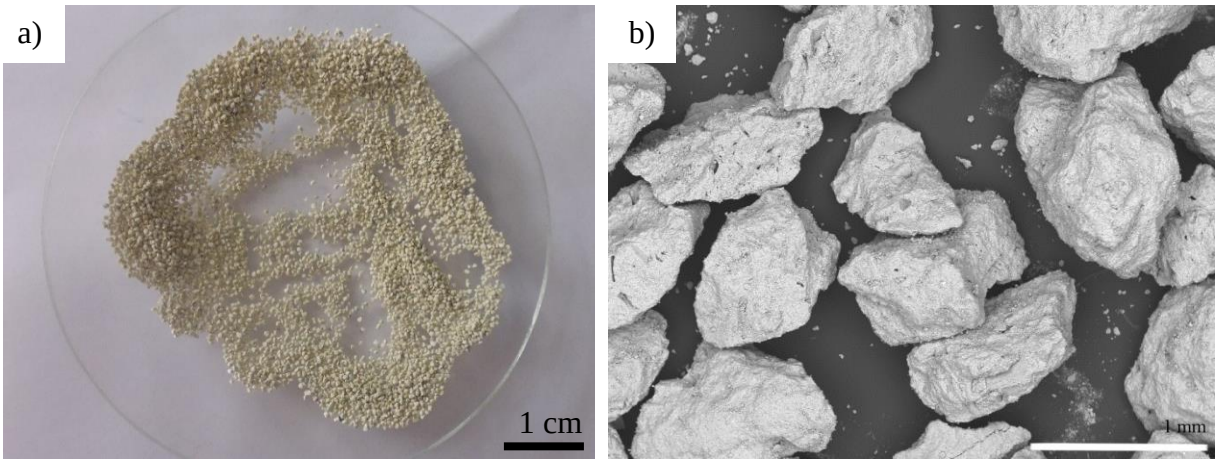

Figure 5-1. a) Photograph of clinoptilolite particles, b) SEM-BSE image of clinoptilolite grains. Some fine material is associated and adhered to the larger grains.

Table 5.1.
Table showing the as analysed composition (normalised) of Cs clinoptilolite through ICP-OES/ ICP-MS. Cl value from XRF.

Oxide	wt%	mol%	Oxide	wt%	mol%
SiO_2	69.11 ± 2.07	81.69 ± 2.45	MgO	0.34 ± 0.02	0.60 ± 0.03
Al_2O_3	10.35 ± 0.31	7.21 ± 0.22	TiO_2	0.10 ± 0.01	0.09 ± 0.01
Cs_2O	12.06 ± 0.37	3.04 ± 0.09	BaO	0.16 ± 0.01	0.07 ± 0.00
CaO	1.37 ± 0.04	1.74 ± 0.05	SO_3	0.10 ± 0.01	0.09 ± 0.01
K_2O	2.01 ± 0.06	1.52 ± 0.05	MnO	0.05 ± 0.01	0.05 ± 0.01
Fe_2O_3	0.95 ± 0.03	0.42 ± 0.01	B_2O_3	0.02 ± 0.00	0.03 ± 0.00
Na_2O	2.05 ± 0.06	2.35 ± 0.07	Cl	1.00 ± 0.05	0.88 ± 0.04
SrO	0.25 ± 0.01	0.17 ± 0.01	Others	0.09 ± 0.01	0.04 ± 0.01

Figure 5-2 shows HTXRD results from room temperature and incrementally higher temperatures to 900 ^{o}C, and after cooling. The crystalline structure of the Cs clinoptilolite (PDF 00-44-1398) is retained up to 750 ^{o}C, between 750 ^{o}C and 850 ^{o}C the relative intensity of the Bragg reflections decrease, indicating that the zeolitic structure has started to collapse. This is particularly evident in the (111), (330) and (400) reflections. By 900 ^{o}C the zeolitic structure has collapsed with weak reflections remaining from quartz, identified as an impurity in the Cs clinoptilolite. Throughout the heat treatment we see a shift in the peak positions to higher angles; this is consistent with the phenomenon of negative thermal expansion (NTE), which is observed for most zeolites, but not all [13]. The mechanism for NTE is subject to debate, but previous authors have suggested it is could be due to anisotropic vibration of Si-O bonds, resulting in smaller bond distances between adjacent structural units and, therefore, NTE in some crystallographic directions [14].

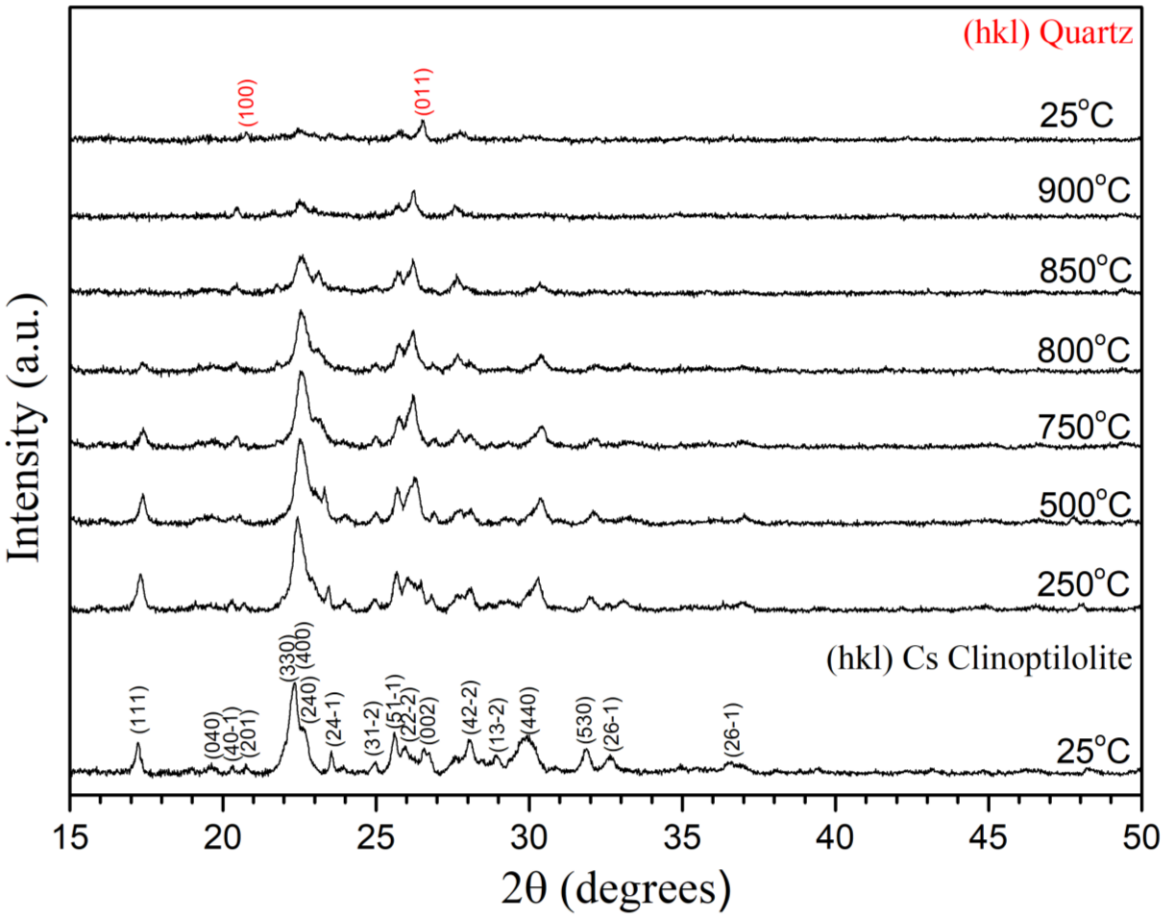

Figure 5-2. HTXRD of Cs Clinoptilolite at room temperature and at higher temperatures.

5.2.2 Glass Formulations

5.2.2.1 Initial Formulation Work

The molecular formula for clinoptilolite is $Na_4K_2Al_6Si_{30}O_{72,}$ therefore, target compositions for vitrification were, initially, alkali aluminosilicate glasses, as high waste loadings for ILW are achieved by utilising the glass-formers already present in the waste. However, to minimise off-gas losses, of caesium in particular, glasses of lower processing temperatures were studied. To achieve this a relatively high B_2O_3 region of the Na_2O-B_2O_3-SiO_2 phase diagram was studied. For initial formulation development, borax was used as a flux to attempt to obtain glasses that melted at or below 900 ^oC. It must be noted that borosilicate glasses are known to be susceptible to phase separation, in certain compositional regions, due to incompatibility of the

silicate network with the borate network [15].

For the initial formulation work clinoptilolite and borax were weighed to 4 d.p., then milled and mixed together on a 4.5 g scale, using Si_3N_4 milling media and a planetary mill. The solid mixture was milled wet (1 wt% solid: 0.66 vol% isopropanol) for 10 mins. The resulting mixtures were pressed in a 1.3 mm die, using a pneumatic pellet press. The pelletised material was then heated up to 900 ^oC at 3 $^oC\ min^{-1}$ and left for 2 h at the melt temperature; they were left to cool at 3 $^oC\ min^{-1}$. Glass formulations are denoted NBS originating from the Na_2O-B_2O_3-SiO_2 ternary, with the percentage in the denotation describing the waste loading of clinoptilolite. Therefore, a waste form with 56.2% waste loading will be denoted NBS-56.2%. Eight compositions at different waste loadings were studied, see Figure 5-3. NBS-74.8% had partially melted, NBS-66.7% and NBS-64.7% had appeared to reach the solidus temperature, but not the liquidus temperature, as unreacted grains could be observed. NBS-62.8%, NBS-60.8% and NBS-58.9% could be observed to have melted but there were large areas of porosity. NBS-53.6% and NBS-56.2% both appeared to have formed a free-flowing liquid.

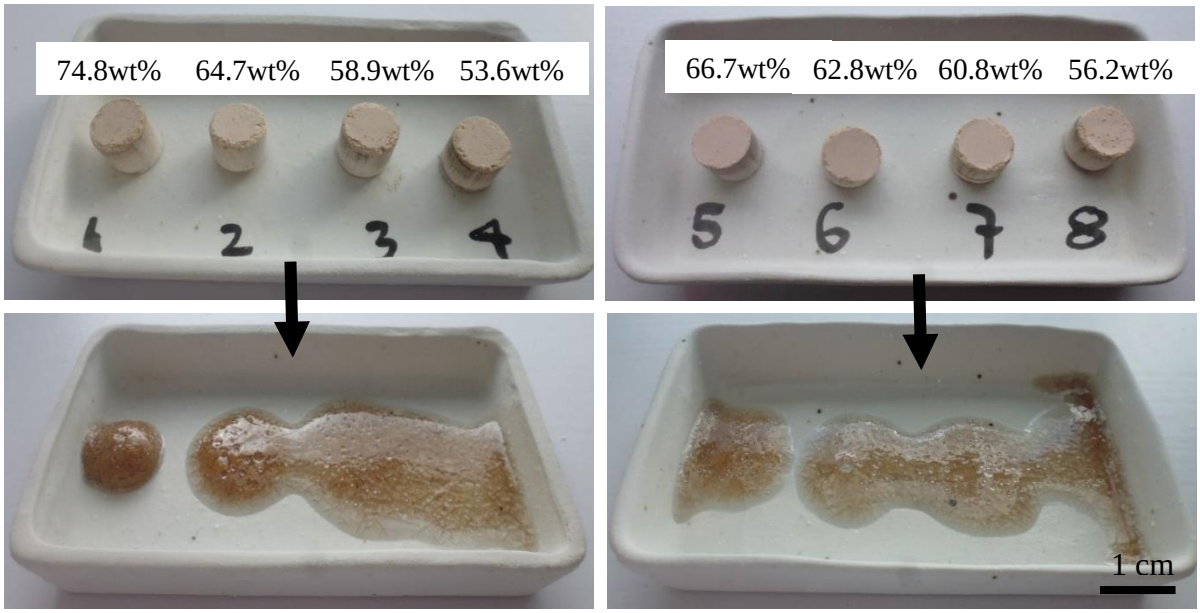

Figure 5-3. Initial formulation work showing the eight compositions, melted at 900 °C. The numbers in the text boxes are the wt% of clinoptilolite. The balance is borax.

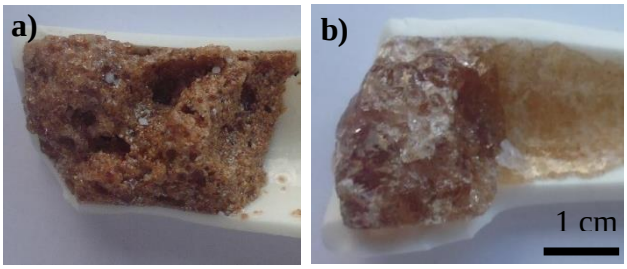

Figure 5-4 a) NBS-62.8% melted at 900 °C with unmilled starting reagents and b) NBS-62.8% with milled reagents.

Another composition NBS-50% was studied and similarly had appeared to have formed a free-flowing liquid (not shown in Figure 5-3). However, an issue with the method used for this initial formulation work arose from the milling. Milling reduces the particle size of the clinoptilolite (≤ 10 μm) making it difficult to identify unreacted grains and reducing the batch-free time significantly. It was clear that the samples that appeared to have formed a free-flowing liquid (NBS-53.6%, NBS-56.2% and NBS-50%) had not when melted, for 2 h at 900 °C, this can be seen in Figure 5-4. This is due to the greater particle size of the clinoptilolite (~900 μm), see Figure 5-1.

5.2.2.2 Further Formulation Work

After the initial 9 melts had been completed, a further 9 melts were attempted. Three were taken forward from the previous test melts: NBS-62.8%, NBS-56.2% and NBS-50%. The three compositions were selected on the basis that NBS-62.8% was the highest waste loading glass that had appeared to have fully melted, NBS-56.2% and NBS-50% were selected as they appeared to be the highest and lowest waste loading glasses that had formed low viscosity liquids. Six new melts were attempted with additional sodium carbonate (N5NBS-59.6%, N5NBS-53.4% and N5NBS-47.5% (which had an additional 5 wt% Na_2O), N10NBS-56.5% and N10NBS-50.6% (which had an additional 10 wt% Na_2O) and N15NBS-53.3% (which had an additional 15 wt% Na_2O)). Glass compositions are summarised in Table 5.2, as well as the processing characteristics.

Table 5.2. Oxide components of glasses and showing whether given compositions had melted.

	NBS-62.8%	NBS-56.2%	NBS-50.0%	N5NBS-59.6%	N5NBS-53.4%	N5NBS-47.5%	N10NBS-56.5%	N10NBS-50.6%	N15NBS-53.3%
Oxides (wt%)									
Na_2O	14.80	16.49	18.06	19.08	20.66	22.16	23.33	24.83	27.60
B_2O_3	25.74	30.30	34.60	24.50	28.79	32.87	23.18	27.26	21.94
SiO_2	48.66	43.54	38.74	46.18	41.37	36.80	43.77	39.20	41.30
Al_2O_3	8.26	7.39	6.57	7.84	7.02	6.24	7.43	6.65	7.01
K_2O	2.54	2.28	2.02	2.41	2.16	1.92	2.29	2.05	2.16
Processing Temperature (^oC) / Compositions Melted (Yes/ No)									
900	No	No	No	No	No	No	No	Yes	Yes
1000	No	Yes	Yes	Yes	Yes	Yes	Yes	Yes	Yes

For this stage of the formulation work clinoptilolite, borax and sodium carbonate were weighed to 3 d.p., on a 25 g scale. This was performed without milling the starting reagents together as previously. The batch was mixed by hand for 15 mins and transferred to a mullite crucible. The batch was then heated to either 900 or 1000 ^oC at $3^oC\ min^{-1}$ and dwelled for 2 h before quenching in air.

The glass compositions on the Na_2O-B_2O_3-SiO_2 ternary can be seen in Figure 5-5. An indication of the immiscibility region is given to illustrate the proximity of these

compositions to that region [16],[17]. The phase diagram indicates that all compositions studied have a liquidus temperature < 900 ºC. However, it was clear that the simple ternary could not be used to accurately predict liquidus temperature. This is due to the additional oxides present, see Table 5.1, in particular the Al_2O_3 content of the final glasses, which would be between 6.2-8.3 wt%, as batched, and would significantly increase the liquidus temperature.

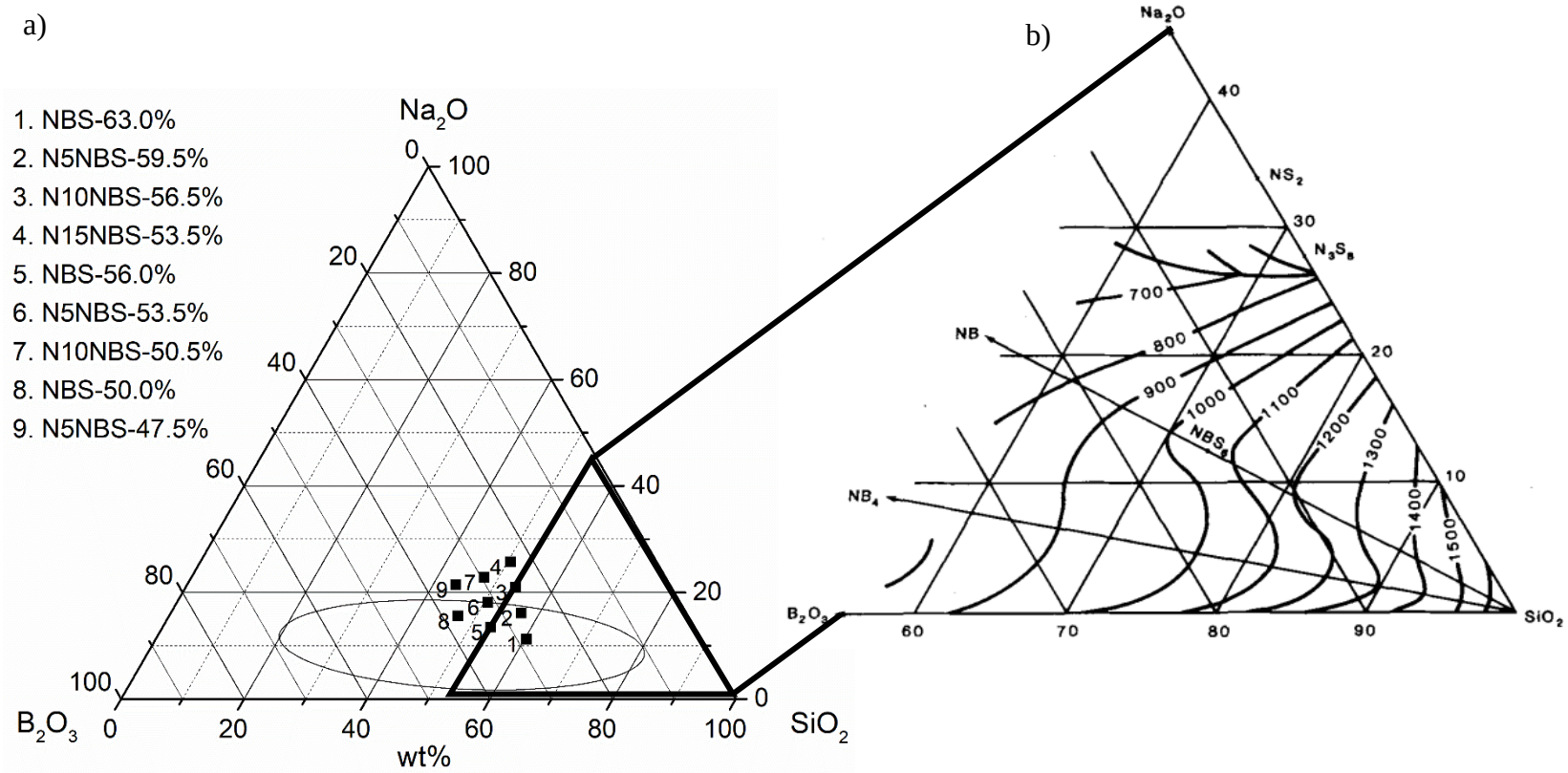

Figure 5-3. a) Na_2O-B_2O_3-SiO_2 phase diagram showing the 9 compositions studied during the glass formulation work and the immiscibility region for this system indicated by the oval, b) Inset showing the phase diagram of the high SiO_2 containing region of the Na_2O- B_2O_3- SiO_2 ternary from [42].

5.2.2.3 Thermal Conditioning of Cs Clinoptilolite in Stainless Steel Crucibles

Of the nine glasses in Table 5.2, four glass compositions were used as starting points and taken forward for further analysis. These are now referred to as NBS-56.0%, N5NBS-59.5%, N10NBS-50.5% and N15NBS-53.5%. They were selected to study the impact of R (i.e. $\frac{Na_2O}{B_2O_3}$) on glass processing and properties (e.g. Cs retention, glass structure and durability). These four glass compositions, see Table 5.3, were melted in stainless steel crucibles (grade 316L), a corrosion resistant grade of steel commonly used in the nuclear industry. This was to assess the feasibility of whether such a vessel could be used as both a melting and a final disposal container. The low temperatures used are thought to make this approach feasible. Precursors were weighed, as above, to 3 d.p. and then mixed, by hand, for 15 min on an ~80 g batch size. They were all then fed into pre-heated stainless steel crucibles S.A./ V. ratio of 0.23 cm^{-1}) and melted for 2 h before being annealed at the temperatures shown in Table 5.3, (estimated to be just above the glass transition temperature from the initial and further formulation work).

Table 5.3.
Table displaying the four glass formulations melted in stainless steel, as well as the melting and annealing temperatures.

	NBS-56.0%	N5NBS-59.5%	N10NBS-50.5%	N15NBS-53.5%
Precursor /wt%				
Cs clinoptilolite	56.00	59.50	50.50	53.50
Borax	44.00	35.50	39.50	31.50
Sodium Carbonate	0.00	8.55	17.10	25.65
	Melting Temperature / ºC			
	1050	1000	950	900
	Annealing Temperature / ºC			
	515	530	495	485

Glasses produced, as described above, were not homogeneous; there were prominent striations present in the glass. Therefore in an attempt to improve homogenisation fritting and re-melting of the NBS-56.0% glass composition was attempted. The glass was size-reduced and then passed through a 5 mm sieve. The fritted glass and crucible were placed directly into the furnace at 1050 ^{o}C and melted for 2 h before being quenched and annealed at 515 ^{o}C for 1 h, and cooled at 1 ^{o}C min^{-1}. After this process striations remained as prominently as before. Therefore, a second technique was used where the precursors were melted statically for 1 h, prior to mixing starting by the insertion of a stainless steel stirrer (for 3 h), giving a total time at the melt temperature of 4 h. However some batches (NBS-56.0% and N5NBS-59.5%) had undissolved material in after quenching. This sintered mass was identified to be largely amorphous with silica grains present. The cause of this was determined to be due to a batch-free time of 1 h being insufficient, leading to the batch to clump and sinter together once stirring began. To digest this silica, and to be consistent for all four glass compositions, all four were fritted and melted for a further 1 h statically in their respective stainless steel crucibles (giving a total time of 5 h at the melt temperature).

Analysed compositions of the static and stirred glasses can be seen in Table 5.4 and 5.5. As can be seen the glasses are essentially (> 90.0 mol%) Na_2O-B_2O_3-SiO_2 with significant quantities of Al_2O_3 (3.9–3.2 mol%) and minor amounts (1.5 mol%) of Cs_2O, K_2O, CaO, SrO and Fe_2O_3. The as measured compositions are within error of the expected calculated compositions, for key elements, except for the static N15NBS-53.5% melt. This had 5.8 wt% more B_2O_3, 4.7 wt% more Na_2O and 5.65 wt% less SiO_2. It is suggested that this may have been due to loss of Cs clinoptilolite when transferring to the crucible, at temperature. Between stirred and static glass melts-stirred NBS-56.0%, N5NBS-53.5% and N15NBS-53.5%, show less Na_2O and B_2O_3 than the static glasses, and N15NBS-53.5% stirred showed more SiO_2. All other key oxides are inside of experimental errors. NBS-56.0% and N5NBS-59.5% are melted at higher temperatures (1050 and 1000 ^{o}C) and it is suggested that these differences are due to loss of borax, due to the stirred glass being melted for 5 h compared to 2 h. The differences for N15NBS-53.5%, between stirred and static, may be due to loss of Cs clinoptilolite when transferring to the crucible, as mentioned above. For the minor elements, there is one major difference between as measured and expected

compositions- the extent of corrosion of the crucibles. For both stirred and static glasses, the Fe is significantly higher from Fe corrosion into the glass, but also from the minor elements in grade 316 L stainless steel (Cr, Ni and Mo).

Table 5.4.
Analysed compositions of the static glasses using ICP-OES / MS.

	NBS-56.0%		N5NBS-59.5%		N10NBS-50.5%		N15NBS-53.5%	
Oxide	wt%	mol%	wt%	mol%	wt%	mol%	wt%	mol%
Na_2O	16.09 ± 0.48	18.00 ± 0.54	19.18 ± 0.57	21.13 ± 1.24	23.91 ± 0.72	26.58 ± 0.80	28.21 ± 0.85	31.13 ± 0.93
B_2O_3	36.05 ± 1.10	35.9 ± 1.08	30.15 ± 0.90	29.58 ± 0.89	30.77 ± 0.92	30.44 ± 0.91	27.74 ± 0.83	27.26 ± 0.82
SiO_2	32.53 ± 0.98	37.54 ± 1.13	36.47 ± 1.09	41.46 ± 1.24	30.74 ± 0.92	35.24 ± 1.06	29.84 ± 0.90	33.98 ± 1.02
Al_2O_3	4.93 ± 0.15	3.35 ± 0.10	5.49 ± 0.16	3.68 ± 0.11	4.67 ± 0.14	3.15 ± 0.09	5.05 ± 0.15	3.39 ± 0.10
Cs_2O	4.87 ± 0.15	1.20 ± 0.04	5.18 ± 0.16	1.26 ± 0.04	5.07 ± 0.15	1.24 ± 0.04	5.27 ± 0.16	1.28 ± 0.04
K_2O	0.90 ± 0.03	0.66 ± 0.02	1.01 ± 0.03	0.73 ± 0.02	0.91 ± 0.03	0.66 ± 0.02	1.00 ± 0.03	0.72 ± 0.02
CaO	0.79 ± 0.02	0.98 ± 0.03	0.78 ± 0.02	0.95 ± 0.03	0.66 ± 0.02	0.81 ± 0.03	0.70 ± 0.02	0.86 ± 0.03
MgO	0.41 ± 0.02	0.70 ± 0.01	0.28 ± 0.01	0.47 ± 0.02	0.22 ± 0.01	0.38 ± 0.01	0.23 ± 0.01	0.38 ± 0.01
SrO	0.14 ± 0.01	0.12 ± 0.01	0.07 ± 0.01	0.06 ± 0.01	0.09 ± 0.01	0.07 ± 0.01	0.07 ± 0.01	0.06 ± 0.01
BaO	0.08 ± 0.01	0.04 ± 0.01	0.13 ± 0.01	0.06 ± 0.01	0.13 ± 0.01	0.06 ± 0.01	0.10 ± 0.01	0.05 ± 0.01
Fe_2O_3	2.61 ± 0.08	1.13 ± 0.03	0.91 ± 0.03	0.39 ± 0.01	2.18 ± 0.07	0.94 ± 0.03	1.28 ± 0.04	0.55 ± 0.02
SO_3	0.01 ± 0.00	0.00 ± 0.00	0.06 ± 0.01	0.05 ± 0.01	0.08 ± 0.01	0.07 ± 0.01	0.07 ± 0.01	0.06 ± 0.01
TiO_2	0.14 ± 0.01	0.12 ± 0.01	0.07 ± 0.01	0.06 ± 0.01	0.09 ± 0.01	0.07 ± 0.01	0.07 ± 0.01	0.06 ± 0.01
MnO	0.09 ± 0.01	0.09 ± 0.01	0.05 ± 0.01	0.04 ± 0.01	0.08 ± 0.01	0.08 ± 0.01	0.05 ± 0.01	0.05 ± 0.01
Cr_2O_3	0.25 ± 0.01	0.11 ± 0.01	0.11 ± 0.01	0.05 ± 0.01	0.24 ± 0.01	0.11 ± 0.01	0.14 ± 0.01	0.06 ± 0.01
Others	0.11 ± 0.01	0.06 ± 0.01	0.06 ± 0.01	0.03 ± 0.00	0.16 ± 0.01	0.10 ± 0.01	0.18 ± 0.01	0.11 ± 0.01

Table 5.5.
Analysed compositions of the stirred glasses using ICP-OES / MS.

	NBS-56.0%		N5NBS-59.5%		N10NBS-50.5%		N15NBS-53.5%	
Oxide	wt%	mol%	wt%	mol%	wt%	mol%	wt%	mol%
Na_2O	14.52 ± 0.44	16.54 ± 0.50	17.63 ± 0.53	19.88 ± 0.60	23.09 ± 0.69	25.63 ± 0.77	25.12 ± 0.75	27.76 ± 0.83
B_2O_3	33.48 ± 1.00	33.96 ± 1.02	29.42 ± 0.88	29.53 ± 0.89	29.85 ± 0.90	29.5 ± 0.88	23.86 ± 0.72	23.48 ± 0.70
SiO_2	33.64 ± 1.01	39.54 ± 1.19	35.45 ± 1.06	41.23 ± 1.24	32.06 ± 0.96	36.7 ± 1.10	35.43 ± 1.06	40.39 ± 1.21
Al_2O_3	5.45 ± 0.16	3.77 ± 0.11	5.71 ± 0.17	3.92 ± 0.12	5.46 ± 0.16	3.68 ± 0.11	5.48 ± 0.16	3.68 ± 0.11
Cs_2O	5.31 ± 0.16	1.33 ± 0.04	5.95 ± 0.18	1.47 ± 0.04	4.74 ± 0.14	1.16 ± 0.03	5.07 ± 0.15	1.23 ± 0.04
K_2O	0.95 ± 0.03	0.71 ± 0.02	1.05 ± 0.03	0.78 ± 0.02	0.89 ± 0.03	0.65 ± 0.02	0.95 ± 0.03	0.69 ± 0.02
CaO	0.73 ± 0.02	0.92 ± 0.03	0.82 ± 0.02	1.02 ± 0.03	0.67 ± 0.02	0.82 ± 0.02	0.67 ± 0.02	0.82 ± 0.02
MgO	0.29 ± 0.01	0.51 ± 0.02	0.18 ± 0.01	0.31 ± 0.02	0.23 ± 0.01	0.4 ± 0.02	0.24 ± 0.01	0.41 ± 0.02
SrO	0.09 ± 0.01	0.08 ± 0.01	0.07 ± 0.01	0.06 ± 0.01	0.07 ± 0.01	0.06 ± 0.01	0.07 ± 0.01	0.06 ± 0.01
BaO	0.10 ± 0.01	0.05 ± 0.01	0.13 ± 0.01	0.06 ± 0.01	0.12 ± 0.01	0.06 ± 0.01	0.12 ± 0.01	0.05 ± 0.01
Fe_2O_3	4.64 ± 0.14	2.05 ± 0.06	2.82 ± 0.08	1.23 ± 0.04	2.17 ± 0.07	0.94 ± 0.03	2.34 ± 0.07	1.00 ± 0.03
SO_3	0.02 ± 0.00	0.02 ± 0.00	0.07 ± 0.01	0.06 ± 0.01	0.08 ± 0.01	0.07 ± 0.01	0.08 ± 0.01	0.07 ± 0.01
TiO_2	0.09 ± 0.01	0.08 ± 0.01	0.07 ± 0.01	0.06 ± 0.01	0.07 ± 0.01	0.06 ± 0.01	0.07 ± 0.01	0.06 ± 0.01
MnO	0.14 ± 0.01	0.14 ± 0.01	0.09 ± 0.01	0.09 ± 0.01	0.07 ± 0.01	0.07 ± 0.01	0.08 ± 0.01	0.07 ± 0.01
Cr_2O_3	0.30 ± 0.01	0.14 ± 0.01	0.31 ± 0.01	0.14 ± 0.01	0.26 ± 0.01	0.12 ± 0.01	0.25 ± 0.01	0.11 ± 0.01
Others	0.25 ± 0.01	0.16 ± 0.01	0.23 ± 0.01	0.16 ± 0.01	0.17 ± 0.01	0.08 ± 0.01	0.17 ± 0.01	0.12 ± 0.01

5.2.3 Phase Assemblage

The phase assemblages of the glasses was studied using XRD and SEM-EDX.

5.2.3.1 XRD

Figure 5-6 demonstrates that the glasses, both stirred and static, are x-ray amorphous evident from the broad diffuse scattering. The XRD patterns also show two components to the diffuse scatter, indicating the presence of two amorphous phases; this can particularly be seen for the static glasses. The first diffuse scatter is centered at 19º (2θ), whereas the second increases as R increases from 26º (for NBS-56.0%), to 30º (for N15NBS-59.5%). NBS-56.0%, N5NBS-59.5% and N10NBS-50.5%, from the static glasses, show low intensity reflections attributed to quartz (PDF 00-85-0335), originating from the unreacted batch. Only NBS-56.0%, from the stirred glasses, shows low intensity reflections from quartz, with some $FeCr_2O_4$ (PDF 00-34-0140) also present.

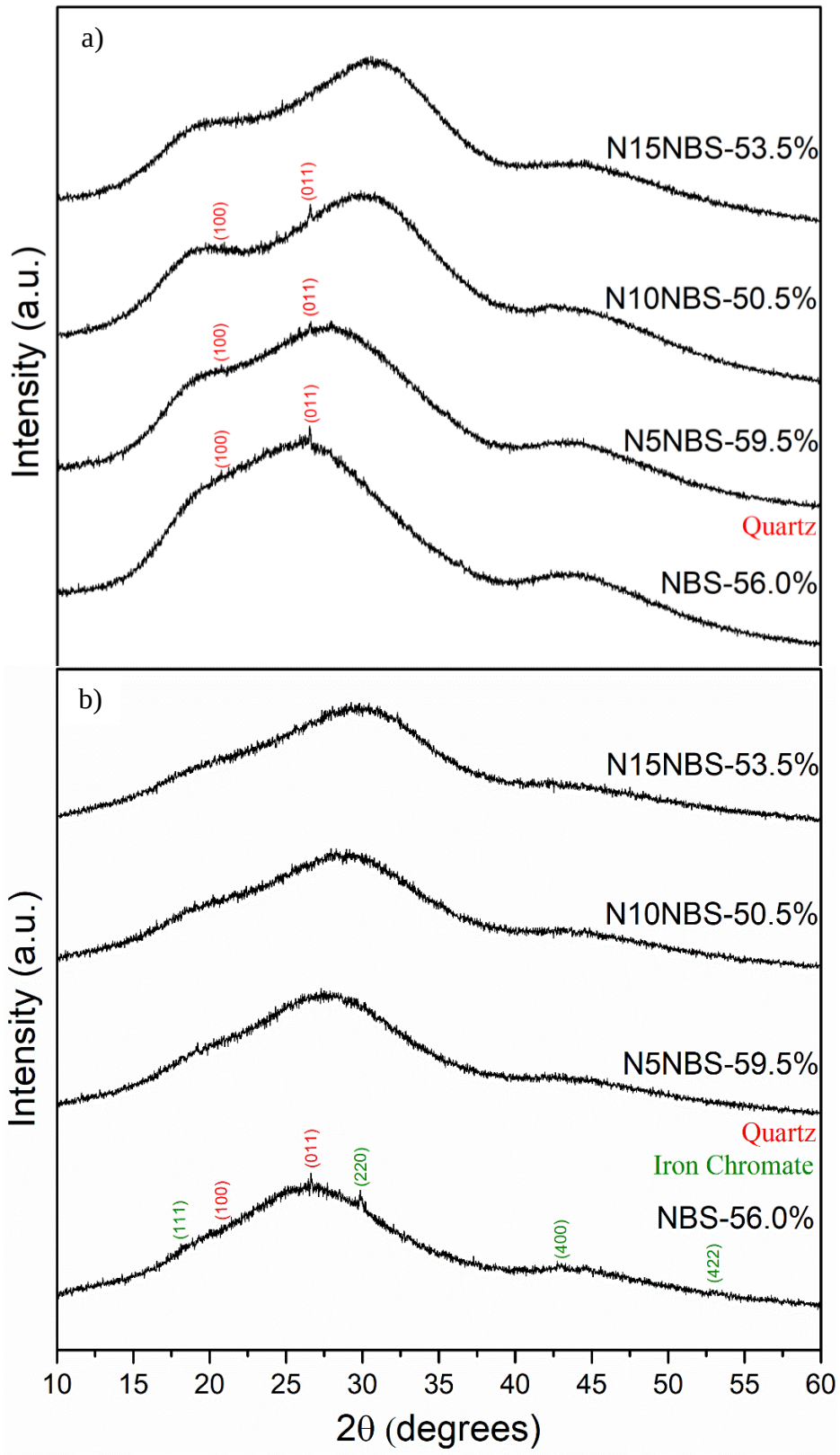

Figure 5-4. a) XRD patterns for static glasses melted in stainless steel crucibles, b) XRD of stirred glasses melted in stainless steel crucibles.

5.2.3.2 SEM-EDX

Representative SEM-BSE images are shown in Figure 5-7 of the static glasses. There are few areas of contrast, but striae can be seen in certain areas, indicating concentration gradients across the glass. Representative SEM-BSE images are show in Figure 5-8 of the static glasses, the striae this time are absent indicating a more homogeneous glass. Stirred NBS-56.0% shows a relatively high concentration of secondary phases. These are spinel phases, which are clustered in areas of the glass, as opposed to being universally dispersed throughout. They have a hexagonal habit and have an approximate crystal size range from a 2-10 μm. They were identified as $FeCr_2O_4$ from EDX, with some minor x-rays from the residual glass between 0.75-1.75 keV, see Figure 5-9. NBS-56.0% had by the far the highest concentration of spinel phases, but isolated spinel crystals could be observed in all other stirred glasses. For the static glasses, the spinels were located in the highest concentration along the striae. Figure 5-10 shows sulfide phases; these were present in most of the glasses (except the higher melting temperature NBS-56.0%), but were present in very low concentrations, being below the detection limit of the XRD. They are globular in habit, have narrow crystal size distribution between 2 and 5 μm and were identified, using EDX, as calcium sulfide, with a minor amount from magnesium.

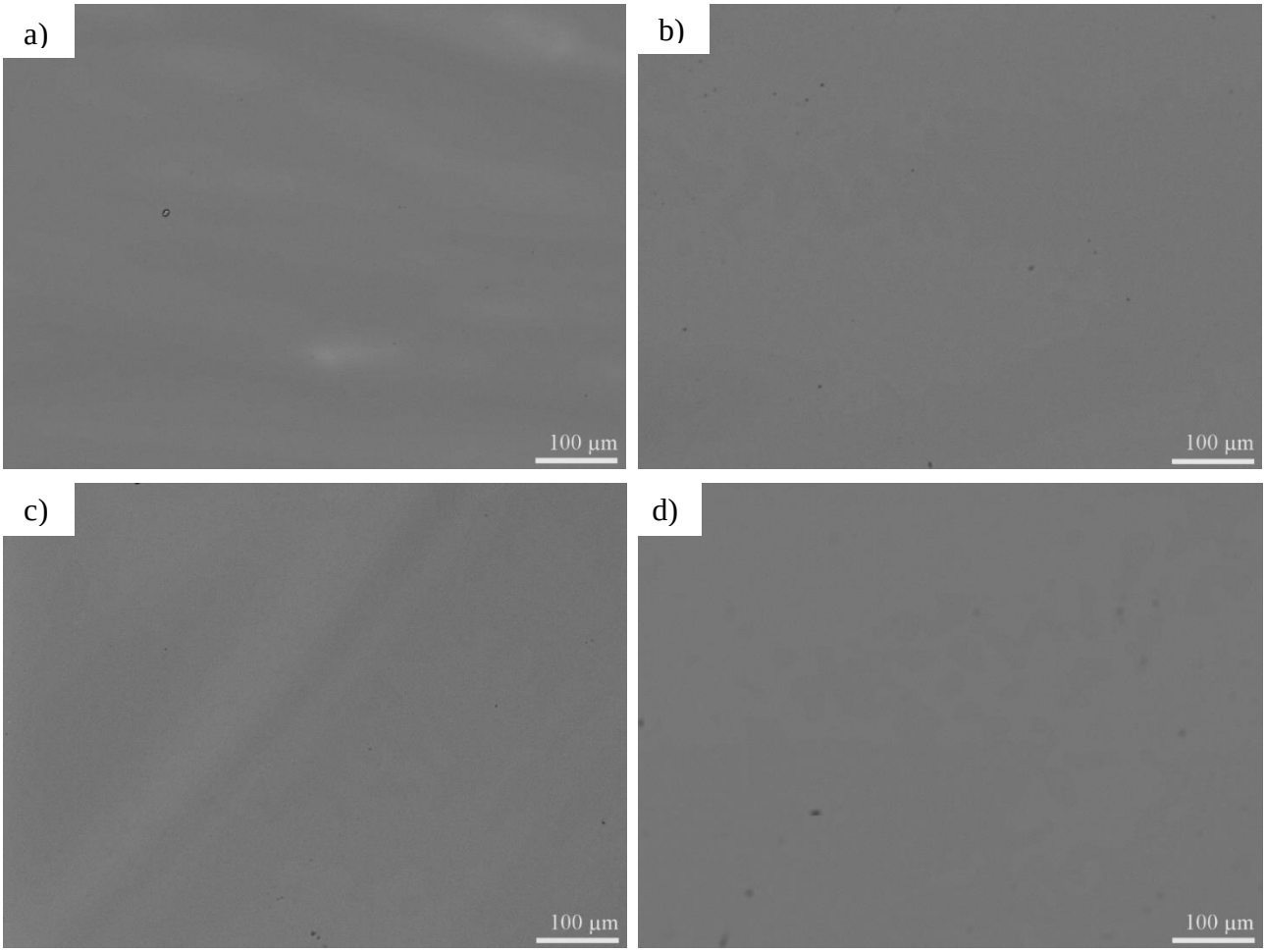

Figure 5-5. SEM-BSE image of the four glasses melted statically, a) NBS-56.0%, b) N5NBS-59.5%, c) N10NBS-50.5% and d) N15NBS-53.5%.

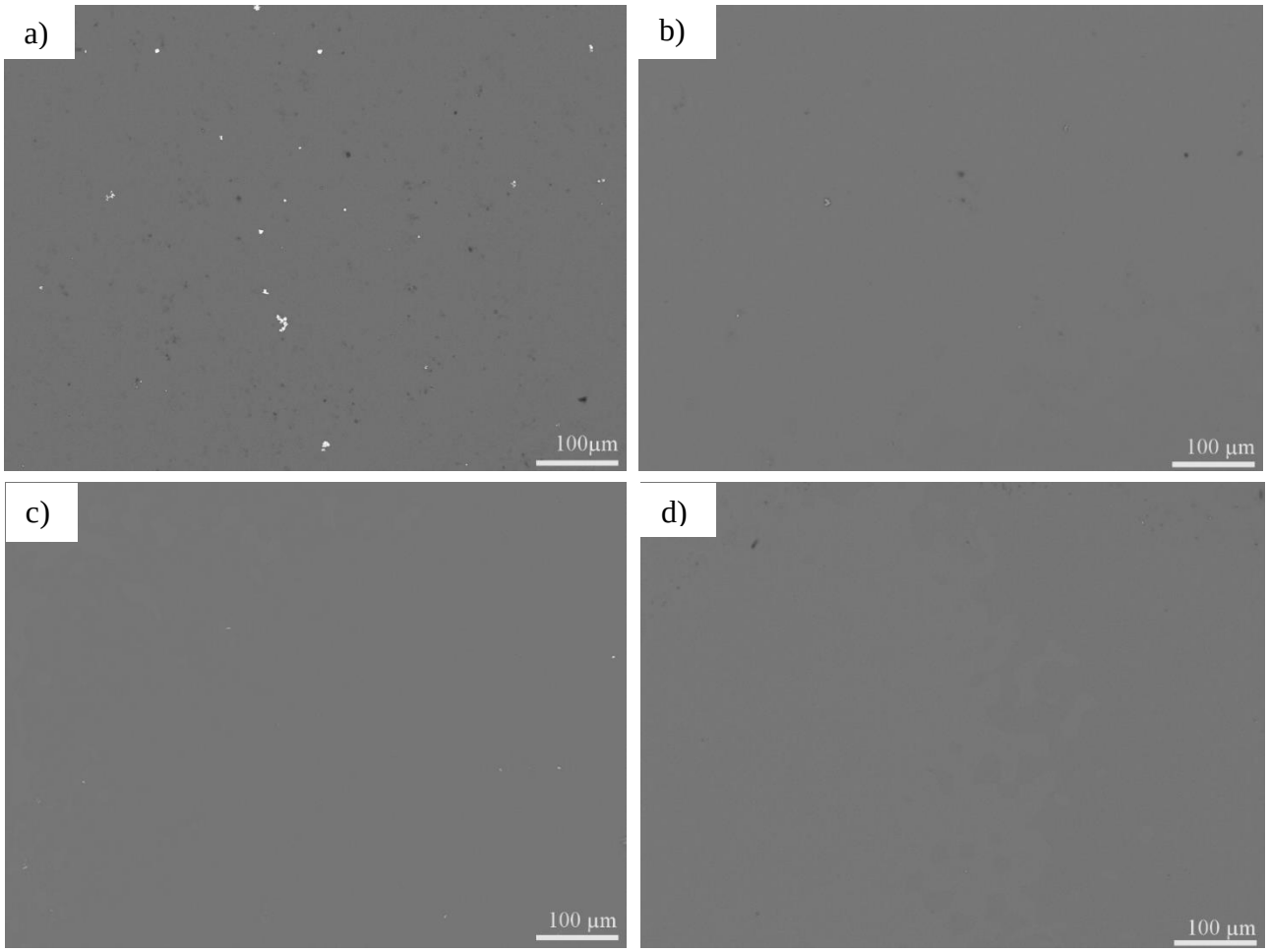

Figure 5-6. SEM-BSE image of the four glasses melted with stirring a) NBS-56.0%, b) N5NBS-59.5%, c) N10NBS-50.5% and d) N15NBS-53.5%.

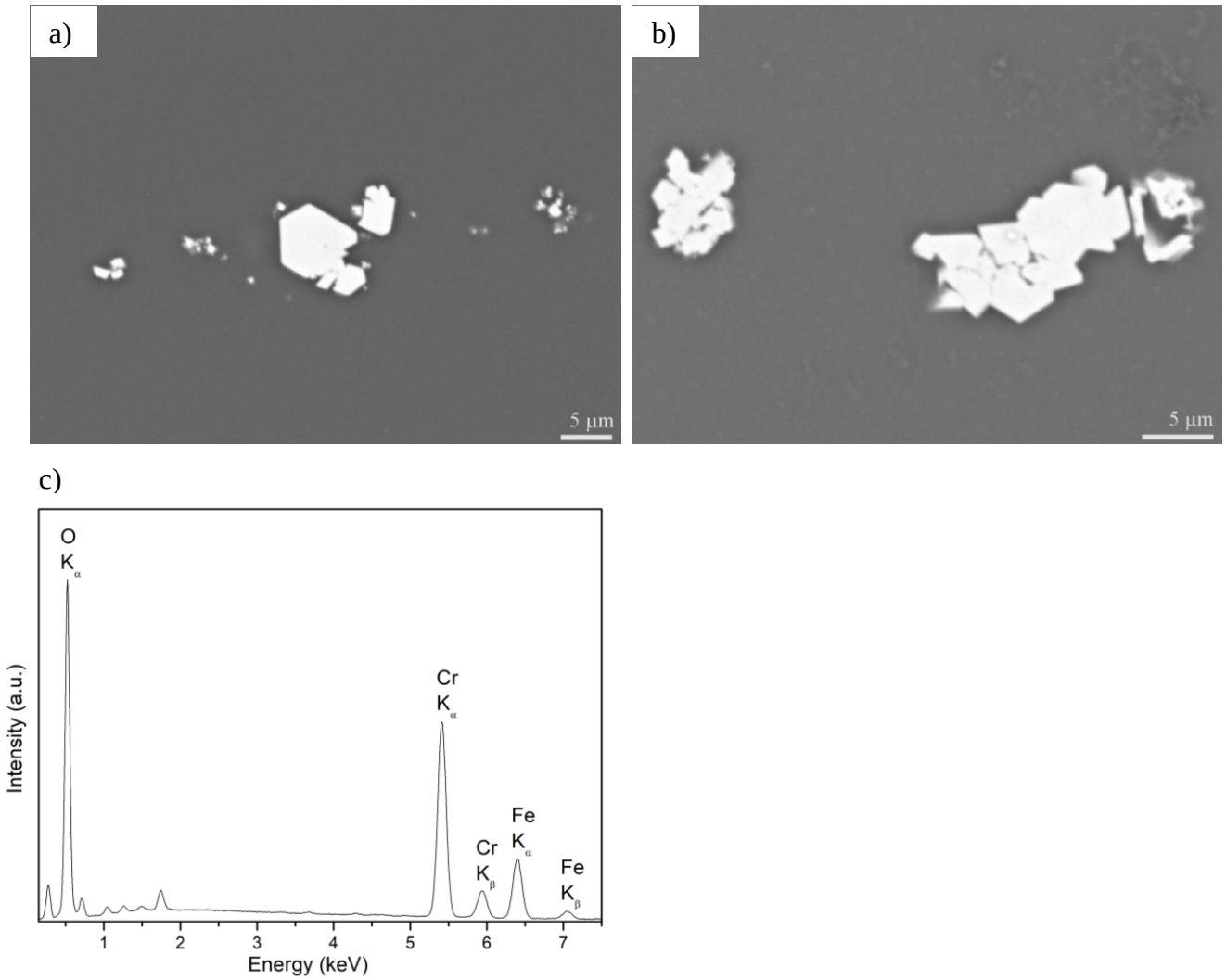

Figure 5-7. Higher magnification SEM-BSE images of spinel crystals present in the glass a) from NBS-56.0% and b) from N5NBS-59.5%, along with c) a representative EDX spectra of the spinel.

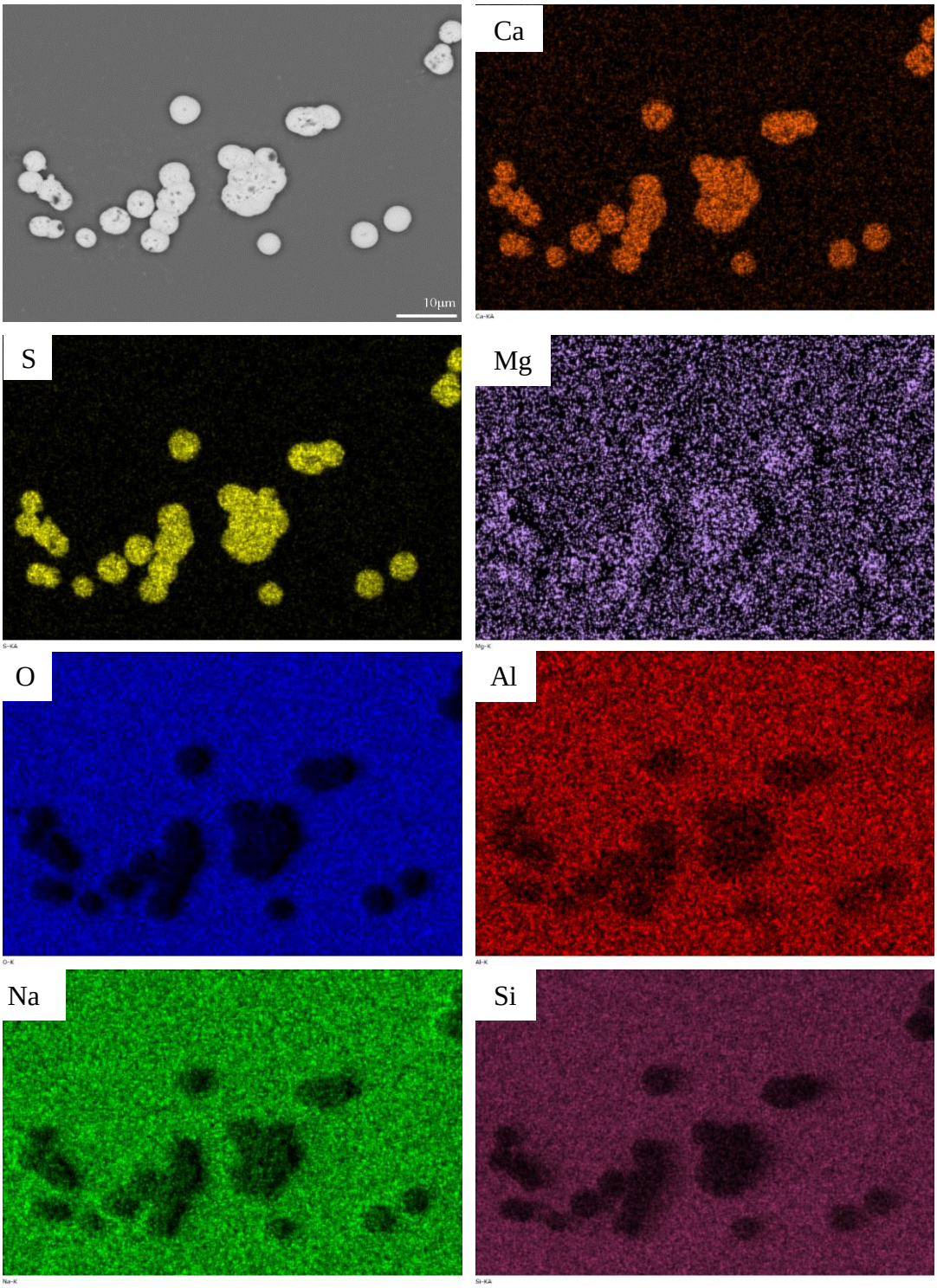

Figure 5-8. EDX maps of CaS phases present in the glass. These were observed in most glass samples. This particular map is from N15NBS-53.5%.

5.2.4 Glass Properties (Density and DTA)

The glasses produced, both static and stirred, were opaque, due to corrosion of transition metals from the stainless steel crucibles. The initial formulation work was performed in mullite crucibles, which produced a light pink glass in cross-section, in steel, the glasses were black (green in cross-section), see Figure 5-11 and Figure 5-14. The density of Cs clinoptilolite was measured to be 2.22 ± 0.02 g cm^{-3}, the glasses had densities between 2.56-2.66 g cm^{-3}, with the densities increasing linearly as the molar modifier content (Na, Cs, K, Ca, Sr, Mg and Ba) increases. (R^2 of 0.84) (see Figure 5-12).

Figure 5-9. Photograph of vitrified clinoptilolite glass typical of all four glasses when melted in stainless steel.

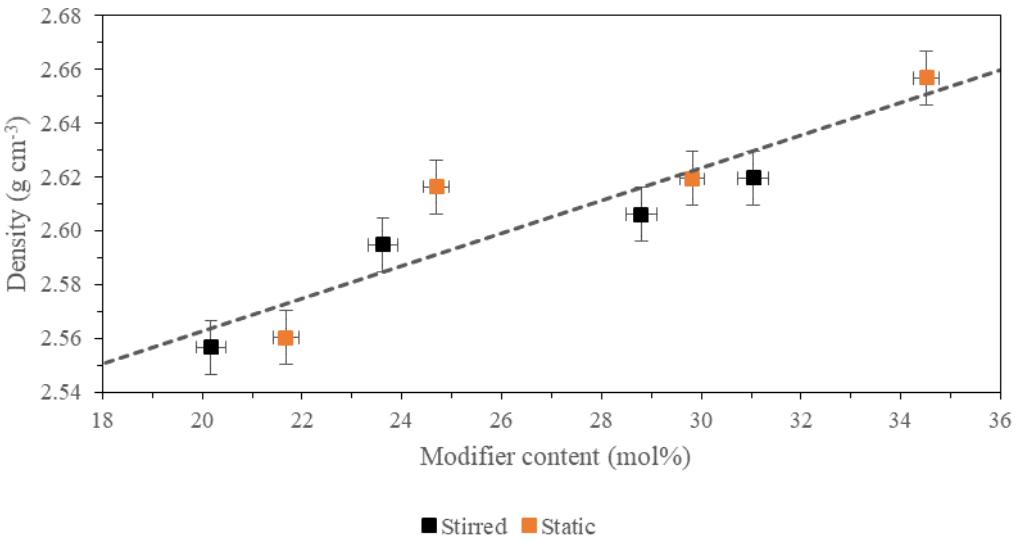

Figure 5-10. Densities against total mol% modifier content for the four glasses studied (black squares stirred, orange squares static).

Table 5.6.
Density measurements of the stirred and static glasses, error is ± 0.02 kg dm^{-3}.

	NBS-56.0%		N5NBS-59.5%		N10NBS-50.5%		N15NBS-53.5%	
	Stirred	Static	Stirred	Static	Stirred	Static	Stirred	Static
Density (kg dm^{-3})	2.56	2.56	2.59	2.62	2.61	2.62	2.62	2.66

Figure 5-13 shows the DTA traces for stirred melts. DTA were performed on both the static and stirred melts and showed the same events occurring at similar temperatures (i.e. a glass transition, Tg_1, a small intensity crystallisation event, T_{x1}, followed by, tentatively, a third, broad crystallisation event, T_{x2}). As the DTA for the static melts were almost identical in appearance to the stirred melts, the graph is omitted, however the temperatures of key thermal events are provided in Table 5.7. The trend in the glass transitions shows that with increasing R, Tg_1 decreases, starting at 518 ^oC for the least modified to 464 ^oC to the most modified. T_{x1} occurs at similar temperatures for NBS-56.0% and N5NBS-59.5% (~625 ^oC), with N10NBS-50.5% and N15NBS-53.5% occuring at lower temperatures (~585 ^oC). The second crystallisation event shows a similar trend to the Tg_1, decreasing with increasing R, except for N15NBS-53.5%, which occurs at a higher temperature than N10NBS-50.5%. There are common features in the DTA traces, between stirred and static, for a given composition. However, after stirring the glass transition temperatures are still in error of one another. Stirring does reduce the intensity of T_{x1}, as well as reducing its temperature (particularly for the NBS-56.0% and N5NBS-59.5% compositions). There is an increase in temperature in the third thermal event (T_{x2}), except for N5NBS-59.5%, where the temperatures are in error of one another.

Table 5.7.
Temperatures of thermal events from the DTA for the four glasses melted statically and with stirring.

	NBS-56.0%		N5NBS-59.5%		N10NBS-50.5%		N15NBS-53.5%	
	static	stir	static	stir	static	stir	static	stir
Tg_1 / ±5 °C	510	500	518	504	485	484	470	464
Tx_1 / ±5 °C	643	626	634	624	590	588	580	579
Tx_2 / ±5 °C	754	778	727	720	684	708	715	726

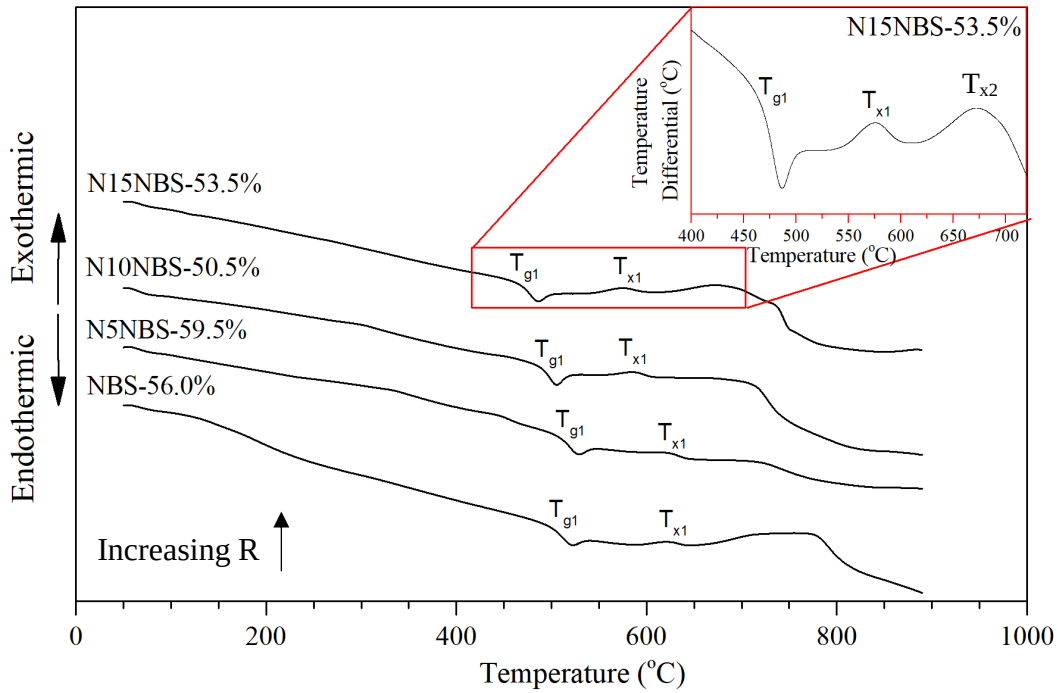

Figure 5-11. DTA for the four stirred glasses with an inset of the region between 400 °C and 750 °C, showing the three thermal events for clarity.

Mixing has the effect of reducing (but not eliminating) the striations, when observed with the naked eye, (see Figure 5-14 for N15NBS-53.5%). All glasses had striations present. They were more prominent for the glasses melted at higher temperatures, and can be observed as opaque lines through the more translucent, light green, bulk glass. After stirring these striae are almost eliminated for samples N15NBS-53.5% and N10NBS-50.5% but are still present for N5NBS-59.5% and NBS-56.0%. The origin of the striations is hypothesised to be due to the corrosion of the stainless steel crucible. At the melt line (the region of the most severe corrosion) 26.0 ± 3.0% of material at

the surface had corroded away (after 12 h at temperatures between 900 and 1050 ^{o}C) compared to the original steel crucible.

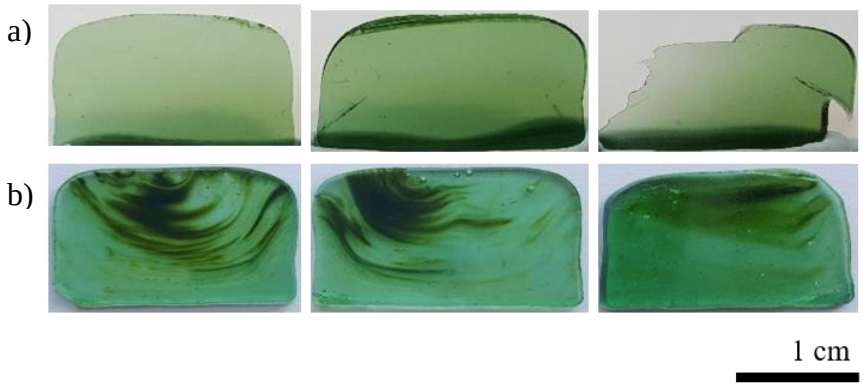

Figure 5-12. Photographs showing the striations for a) stirred and b) static melts of N15NBS-53.5%. The left and right images are either end of the glass block and the central image is from the centre of the cast block.

Figure 5-15 shows EDX line scans across the striae, these striae correspond to localised concentration gradients, with the darker regions in the photographs enriched in iron (and perhaps sodium) and the lighter regions enriched in aluminium, silicon and caesium.

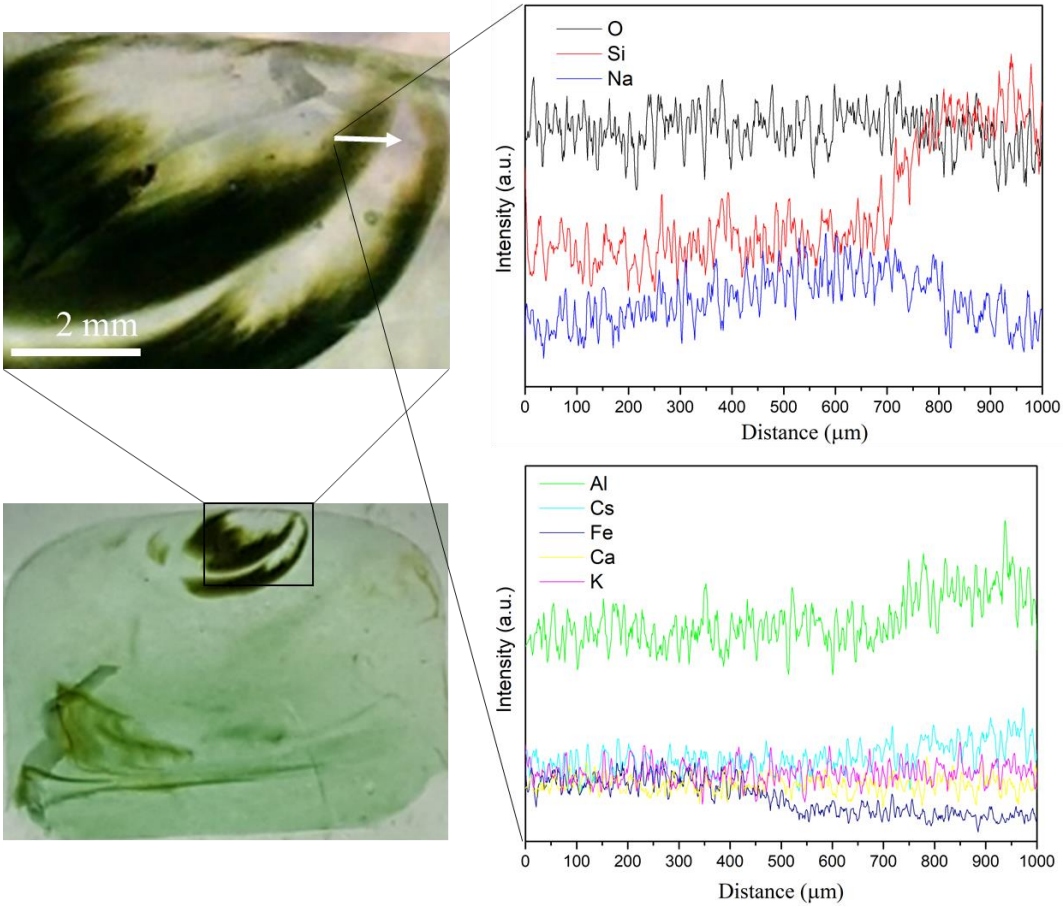

Figure 5-13a) Photograph showing a striation within the glass matrix, b) zoom-in on the striation with the arrow showing the position of the line scan, c) EDX maps of the key elements across the striae.

5.2.5 Redox Properties and Iron in the Glass

Corrosion of the stainless steel melting vessels was prominent. After 2 h of melting statically, significant striations in the glass were present. To improve homogeneity fritting and re-melting was attempted, which proved unsuccessful. Mixing with a stirrer was subsequently attempted and this achieved its objective of producing more homogeneous samples. However, it did lead to further issues, these were: increased corrosion of the crucible, and corrosion of the stirrer) due to the longer melt time (4 h). This can be seen in Figure 5-16. The profile of the steel paddle shows not only the corrosion present on the stirrer, but is also representative of that found in the crucible. There was some corrosion on the surface of the crucibles in contact with the glass, but

the greatest areas of corrosion were at the melt line, and at ~1 cm above, where there was significant localised corrosion due to volatile species attacking the crucible.

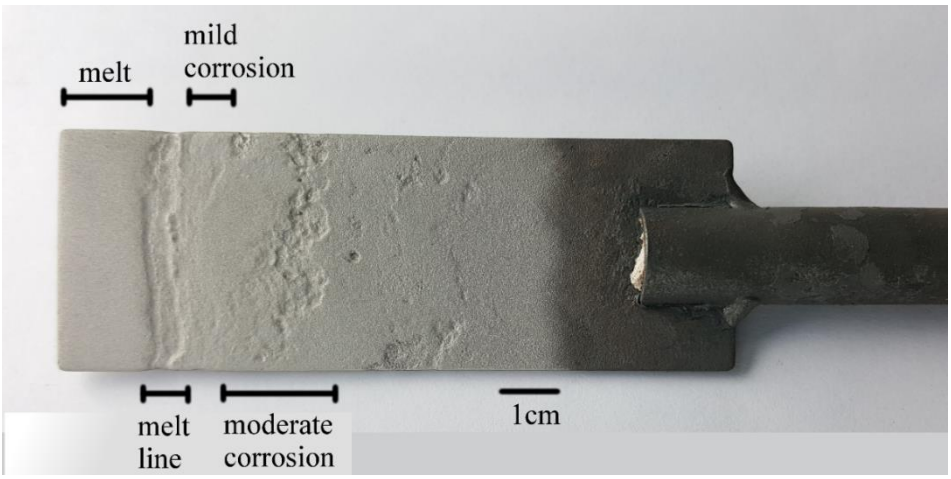

Figure 5-14. Photograph illustrating the corrosion of the stainless steel mixing paddle.

For NBS-56.0%, with stirring, the concentration of iron is x10 greater in the glass than that expected from the Fe present in the Cs clinoptilolite. Also, it is clear that with higher temperatures, the steel corrosion is more significant (for the stirred glasses: 2.05 mol% of Fe for NBS-56.0%, 1.23 mol% for N5NBS-59.5%, 0.94 mol% for N10NBS-50.5% and 1.00 mol% for N15NBS-53.5%). The Fe content in the glass is x2 greater in NBS-56.0% (processed at 1050 ^{o}C) compared to N10NBS-50.5% and N15NBS-53.5% (processed at 950 and 900 ^{o}C respectively).

XANES data of the static glasses was collected with the aim of obtaining redox information and coordination environments of iron. Figure 5-17 show the XANES data of static glasses (measured in fluorescence mode on a cross-section of the glass) and an inset of the pre-edge features. The pre-edge features show the similarity between N15NBS-53.5% and the Fe^{2+} standard (Fe_2SiO_4) and between NBS-56.0% and the Fe^{3+} standard ($FeNaSi_2O_4$). N10NBS-50.5% is similar to NBS-56.0% (i.e. a significant Fe^{3+} contribution) and N5NBS-59.5% is similar to N15NBS-53.5%. However there are contributions to N10NBS-50.5% from the Fe^{2+} as well as a contribution to N5NBS-59.5% from Fe^{3+} indicating that these two compositions are intermediate between the two standards. XANES data was collected in fluorescence mode, due to the relatively low concentration of Fe in the glasses, unfortunately this resulted in data being unrepresentative due to the Fe concentration gradients, and

inhomogeneous distribution of the spinel phases outlined earlier. Indeed, it can be seen from the pre-edge features that the Fe, in N15NBS-53.5%, (processed at 900 ^{o}C) is essentially all iron(II) due to its similarity with Fe_2SiO_4, and that the Fe, in NBS-56.0%, (processed at 1050 ^{o}C) is essentially all iron(III). However glass melt atmospheres become more reducing with higher temperatures, therefore, it would be expected that an increase of 150 ^{o}C would lead to a more reducing glass melt. Striae in static melts vary in width and length but a typical width is 1-5 mm and a typical length is 1-1.5 cm, see Figure 5-14. The beam size, at the sample, at BM26A (ESRF) is ~1 mm^2, therefore it is probable regions of the glass interacting with the beam are more reduced than others due to the concentration gradient of Fe, resulting in data that is not representative.

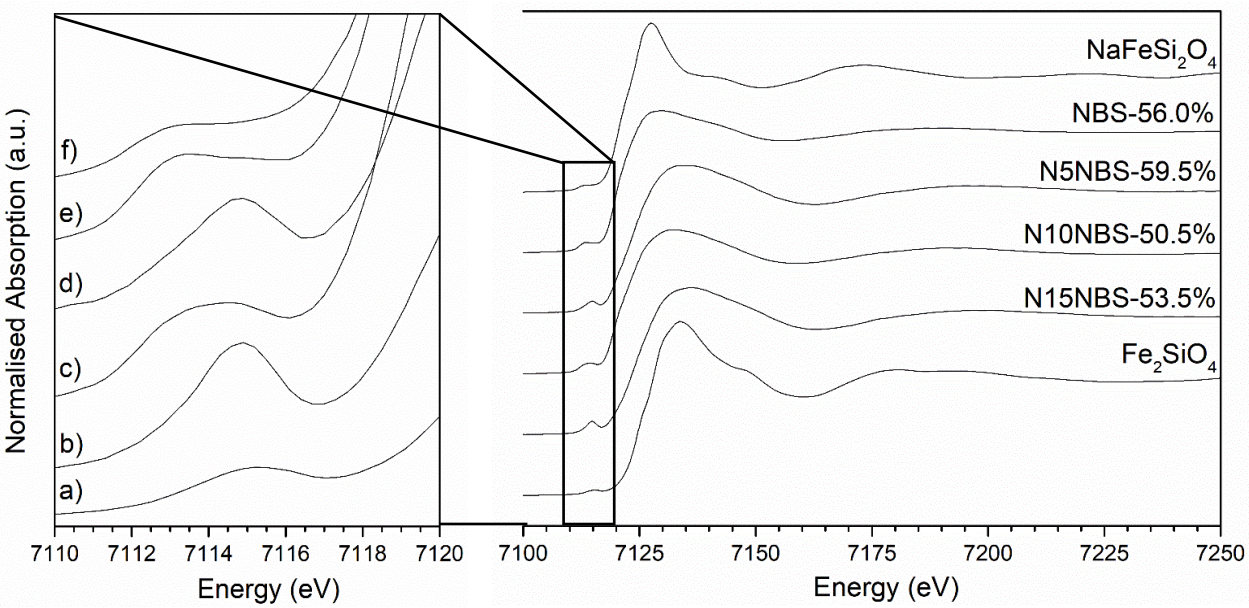

Figure 5-15. XANES of static glass melts and iron standards on the right, on the left are the pre-edge features of a) Fe_2SiO_4, b) N15NBS-53.5%, c) N10NBS-50.5%, d) N5NBS-59.5%, e) NBS-56.0% and f) $NaFeSi_2O_4$.

Instead to quantify $\frac{Fe^{2+}}{\sum Fe}$ in the glass, Mössbauer spectroscopy was used on the stirred glasses. As glass samples were powdered, and the striae less prominent for stirred glasses, representative redox conditions could be obtained. Extended Voigt-based fitting analysis was used to fit individual peaks to multiple sites in the spectrum, see

Figure 5-18. The Mössbauer data was fitted with two sites: one with isomer shift ~1.08 (corresponding to Fe^{2+} environments in the glass) and Q.S. of ~1.81, and one with I.S. ~0.33 (corresponding to Fe^{3+} environments in the glass) and Q.S. ~1.35. Note these do not correspond to the final fit parameters but to the initial fit parameters, as found in the literature [18]. The recoil-free fraction for the Fe^{2+} and Fe^{3+} site were assumed to be equal [19]. The order of refinement for site fitting was- areas (using the initial peak parameters and kept unconstrained throughout); Lorentzian HWHM; isomer shift of both sites; Q.S. of the Fe^{2+} site; both isomer shifts again; Q.S. of the Fe^{3+} site; finally both isomer shifts again. Initially, a third site was fitted belonging to an Fe^{2+} site, to account for the $FeCr_2O_4$ phase, however this site produced a poor fit compared to using just two sites. It was decided that one site would be fitted for the Fe^{2+}, even though Fe^{2+} may be present in the spinel giving two Fe^{2+} sites in the samples (one from the glass and one from the spinel). This can be justified by the relatively low volume fraction of spinel in the glass, see Figure 5-6, (all below the detection limit of the XRD, except for NBS-56.0%, where weak reflections can be observed). For a spinel a typical Fe^{2+} site will have an I.S. (mm s^{-1}) of 0.86-0.90 but a smaller Q.S. (mm s^{-1}) of either 0.96-1.15 or 1.56-1.63 depending on the spinel in question (e.g. spinel, hercynite, chromite or ulvospinel)[18].

Table 5.8.
Mössbauer parameters (± 0.02 mm s^{-1}), with I.S., Q.S. and HWHM.

Sample	Isomer Shift (mm s^{-1})	Quadrupolar Splitting (mm s^{-1})	HWHM (mm s^{-1})	Area (%)	Assigned Phase	Reduced χ^2
NBS-56.0%	1.03	1.94	0.36	75.1	Fe^{2+}	1.00
	0.24	1.01	0.36	24.9	Fe^{3+} glass	1.00
N5NBS-59.5%	1.01	1.95	0.35	73.6	Fe^{2+}	0.75
	0.20	0.99	0.35	26.4	Fe^{3+} glass	0.75
N10NBS-50.5%	0.96	1.98	0.36	76.2	Fe^{2+}	0.59
	0.16	0.86	0.36	23.8	Fe^{3+} glass	0.59
N15NBS-53.5%	1.00	1.92	0.34	70.3	Fe^{2+}	0.57
	0.26	1.06	0.34	29.7	Fe^{3+} glass	0.57

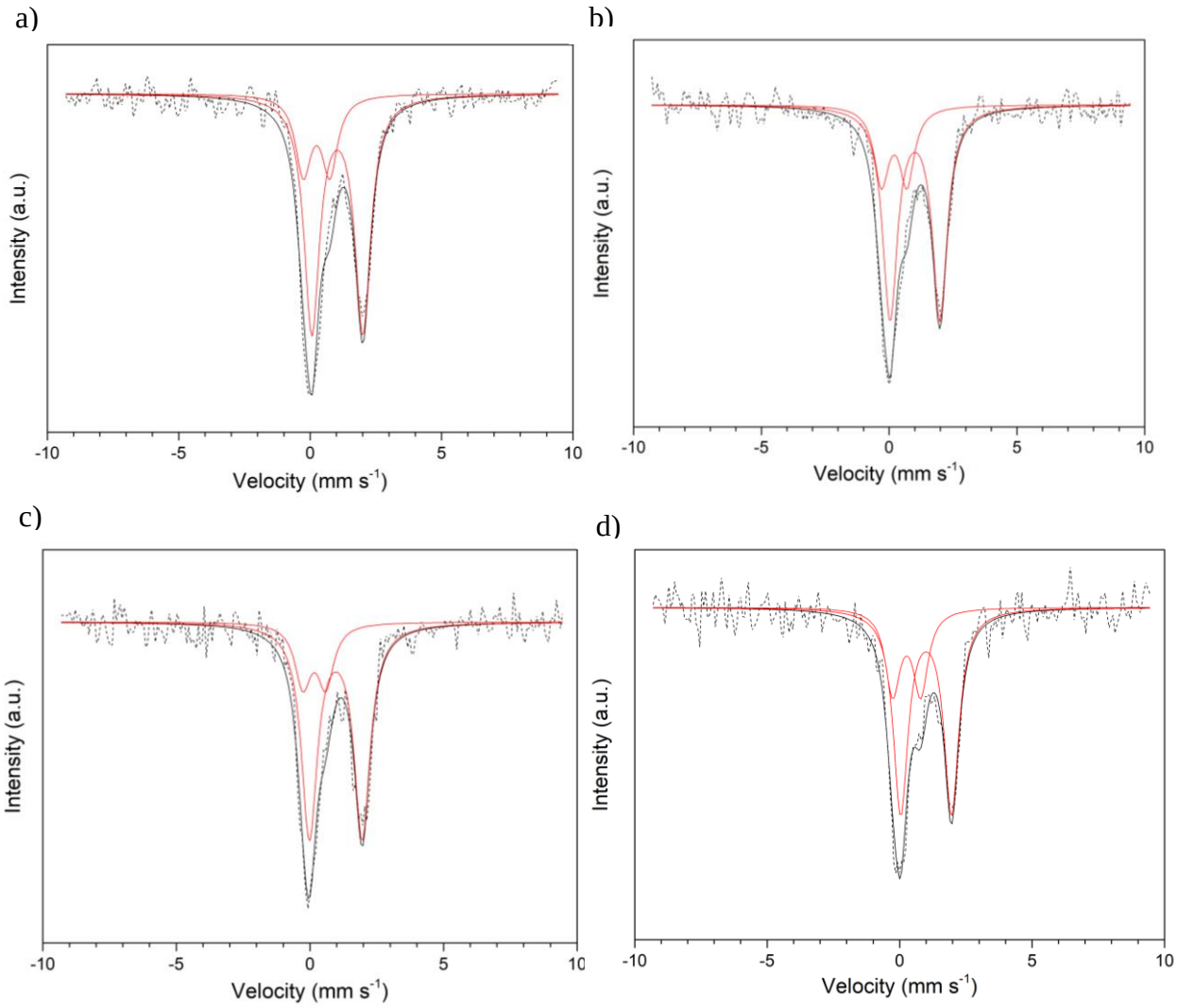

Figure 5-16. Mössbauer spectra showing fitted profiles, a) NBS-56.0%, b) N5NBS-59.5%, c) N10NBS-50.5% and d) N15NBS-53.5%.

5.2.6 Volatility During Glass Processing

Figure 5-19 shows the Simultaneous Thermal Analysis- Mass Spectroscopy (STA-MS) data of Cs clinoptilolite. Two events are labelled: i) and v); with i) corresponding to weight loss of water. This was confirmed with the mass spectrometry, showing a volatile species at 18 a.u.. As a zeolite mineral, clinoptilolite retains some water, tightly-bound, within its structure [20]. Drying at 90 ^{o}C, as for these samples, is insufficient to remove it. The TGA shows that the loss of tightly bound water associated with Cs clinoptilolite is 2.65 wt%, which is similar to that reported by other authors [20]. Thermal event v) (occurring at 810 ^{o}C) corresponds to a shift in the DTA baseline, and occurs at a similar temperature to the collapse of the zeolitic framework as observed in the HTXRD data, show in Figure 5-2. This suggests that the shift in the baseline may be explained by a change in the thermal properties after the structure of the zeolite has collapsed.

.

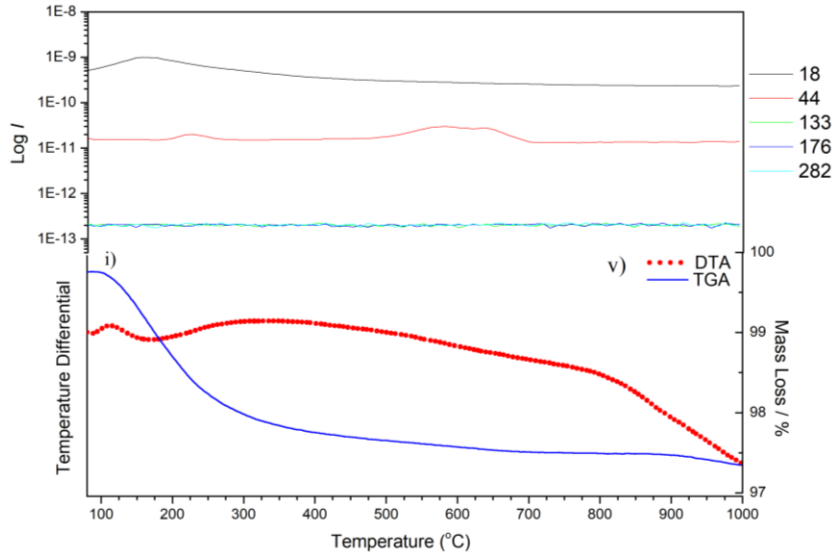

Figure 5-17. DTA and TGA in bottom half of graph and associated mass spectroscopy (top half) for Cs clinoptilolite.

Pre-mixed Cs clinoptilolite and glass additives were also subjected to STA-MS, (see Figure 5-20.) This was performed to understand the evolution of Cs clinoptilolite and glass-additives, with temperature. Most previous studies, on off-gas species from glass melts, are performed on pre-formed glasses rather than pre-mixed batch materials as

undertaken here [6], [11], [21]. Five thermal events labelled: i), ii), iii), iv) and v) were identified from the STA-MS and are explained in Table 5.9, along with the STA temperatures from Cs clinoptilolite.

i) corresponds to water loss, as outlined above,

ii) corresponds to the decarbonation of sodium carbonate,

iii) corresponds to the crystallisation of anhydrous borax, as in [22],

iv) corresponds to its melting, again, as in [22], and

v) is hypothesised to correspond to the collapse of the residual Cs clinoptilolite.

Also included in Figure 5-20 are common species that volatilise with Cs- these are $Cs_{(g)}$ (133 a.u.), $CsBO_{2(g)}$ (176 a.u.) and $Cs_2O_{(g)}$ (282 a.u.), however, no signal above background was detected for these. Table 5.4 shows that Cs_2O forms between 4.74 to 5.95 wt% of the final glass samples, with the STA-MS data showing that there is no significant loss in the TGA, which cannot be accounted for through loss of H_2O or CO_2. Above 700 ^oC, there is no loss recorded on the TGA, coupled with the fact that there are no ions detected in the mass spectroscopy data, above 133 a.u.. It can be concluded that there is no significant loss of Cs from these glasses during heating to 900 ^oC on a 35-40 mg scale. Heating the Cs Clinoptilolite (which contains 12.18 wt% Cs_2O) similarly leads to a wt% loss of 0.23% between 700 and 1000 ^oC showing the clinoptilolite retains the Cs_2O on heating until at least 1000 ^oC. This data though does not take into account the equilibrium between $Cs_{(g)}$ and $Cs_{(glass)}$ that will form after prolonged periods at elevated temperatures.

Table 5.9.
Temperatures of events identified from the STA-MS data.

Sample	i) ± 5 ^oC	ii) ± 5 ^oC	iii) ± 5 ^oC	iv) ± 5 ^oC	v) ± 5 ^oC
Cs Clinoptilolite	165	/	/	/	806
NBS-56.0%	170	/	541	670	802
N5NBS-59.5%	147	401	523	667	812
N10NBS-50.5%	142	409	516	664	738
N15NBS-53.5%	143	412	517	688	782

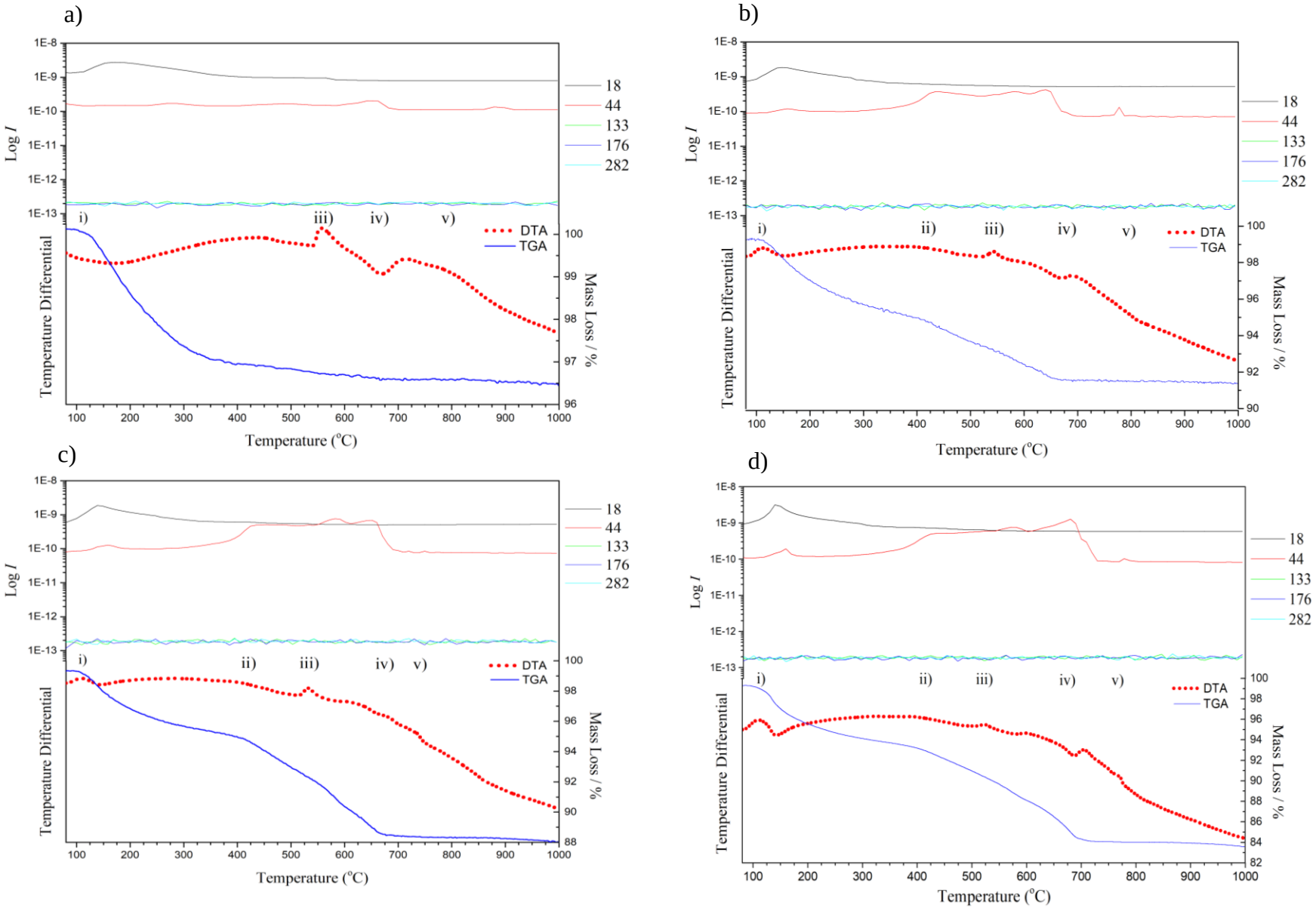

Figure 5-18. DTA (red dotted line), TGA (blue solid line) and associated mass spectroscopy for H_2O (18 a.u.), CO_2 (44 a.u.), Cs (133 a.u.), $CsBO_2$ (176 a.u.) and Cs_2O (282 a.u.) for a) NBS-56.0%, b) N5NBS-59.5%, N10NBS-50.5% and N15NBS-53.5%, endothermic is downwards and exothermic is upwards.

A Cs mass balance on stirred glasses was also performed. This consisted of measuring the wt% of Cs in the Cs clinoptilolite and the corresponding wt% of Cs in the glasses afterwards, using a total digest of the glass and ICP-MS as in section 3.11. Figure 5-21 illustrates the mass losses of Cs in a bar graph. This demonstrates that the Cs retentions are between 91.6 and 99.4% for these glasses, with all Cs retentions in error of one another. The STA-MS data and Cs mass balance data both indicate that these glass formulations demonstrate promising retention of Cs.

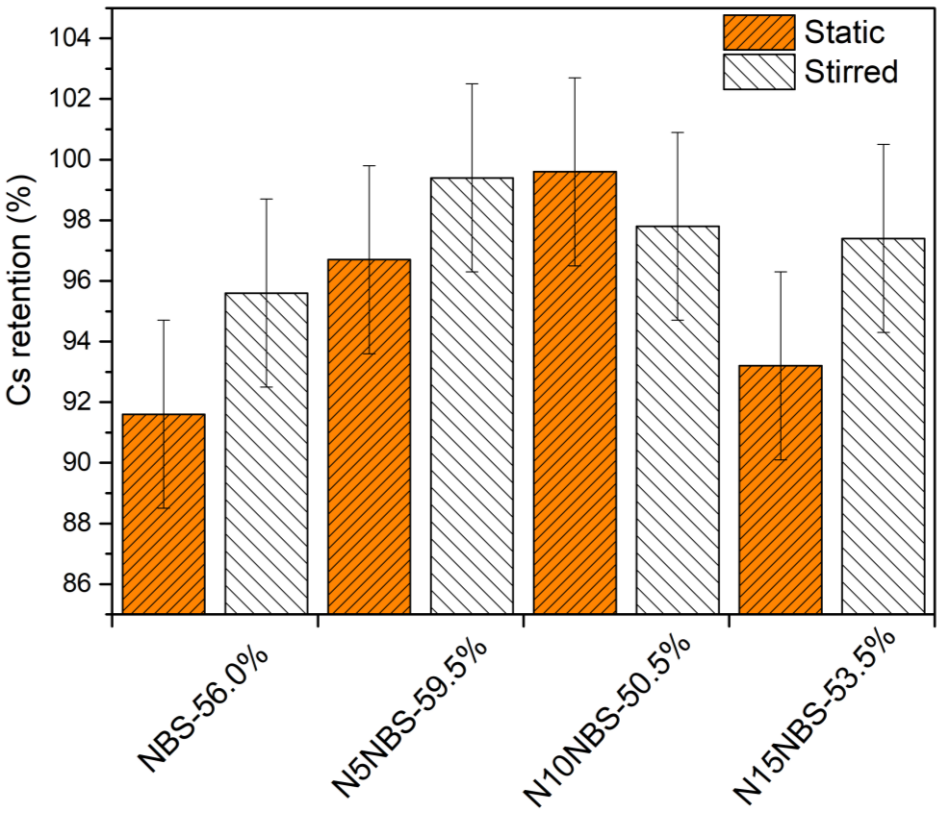

Figure 5-19. Cs retentions for the four glass compositions studied, for both stirred and static glass melts.

5.2.7 Glass Dissolution and Glass Structure

Raman spectra were collected for the four stirred glass compositions, see Figure 5-22. The region from 800 to 1200 cm^{-1} can be used to infer changes in SiO_2 coordination, whereas the region from 600 to 800 cm^{-1} is indicative of changes in the boron ring structure [23]–[26]. These two regions were of most interest in this study as they provide the most information on the effect of increasing R (i.e. $\frac{Na_2O}{B_2O_3}$) on glass structure. Note that the molar content of SiO_2, for the four glass compositions, is similar throughout (between 36.7 to 41.2 mol%). As can be observed increasing R, from NBS-56.0% to N15NBS-53.5% (highest R) has a significant effect on Si speciation between 800 to 1200 cm^{-1}, as well as effects on the boron ring structure at ~760 cm^{-1} and also the silicon ring structure at ~490 cm^{-1}.

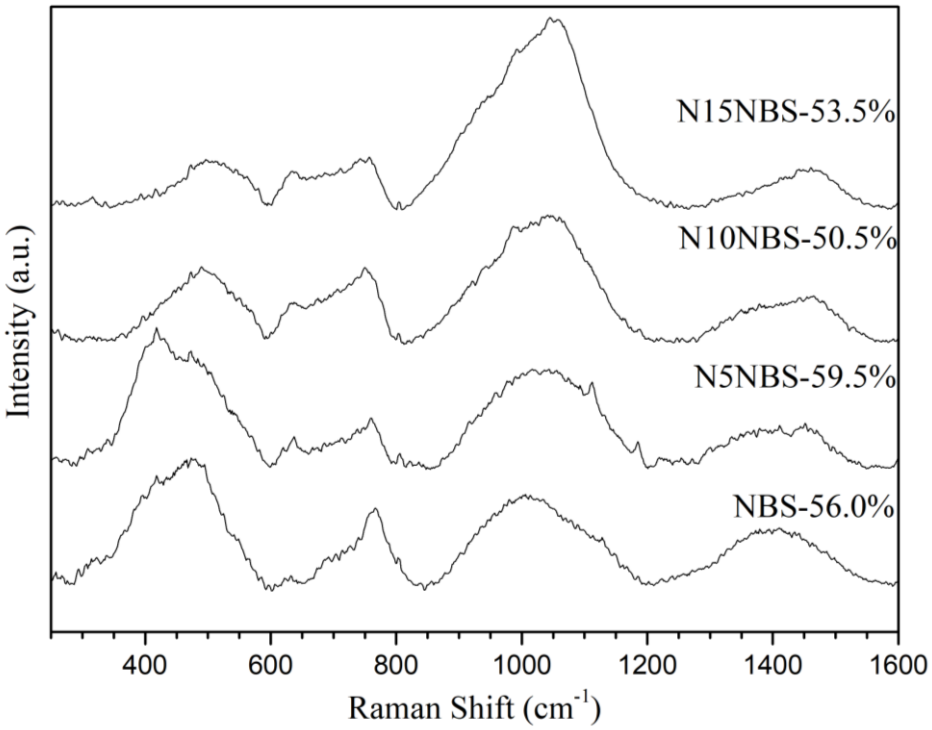

Figure 5-20. Raman spectra for the four glasses with increasing R from bottom to top.

The spectra in Figure 5-22 were fitted with Gaussian curves to quantify the relevant intensity of different Raman bands. The following procedure was used: an initial fit was performed with the peak wavenumbers fixed, using the values reported in the

literature, but the widths and intensities kept as independent and unconstrained variables [23], [24], [27]. Then, once the fit was acceptable, the peak wave numbers were refined as unconstrained values for a final curve fitting. Figure 5-23 shows the fitted Raman spectra and Table 5.10 contains the fit parameters. As can be observed, increasing R causes a decrease in Q_4 species and an increase in Q_3 species until all the Q_4 species has been depleted. At this point Q_3 species begin to be converted to Q_2 species. Increasing R, also causes a decrease in the quantity of the diborate composition, as boron ring superstructural units are disrupted.

Table 5.10.
Fit parameters for the Raman spectra for the two main regions of interest between 600 and 800 cm^{-1} and 800 and 1200 cm^{-1}. Estimated wavenumber errors are ± 5 cm^{-1} and areas are ± 2% (derived from the variation of multiple fits).

	NBS-56.0%			N5NBS-59.5%			N10NBS-50.5%			N15NBS-53.5%		
Raman Band	Raman Shift (cm^{-1})	Width (cm^{-1})	Area (%)	Raman Shift (cm^{-1})	Width (cm^{-1})	Area (%)	Raman Shift (cm^{-1})	Width (cm^{-1})	Area (%)	Raman Shift (cm^{-1})	Width (cm^{-1})	Area (%)
Q_4	1129	78	10	1127	78	10	0	0	0	0	0	0
Q_3	1032	131	49	1037	131	53	1050	136	53	1052	129	60
Q_2	947	95	16	947	95	16	942	115	21	936	118	26
Di-borate	765	54	18	760	54	10	754	46	9	753	45	5
Tetra-borate	703	56	7	699	75	8	699	90	14	693	85	7
Dan-burite	630	19	1	633	33	3	631	40	3	631	40	3

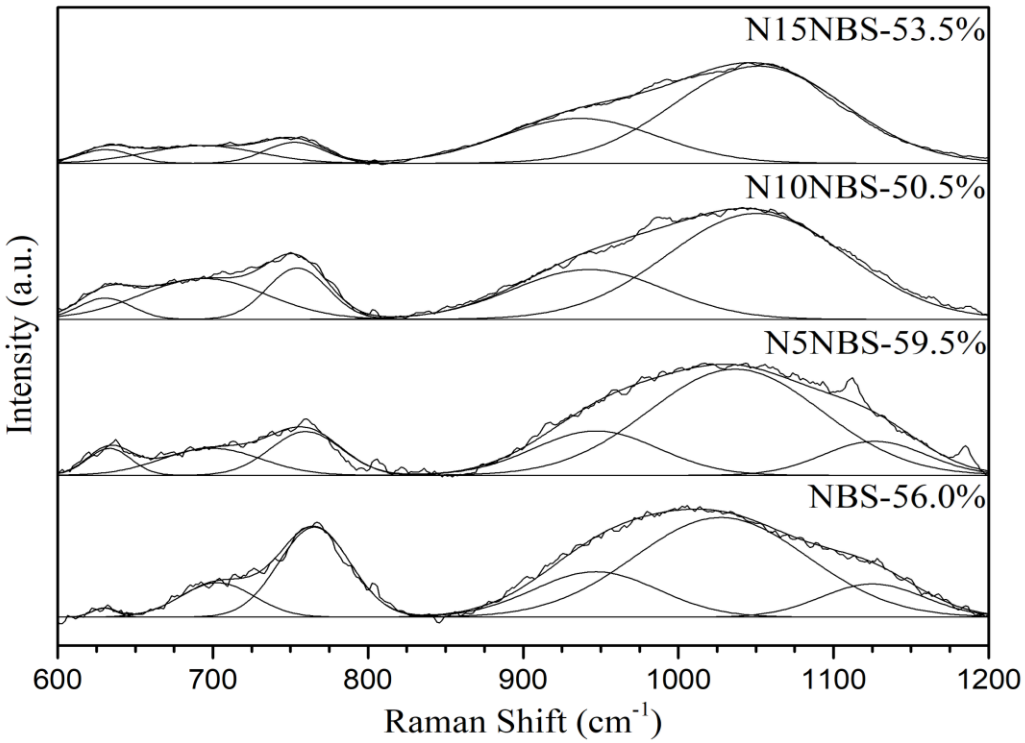

Figure 5-21. Fitted Raman spectra for the four glasses with increasing R from bottom to top.

The structure of borosilicate glasses evolves with increasing molar content of B_2O_3 and can be described by two molar ratios, R, and K (i. e $\frac{SiO_2}{B_2O_3}$). Borosilicate glasses can be categorised into four groups, see Section 2.3, dependent upon these two ratios [28]–[31]. Notwithstanding that R and K were developed for the SiO_2-B_2O_3-Na_2O ternary and therefore caution should be used when using these ratios for describing the structures of multi-oxide systems, they are useful here as SiO_2, B_2O_3 and Na_2O form the highest concentration oxides in the glass. For the NBS-56.0% composition, with a composition in group 1, there could be phase separation (with R = 0.44). This is corroborated with its position in the immiscibility region of Figure 5-3, with the lack of a peak at 630 cm^{-1} (corresponding to the danburite superstructural unit) and the strong peak at 765 cm^{-1}. Table 5.10 shows that the silicate network has started to depolymerise for NBS-56.0% with Q_4 (13%), Q_3 (65%) and Q_2 (22%). For the N5NBS-59.5% composition some of the boron has started to enter the silicate network, as is evidenced by the peak at 633 cm^{-1} and the decrease of the peak at 760 cm^{-1}. The silicate network polymerisation is unchanged with Q_4 (13%), Q_3 (67%) and Q_2 (20%). For N10NBS-50.5% the silicate network becomes impacted by the

increases in R with Q_4 (0%), Q_3 (72%) and Q_2 (28%) and for N15NBS-53.5% with Q_4 (0%), Q_3 (70%) and Q_2 (30%). Both these compositions have similar Si speciation with the distributions of Q_x in error of one another. For N5NBS-59.5%, N10NBS-50.5% and N15NBS-53.5% the impact on the diborate and danburite distribution is minimal indicating that the silicate has become saturated with boron.

5.2.7.1 Dissolution Experiments in Water

The short-term chemical durability of the NBS-56.0% and the N15NBS-53.5% compositions were investigated by leaching, at 90 ºC, in deionised water, in accordance with the PCT-B protocol [32]. These two compositions were selected as NBS-56.0% had the highest B_2O_3 and the lowest Na_2O concentrations and N15NBS-53.5% had the lowest B_2O_3 and the highest Na_2O concentrations, effectively bounding the two other compositions. Figure 5-24 shows the dissolution behaviour of NBS-56.0% and N15NBS-53.5% using Na, B, Si and Cs as tracer elements. Al, Ca and Fe concentrations were also measured in solution, using ICP-OES, but concentrations of Al and Ca in solution were close to the detection limit of the instrument and had significant variation between measurements at the same time point. Fe was not detected in solution. Glass dissolution is incongruent with $NL_{Na} > NL_B > NL_{Cs} > NL_{Si}$. The residual rate regime is reached between day 4 and day 7, from which point the normalised mass losses do not change with time. Using NL_B and NL_{Na}, from Figure 5-24, N15NBS-53.5% is more durable than NBS-56.0%, however taking NL_{Cs} and NL_{Si}, NBS-56.0% is more durable. The pH of the leachate containing NBS-56.0% is between 8.9 and 9.2 throughout the experiment whereas for N15NBS-53.5% it is significantly higher between 11.3 and 11.7. Over 7 days the normalised release rates (g m^{-2} d^{-1}) for N15NBS-53.5% for B is 1.34, for Na is 2.44, for Cs is 0.80 and for Si is 0.33. The normalised release rates (g m^{-2} d^{-1}) for NBS-56.0% for B is 1.78, for Na is 2.83, for Cs is 0.65 and for Si is 0.05. NL_{Si}, in particular, is much higher for N15NBS-53.5% compared to NBS-56.0%, due to the higher pH that the leachate buffers to.

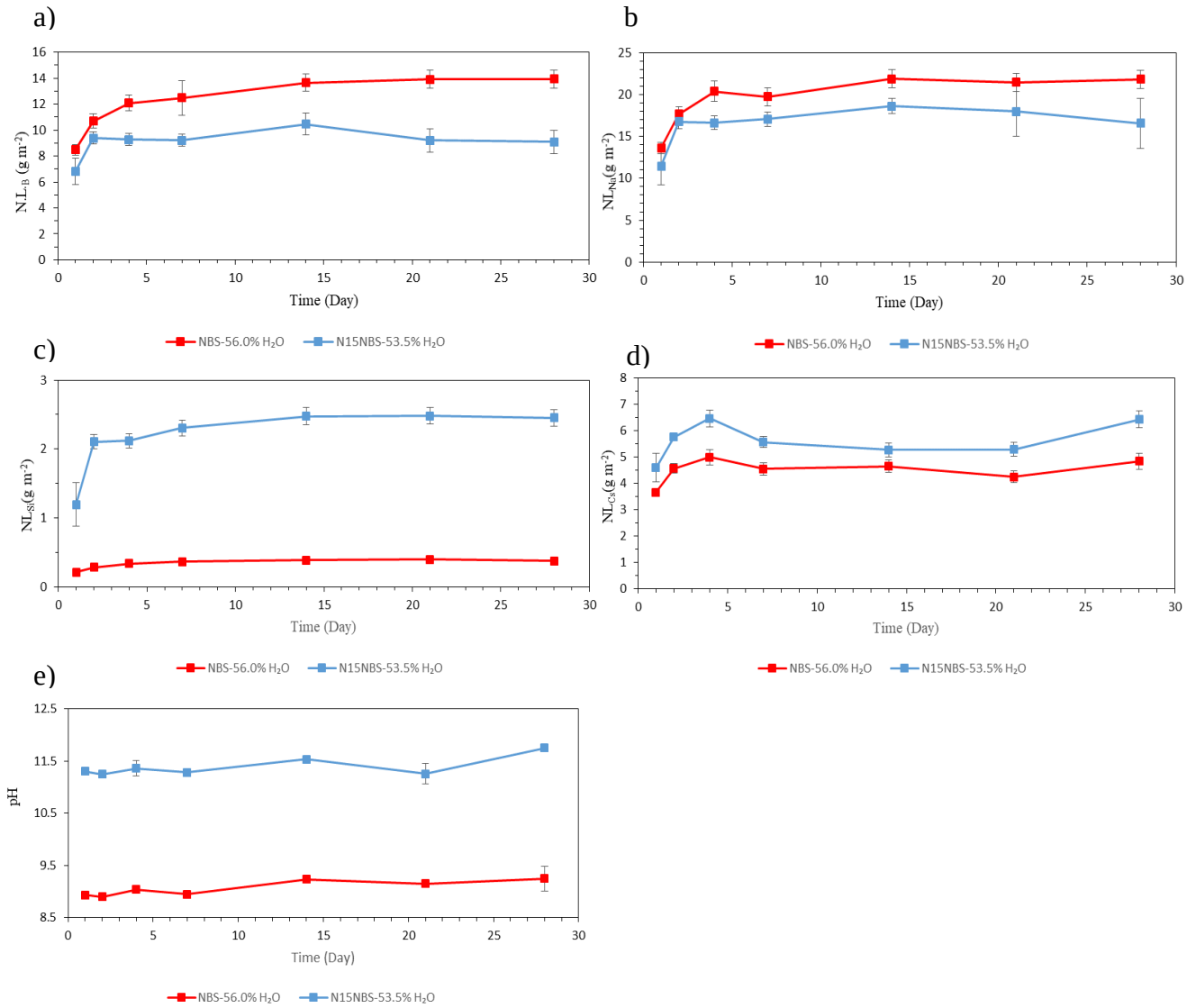

Figure 5-22. Normalised mass losses for NBS-56.0% and N15NBS-53.5% in water. a) NL_B, b) NL_{Na}, c) NL_{Si}, d) NL_{Cs} and e) pH.

5.2.7.2 Dissolution Experiments in Saturated $Ca(OH)_2$

N15NBS-53.5% was also leached in saturated $Ca(OH)_{2(aq)}$ solution at 90 ºC. The results of this experiment, and the results from the dissolution of N15NBS-53.5% in deionised water, are shown in Figure 5-25. Note the results from the dissolution of N15NBS-53.5%, in water at 90 ºC, are the same as the data shown in Figure 5-24 but are included here to allow comparisons to be made between the different leachates. Na, Si and B were used as dissolution tracers. Al, Ca, Fe and Cs concentrations were also measured, but concentrations of Al and Ca in solution were close to the detection limit and had significant variation between measurements at the same time point. Fe

was not detected and for Cs there was insufficient leachate to use ion chromatography. The reason for this was due to initially running the samples through the ICP-OES, with an internal standard, which was undertaken due to interference from the high concentration of Ca in solution, see Section 3.10. The use of an internal standard requires a program that uses a higher volume of sample and following the ICP-OES measurements insufficient leachate remained to use ion chromatography. Similar dissolution behaviour is observed to that in water with $NL_{Na} > NL_B > NL_{Si}$ and the residual rate reached by day 7. In saturated $Ca(OH)_{2(aq)}$, NL_B and NL_{Si} are lower than in deionised water, with NL_{Na} lower during the initial rate but of a similar value during the residual rate. This demonstrates that saturated $Ca(OH)_{2(aq)}$ leachate does retard glass dissolution. The $Ca(OH)_2$ in solution drops rapidly when in contact with N15NBS-53.5%, dropping to 126 ppm within 24 h to 5 ppm after 28 days. The blank solutions of saturated $Ca(OH)_{2(aq)}$ remain saturated throughout the experiment at ~555 ppm, demonstrating that the experimental set-up succeeded in preventing CO_2 ingress and subsequent carbonation. N15NBS-53.5% in deionised water buffered to a pH between 11.3 and 11.7, and remained largely constant throughout the experiment. N15NBS-53.5% in $Ca(OH)_{2(aq)}$ buffered to an average pH of ~11.9 with the blank solutions having an average pH of ~12.3. The pH between day 1 and day 7, for the studies in $Ca(OH)_{2(aq)}$, drops from pH 12.0 to 11.6, due to the $Ca(OH)_2$ beginning to precipitate out of solution. However, due to the release of alkali and alkaline earth from the glass, after the residual rate has been reached, the pH increases again to 12.0. In $Ca(OH)_{2(aq)}$ the normalised release rates (g m^{-2} d^{-1}) for N15NBS-53.5% over 7 days for B is 1.10, for Na is 2.64 and for Si is 0.22.

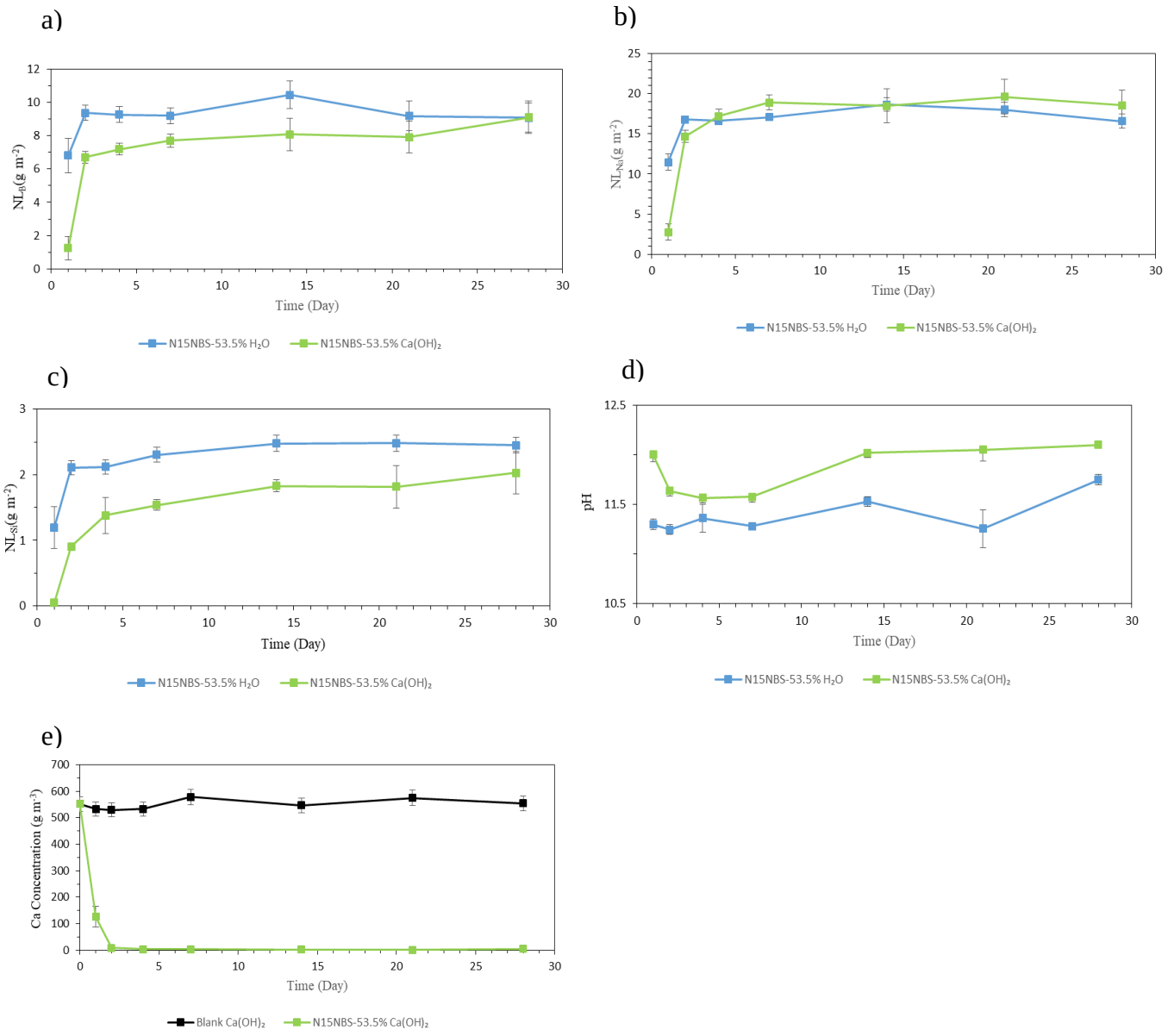

Figure 5-23. Normalised mass losses for N15NBS-53.5% in water and saturated $Ca(OH)_2$, a) NL_B, b) NL_{Na}, c) NL_{Si}, d) pH and e) Ca concentration in solution (ppm).

Figure 5-26 contains SEM-BSE images and EDX line scans of the pristine glass and alteration layers after 28 days, for NBS-56.0% in water and N15NBS-53.5% in both water and saturated $Ca(OH)_2$ solution. Alteration layer thickness varied between different glass particles but was typically between 5 and 10 μm, and qualitatively was thicker for NBS-56.0% than for both N15NBS-53.5% in deionised water and in $Ca(OH)_{2(aq)}$ solution. The SEM-BSE images for NBS-56.0% and N15NBS-53.5% illustrate differences in chemical composition due to the contrast between the

alteration layer and the pristine glass; as does N15NBS-53.5% in $Ca(OH)_2$ solution, however, the altered layer has detached from the surface with a clear gap between it and the surface of the glass. NBS-56.0% shows an alteration rim that is enriched in Si, Al and some Cs with no Na or Ca present. N15NBS-53.5%, in water, shows an alteration rim that is enriched in Si, Al and some Ca with no Cs or Na. In $Ca(OH)_2$ solution, N15NBS-53.5% shows an altered later that is rich in Ca and Si with no Al, Na or Cs detected; this is indicative of a C-S-H precipitate that has formed on the surface of the glass particles.

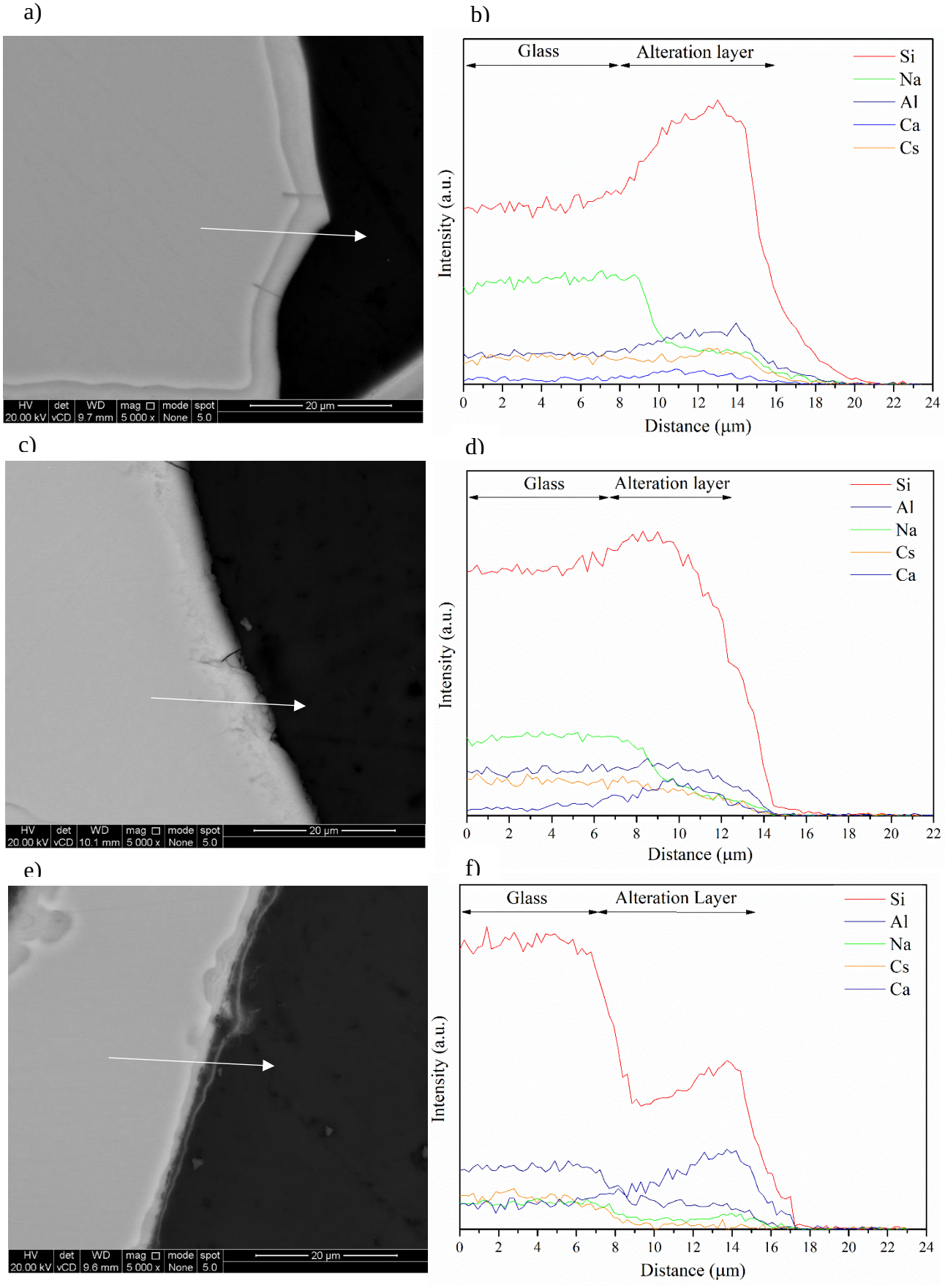

Figure 5-24. SEM-BSE and EDX line scans of leached powders and line scans across the alteration layers with arrows indicating where the line scans were collected, a) glass particle of leached NBS-56.0% and b) its EDX line scan, c) glass particles of leached N15NBS-53.5% and d) its EDX line scan, e) glass particle of leached N15NBS-53.5% and f) its EDX line scan.

5.3 Discussion

5.3.1 Thermal Conditioning of Clinoptilolite

The evolution of phase assemblage with temperature for Cs clinoptilolite was studied using HTXRD; it was found that a temperature between 750 and 850 ^{o}C is sufficient to collapse the zeolitic structure, however, these temperatures produce a porous, partially sintered, waste product. In order to thermally condition the Cs clinoptilolite into a glass matrix, fluxes are required. In this study four glasses (denoted NBS-56.0%, N5NBS-59.5%, N10NBS-50.5% and N15NBS-53.5%), in the relatively high B_2O_3 region of the Na_2O-B_2O_3-SiO_2 ternary, were studied, and their melting behaviour, at temperatures between 900 and 1050 ^{o}C, in grade 316L stainless steel crucibles examined. The glasses corrode the stainless steel, and those compositions richest in Fe, and other elements from the stainless steel (Cr, Ni and Mo), show the highest concentration of spinel phases. This can be observed from stirred NBS-56.0%, where the crucible corrosion is strongest and Fe_2CrO_4 can be identified in the XRD pattern. The EDX data suggests that all the iron is in the A site of the spinel. As a batch melting process the presence of spinel, and also sulfates, is not problematic, as settling at the base of the melter is not an issue. The glasses have striae, manifesting concentration gradients of key glass formers across the glass. Initially, fritting the glass and re-melting was attempted to minimise the striae, however, this was unsuccessful, as simply more steel was corroded and diffusion was still the only mechanism for homogenisation of the melt. It was found previously that stirring in itself does not produce homogeneous glasses but converts larger striae into smaller ones and creates a greater size distribution of them. Striae are only removed when the diffusion length in the melt is greater than twice the size of the striae [33]. It is suggested that the melting conditions could be optimised. In particular, the glass melt should be left for longer, before the introduction of the stirrer. Melts were left for 1 h before stirring began; this was significantly before the batch-free time for NBS-56.0% and N5NBS-59.5%, which both had a small amount of undissolved batch (quartz) that agglomerated upon stirring. The difference in particle size between the Cs clinoptilolite and fluxes means more time is required for digestion of the Cs clinoptilolite into the melt. A shorter time of mixing <3 h, or no stirring at all, is

recommended to minimise crucible corrosion and time at the melt temperature. Alternatively, rather than using grade 316L stainless steel, a grade of steel with higher resistance to high temperature oxidation could be explored. The two components to the broad diffuse scatter observed in the XRD is due to the pronounced concentration gradients of glass forms across the glass matrix.

5.3.2 Glass Properties and Waste Volume Reduction

There is a linear relationship between the density and the mol% content of modifier in the glasses, as the mol% of modifier increases, the density increases. DTA identified three thermal events on heating- the glass transition and two crystallisation events. The effect of increasing R is to decrease the temperature at which the glass transition occurs (from 500 ^{o}C for NBS-56.0% to 464 ^{o}C for N15NBS-53.55), as well as decreasing the temperature that the second crystallisation event occurs at, indicating a general weakening of the glass structure. The densities can be used to infer volume reduction potential of the conditioned glass against the original waste. The bulk density of clinoptilolite is ~1.4 kg L^{-1} resulting in 1.0 kg of waste having a volume of 0.71 L [1]. Using the waste loadings and respective densities of the waste forms in this study 1.0 kg of clinoptilolite waste results in 0.65 to 0.76 L of conditioned waste. Assuming a 20 wt% waste loading for cement encapsulation, 1 kg of clinoptilolite will result in 2.7 L of waste. Therefore, at the waste loadings studied here, conditioning via vitrification would result in a conditioned waste volume 1.0 ± 0.1 the original waste volume, whereas cementation would result in a conditioned waste volume 3.8 ± 0.4 times the original waste volume. This is a significant decrease in the conditioned waste volume.

5.3.3 Redox Environment in the Glass Melt

Melting in stainless steel crucibles (grade 316L) produced a reducing glass melt; in addition to this, crucible corrosion is aggressive, with the majority of the corrosion occurring at the melt line. Crucible corrosion is minimised for the lower temperature melting glasses with fewer spinel crystals observed, lower mol% of Fe in the glass and weaker Mössbauer signals. Some Fe and Cr incorporates into the melt, but also some form Fe_2CrO_4 phases, which are suspended in the glass. It is clear that the stainless

steel vessels led to a very reducing environment with $\frac{Fe^{2+}}{\Sigma Fe}$ between 70% and 76%, depending on composition. There is a trend for more reducing atmospheres with increasing melting temperatures for the glasses, except for N10NBS-50.5%. This anomaly may be due to the noisy data obtained for N10NBS-50.5%, which, (along with N15NBS-53.5%) had a lower iron concentration and a poor goodness of fit (reduced χ^2 of 0.59). For the Fe^{2+} site centre shifts range from 0.96 to 1.03 and Q.S. range from 1.94 to 1.98 indicating that the Fe^{2+} is likely to be tetrahedrally coordinated. Previous studies have shown that Fe^{2+} values of I.S. > 1.2 mm s^{-1} are generally attributed to eightfold coordination, values of 1.2 > I.S. > 1.05 are octahedral and 1.05 > I.S. > 0.9 are tetrahedral. It is possible that the Fe^{2+} is distributed between the glass phase and the spinel phase. Its tetrahedral coordination suggests that Fe^{2+} is likely to be a network intermediate in the glass and if in the spinel phase it will occupy the A site. For the Fe^{3+} site the centre shifts range from 0.16 to 0.26 and the Q.S. range from 0.86 to 1.06 indicating that the Fe^{3+} could either be octahedrally or tetrahedrally coordinated [18]. The upper limit for Fe^{3+} in tetrahedral coordination is ~0.25 mm s^{-1}, whereas the lower limit for octahedral coordination Fe^{3+} is ~0.29 mm s^{-1}. It is likely that Fe^{3+} is an intermediate in the glass.

5.3.4 Volatility of Caesium

Small glass batches were prepared and studied, under heating, using STA-MS to study glass batch evolution with temperature. Events i) and ii) were attributed to loss of water and carbon dioxide respectively. Event iii) at 515-535 ºC and event iv) at 670 ºC occur in all four glass compositions, including NBS-56.0%, which contains no sodium carbonate (only borax), therefore, these two thermal events are due to borax. The peak at 575 ºC is due to the crystallisation of $Na_2O.2B_2O_3$ from the amorphous matrix and the subsequent endothermic event is due to crystalline $Na_2O.2B_2O_3$ melting at 735 ºC. The lower measured temperatures, than those quoted in the literature, are due to the referenced study using borax decahydrate; amorphous borax (used in this study) will crystallise at lower temperatures [22], [34]. It was hypothesised that the shift in the baseline at ~800 ºC is due to a change in the thermal properties of the Cs clinoptilolite as the structure collapses.

A previous study, vitrifying organic, sulfonated, phenol-formaldehyde based, ion exchange resin, melting at 1200 ºC, for 3 h, observed retentions in the 64.3-78.9 wt%, with an average of 74.2 wt% [35]. Another study, vitrified four different waste streams- an organic, sulfonated, styrene-divinylbenzene based, ion exchange resin; effluent treatment sludge; pond water treatment sludge and sand filters, at 1200 ºC, for 8 h. Cs retentions were between 59%-76%, with an average of 68.5 wt% [36]. The average Cs retention here is 96.5 ± 2.7 wt%. Although there are significant differences in the nature of the waste streams (the resins are organic, whereas clinoptilolite is inorganic) and glass compositions (in the above studies there is significantly less B_2O_3 and more BaO and CaO in the base glasses). The 25 wt% increase in Cs retention is a significant finding. Most of the Cs retentions are within error of one another, although there is an indication that NBS-56.0%, melted at 1050 ºC, shows slightly lower Cs retentions than the other three glasses. Although the high Cs retentions are promising, further investigation of Cs retentions could be utilised using replicate measurements to determine variation in the data, and the relatively large errors associated with the measurement of Cs retention undertaken. Furthermore monitoring of Cs in an off-gas system could be used to more accurately quantify Cs losses during melting.

5.3.5 Glass Dissolution and Glass Structure

Raman spectroscopy was used to study the impact of increasing R on glass structure. There is a change in the Si speciation as the value of R increases across the glass compositions in this study, with a decrease in Q_4 units (from 13 ± 2% for NBS-56.0%, to 0 ± 2% for N15NBS-53.5%) and a concomitant increase in Q_2 (from 22 ± 2% for NBS-56.0% to 30 ± 2% for N15NBS-53.5%). There is a strong peak at 765 cm^{-1}, for NBS-56.0%, which decreases in intensity, for the other three compositions, as the value of R increases. This is due to the additional modifier disrupting the Raman bending modes of the diborate superstructural units. The overall effect of increasing R is to depolymerise the glass network and disrupt the silicate and borate super-structural units within the glass.

Glass dissolution is incongruent, with approximately 10x more $Si_{(aq)}$ in solution for N15NBS-53.5%, than for NBS-56.0%. Silica in aqueous solution is present as silicic acid ($Si(OH)_4$), and silica solubility increases with pH [37]. The dissociation of silicic

acid that occurs at higher pH ranges is given by Equation 5-1, this dissociation of silicic acid at higher pH leads to increased overall solubility of the silica. The reaction quotients for this reaction being on the order of 10^3 [38].

$$H_4SiO_4 + OH^- \rightarrow H_3SiO_4^- + H_2O \qquad \text{Equation 5-1}$$

When silicic acid precipitates amorphous silica is the kinetically favoured product. The silica solubility of amorphous silica is estimated to be ~200 times greater at an average pH of 11.4 compared to a pH of 9.1 for a given temperature [37]. This is used to explain the lower silicon release rates observed for NBS-56.0% compared to N15NBS-53.5%.

The lower NL_{Cs} for NBS-56.0%, than for N15NBS-53.5%, can be explained by precipitation from the leachate too. Figure 5-26 clearly shows that Cs forms part of the alteration layer for NBS-56.0%, but not for N15NBS-53.5%. The striations and the potential for phase separation complicates the analysis of the glass structure and glass dissolution. Cs is more strongly associated with silica and alumina when observing the chemical gradients across the striae, see Figure 5-15. This is due to the breakdown of the clinoptilolite grains, with the elements originating from the clinoptilolite associating together. In contrast, in the dark regions of the glass, the iron is associated with the Na_2O, and possibly B_2O_3, due to the fluxes attacking the stainless steel crucible, during early melting. Although N15NBS-53.5% has a slightly more depolymerised network and should, therefore, be less durable, there is the possibility that NBS-56.0% is phase separated, as it straddles the immiscibility region.

For NBS-56.0% and N15NBS-53.5%, NL_B is 1.3–1.8 g m^{-2} d^{-1} and for waste loaded MW glass, NL_B is ~0.8 g m^{-2} d^{-1}. Therefore, the durability of these glasses, in water, using $N.L._B$ is 2.3 to 1.6 times less durable than waste loaded MW glass frit over 7 days [39],[40]. The percentage loss of caesium after 24 h from composite cements was between 8–25 wt%, at an estimated S.A./ V. ratio of 14000 ± 1000 cm^{-1}. Here, after 24 h, we observe a loss of caesium between 0.52-0.65 wt%, with a S.A./ V. ratio of 1200 cm^{-1}. Making an assumption that the percentage caesium loss scales linearly with S.A./ V. ratio we have a loss of 6-8 wt% loss of caesium comparable to the conditions performed for composite cement encapsulation. This suggests that these low melting glass formulations are, at worst, as effective as the most durable composite cement for

clinoptilolite encapsulation.

In saturated $Ca(OH)_{2(aq)}$ solution, NL_B and NL_{Si} are significantly lower than in water; this is due to oversaturation of Si in the $Ca(OH)_2$ leachates leading to the formation of a C-S-H phase on the surface of the glass, which decreases glass alteration. Due to the relatively low durability of these glass waste forms, there is a high concentration of Si in solution after a short period of time, causing the concentration of $Ca(OH)_{2(aq)}$ to drop from 555 ppm to 126 ppm after 24 h, due to C-S-H precipitation. Previously reported simulant ILW glasses (from PCM vitrification) (in saturated $Ca(OH)_{2(aq)}$ at 50ºC) had initial dissolution rates between 0.04-0.18 g m^{-2} d^{-1} for NL_{Na}, dependent upon the particular PCM waste stream [41]. NL_{Na} over 7 days in $Ca(OH)_{2(aq)}$ is 2.64 g m^{-2} d^{-1} for N15NBS-53.5% demonstrating these waste forms perform at least an order of magnitude worse than other thermally conditioned ILW waste streams. However it must be noted that this experiment was conducted at 90 ºC, which will results in an increased dissolution rate.

5.4 Conclusions

Thermal conditioning of clinoptilolite waste streams, using low melting glass formulations, has been demonstrated to have several advantages and is a promising waste conditioning strategy for both low volumes of waste, with the potential to scale up to larger volumes. The low volatility of Cs, during glass processing (92 to 99% retention), in particular, is one benefit. However further investigation of this is suggested, in particular monitoring, of Cs in an off-gas system, rather than measuring the Cs content of the glass. Temperatures of < 850 ºC are sufficient to collapse the zeolitic structure and, therefore, prevent ion exchange of Cs out of the structure; however, glass additives are needed to produce a vitreous waste form. Melting in grade 316L stainless steel causes corrosion of the crucible, directly leading to spinel phases in the glass. Therefore, the study of a more corrosion-resistant material at high temperatures would be useful, however, it was noted that melting at 900 ºC, compared to 1050 ºC, significantly reduced corrosion of the grade 316L crucibles. These studies were performed with the knowledge that greater glass melting scales could be achieved using the FINGAL process developed at Harwell, these studies confirm that this is a viable option and should be considered. Melting in stainless steel produces

highly reducing melts with a $\frac{Fe^{2+}}{\Sigma Fe}$ ratio of between 70% and 76%. R (given by $\frac{Na_2O}{B_2O_3}$) has a large impact on glass structure with increasing R value leading to a more depolymerised network, and also leading to the leachate buffering to a much higher pH significantly increasing Si solubility. The durability of glass compositions in this study is relatively low and perform worse than HLW and ILW glasses (at best 1.6-2.3 times worse over 7 days). However, the Cs leaching is estimated to be, at worst, slightly better than cement encapsulated clinoptilolite. Using these glass compositions significant waste volume reductions (~3.8 times less waste), versus cement encapsulation, are possible.

5.5 References

[1] NDA, "Waste Stream 2D26 Ion Exchange Material (Clinoptilolite) and Sand," 2013. [Online]. Available: http://ukinventory.nda.gov.uk/wp-content/uploads/sites/18/2014/04/2D26.pdf. [Accessed: 15-Nov-2014].

[2] T. Armbruster, "Clinoptilolite-heulandite: applications and basic research," *Stud. Surf. Sci. Catal.*, vol. 135, pp. 13–27, 2001.

[3] L. Gordon, "Encapsulation of clinoptilolite in cement-based system," 2008.

[4] H. F. W. Taylor, "A Method for Predicting Alkali Ion Concentrations in Cement Pore Solutions," *Adv. Cem. Res.*, vol. 1, pp. 5–16, 1987.

[5] P. H. R. Borges, J. O. Costa, N. B. Milestone, C. J. Lynsdale, and R. E. Streatfield, "Carbonation of CH and C-S-H in composite cement pastes containing high amounts of BFS," *Cem. Concr. Res.*, vol. 40, no. 2, pp. 284–292, 2010.

[6] H. Kamizono, S. Kikkawa, Y. Togashi, and S. Tashiro, "Volatilisation of ^{137}Cs and ^{106}Ru from Borosilicate Glass Containing Actual High-Level Waste," *J. Am. Ceram. Soc.*, vol. 72, no. 8, pp. 1438–1441, 1989.

[7] M. Asano, T. Kou, and Y. Yasue, "Mass Spectrometric Study Of Vaporisation Of Caesium-Containing Borosilicate Glasses," *J. Non. Cryst. Solids*, vol. 92, pp. 245–260, 1987.

[8] R. Terai and E. Kosaka, "Osaka Kogyo Gijutus Shikenjo Kiho 27:150. Volatilisation of Low Temperature Borosilicate Glasses for High-Level Radioactive Wastes at Elevated Temperatures," 1976.

[9] B. P. Spalding, "Volatilisation of caesium-137 from soil with chloride amendments during heating and vitrification," *Environ. Sci. Technol.*, vol. 28,

pp. 1116–1123, 1994.

[10] J. H. Carpenter, J. C. McMullen, B. A. Olmscheid, P. A. Chezick, and C. Olig, "Caesium Vaporisation Losses from Synroc Mineral Barium-Caesium Hollandite," in *Nuclear Waste Management, Advances in Ceramics*, 1st ed., G. Wicks and W. Ross, Eds. Columbus, Ohio: American Ceramic Society.

[11] M. Cable and M. A. Chaudry, "Volatisation from soda-lime-silica melts at one atmosphere and reduced pressures," *Glas. Technol*, vol. 16, pp. 125–134, 1975.

[12] M. N. Elliot, R. Gayler, J. R. Grover, and W. H. Hardwick, "Fixation of radioactive waste in glass. Part I. Pilot-Plant Experience at Harwell," *Treat. Storage High-Level Radioact. Wastes*, pp. 465–487, 1962.

[13] P. Lightfoot, D. A. Woodcock, M. J. Maple, L. A. Villaescusa, and P. A. Wright, "The widespread occurrence of negative thermal expansion in zeolites," *J. Mater. Chem.*, vol. 11, no. 1, pp. 212–216, 2001.

[14] D. A. Woodcock, P. Lightfoot, P. A. Wright, and L. A. Vilaescusa, "Strong negative thermal expansion in-the siliceous zeolites ITQ-1, a ITQ-3 and SSZ-23 3," vol. 70, no. c, pp. 349–351, 1999.

[15] W. F. Du, K. Kuraoka, T. Akai, and T. Yazawa, "Study of Al_2O_3 effect on structural change and phase separation in Na_2O-B_2O_3-SiO_2 glass by NMR," *J. Mater. Sci.*, vol. 35, pp. 4865–4871, 2000.

[16] W. Vogel, "Glass Chemistry," 2nd ed., Berlin: Springer-Verlag, 1994, pp. 123–157.

[17] L. S. Du and J. F. Stebbins, "Solid-state NMR study of metastable immiscibility in alkali borosilicate glasses," *J. Non. Cryst. Solids*, pp. 239–255, 2003.

[18] M. D. Dyar, D. G. Agresti, M. W. Schaefer, C. A. Grant, and E. C. Sklute, "Mössbauer Spectroscopy of Earth and Planetary Materials," *Annu. Rev. Earth Planet. Sci.*, vol. 34, pp. 83–125, 2006.

[19] O. J. McGann, P. . Bingham, R. J. Hand, A. S. Gandy, M. Kavčič, M. Žitnik, K. Bučar, R. Edge, and N. C. Hyatt, "The effects of gamma radiation on model vitreous wasteforms intended for the disposal of intermediate and high level radioactive wastes in the UK," *J. Nucl. Mater.*, vol. 429, pp. 353–367, 2012.

[20] G. D. Knowlton, T. R. White, and H. L. Mckague, "Thermal Study of Types of Water Associated With Clinoptilolite," *Clays Clay Miner.*, vol. 29, no. 5, pp. 403–411, 1981.

[21] B. G. Parkinson, D. Holland, M. E. Smith, A. P. Howes, and C. R. Scales, "The effect of Cs2O additions on HLW wasteform glasses," *J. Non. Cryst. Solids*, vol. 351, no. 30, p. 2425, 2005.

[22] I. Waclawska, “Thermal Decomposition of Borax,” *J. Therm. Anal.*, vol. 43, pp. 261–269, 1995.

[23] W. L. Konijnendijk and J. M. Stevels, “The Structure of Borosilicate Glasses Studied By Raman Scattering,” *J. Non. Cryst. Solids*, vol. 20, pp. 193–224, 1976.

[24] B. N. Meera and J. N. Ramakrishna, “Raman Spectral Studies of Borate Glasses,” *J. Non. Cryst. Solids*, vol. 159, pp. 1–21, 1993.

[25] D. W. Matson, S. K. Sharma, and J. A. Philpotts, “The Structure of High-Silica Alkali-Silicate Glasses. A Raman Spectroscopic Investigation,” *J. Non. Cryst. Solids*, vol. 58, pp. 323–352, 1983.

[26] S. V. Raman, “The Effect of Mixed Modifiers on Nuclear Waste Glass Processing, Leaching and Raman Spectra,” *J. Mater. Res.*, vol. 13, pp. 8–15, 1998.

[27] D. Manara, A. Grandjean, and D. R. Neuville, “Advances in Understanding the Structure of Borosilicate Glasses: A Raman Spectroscopy Study,” *Am. Mineral.*, vol. 94, pp. 777–784, 2009.

[28] W. J. Dell, P. J. Bray, and S. Z. Xiao, “^{11}B NMR Studies and Structural Modelling of Na_2O-B_2O_3-SiO_2 glasses of high soda content,” *J. Non. Cryst. Solids*, vol. 58, pp. 1–16, 1983.

[29] Y. H. Yun and P. J. Bray, “Nuclear Magnetic Resonance Studies of Glasses in the System Na_2O- B_2O_3- SiO_2,” *J. Non. Cryst. Solids*, vol. 27, pp. 363–380, 1978.

[30] Y. H. Yun, S. A. Feller, and P. J. Bray, “Correction and Addendum to ‘Nuclear Magnetic Resonance Studies of the Glasses in the system Na_2O-B_2O_3-SiO_2,’” *J. Non. Cryst. Solids*, vol. 33, pp. 273–277, 1979.

[31] B. C. Bunker, D. R. Tallant, R. J. Kirkpatrick, and G. L. Turner, “Multinuclear nuclear magnetic resonance and Raman investigation of sodium borosilicate glass structures,” *Phys. Chem. Glas.*, vol. 31, pp. 30–41, 1990.

[32] ASTM, “C1285 - 14. Standard Test Methods for Determining Chemical Durability of Nuclear, Hazardous, and Mixed Waste Glasses and Multiphase Glass Ceramics: The Product Consistency Test (PCT),” West Conshohocken, PA, 2014.

[33] M. Jensen and Y. Yue, “Effect of stirring on striae in glass melts,” *J. Non. Cryst. Solids*, vol. 358, no. 2, pp. 349–353, 2012.

[34] D. M. Schubert, “Borates in Industrial Use,” in *Group 13 Chemistry III. Industrial Applications*, 2003, pp. 25–28.

[35] O. J. McGann, “The Development of Glass Compositions for the Vitrification of Ion Exchange Resin Wastes from the Nuclear Industry,” 2013.

[36] P. A. Bingham, N. C. Hyatt, and R. J. Hand, “Vitrification of UK intermediate level radioactive wastes arising from site decommissioning. Initial laboratory trials,” *Glas. Technol Eur. J. Glas. Sci. Technol. A.*, vol. 54, no. 1, pp. 1–19, 2013.

[37] B. A. Fleming and D. A. Crerar, “Silicic Acid Ionisation and Calculation of Silica Solubility at Elevated Temperature and pH,” *Geothermics*, vol. 11, pp. 15–29, 1982.

[38] R. H. Busey and R. E. Mesmer, “Ionisation equilibriums of silicic acid and polysilicate formation in aqueous sodium chloride solutions to 300oC,” *Inorg. Chem.*, vol. 16, pp. 2444–2450, 1997.

[39] M. T. Harrison, “The Effect of Composition on short- and long-term durability of UK HLW glass,” *Procedia Mater. Sci.*, vol. 7, pp. 186–192, 2014.

[40] H. Zhang, C. L. Corkhill, P. G. Heath, R. J. Hand, M. C. Stennett, and N. C. Hyatt, “Effect of Zn- and Ca- oxides on the structure and chemical durability of simulant alkali borosilicate glasses for immobilisation of UK high level wastes,” *J. Nucl. Mater.*, vol. 462, pp. 321–328, 2015.

[41] N. C. Hyatt, R. R. Schwarz, P. A. Bingham, M. C. Stennett, C. L. Corkhill, P. G. Heath, R. J. Hand, M. James, A. Pearson, and S. Morgan, “Thermal Treatment of Simulant Plutonium Contaminated Materials From The Sellafield Site By Vitrification In A Blast-Furnace Slag,” *J. Nucl. Mater.*, vol. 444, pp. 186–199, 2014.

[42] T. J. Rockett and W. R. Foster, “The High-Silica Liquidus Surface of the System Na_2O-B_2O_3-SiO_2,” *J. Am. Ceram. Soc.*, vol. 64, pp. 148–149, 1981.

6 Maximising Waste Loadings by Co-conditioning of SIXEP Clinoptilolite / Sand Waste and Bulk Storage Tank Sludge

6.1 Introduction

By combining two different waste streams, and conditioning thermally, significant reductions in waste volume should be possible. Two waste streams arise from the operation of the Site Ion eXchangE Plant (SIXEP) at the Sellafield site, U.K.. Here, waste effluent is filtered with sand particles, before being passed through ion exchange columns filled with the naturally occurring mineral clinoptilolite. This is to decrease the activity associated with the waste effluent prior to discharge to sea. Periodically the sand bed filters are back-washed into storage tanks (called the Bulk Storage Tanks (BST)) and allowed to settle, this has formed a sludge over time [1]. The waste clinoptilolite and sand particles are stored wet with the composition 60 wt% clinoptilolite, 7 wt% sand and 33 wt% water [2]. The composition of the sludge is more heterogeneous due to the nature of its formation, but will have a high concentration of $Mg(OH)_{2(aq)}$[3],[4]. The effect of Mg on glass processing and performace will be a key consideration for selecting glass formulations. When co-conditioning these two waste streams key considerations will be the viscosity of the glass, the structural role of Mg, solubility limit of Mg and durability of the waste form.

6.1.1 Role of Magnesia in Glass Structure

Magnesia, with a field strength of 0.53 $Å^{-2}$, has been shown to be a conditional glass-former under certain conditions, with a coordination number of four. Invert glasses, produced from forsterite, show edge and corner sharing MgO_x polyhedra in four, five and six coordinate arrangements, with MgO_4 units in a tetrahedral environment. The low (33 mol%) SiO_2 content (in invert glasses from forsterite) prevents the formation of an extended silica based network so that only isolated SiO_4 and Si_2O_7 dimers exist [5], [6]. Others have found that by substituting MgO for CaO in essentially soda lime silicate glasses, the network is polymerised with magnesia entering into the silicate

network as a four coordinate unit [7]. This was confirmed with ^{29}Si NMR data showing an increase in the Q_3 speciation (from 17 to 41%) of an essentially Q_2 based glass structure as the MgO substitutes for CaO from 0 to 100% (with MgO + CaO forming a total of 23 mol% of the glass). The MgO_4 units are charged and take more modifier from the glass network to charge compensate further promoting network polymerisation [8]. By studying Mg K-edge XANES and EXAFS the structural role of Mg was determined to be mixed between modifier and conditional former with Mg-O bond distance between 2.00 ± 0.04 Å and an average coordination number of five for a series of diopside-albite based glasses [9]. Another study based upon ^{25}Mg NMR found that the structural role of Mg is heavily composition dependent with high field strength ions inducing the bond length of Mg-O to increase and increases in coordination number of MgO_x units [10].

Previous studies have looked at conditioning sludge from the BSTs and clinoptilolite / sand waste from SIXEP, but separately, not combining the two. JHCMs were used to determine whether these waste streams could be processed using a continuous melter system. The sludge waste glasses were processed at 1200 ^oC, with a relatively high B_2O_3 content (28.6 wt%) in an attempt to increase the solubility of refractive components, which forms a high proportion of the waste stream. Magnox sludge was spiked with 0.1 wt% fission products to ensure there was sufficient to be above the detection limit of detectors [11]. Magnox sludge was processed at 30-40 wt% waste loading. The primary problem was the formation of forsterite crystals in the glass (Mg_2SiO_4) for the Magnox waste stream. For the clinoptilolite waste, it was assumed that the clinoptilolite to sand ratio was 10:1. It was observed that the clinoptilolite waste vitrified without many problems due to the high concentration of glass-formers in the waste [11].

6.2 Results

The approach to this study was to produce three base glass formulations from the clinoptilolite / sand waste and glass additives, melting at either 1200 or 1300 ^oC, and to then add $Mg(OH)_2$ to frits of these base glasses to observe the effect of MgO on the glass structure. The three clinoptilolite / sand base glass formulations are denoted:

N10BS-70%, NL7.5BS-75% and NL15BS-67.5%. These glass formulations can be seen in Table 6-1. The glasses are designated based upon waste loading and wt% of glass additives. For example, NL7.5BS-75% corresponds to a glass containing Na_2O and Li_2O at 7.5 wt% and a clinoptilolite / sand waste loading of 75 wt% with the balance being B_2O_3.

The clinoptilolite was provided by the National Nuclear Laboratory (NNL). Sand was high-purity glass making sand from Glassworks Services Ltd. (99% purity), boric acid was from Acros Chemicals (99% purity), sodium carbonate was from Alfa Aesar (98% purity) and lithium carbonate was from Sigma-Aldrich (99% purity). It was decided not to ion exchange the clinoptilolite simulant waste, due to the low mass fraction of caesium and strontium in the actual waste stream. Even though they have important radiological implications, from a chemical perspective, they will not have a major impact on waste form structure and performance.

Table 6-1.
Glass formulations for the sand / clinoptilolite waste glasses and the melting temperatures.

Precursor (wt%)	N10BS-70%	NL7.5BS-75%	NL15BS-67.5%
Clinoptilolite	62.70	67.16	60.45
Sand	7.30	7.84	7.05
H_3BO_3	34.37	31.08	31.08
Na_2CO_3	18.21	8.41	16.83
Li_2CO_3	0.00	6.35	12.72
	Melting Temperature (^oC)		
	1300	1300	1200

The batch materials (250-300 g scale) were mixed together for 15 min, by hand, and then added to a Pt crucible at temperature (1300 ^oC or 1200 ^oC). This occurred over 3-4 additions covering a ~15 min period to allow the batch to melt down. The batch was melted for 1.5 h statically (unreacted batch was observed after 1 h) before a Pt stirrer was inserted into the melt and left for 2.5 h. After 4 h the glass was cast, water-quenched and then fritted. The introduction of Li_2O, as well as Na_2O, for NL7.5BS-75% allowed an increase in the waste loading (5 wt%) and for NL15BS-67.5%

allowed a lower processing temperature (1200 ^{o}C). The reason for this is due to a eutectic point in the Na_2CO_3: Li_2CO_3 phase diagram at 48 mol% Na_2CO_3: 52 mol% Li_2CO_3 with the eutectic point 358 ^{o}C lower than that for pure Na_2CO_3 [12], [13].

6.2.1 Glass Formulations

To study the maximum sludge loading into the clinoptilolite / sand base glass a series of melts were performed where incrementally more MgO was added (in the form of $Mg(OH)_2$) until crystallisation occurred; either within the glass matrix or settled out in the base of the crucible, see Table 6-2. The glasses in this section are designated based upon the base glasses, see Table 6-1, and the waste loading of MgO, for example Mg22.5NL7.5BS-75% denotes the NL7.5BS-75% base glass waste loaded with 22.5 wt% MgO (in the form of $Mg(OH)_2$).

These test melts were performed on a 60.0-67.5 g scale. The samples were mixed by hand for 5 mins, poured into a mullite crucible and packed down. The batch and crucible were heated at 3 ^{o}C min^{-1} to 1300 ^{o}C or 1200 ^{o}C, dwelled for 2h, and cast onto a pre-heated steel plate.

Table 6-2.
$Mg(OH)_2$ waste loading into the clinoptilolite / sand base glasses, whether crystalline material was obtained from these glasses and the melting temperature.

	Base Glass										
	N10BS-70%			NL7.5BS-75%					NL15BS-67.5%		
MgO waste loading (wt%)	20	25	30	17.5	20	22.5	25	27.5	20	22.5	25
Forsterite in XRD	No	Yes	Yes	No	No	No	No	Yes	Yes	Yes	Yes
Crystalline Material at base	No	Yes	Yes	No	No	No	Yes	Yes	Yes	Yes	Yes
Melting Temperature (^{o}C)	1300			1300					1200		

In all cases the glass produced was lime in colour. One effect of $Mg(OH)_2$, on the base glasses NL7.5BS-75%, N10BS-70% and NL15BS-67.5%, was to decrease the viscosity significantly. This occurred up to the point forsterite crystals were observed, at which point the viscosity increased. There was little crucible corrosion evident (small amount at the melt line) for all glass compositions. For the NL7.5BS-75% series there were no secondary phases observed up to the Mg25NL7.5BS-75% composition where some crystals are observed at the base of the crucible. For Mg27.5NL7.5BS-75% composition some of the glass could be cast, but there was a significant quantity of undigested material left in the crucible. That which would cast had a high quantity of crystalline material suspended in the glass. For the N10BS-70% series there were no secondary phases up to the Mg25N10BS-70% composition were there were crystals suspended in the cast glass and undissolved material sintered at the base of the crucible. For the Mg30N10BS-70% composition the waste product formed a sintered crystalline mass incapable of being cast, with a glassy phase at the interface of the crucible. There were high levels of porosity, ranging from small bubbles (<1 mm) to larger bubbles (>5 mm), however the waste form was monolithic and was difficult to size-reduce. For the NL15BS-67.5% series forsterite was present in all glass compositions with a higher concentration of crystals observed as the concentration of $Mg(OH)_2$ increased. Crystals were suspended in the glass and sintered to the base of the crucible for all compositions, with a greater quantity of glass able to be cast from the Mg20NL15BS-67.5% composition and incrementally less as the $Mg(OH)_2$ concentration increases. None of the glasses produced in the NL15BS-67.5% series were suitable waste forms due to the non-monolithic, highly porous and heterogeneous nature of the waste products produced.

6.2.2 Phase Assemblage

The phase assemblage of clinoptilolite / sand base glasses, processed with $Mg(OH)_2$ were studied, using XRD and SEM-EDX.

6.2.2.1 XRD

Figure 6-1 shows the XRD for the N10BS-70% base glasses processed with $Mg(OH)_2$. Mg20N10BS-70% and Mg25N10BS-70% show broad diffuse scattering due to a major amorphous phase, whereas Mg30N10BS-70% has weak diffuse scatter with reflections from a crystalline phase, indicating a glass-ceramic material. These crystalline reflections are from forsterite (PDF 34-0189). Forsterite is also observed in M25N10BS-70%.

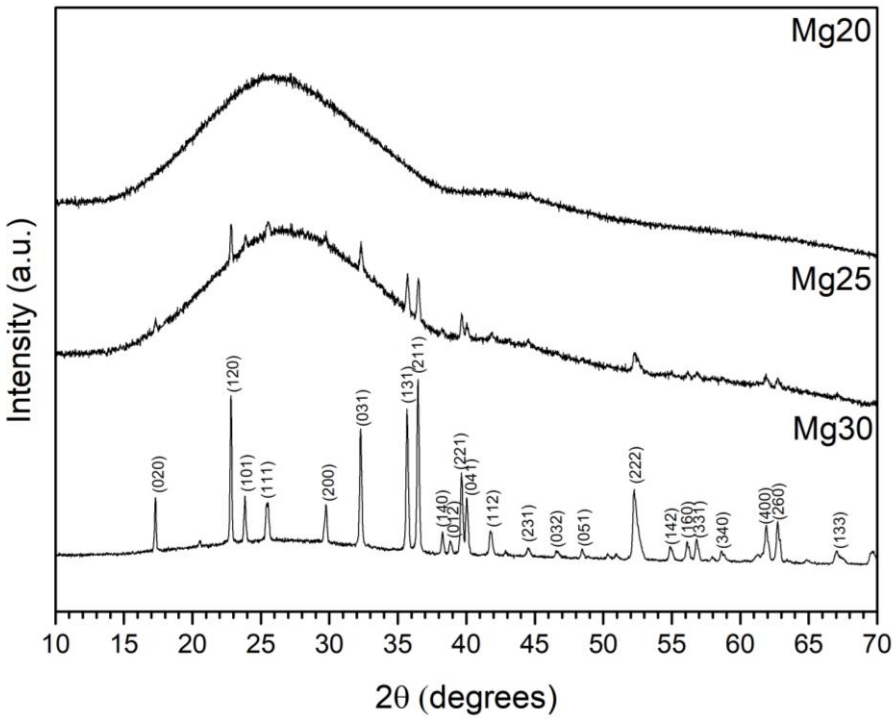

Figure 6-1. Powder XRD for sludge-loaded N10BS-70% base glasses processed with $Mg(OH)_2$.

Figure 6-2 shows the XRD data for the NL7.5BS-75% series of glasses processed with $Mg(OH)_2$. All glasses display broad diffuse scattering characteristic of a major amorphous phase. Mg17.5NL7.5BS-75%, Mg20NL7.5BS-75% and Mg27.5NL7.5BS-75% display minor reflections from quartz indicating incomplete digestion of the sand during the clinoptilolite/ sand base glass processing. Forsterite is only present in the XRD trace of Mg27.5NL7.5BS-75%. Figure 6-3 displays the XRD traces for NL15BS-67.5% glasses processed with $Mg(OH)_2$. All glasses display broad diffuse scattering characteristic of a major amorphous phase, as well as reflections from

forsterite. Forsterite is present in all glasses but is particularly strong in Mg25NL15BS-67.5%.

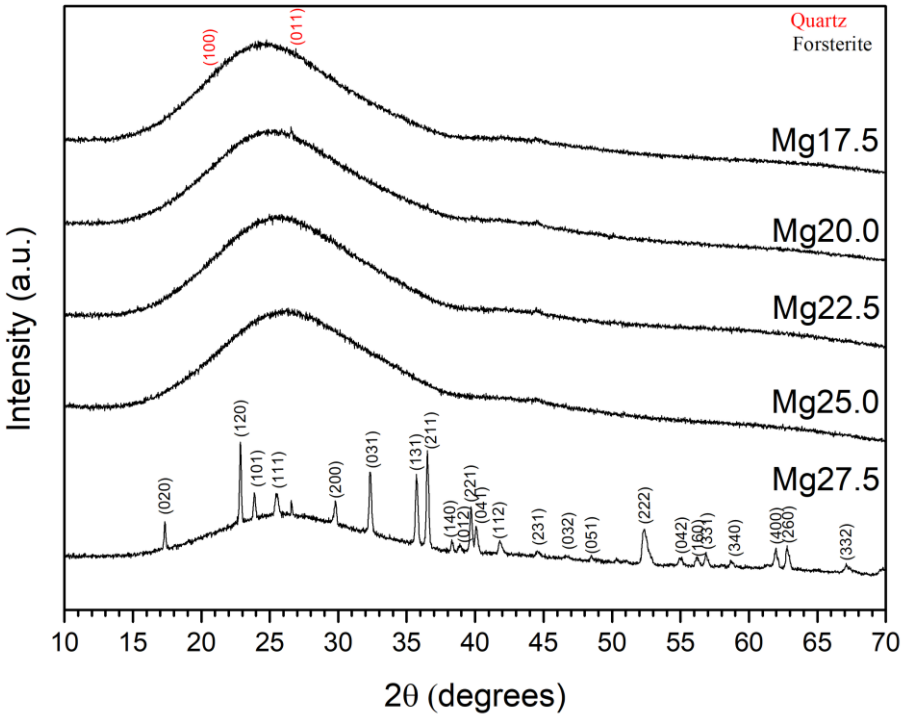

Figure 6-2. Powder XRD of the NL7.5BS-75% base glasses, processed with $Mg(OH)_2$.

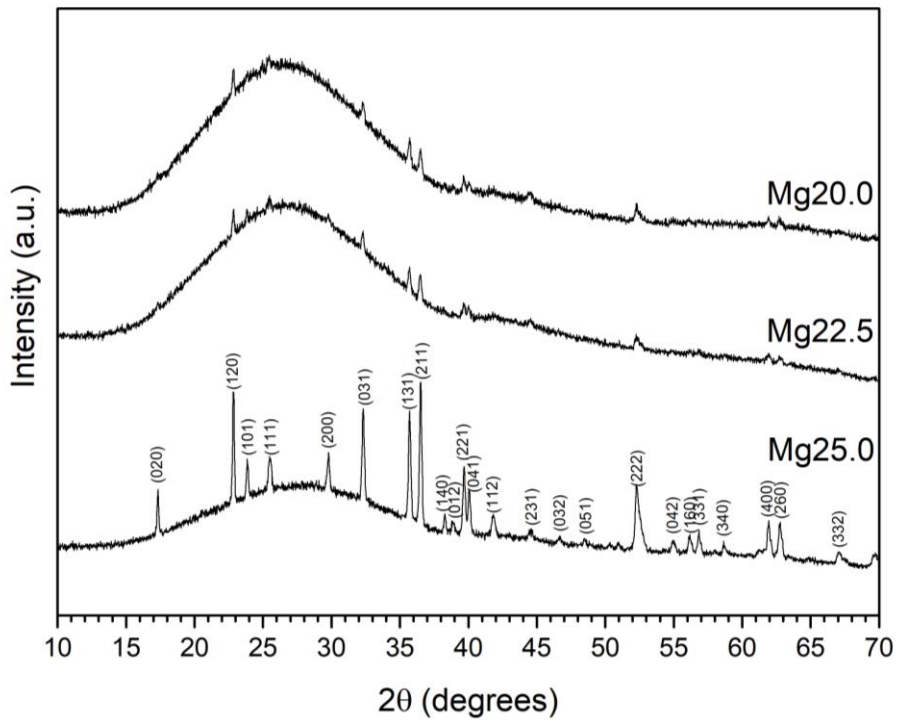

Figure 6-3. Powder XRD of the NL15BS-67.5% base glasses, processed with $Mg(OH)_2$.

6.2.2.2 SEM-EDX

SEM-EDX was used to characterise all clinoptilolite / sand base glass compositions processed with $Mg(OH)_2$, in particular, to identify any secondary phases. The glass phase is observed as a light grey phase. Figure 6-4 contains SEM-BSE images of forsterite crystals from each of the three base glass formulations in which forsterite is first observed to occur (i.e. the lowest MgO containing glasses at which forsterite is observed). The forsterite crystals have a columnar or tabular habit and the EDX spectra confirms that they are composed of Mg_2SiO_4 with a small amount of Na_2O detected from the residual glass.

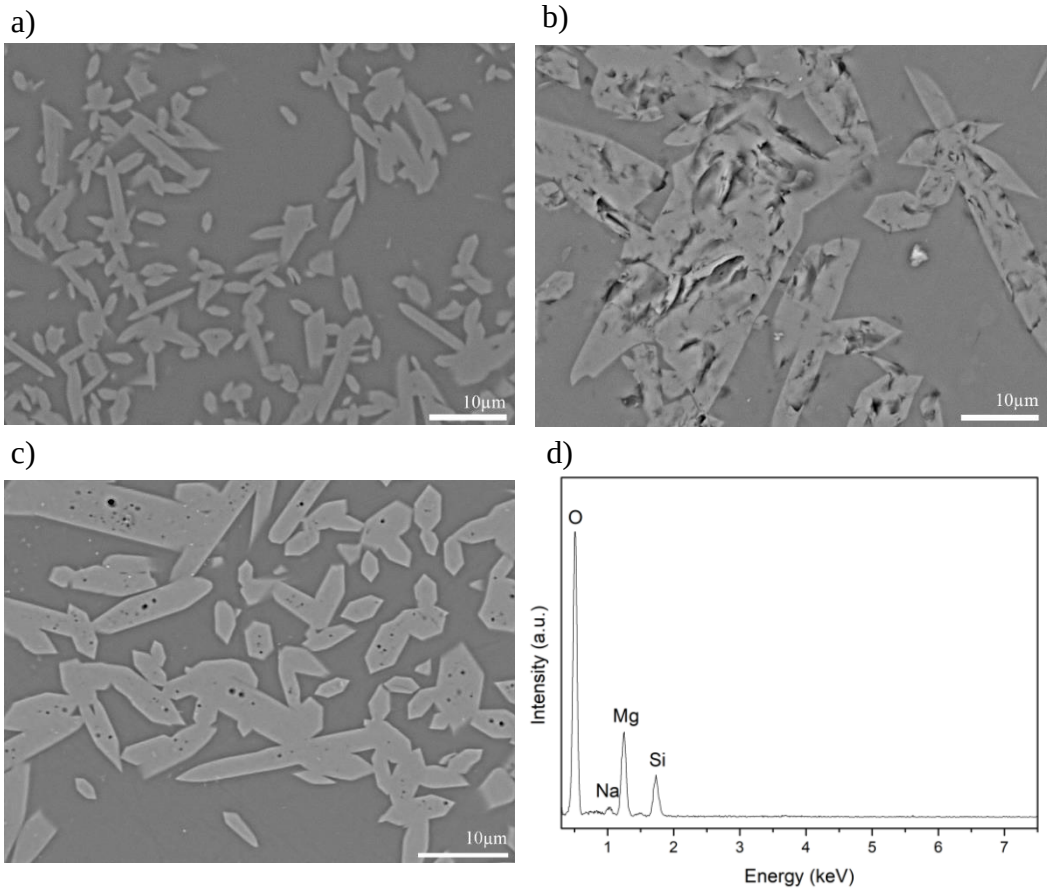

Figure 6-4. SEM-BSE images showing forsterite crystals embedded in glass phases from a) Mg30N10BS-70%, b) Mg27.5NL7.5BS-75% and c) Mg25NL15BS-67.5%. d) representative EDX spectrum of the forsterite phase.

6.2.3 NL7.5BS-75% Glass Series

The NL7.5BS-75% glass series processed with $Mg(OH)_2$ was studied further for two reasons: the first was that this series of glasses were produced without major forsterite crystallisation, up to Mg27.5NL7.5BS-75% (in contrast to the NL15BS-67.5% base glasses processed with $Mg(OH)_2$, which showed forsterite crystallisation in all glasses). The second was due to the higher waste loadings possible, before forsterite was detected, for the NL7.5BS-75% series, compared to the N10BS-70% glasses. These were 81 wt% for Mg25NL7.5BS-75% compared to 76 wt% for Mg20N10BS-70% (the two highest waste loading compositions in those series without forsterite present). Note in this section the descriptors are abbreviated, for example Mg17.5NL7.5BS-75%, is shortened to Mg17.5 and so on. The chemical composition of these glasses can be observed in Table 6-3.

Table 6-3.
As analysed compositions for the NL7.5BS-75% glasses processed with $Mg(OH)_2$, using total acid digest and ICP-OES analysis.

	Mg17.5		Mg20		Mg22.5		Mg25		Mg27.5	
	Wt%	Mol%	Wt%	Mol%	Wt%	Mol%	Wt%	Mol%	Wt%	Mol%
SiO_2	47.96 ± 1.44	47.50 ± 1.43	45.92 ± 1.38	44.93 ± 1.35	46.40 ± 1.39	44.24 ± 1.33	45.20 ± 1.36	42.23 ± 1.27	44.00 ± 1.32	40.83 ± 1.22
CaO	2.08 ± 0.07	2.21 ± 0.07	1.93 ± 0.06	2.02 ± 0.06	2.19 ± 0.07	2.24 ± 0.07	2.17 ± 0.07	2.17 ± 0.07	2.15 ± 0.07	2.14 ± 0.07
MgO	15.89 ± 0.48	23.46 ± 0.70	18.61 ± 0.56	27.15 ± 0.81	21.12 ± 0.63	30.02 ± 0.90	24.63 ± 0.74	34.30 ± 1.03	26.18 ± 0.79	36.21 ± 1.09
Na_2O	3.97 ± 0.12	3.81 ± 0.11	3.64 ± 0.11	3.45 ± 0.10	4.00 ± 0.12	3.70 ± 0.11	3.92 ± 0.12	3.55 ± 0.11	3.84 ± 0.12	3.45 ± 0.10
Al_2O_3	11.68 ± 0.35	6.82 ± 0.20	12.28 ± 0.37	7.08 ± 0.21	9.11 ± 0.27	5.12 ± 0.15	8.52 ± 0.26	4.69 ± 0.14	8.52 ± 0.26	4.66 ± 0.14
B_2O_3	14.67 ± 0.44	12.54 ± 0.38	14.30 ± 0.43	12.08 ± 0.36	13.80 ± 0.41	11.36 ± 0.34	12.23 ± 0.37	9.86 ± 0.30	11.81 ± 0.35	9.46 ± 0.28
Fe_2O_3	0.91 ± 0.04	0.34 ± 0.02	0.87 ± 0.04	0.32 ± 0.02	0.86 ± 0.04	0.31 ± 0.02	0.80 ± 0.04	0.28 ± 0.02	0.92 ± 0.04	0.32 ± 0.02
K_2O	1.49 ± 0.06	0.94 ± 0.03	1.18 ± 0.04	0.74 ± 0.02	1.15 ± 0.03	0.70 ± 0.02	1.24 ± 0.04	0.74 ± 0.02	1.25 ± 0.04	0.74 ± 0.02
Li_2O	1.13 ± 0.04	2.24 ± 0.07	1.07 ± 0.03	2.11 ± 0.06	1.09 ± 0.03	2.18 ± 0.07	1.10 ± 0.04	2.06 ± 0.06	1.10 ± 0.04	2.06 ± 0.06
Other	0.22 ± 0.02	0.14 ± 0.01	0.31 ± 0.02	0.12 ± 0.01	0.28 ± 0.02	0.13 ± 0.01	0.19 ± 0.02	0.12 ± 0.01	0.23 ± 0.02	0.13 ± 0.01

As can be observed the glasses are effectively Li_2O-Na_2O-K_2O-MgO-CaO-Fe_2O_3-Al_2O_3-B_2O_3-SiO_2 in composition. As the waste loading of $Mg(OH)_2$ increases into the base glasses, the main effects on the composition are an incremental increase in MgO, and incremental decreases in SiO_2, Al_2O_3 and B_2O_3. The lower concentration alkali ions CaO and Fe_2O_3 are effectively in error of one another.

6.2.3.1 Density

Figure 6-5 shows the relationship between density and mol% of MgO, for glasses in the NL7.5BS-75% series. As the mol% of MgO increases the density increases in a linear relationship (R^2 of 0.99) until the Mg27.5NL7.5BS-75% composition, where the density is higher than the line produced from linear regression. This is because of the high concentration of forsterite, which has a higher density, thus increasing the overall density of the waste form. Table 6-4 contains the measured densities.

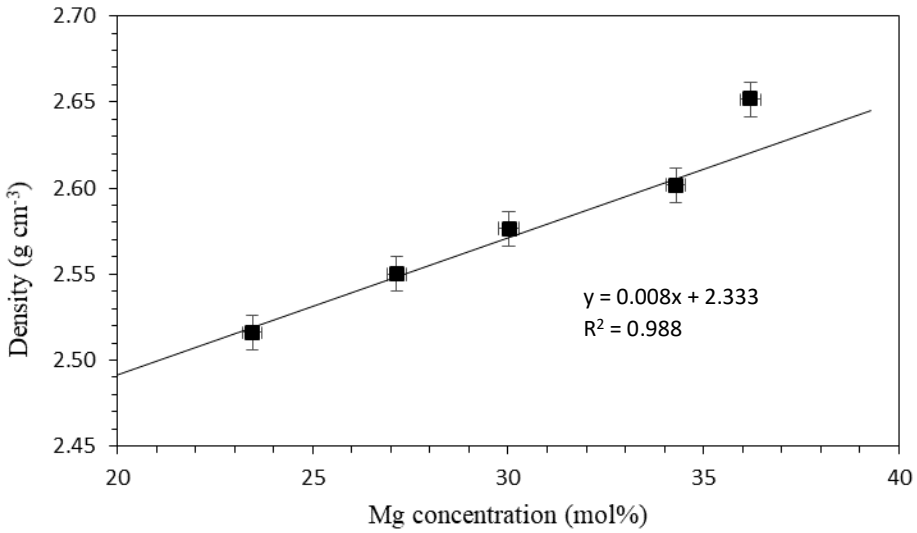

Figure 6-5. Measured densities of the glasses in the NL7.5BS-75% glasses processed with $Mg(OH)_2$.

Table 6-4.
Table showing the measured densities (± 0.02 kg dm^{-3}) of glasses from the NL7.5BS-75% composition range.

	Mg17.5	Mg20	Mg22.5	Mg25	Mg27.5
Density (kg dm^{-3})	2.52	2.55	2.58	2.60	2.65

6.2.3.2 DTA

Figure 6-6 shows DTA data from the NL7.5BS-75% series of glasses with four thermal events identified- a glass transition (T_g), a crystallisation event (T_{x1}), followed by another crystallisation event (T_{x2}), for two of the glasses only (Mg25 and Mg27.5NL7.5BS-75%), and a melting event (T_m). Table 6-5 contains the temperatures at which the events occur. The glass transitions are between the range of 558 and 566 ^oC for the compositions Mg17.5 to Mg25 and are in error of one another. However, the Mg27.5NL7.5-BS-75% has a lower T_g at 540 ^oC. As the concentration of MgO increases, the temperature of T_{x1} decreases by ~10 ^oC between each composition up to Mg25NL7.5BS-75% before a more significant drop of ~30 ^oC for Mg27.5NL7.5BS-75%. T_{x2} (for the Mg25 and Mg27.5BS-75% compositions) occurs at approximately the same temperature for both compositions, although its determination is complicated due to its overlap with T_{x1} for Mg25NL7.5BS-75%. The melting temperatures (T_m) are within error of one another for the Mg17.5 to Mg25NL7.5BS-75% compositions, but decrease for the Mg27.5NL7.5BS-75% composition, by 25 ^oC.

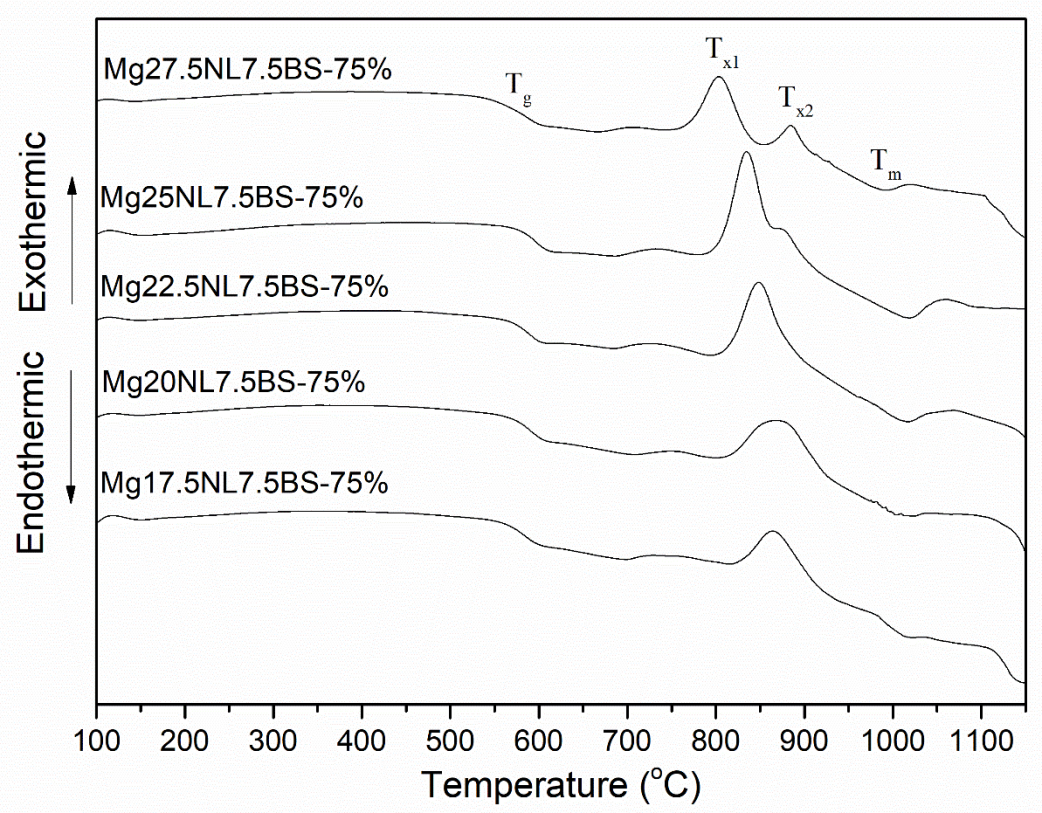

Figure 6-6. DTA of the five glasses in the NL7.5BS-75% series, with the four thermal events labelled on the top trace.

Table 6-5.
Temperatures of thermal events identified from DTA traces.

	$T_g \pm 5$ °C	$T_{x1} \pm 5$ °C	$T_{x2} \pm 10$ °C	$T_m \pm 5$ °C
Mg17.5	558	820	/	1015
Mg20	561	807	/	1014
Mg22.5	560	799	/	1010
Mg25	566	787	855	1012
Mg27.5	540	759	858	987

6.2.3.3 Raman Spectra

Raman spectra were collected between 200 and 1200 cm^{-1} for glasses in the NL7.5BS-75% series, see Figure 6-7. The main changes in the glass structure are in the regions between 850 and 1200 cm^{-1}, providing information on Si speciation and between 400 and 550 cm^{-1} due to changes in the silicate ring structure of the glass [14]–[17]. The

shoulder at ~480 cm^{-1} is associated with 5 and 6 membered Si rings and it is observed that there is a decrease in the intensity of this feature as the concentration of Mg in the glass increases, particularly through the Mg17.5 to Mg25NL7.5BS-75% composition. There are also changes in the silicate polymerisation which can be observed between 850 and 1200 cm^{-1}.

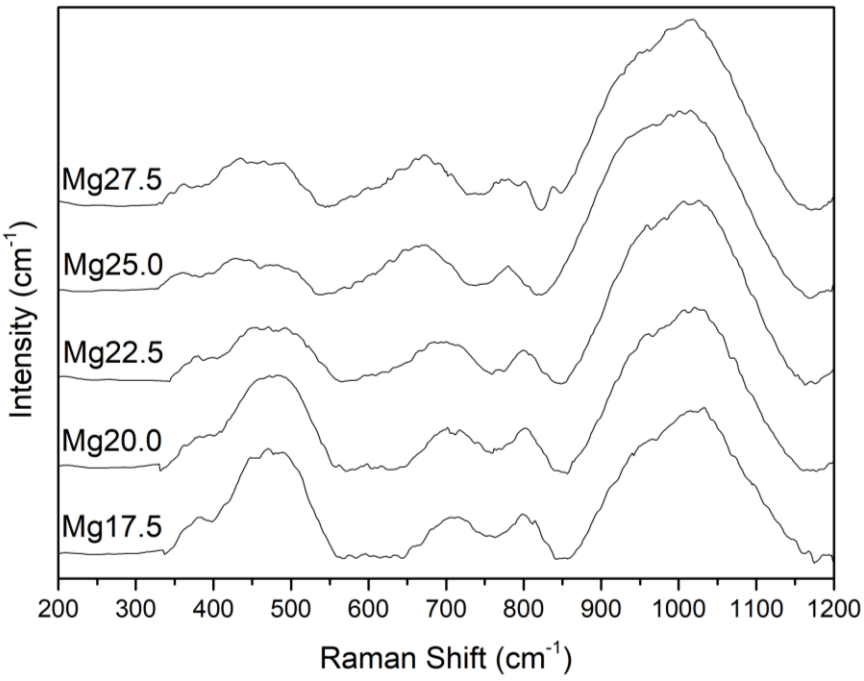

Figure 6-7. Raman spectra of NL7.5BS-75% series of glasses.

To quantify the changes in the silicate polymerisation, Gaussian curves were fitted to the Raman bands between 850 and 1200 cm^{-1} in order to quantify the Q speciation of the glasses, see Figure 6-8. The following procedure was used: the peak wavenumbers were first fixed, using values reported in the literature, but the widths and intensities were kept as independent and unconstrained variables [14], [15], [18]. Then, once the fit was acceptable, the peak wave numbers were retained as initial values for a final curve fitting, in which they were also unconstrained variables. As can be observed the increasing mol% of Mg and the decreasing mol% of Si causes a decrease in the silica polymerisation. For Mg17.5NL7.5BS-75% the Q_3 speciation is at 79% and the Q_2 speciation is at 21%, see Table 6-6. The Q_3 species incrementally decreases to the Mg25NL7.5BS-75% where the Q_3 speciation is at 66% and the Q_2 speciation is at 34%. For the Mg27.5NL7.5BS-75% (for Raman analysis of the glass phase) the Q_3 speciation is at 72% whereas the Q_2 species is at 28%. This is due to the forsterite crystals, which alter the composition of the glass and, therefore, the polymerisation.

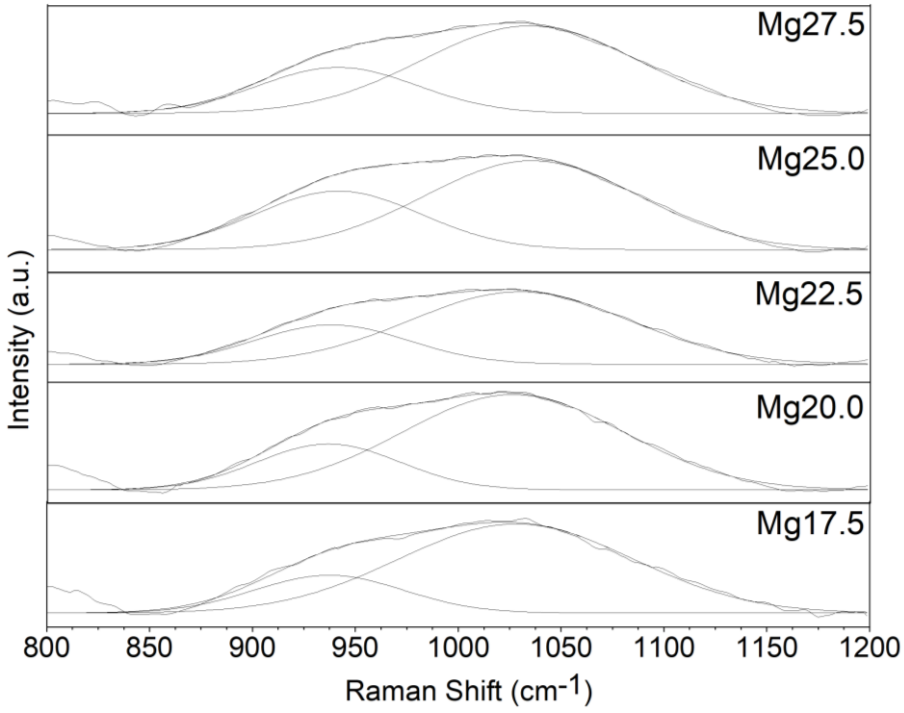

Figure 6-8. Fitting of Raman spectra between 850 and 1200 cm^{-1} using two Gaussian peaks.

Table 6-6.
Fit parameters for Raman bands in the 850-1200 cm^{-1} region for the NL7.5BS-75% series of glasses. Wavenumbers are ± 5 cm^{-1} and areas are ± 2%.

Raman Band	Q_3			Q_2		
Glass	Position (cm^{-1})	Width (cm^{-1})	Area (%)	Position (cm^{-1})	Width (cm^{-1})	Area (%)
Mg17.5	1028	134	78.8	937	85	21.2
Mg20.0	1026	126	76.3	937	82	23.7
Mg22.5	1030	125	72.5	938	88	27.5
Mg25.0	1035	122	66.2	941	95	33.8
Mg27.5	1034	125	72.2	941	91	27.8

6.2.4 Crystallised Glass

Mg22.5NL7.5BS-75% was selected to study the effect of crystallisation of magnesium silicate phases (in particular forsterite) on the properties of the waste form. In Section 6.2.3, it was demonstrated that increasing the ratio of $Mg(OH)_2$ to base glasses decreases the concentration of SiO_2, Al_2O_3 and B_2O_3. Two samples of the same composition, but where one is partially crystallised and one is amorphous, were produced in order to understand the effect of forsterite crystallisation on glass properties. This composition was selected as it was the highest waste loading composition, in the NL7.5BS-75% glass series, that didn't contain any forsterite in the XRD trace, nor have any forsterite remaining in the crucible, see Table 6-2. The sample was heat treated (at 3 $^oC\ min^{-1}$) to 900 ^oC (judged to be ~100 ^oC above the crystallisation temperature) and left at this temperature for 24 h, before slow cooling in the furnace. It was observed that after heat treatment the block of glass had swelled and become opaque, with the surface turning dark yellow and the material in the centre white upon cross-section. The chemical composition of the crystallised Mg22.5NL7.5BS-75% (termed crysMg22.5NL7.5 hereafter) was determined using the total digest and ICP-OES analysis as described in Section 3.10 and is shown in Table 6-7. Along with the crysMg22.5NL7.5 composition, the Mg22.5NL7.5 composition is also presented to enable a comparison of their compositions. As can be observed all

oxides are in error of another. Note that "others" includes impurities (predominantly ZrO_2, TiO_2, BaO, MnO and SrO) of which different proportions contribute to the total, this is the reason for the difference in mol% of the two samples.

Table 6-7.
Analysed chemical compositions of Mg22.5 and crysMg22.5NL7.5BS-75% compositions.

	Mg22.5NL7.5		CrysMg22.5NL7.5	
	Wt%	Mol%	Wt%	Mol%
SiO_2	46.40 ± 1.39	44.24 ± 1.33	46.46 ± 1.39	44.35 ± 1.33
CaO	2.19 ± 0.07	2.24 ± 0.07	2.21 ± 0.07	2.26 ± 0.07
MgO	21.12 ± 0.63	30.02 ± 0.90	21.02 ± 0.63	29.91 ± 0.9
Na_2O	4.00 ± 0.12	3.70 ± 0.11	3.89 ± 0.12	3.60 ± 0.11
Al_2O_3	9.11 ± 0.27	5.12 ± 0.15	9.35 ± 0.28	5.26 ± 0.16
B_2O_3	13.80 ± 0.41	11.36 ± 0.34	13.79 ± 0.41	11.36 ± 0.34
Fe_2O_3	0.86 ± 0.04	0.31 ± 0.02	0.82 ± 0.04	0.30 ± 0.01
K_2O	1.15 ± 0.03	0.70 ± 0.02	1.16 ± 0.03	0.70 ± 0.02
Li_2O	1.09 ± 0.03	2.18 ± 0.07	1.11 ± 0.03	2.13 ± 0.06
Others	0.28 ± 0.02	0.13 ± 0.01	0.19 ± 0.02	0.13 ± 0.01

6.2.4.1 XRD and Rietveld

To identity and quantify the crystalline phases in crysMg22.5NL7.5, powder XRD with Rietveld refinement and SEM-EDX were used. Figure 6-9 shows the XRD spectrum for crysMg22.5NL7.5; as can be observed there still remains broad diffuse scatter indicating that the glass phase is still the major phase. However, the glass is now partially crystallised with two major phases identified- forsterite and enstatite. There are also minor phases of periclase and diopside present as well some reflections from an unidentified minor phase(s).

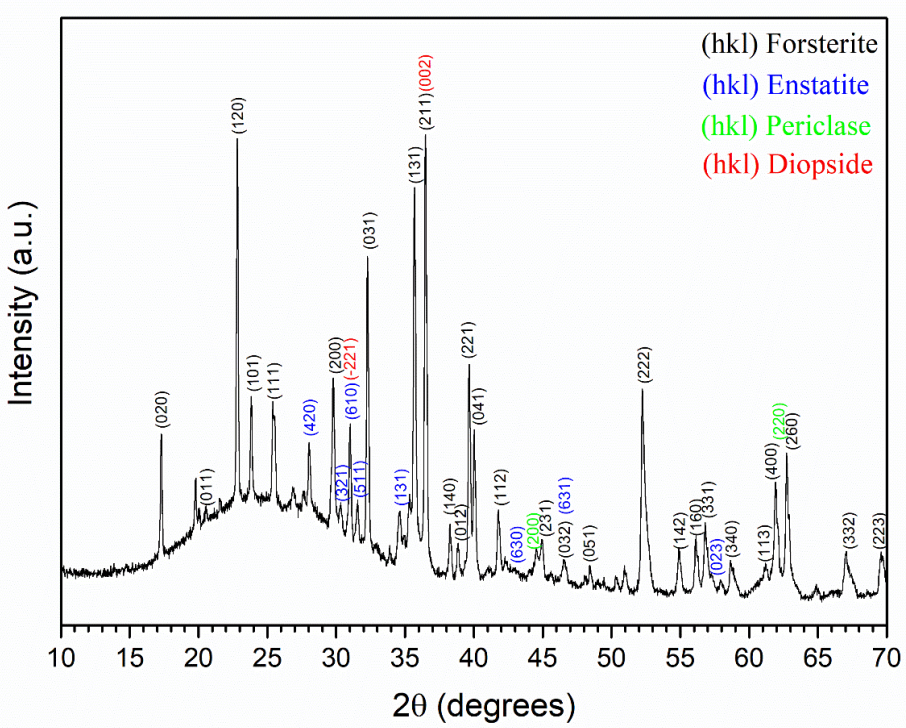

Figure 6-9. Powder XRD of crysMg22.5NL7.5 with major reflections from forsterite, enstatite and periclase indexed.

Figure 6-10 show the fit obtained from Rietveld refinement of the XRD trace for crysMg22.5NL7.5 along with the difference plot underneath. As can be observed, the major phase is an amorphous phase quantified at 62 ±5%, with the major crystalline phase being forsterite at 24 ±3%, followed by minor phase enstatite (6 ±3%), diopside (4 ±4%) and periclase (4 ±4%). This fit gave a weighted profile R-factor (R_{wp}) of 5.0, an expected R factor (R_{exp}) of 2.3 and a χ^2 of 2.2 indicative of a relatively good fit for a complex XRD pattern [19]. The process of refinement is given in Section 3.5.2. Note there are reflections present in the Rietveld fit, not present in Figure 6-9, originating from silicon used as an internal standard. The main sources of the differences between the fit and the actual data (at ~28.5^o and ~47.5^o) originate from the Si reflections, hence the relatively large error associated with this value for quantifying the amorphous phase.

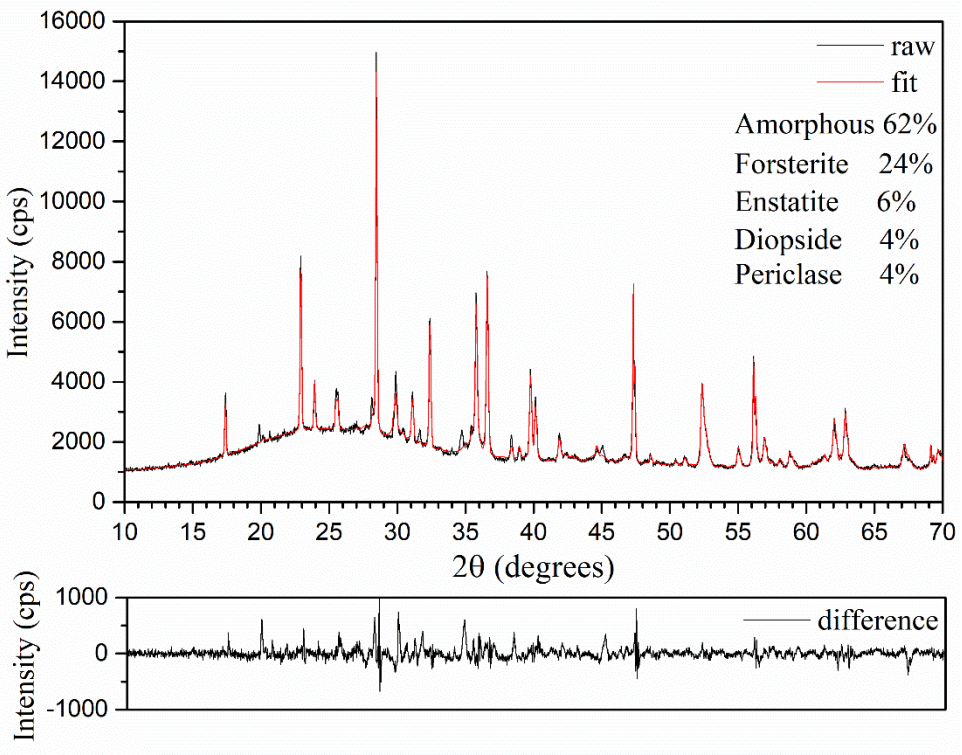

Figure 6-10. Graph showing Rietveld refinement fit of powder XRD pattern for crysMg22.5NL7.5, as well as the difference pattern.

6.2.4.2 SEM-EDX

Figure 6-11 contains SEM-BSE images and EDX spectra of crysMg22.5NL7.5. The microstructure consists of a partially crystalline material with a residual amorphous phase, containing predominant regions of forsterite crystals and interspersed regions of enstatite, periclase and diopside crystals. Forsterite crystals have a columnar or tabular habit. Enstatite crystals are long, thin and jagged, whereas periclase crystals are circular (~5 µm diameter) and are the dark crystals in Figure 6-11c. Diopside crystals are not uniformly distributed, but are found in the enstatite and periclase-rich regions having a lighter contrast (due to the presence of the relatively higher atomic number of Ca). They are associated with the enstatite crystals. EDX spectra of forsterite (Mg_2SiO_4), enstatite ($MgSiO_3$) and periclase (MgO) are included, unfortunately, due to their small size an EDS spot of diopside ($MgCaSi_2O_6$) was not possible. Forsterite and enstatite have some minor background signal from Na and Al originating from the glass. Periclase contains some background from Si, also from the glass. It's likely that the Ca content varies along the enstatite-diopside join and partially substitutes up to 50% of the Mg.

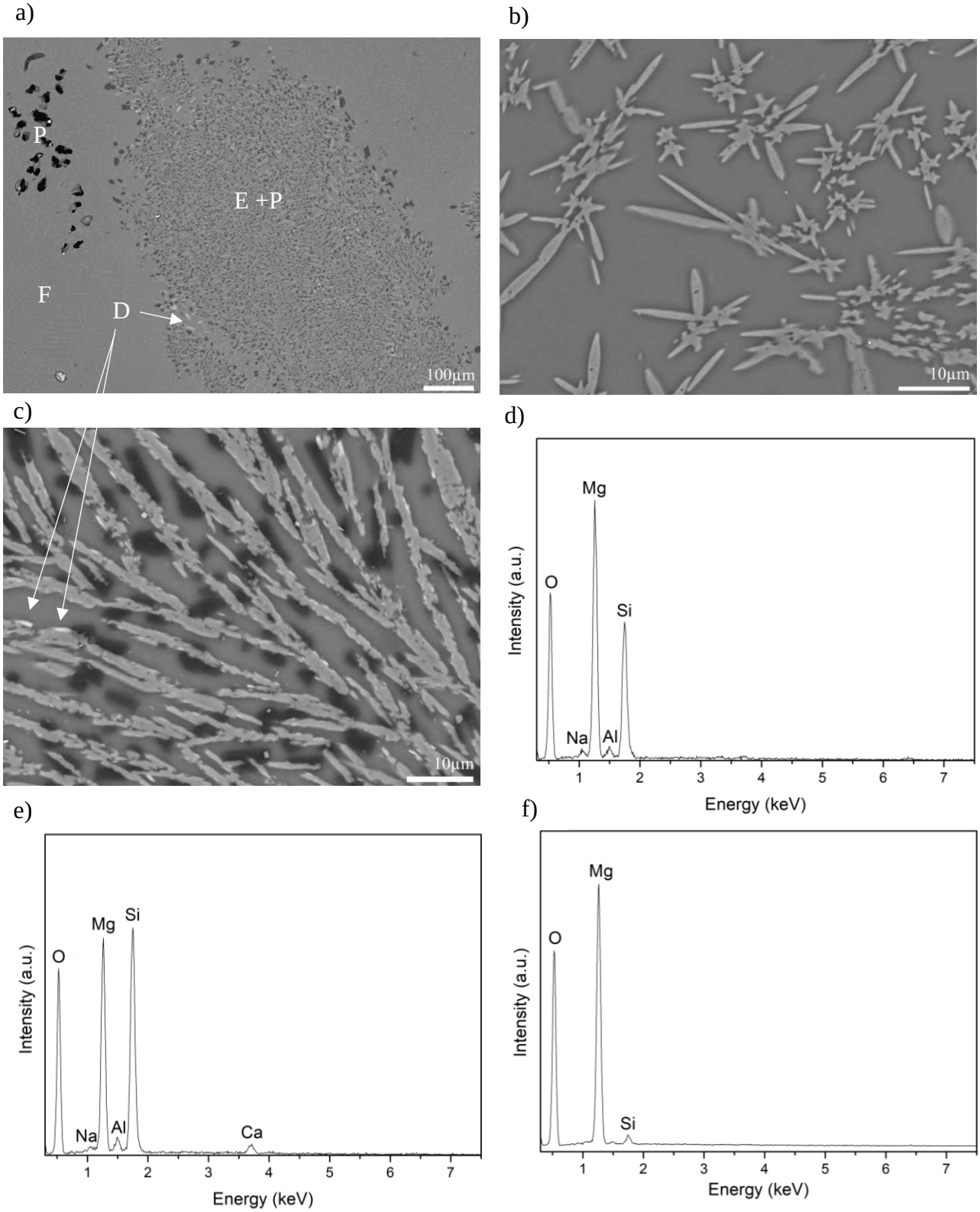

Figure 6-11 a) Low magnification SEM-BSE image showing microstructure of crysMg22.5NL7.5, F = forsterite, E+P = enstatite + periclase, D = diopside and P = porosity, b) forsterite crystals, c) enstatite crystals and periclase crystals, d) EDX spectrum of forsterite, e) EDX spectrum of enstatite and f) EDX spectrum of periclase.

6.2.5 Glass Dissolution

The short-term (28 days) chemical durability of glass compositions Mg22.5NL7.5 and crysMg22.5NL7.5 were investigated using the PCT-B test protocol, in deionised water, at 50 ^{o}C. This was to determine the impact of crystalline Mg silicate phases on the durability of a glass, for a given composition. As can be observed in Table 6-7 the concentration of all oxides of both Mg22.5NL7.5BS-75% and crysMg22.5NL7.5 are within error of one another. Figure 6-12 shows NL_B, NL_{Ca}, NL_K, NL_{Li}, NL_{Na}, NL_{Mg}, NL_{Si} and pH for the two samples over the 28 days. Both samples dissolved incongruently with $NL_{Li} > NL_K > NL_B > NL_{Na} > NL_{Ca} > NL_{Mg} > NL_{Si,}$ with NL_{Mg} and NL_{Si} an order of magnitude less than other tracer elements, indicating precipitation from solution. The dissolution rate is rapid during the first four days before tailing off during the final 21 days; this is due to the residual rate regime being reached. Ca and Si are both close to the detection limit of the detector and, therefore, there is a lot of variation in the data points. Al was not detected in solution, due to the precipitation of $Al(OH)_3$ (likely as gibbsite) occurring at this pH. NL_{Si} decreases during the course of the experiment indicating it becomes less soluble as other elements from the glass are leached. There is no evidence of rate resumption. For all tracer elements Mg22.5NL7.5 was less durable than crysMg22.5NL7.5 indicating that the crystallisation of Mg silicate phases, in particular forsterite, increases the durability of the overall waste form. The pH of the leachate for Mg22.5NL7.5 is between 9.5 and 9.6 during the first 14 days, before dropping slightly for the final two time points, finishing at 9.1 at day 28. For crysMg22.5NL7.5 the pH is much more variable during the course of the experiment varying between pH 8.8 and 9.2. Figure 6-11 shows the heterogeneity of this sample and it may be that different proportions of each phase are present in each of the crysMg22.5NL7.5 test vessels. Over 7 days the normalised release rates (g m^{-2} day^{-1}) for Mg22.5NL7.5 for Li is 0.23 for K is 0.12 for B is 0.08 for Na is 0.06 and for Si is 0.002. For crysMg22.5NL7.5 the normalised release rates are Li 0.03, for K is 0.01, for B is 0.009, for Na is 0.005 and for Si is 0.0001.

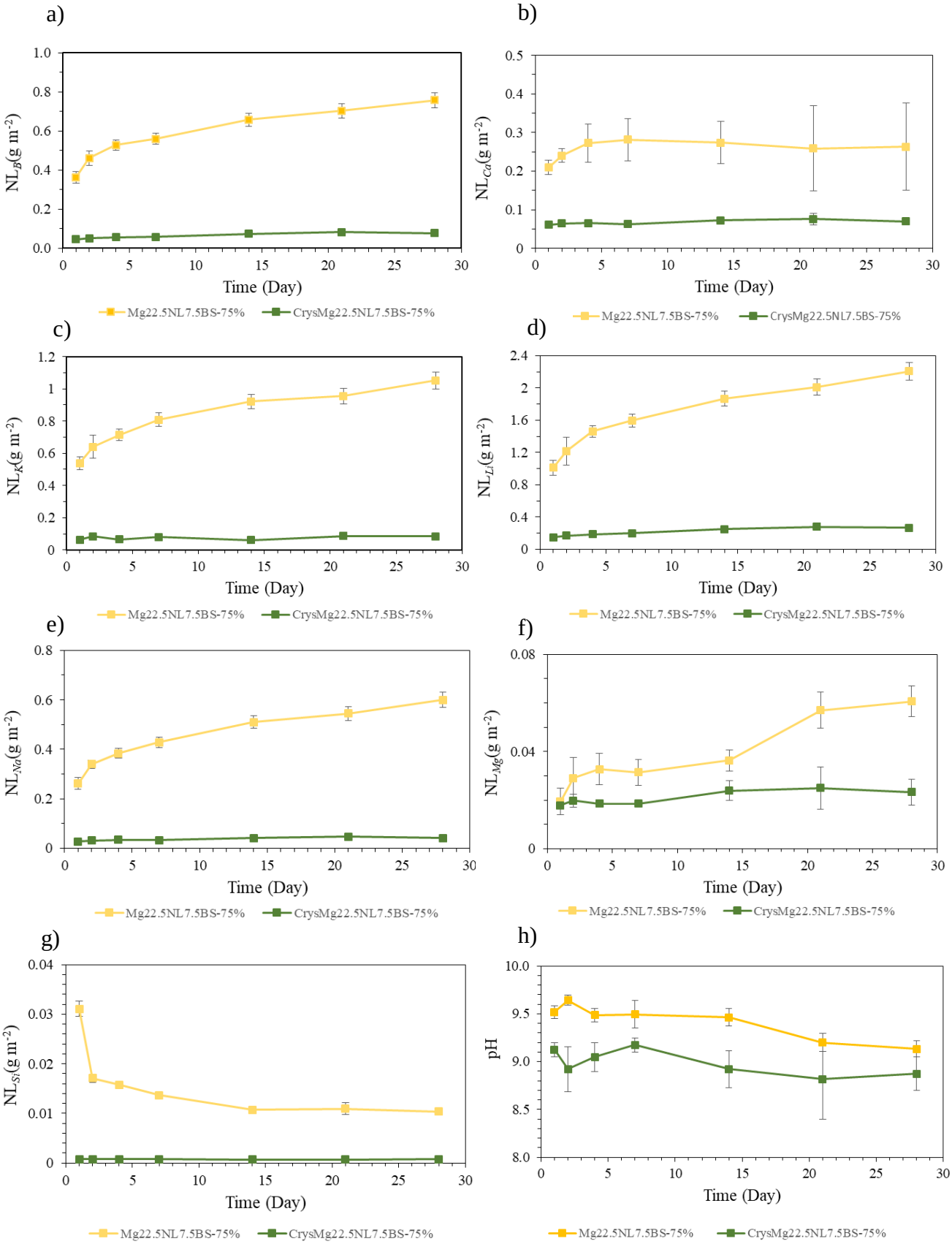

Figure 6-12. Normalised mass losses for Mg22.5NL7.5BS-75% (yellow) and crysMg22.5NL7.5BS-75% (green) for a) NL_B, b)NL_{Ca}, c) NL_K, d)NL_{Li}, e) NL_{Na}, f) NL_{Mg}, g) NL_{Si} and h) pH.

Figure 6-13 shows SEM-BSE images and EDX scans of altered glass particles. A clear alteration layer can be observed for Mg22.5NL7.5, however, no alteration layer could be discerned for crysMg22.5NL7.5. This corroborates with low NL_x for this sample, indicating that waste form alteration is minimal. For Mg22.5NL7.5 the alteration layer is uniform and thin (~ 1 μm thick) and is composed of Si and Mg with some minor traces of Al and K. For crysM22.5NL7.5 there is evidence of some corrosion, see Figure 6-13c, demonstrating where the glass has been corroded and Figure 6-13d highlighting how the glass has been attacked, but the crystals of forsterite remain resisting corrosion. The crystals of forsterite effectively creating a front at which alteration is limited.

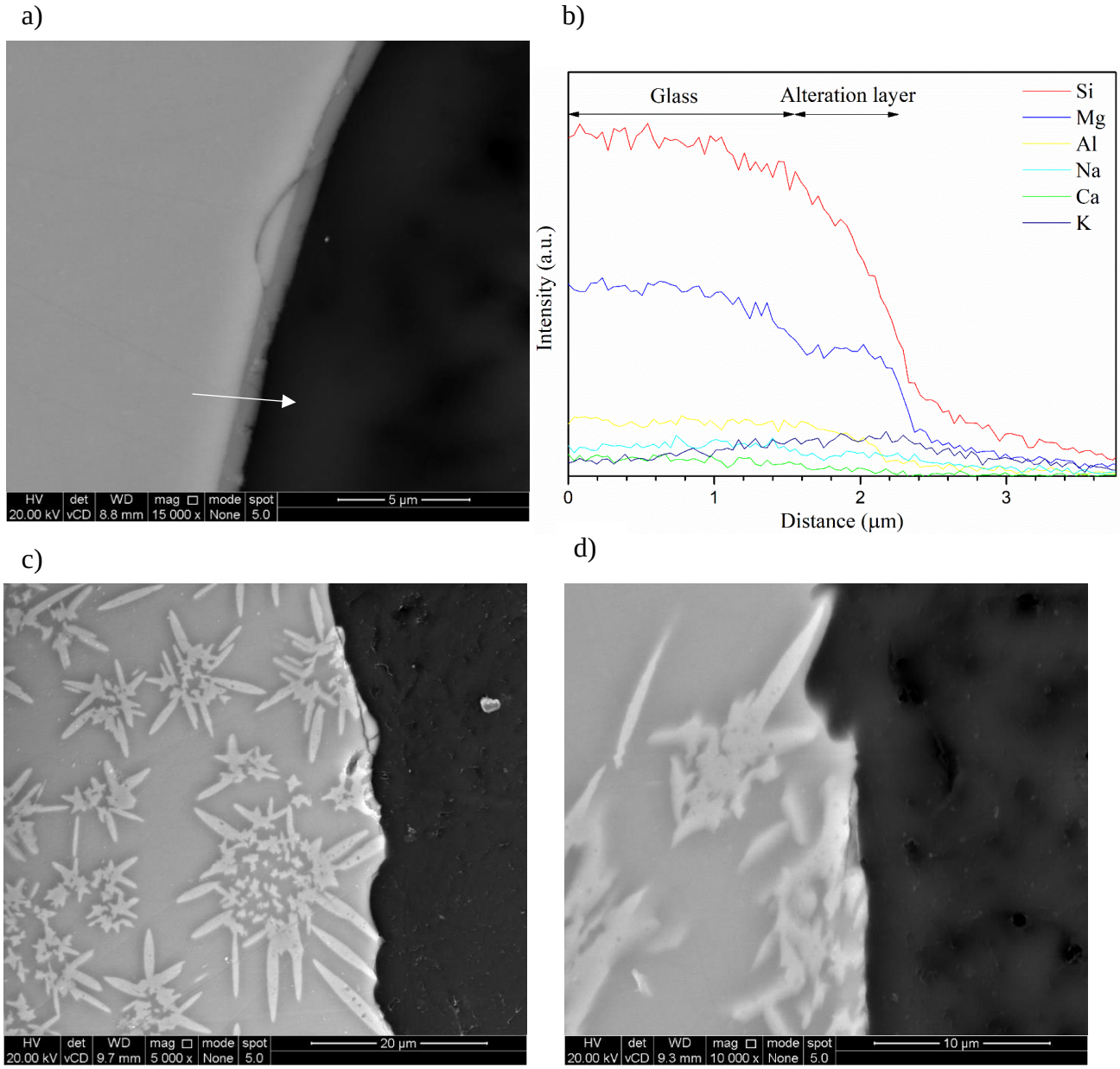

Figure 6-13 a) SEM-BSE image of glass and alteration layer of Mg22.5NL7.5BS-75%, b) EDX line scan across Mg22.5NL7.5BS-75%, c) an altered particle of crysMg22.5NL7.5BS-75% and d) a higher magnification image of an altered crysMg22.5NL7.5BS-75% glass particle.

6.2.6 U-Containing Glasses

In previous sections within this chapter, to account for the sludge waste, $Mg(OH)_2$ was used. This is because this species is the highest concentration constituent of the sludge [3], [11]. In this section, glass compositions were produced with a more representative simulant for BST sludge. However it should be reiterated that this data is the best estimate available, and it is clear that the sludges remain poorly characterised. Nonetheless this data was used and the composition can be seen in Table 6-8. Note the samples were spiked to give 0.5 wt% Cs_2O and 0.5 wt% SrO to observe how these fission products would be retained in the glass, as Table 2-6 shows these are two of the biggest contributors to the specific activity of the sludge.

$Mg(OH)_2$ was from Alfa Aesar (95-100.5% purity), U_3O_8 was from The British Drug Houses Ltd (BDH) (estimated 95% purity), $Ca(OH)_2$ was from Acros Organics (98% purity), NaCl was from Laboratory FSA supplies (99.5% purity), KCl was from Sigma Aldrich (99% purity), Na_2SO_4 was from Alfa Aesar (99% purity), K_2SO_4 was from Sigma Aldrich (99% purity), Cs_2CO_3 was from Acros Organics (99.5% purity) and $SrCO_3$ was from Fisher (98% purity).

Table 6-8.
Reagents used to produce simulant sludge.

Reagent	Sludge Simulant (wt%)
$Mg(OH)_2$	75.16
U_3O_8	38.08
$Ca(OH)_2$	4.78
NaCl	2.41
KCl	2.48
Na_2SO_4	0.75
K_2SO_4	0.72

The sludge was produced by weighing the above to four d.p. $Mg(OH)_2$ and $Ca(OH)_2$ were added to give 51.94 wt% and 3.62 wt% of MgO and CaO respectively. NaCl, KCl, Na_2SO_4 and K_2SO_4 were dried for 24 h at 180 ^oC prior to batching. These were then mixed with the $Mg(OH)_2$ and $Ca(OH)_2$ for 10 mins by hand. U_3O_8 was not added

to the simulant sludge initially but was added to the pre-mixed starting reagents, within the crucible, in three batches with mixing in between each addition. The two glass compositions can be seen in Table 6-9. The NL7.5BS-75% clinoptilolite / sand base glass composition was selected for the same reasons as outlined in section 6.2.3.

Table 6-9.
Composition of glass batches for representative sludge with NL7.5BS-75% clinoptilolite / sand waste base glass melting.

Reagent	UMg42.8NL7.5BS-75%	UMg34.2NL7.5BS-75%
NL7.5BS-75%	56.16	64.83
Simulant Magnox sludge	42.84	34.17
Cs_2CO_3	0.578	0.578
$SrCO_3$	0.712	0.712

NL7.5BS-75% glass frit and the simulant Magnox sludge (excluding the U_3O_8 content) were weighed to 3 d.p. and mixed by hand for 10 mins in a plastic bag. The Cs_2CO_3 was dried at 180 ^oC for 24 h, and then weighed, along with the $SrCO_3$ to 3 d.p. and mixed together, with the above, for 10 min, in a plastic bag. This was then poured into a mullite crucible and packed down. The U_3O_8 from the sludge simulant was added directly to the crucible and mixed together using a spatula. The samples were heated to 1300 ^oC at 3 ^oC min^{-1}, dwelled for 2 h, before quenching onto a mild steel casting plate. After the glass had cooled sufficiently for it not to flow, it was transferred to an annealing furnace at 580 ^oC for 1 h, before cooling at 1 ^oC min^{-1}.

The glass composition UMg42.8NL7.5BS-75% forms a dark black glass with some material sintered to the base of the crucible. The low viscosity of the glass meant that some of this material was suspended and cast with it. There is crucible corrosion at the melt line; by measuring the thickness at the melt line, at 10 different places, it was estimated that 35.0 ± 6.0% of the material had corroded. Similarly, UMg34.2NL7.5BS-75% forms a dark black glass, with no residual batch material at the base. Again crucible corrosion is evident at the melt line, by measuring the thickness at the melt line at 10 different places, it was estimated that 35.0 ± 4.0% of the material had corroded. UMg42.8NL7.5BS-75% had a notably lower viscosity than

UMg34.2NL7.5BS-75%. Figure 6-14 displays photographs of UMg34.2NL7.5BS-75% (also representative of UMg42.8NL7.5BS-75%) and the base of the crucible of UMg42.8NL7.5BS-75%, with the severe corrosion at the melt line visible. For the rest of this chapter, for brevity, UMg34.2NL7.5BS-75% will be abbreviated as UMg34.2 and UMg42.8NL7.5BS-75% will be abbreviated as UMg42.8.

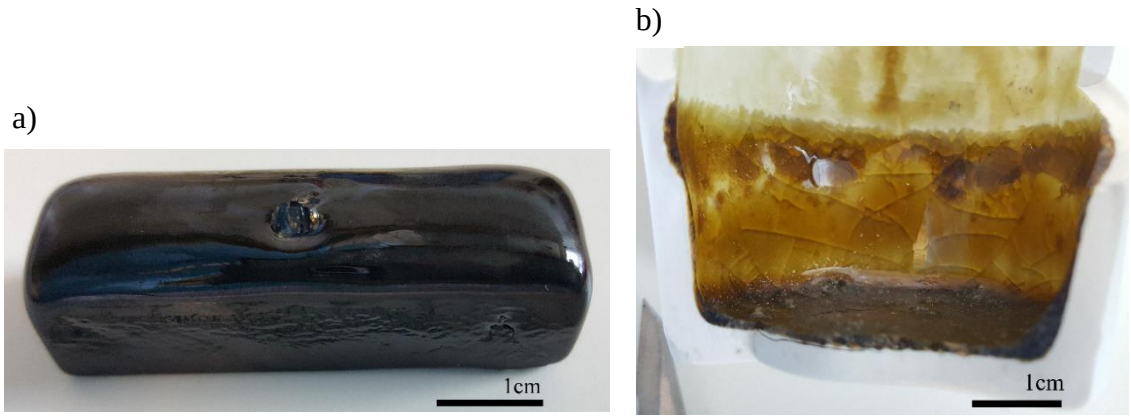

Figure 6-14. a) Photograph of UMg34.2 glass and b) base of UMg42.8 showing forsterite sintered to the base of the crucible.

Table 6-10 shows the as analysed compositions of UMg34.2 and UMg42.8, the glasses are effectively (99.1 mol% for UMg34.2 and 96.9 mol% for UMg42.8) Li_2O- Na_2O- K_2O- MgO- CaO- U_3O_8- B_2O_3- Al_2O_3- SiO_2 glasses. The major differences in compositions are that UMg42.8 has an additional 5 mol% of MgO and 5.67 mol% less of SiO_2 than UMg34.2. It must be noted that UMg42.8 composition is slightly contaminated with ~1.3 mol% of TiO_2 and ~0.9 mol% ZrO_2 and slightly less U_3O_8 than batched indicating slight contamination of the U_3O_8 used for this composition.

Table 6-10.
Analysed compositions of the representative sludge glass melts.

	UMg34.2		UMg42.8	
Oxide	Wt%	Mol%	Wt%	Mol%
SiO_2	41.95 ± 1.26	44.63 ± 1.34	37.40 ± 1.12	38.96 ± 1.17
CaO	2.88 ± 0.09	3.28 ± 0.10	3.54 ± 0.11	3.95 ± 0.12
MgO	16.88 ± 0.51	26.77 ± 0.80	20.44 ± 1.02	31.74 ± 1.59
Na_2O	3.42 ± 0.10	3.52 ± 0.11	2.92 ± 0.09	2.94 ± 0.09
Al_2O_3	7.85 ± 0.24	4.92 ± 0.15	7.37 ± 0.22	4.52 ± 0.14
B_2O_3	11.56 ± 0.35	10.61 ± 0.32	11.46 ± 0.34	10.30 ± 0.31
U_3O_8	11.12 ± 0.33	2.41 ± 0.07	9.42 ± 0.47	1.99 ± 0.10
Fe_2O_3	0.76 ± 0.04	0.31 ± 0.02	0.63 ± 0.03	0.25 ± 0.01
K_2O	1.52 ± 0.05	1.03 ± 0.03	1.40 ± 0.04	0.93 ± 0.03
TiO_2	0.16 ± 0.01	0.13 ± 0.01	1.87 ± 0.09	1.47 ± 0.04
SrO	0.48 ± 0.02	0.30 ± 0.01	0.47 ± 0.02	0.28 ± 0.01
ZrO_2	0.13 ± 0.01	0.07 ± 0.01	1.92 ± 0.10	0.98 ± 0.05
Cs_2O	0.30 ± 0.02	0.07 ± 0.01	0.35 ± 0.02	0.08 ± 0.00
Li_2O	0.89 ± 0.04	1.90 ± 0.10	0.75 ± 0.04	1.56 ± 0.08
Others	0.10 ± 0.01	0.05 ± 0.00	0.06 ± 0.00	0.05 ± 0.00

6.2.6.1 Phase Assemblage

UMg34.2 and UMg42.8 were studied using XRD and SEM-EDX to characterise the amorphous and any crystalline phase(s) present in the waste forms. Figure 6-15 contains the powder XRD for both UMg42.8 and UMg34.2, both traces display broad diffuse scatter consistent with a major amorphous phase. UMg34.2 is completely amorphous, whereas UMg42.8 has minor reflections from forsterite (PDF 00-34-0189).

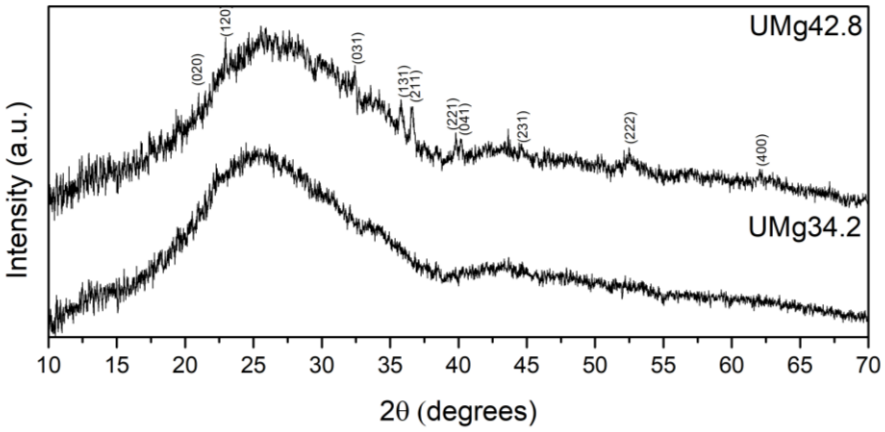

Figure 6-15. Powder XRD patterns for UMg42.8 and UMg34.2.

Figure 6-16 shows SEM-BSE images and EDX scans of the glass from UMg34.2 and UMg42.8. There are no regions of contrast in UMg34.2, showing no secondary phases. The EDS shows that uranium is incorporated into the glass structure. For UMg42.8 there are forsterite crystals present, embedded in the glass matrix. The crystal have a columnar or tabular habit, are dark and the glass phase lighter than in Figure 6-4 and Figure 6-11, due to the high atomic mass of uranium. Similarly for UMg34.2, all of the uranium is incorporated into the glass phase of UMg42.8.

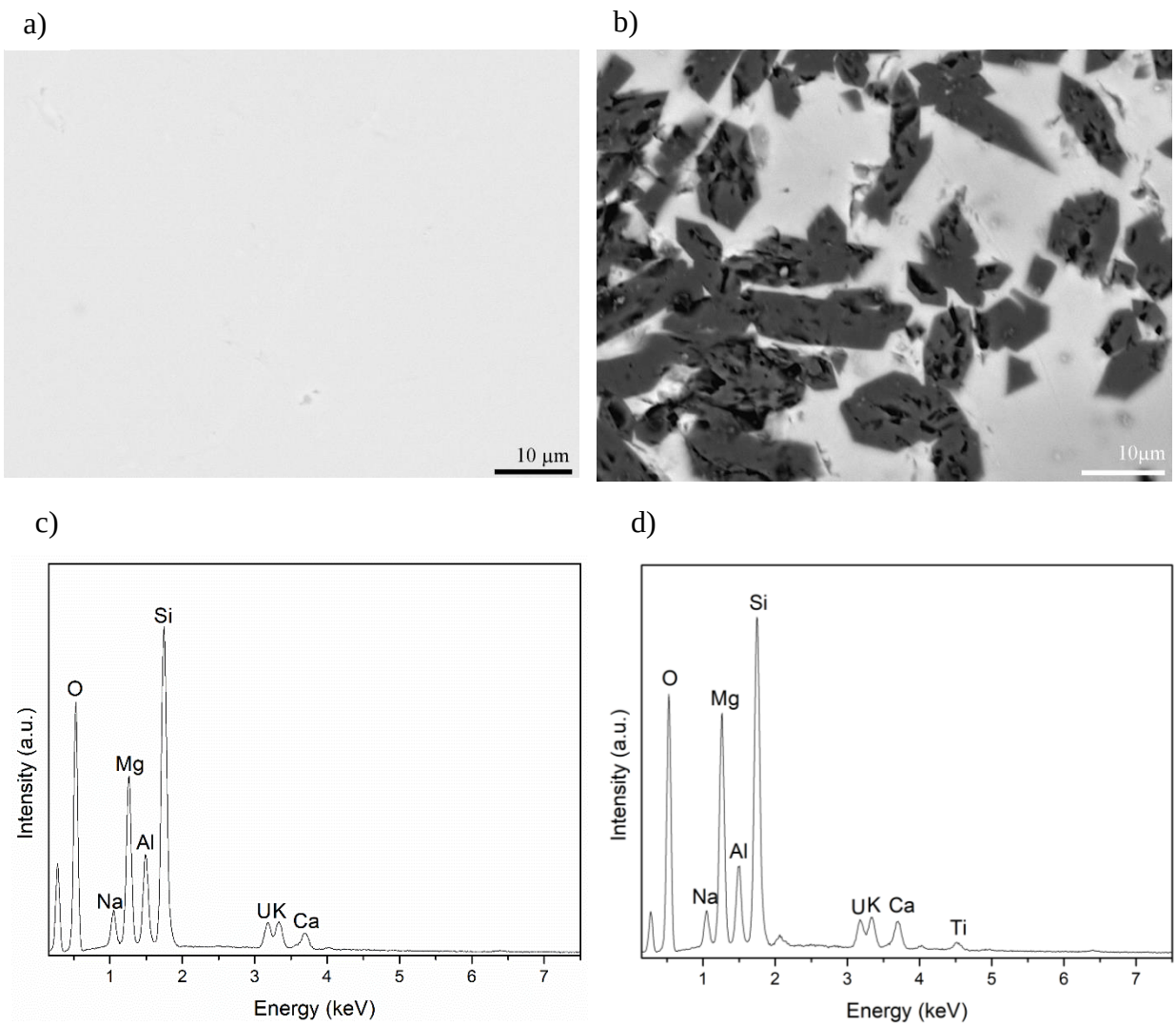

Figure 6-16. SEM-BSE images of UMg34.2 and UMg42.8 and EDS of the glass phases, a) SEM image of UMg34.2, b) SEM image of UMg42.8, c) EDS of UMg34.2 and d) EDS of UMg42.8.

6.2.6.2 XANES

XANES spectra of the uranium L_{III} edge in UMg34.2 and UMg42.8 were collected to determine the average oxidation station of uranium within the glass, see Figure 6-17. To facilitate this XANES of standards of uranium(IV) (UTi_2O_6), uranium(V) ($Yb_{0.5}U_{0.5}Ti_2O_6$) and uranium(VI) ($CaUO_4$) were also collected. The white lines of UMg34.2 and UMg42.8 are broader than the standards, but the edge position is closest to the $Yb_{0.5}U_{0.5}Ti_2O_6$ and $CaUO_4$ standards indicating a high valency for these glasses. However, it lacks the double feature of the post-edge oscillation evident for $CaUO_4$, between 17200 and 17250 eV and instead contains a single low intensity peak. Even though UMg34.2 and UMg42.8 are both relatively broad, the shape, edge position and

post-edge features more closely resemble the higher valency standards rather than the UTi_2O_6 standard.

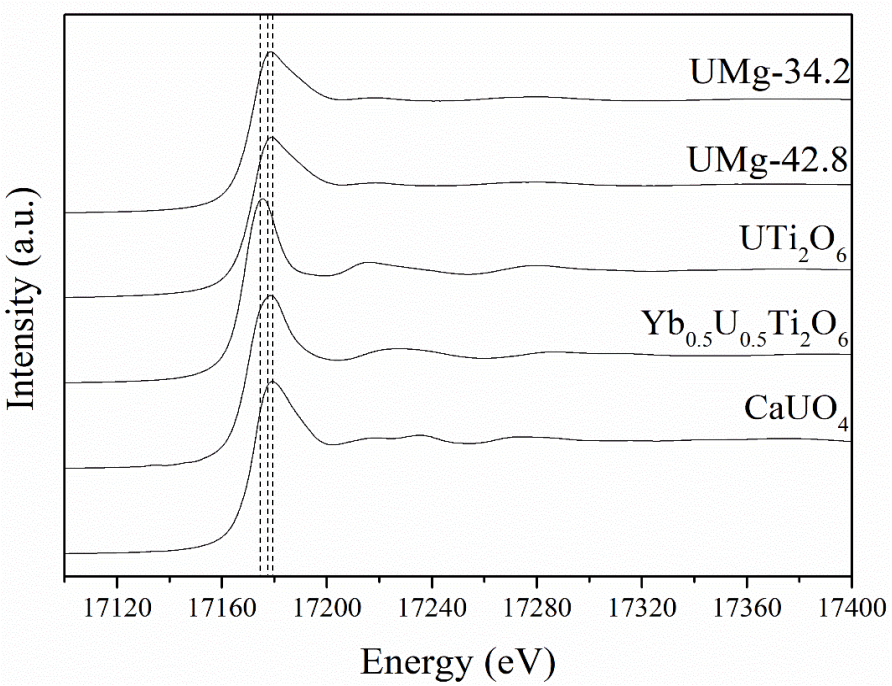

Figure 6-17. XANES of the U L_{III}-edge for the UMg42.8 and UMg34.2 glasses uranium(IV) (UTi_2O_6), V ($Yb_{0.5}U_{0.5}Ti_2O_6$) and VI ($CaUO_4$) standards. Dashed lines indicate the edge position of the standards.

Regression lines of features in the XANES and oxidation states were plotted of the standards (i.e. UTi_2O_6, $Yb_{0.5}U_{0.5}Ti_2O_6$ and $CaUO_4$) and can be seen in Figure 6-18.

a) half the normalised absorption energy

b) peak of the first derivative of the absorption energy, and

c) peak position of the white line.

The average oxidation state of uranium using a) half the normalised absorption energy is 6.0 ± 0.2 for both UMg42.8 and UMg34.2, b) the peak of the first derivative is 6.1 ± 0.2 for both UMg42.8 and UMg34.2 and c) the peak position of the white line is 5.7 ± 0.2 for UMg42.8 and 5.6 ± 0.2 for UMg34.2. The best trend line of oxidation state versus energy of a particular feature, for the standards was, for a) (R^2 of 0.99), followed by b) (R^2 of 0.98). The worst linear relationship was for c) (R^2 of 0.88).

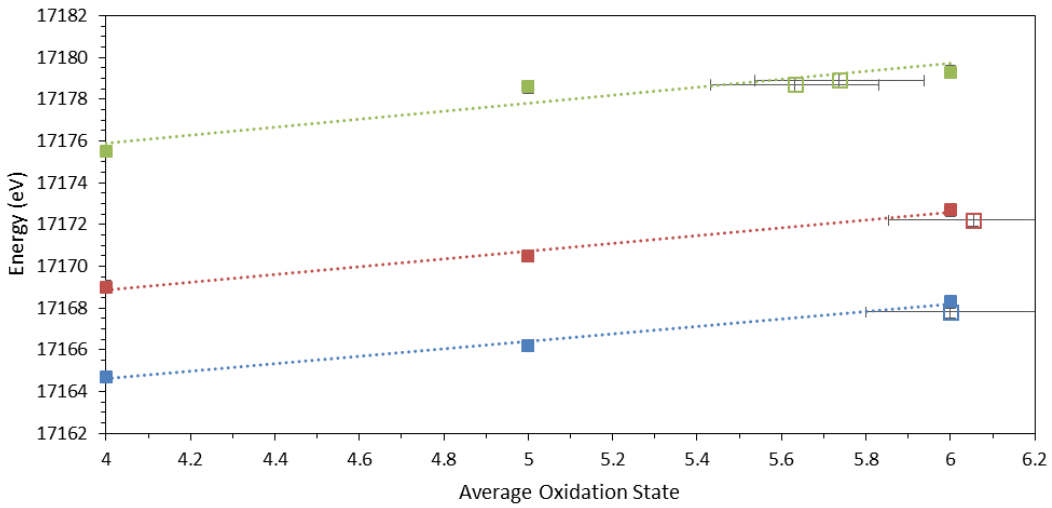

Figure 6-18. Linear regression plots of peak position of white line (green), peak of the first derivative of the XANES data (red) and half the normalised absorption energy (blue). Standards are filled squares, UMg42.8 and UMg34.2 are empty squares.

6.3 Discussion

Co-conditioning of clinoptilolite / sand waste from SIXEP with sludge waste from the Bulk Storage Tanks is an attractive conditioning strategy. The waste streams are compatible and high waste loadings are possible when combining the waste streams, due to the high SiO_2 and Al_2O_3 content of the clinoptilolite / sand waste. In terms of glass formulation development the two main challenges are minimising the glass additives needed, in order to process at a feasible temperature, and the ratio of clinoptilolite / sand waste to BST sludge to prevent the excessive formation of forsterite, in the glass melt, resulting in a highly porous waste form. Forsterite, Mg_2SiO_4, belongs to the olivine group. In its structure, (hexagonal close packed lattice) magnesium atoms occupy half the octahedral holes and the silicon atoms

occupy an eighth of the tetrahedral holes. In effect the silica tetrahedra are isolated and are connected by interstitial magnesium and other ions substituted into that site [20]. In terms of glass description, the silica tetrahedra are Q^0 in forsterite. The formation of this phase could be detrimental to waste form processing and performance, this was the motivation for the studies in this section.

6.3.1 Glass Formulations to Co-Process Sand / Clinoptilolite and BST sludge

Three different clinoptilolite / sand base glasses were produced. Two were processed at 1300 ºC (N10BS-70% and NL7.5BS-75%) and one was processed at 1200 ºC (NL15BS-67.5%). In general it is preferable to process at lower temperatures to minimise corrosion of the melting vessel, and off-gas components, and to minimise loss of volatile radionuclides. By using Li_2CO_3, in addition to Na_2CO_3 as a flux, an increase in waste loading was achieved. At 1200 ºC this allowed the clinoptilolite / sand waste to be processed at only 2.5 wt% less than N10BS-70%, and allowed an additional 5 wt% waste loading at 1300 ºC for NL7.5BS-75% compared to N10BS-70%. This is because the 48 mol% Na_2CO_3: 52 mol% Li_2CO_3 flux is stronger than 100% Na_2CO_3, therefore less of it can be used. The main effect of increasing sludge loading into the clinoptilolite / sand base glasses, on glass composition, is to increase the MgO concentration and to decrease SiO_2, Al_2O_3 and B_2O_3 concentrations. Glass compositions processed with simulant sludge, at 1300 ºC, are plotted on a ternary phase diagram in Figure 6-19. An oval is overlaid to indicate those glasses that contained forsterite. Forsterite crystallisation occurs from 30-33 mol%, and above, Mg in the glass.

6.3.2 Effect of MgO on Glass Structure and Properties

The effect of MgO is to increase the densities of the glass, with a linear relationship between mol% MgO and density. There is a large increase in density of the overall waste form when forsterite crystallises (Mg27.5NL7.5BS-75%), due to its relative high density. MgO has little impact on the glass transition temperatures (which were between 558-566 ^{o}C), indicating that substituting MgO for SiO_2, Al_2O_3 and B_2O_3 does little to weaken the glass network, for this compositional range. Indeed the crystallisation of forsterite (removing 2MgO and SiO_2 from the glass) actually lowers the glass transition temperature indicating that MgO and SiO_2 both strengthen the glass network. (Decreases in T_g is associated with a decrease in average bond strengths) [8]. Tx_1 occurs for all samples, decreasing in temperature (from 820 to 759 ^{o}C) as the MgO concentration increases. Similar events was obtained when heating pastes produced from MgO and SiO_2 slurries with an exothermic event occurring at 850 ^{o}C attributed to forsterite and enstatite crystallisation. Similarly this thermal event split for some of the samples (those aged for longer and at a higher temperature) with Tx_1 attributed to forsterite and Tx_2 attributed to enstatite. This splitting of the thermal event was explained, as is here, by the presence of new nucleation sites in those samples (from the dihydroxylation of M-S-H phases) lowering the temperature at which crystallisation occurs [21]. However the increasing MgO content does cause the crystallisation temperatures to decrease, thus significantly lowering the glass's thermal stability $\Delta(T_x - T_g)$ (~260 ^{o}C for Mg17.5NL7.5BS-75%, compared to ~220 ^{o}C for Mg25NL7.5BS-75%). For compositions Mg25 and Mg27.5NL7.5BS-75% there is a second crystallisation event (T_{x2}); the presence of this is likely to be linked to forsterite, which is present in these two compositions. The crystals may form nucleating sites promoting crystallisation of a secondary phase. The addition of MgO has little impact on the melting temperature (T_m) of crystallised phases within the glass. The effect of MgO on the glass structure is to decrease the silicate network polymerisation. The bridged silicate network band at ~480 cm^{-1} significantly decreases with increasing mol% of MgO and there is a clear increase in Q_2 speciation compared to Q_3 speciation. Mg17.5NL7.5BS-75% has 79 ±2% Q_3 and 21 ±2% Q_2, whereas Mg25NL7.5BS-75% has 66 ±2% Q_3 and 34 ±2% Q_2. The effect on density, the Raman

band at ~480 cm^{-1} and silica speciation between 850 and 1100 cm^{-1} all suggest that MgO is behaving as a modifier in the glass structure.

6.3.3 Effect of Forsterite on Waste Form Performance

The effect of forsterite (Mg_2SiO_4) crystallisation is to remove 2 moles of MgO and 1 mole of SiO_2 from the glass, the net effect of this is to polymerise the glass as more modifier is removed than network former. Indeed for Mg27.5NL7.5BS-75% Q_3 is 72 ± 2% and Q_2 is 28 ± 2% (with ~41 mol% SiO_2 and ~36 mol% MgO) for Mg25NL7.5BS-75% there is 66 ± 2% Q_3 and 34 ± 2% Q_2 (with ~42 mol% SiO_2 and ~34 mol% MgO) suggesting that the precipitation of forsterite actually serves to polymerise the glass network. In order to study this effect further, one glass composition (Mg22.5NL7.5BS-75%) was studied, along with a crystallised sample of the same glass. This produced a crystallised glass (crysMg22.5NL7.5BS-75%) with a similar microstructure to some of the other glasses over the solubility limit of forsterite (e.g. Mg27.5NL7.5BS-75%, as well as Mg30N10BS-70% and Mg25NL15BS-67.5%). This can be observed by comparing Figure 6-4 and Figure 6-11. However in addition to crystallising forsterite (24 ± 3%) several minor phases were also crystallised: enstatite (6 ± 3%), diopside (4 ± 4%) and periclase (4 ± 4%). Diopside and enstatite are both pyroxenes, but diopside has a solid solution of Ca and Mg. Periclase and enstatite have mass fractions within error of one another and partition the same quantity of MgO and SiO_2 from the glass as forsterite would. Therefore, in effect, the glass composition would be very similar to that of the sample in which all of the crystals were forsterite.

To study the effect of forsterite crystallisation on waste form durability, Mg22.5NL7.5BS-75% (100% amorphous) and crysMg22.5NL7.5BS-75% (62 ±5% amorphous) were both subjected to short-term glass durability test (PCT-B protocol). Forsterite crystallisation improves waste form durability. Taking the common dissolution tracers Na, B and Li, crysMg22.5NL7.5BS-75% is ~12, ~9 and ~8 (respectively) times more durable than its completely amorphous counterpart. The reason for this increase in durability is hypothesised to be due to an increase in network polymerisation. With forsterite crystallisation, 2 moles of Mg are removed

from the glass structure for every mole of Si. This is evident from the Raman of Mg27.5NL7.5BS-75% with forsterite crystallisation creating a more polymerised network, which will be more resistant to dissolution. In addition to this, Figure 6-13 demonstrates that the forsterite crystals strongly resist alteration. Mg22.5NL7.5BS-75% dissolve incongruently with NL_{Mg} and NL_{Si} an order of magnitude less than the alkali ions and boron. This indicates that these precipitate from solution and this can be observed in the alteration layers shown in Figure 6-13a and b; there is also evidence that Al and K form part of the alteration layer too. Mg22.5NL7.5BS-75% buffers to an average pH of 0.4 units higher than crysMg22.5NL7.5BS-75% due to the high concentration of alkali ions in solution from the increased glass alteration. Si in solution is initially high (day 1) before it precipitates out as the experiment progresses, indicating it becomes over-saturated as glass alteration continues and the composition of the leachate evolves. This is a pH effect as Si solubility is pH dependent, and the pH in this experiment drops over the 28 days from 9.5 to 9.1 [22]. For waste loaded MW glass, NL_B is ~0.8 g $m^{-2}d^{-1}$, over 7 days, here NL_B is 0.08 g $m^{-2}d^{-1}$ for Mg22.5NL7.5BS-75% and 0.008 g $m^{-2}d^{-1}$ for crysMg22.5NL7.5BS-75% demonstrating that Mg22.5NL7.5BS-75% is an order of magnitude and crysMg22.5NL7.5BS-75% two orders of magnitude more durable than UK HLW glass [23]. This suggests that waste forms produced have a high durability.

6.3.4 Representative Sludge Glass Melts

To better understand the thermal co-conditioning of clinoptilolite / sand waste with sludge a more representative sludge was produced, rather than using $Mg(OH)_2$ only. Two glass compositions were selected, in an attempt to constrain, with two compositions, the point at which forsterite is observed in the glass. The NL7.5BS-75% suggests the solubility limit is between 30.0 mol% for Mg22.5NL7.5BS-75% and 34.4 mol% for Mg25NL7.5BS-75%. UMg34.2NL7.5BS-75% did not show evidence of forsterite crystallisation and had 26.8 mol% of MgO, whereas UMg42.8NL7.5BS-75% did show evidence of forsterite and had 31.7 mol% of MgO. For the composition ranges in this study, at 1300 ^{o}C, the solubility limit of MgO in the glass is between 30.0 and 31.7 mol% (as 30.0 mol% was the highest MgO concentration obtained

without forsterite present and 31.7 mol% was the lowest MgO concentration obtained without forsterite present). Using a more representative sludge simulant, and designing compositions close to the solubility limit of MgO, results in a decrease in SiO_2, Na_2O, Al_2O_3, B_2O_3 and Li_2O and an increase in CaO and U_3O_8 for compositions of similar mol% of MgO in the NL7.5BS-75% series studied in Sections 6.2.3, 6.2.4 and 6.2.5. The net effect of increasing the ratio of BST sludge to sand / clinoptilolite waste is to depolymerise the glass network as the modifiers (Mg and U) increase and SiO_2 decreases (Al_2O_3 and alkalis decreases proportionally as they charge balance one another). This is likely to decrease polymerisation and durability up to the point forsterite crystallisation occurs, at this point glass polymerisation and durability increases.

The glass melts were spiked with 0.5 wt% Cs_2O and 0.5 wt% SrO to account for two of the main radionuclides associated with this waste. The Cs retention was measured at 60 ±7%, and Sr retention at 96 ±4% for UMg34.2NL7.5BS-75%; for UMg42.8NL7.5BS-75% the Cs retention was measured at 70 ±6%, and the Sr retention at 94 ±4%. This suggests that there is a significant loss of Cs at the glass melting temperature but that Sr remains well retained within the glass. A previous study, vitrifying organic, sulfonated, phenol-formaldehyde based, ion exchange resin, melting at 1200 ^oC, for 3 h, observed retentions in the 64.3-78.9 wt%, with an average of 74.2 wt% [24]. Another study, vitrified four different waste streams- an organic, sulfonated, styrene-divinylbenzene based, ion exchange resin, effluent treatment sludge, pond water treatment sludge and sand filters, at 1200 ^oC for 8 h. For the organic ion exchange resins Cs retentions were between 59%-76%, with an average of 68.5 wt% [25]. It is clear that melting at a lower temperature (i.e. $\leq$ 1200 ^oC) should be explored to increase Cs retentions in the glass melt. In addition to Cs and Sr being added to the glass melts, Na and K chlorides and sulfates were included, as it is likely these will form a large part of the sludge inventory. Cl and SO_3 are both known to be volatile at glass melting temperatures too. The intense corrosion at the melt line, see Figure 6-14, is likely due to attack from Cl and SO_3, as that level of corrosion was absent for the clinoptilolite / sand base glasses processed only with $Mg(OH)_2$. It is likely that presence of Cl increases the volatile loss of Cs from the glass [26]. It was

estimated that 35 ± 6% of the material at the melt line had corroded. This, along with the Cs volatile loss, severely restricts the length of time permissible at the processing temperature using mullite refractory. The representative sludge also contains a high mass fraction of U_3O_8; this oxidises in the glass melt. Three methods of determining the average oxidation state of uranium were attempted, see Section 6.2.6. The peak position of the white line gave a poor linear regression and the peak of the first derivative gave a slight overestimation of the average oxidation state (6.2 ±0.2). Therefore, the regression lines of standards using half the normalised absorption energy was used and gave an average oxidation state of both glasses of 6.0 ± 0.2. This indicates that uranium is likely to behave as a modifier in these glasses as the uranyl ion [27].

The main advantage of co-processing sand / clinoptilolite waste from SIXEP with sludge waste from the BST is the high waste loadings possible. For UMg34.2NL7.5BS-75%, a waste loading of 83.6 wt% was obtained, without forsterite crystallising. For UMg42.8NL7.5BS-75%, a waste loading of 85.7 wt% was obtained, with forsterite crystallising, but with the glass still of a low enough viscosity for it to be processed. It is suggested that the presence of forsterite is not detrimental, particularly if an in-container vitrification (ICV) technology was employed where the settling of crystalline material is not as major an issue as with continuous melters. Indeed, from a waste form performance perspective, the presence of forsterite actually enhances durability. However too high a MgO concentration as in Mg30N10BS-70% for example is undesirable, as this leads to the production of a partially sintered, highly porous, non-monolithic waste form.

6.4 Conclusions

Clinoptilolite / sand waste from SIXEP can be processed to form glassy waste forms with relative ease due to the high concentration of SiO_2, Al_2O_3 and alkali ions in the waste stream. The potential of combining this waste stream with sludge from the BST (a waste steam that arises from operation of SIXEP) is attractive as significant waste volume decreases are obtained. This study demonstrated that waste loadings up to 84 wt% were achieved without forsterite crystallising, but potentially glasses could be processed at ~86 wt% with a permissible quantity of forsterite present. Co-processing

of sand / clinoptilolite with sludge waste is suitable using both continuous and ICV melters [11]. However, there are potentially several advantages to processing with an ICV melter including increased tolerance for forsterite crystallisation and the fact that corrosion of off-gas systems is less of a concern. It was demonstrated, using Raman, that for the glass compositions used in this study, increasing the ratio of BST sludge to sand / clinoptilolite waste, depolymerises the glass network and that Mg behaves as a glass modifier in the glass structure, rather than as a conditional glass-former as others have demonstrated [7]–[10]. It was found that the presence of forsterite, and other Mg-containing secondary phases, for a given glass composition, served to increase the chemical durability of these glasses, at least in the short-term. Using Na, Li and B as tracers, the enhanced durability (of 62 ±4% amorphous vs. 100% amorphous), was found to be approximately an order of magnitude greater.

6.5 References

[1] S. G. Baxter and D. C. Berghauser, "The selection and performance of the natural zeolite clinoptilolite in British Nuclear Fuels' site ion exchange effluent plant, SIXEP," *Waste management,* vol. 2, no. 86. pp. 347–358, 1986.

[2] NDA, "Waste Stream 2D26 Ion Exchange Material (Clinoptilolite) and Sand," 2013. [Online]. Available: http://ukinventory.nda.gov.uk/wp-content/uploads/sites/18/2014/04/2D26.pdf. [Accessed: 15-Nov-2014].

[3] NDA, "Waste Stream 2D34 Sludge from Sand Filters and Transfers," 2016. [Online]. Available: http://ukinventory.nda.gov.uk/wp-content/uploads/sites/18/2014/04/2D34.pdf. [Accessed: 14-Mar-2017].

[4] Z. Maher, P. Ivanov, L. O'Brien, H. Sims, R. J. Taylor, S. L. Heath, F. R. Livens, D. Goddard, S. Kellet, P. Rand, and N. D. Bryan, "Americium and plutonium association with magnesium hydroxide colloids in alkaline nuclear industry process environments," *J. Nucl. Mater.*, vol. 468, pp. 84–96, 2016.

[5] S. Kohara, K. Suzuya, K. Takeuchi, C.-K. Loong, M. Grimsditch, J. K. R. Weber, J. A. Tangeman, and T. S. Key, "Glass Formation at the Limit of Insufficient Network Formers," *Science (80-.).*, vol. 303, pp. 1649–1652, 2004.

[6] S. Sen, H. Maekawa, and G. N. Papatheodorou, "Short-Range Structure of Invert Glasses along the Pseudo-Binary Join MgSiO3-MgSiO4: Results from 29Si and 25Mg MAS NMR spectroscopy," *J. Phys. Chem. B*, vol. 113, pp.

15243–15248, 2009.

[7] A. Pedone, G. Malavasi, M. Menziani, U. Segre, and A. Cormack, “Role of magnesium in soda-lime glasses: insight into structural, transport, and mechanical properties through computer simulations,” *J. Phys. Chem. C*, vol. 112, pp. 11034–11041, 2008.

[8] S. J. Watts, R. G. Hill, M. D. O’Donnell, and R. V. Law, “Influence of magnesia on the structure and properties of bioactive glasses,” *J. Non. Cryst. Solids*, vol. 356, no. 9–10, pp. 517–524, 2010.

[9] D. Li, M. Peng, and T. Murata, “Coordination And Local Structure Of Magnesium In Silicate Minerals and Glasses: Mg K-Edge XANES Study,” *Can. Mineral.*, vol. 37, pp. 199–206, 1999.

[10] S. Kroeker and J. F. Stebbins, “Magnesium coordination environments in glasses and minerals: New insight from high-field magnesium-25 MAS NMR,” *Am. Mineral.*, vol. 85, no. 10, pp. 1459–1464, 2000.

[11] K. S. Matlack, W. K. Kot, H. Gan, I. L. Pegg, G. A. Diener, and B. W. Bowan, “Sellafield Thermal Treatment Trials Using Advanced Joule Heated Ceramic Melter Technology,” *Waste Manag.*, pp. 1–13, 2010.

[12] M. Rolin and J. Recapet, “Contribution Letude Des Proprietes Thermodynamiques Des Carbonates Alcalins 1. Le Diagramme Ternaire Na_2CO_3- K_2CO_3- Li_2CO_3,” *Bull. Soc. Chim. Fr.*, no. 9, pp. 2104–2110, 1964.

[13] G. J. Janz and M. R. Lorenz, “Solid-liquid phase equilibriums for mixtures of lithium, sodium, and potassium carbonates,” *J. Chem. Eng. Data*, vol. 6, no. 3, pp. 321–323, 1961.

[14] W. L. Konijnendijk and J. M. Stevels, “The Structure of Borosilicate Glasses Studied By Raman Scattering,” *J. Non. Cryst. Solids*, vol. 20, pp. 193–224, 1976.

[15] B. N. Meera and J. N. Ramakrishna, “Raman Spectral Studies of Borate Glasses,” *J. Non. Cryst. Solids*, vol. 159, pp. 1–21, 1993.

[16] D. W. Matson, S. K. Sharma, and J. A. Philpotts, “The Structure of High-Silica Alkali-Silicate Glasses. A Raman Spectroscopic Investigation,” *J. Non. Cryst. Solids*, vol. 58, pp. 323–352, 1983.

[17] S. V. Raman, “The Effect of Mixed Modifiers on Nuclear Waste Glass Processing, Leaching and Raman Spectra,” *J. Mater. Res.*, vol. 13, pp. 8–15, 1998.

[18] D. Manara, A. Grandjean, and D. R. Neuville, “Advances in Understanding the Structure of Borosilicate Glasses: A Raman Spectroscopy Study,” *Am.*

Mineral., vol. 94, pp. 777–784, 2009.

[19] B. H. Toby, "R factors in Rietveld analysis: How good is good enough?," *Powder Diffr.*, vol. 21, no. 01, pp. 67–70, 2006.

[20] J. D. Birle, G. V. Gibbs, P. B. Moore, and J. V. Smith, "Crystal Structures of Natural Olivines," *Am. Mineral.*, vol. 53, pp. 807–823, 1968.

[21] J. Szczerba, R. Prorok, E. Snie, D. Madej, and K. Ma, "Influence of time and temperature on ageing and phases synthesis in the MgO- SiO_2- H_2O system," *Thermochim. Acta*, vol. 567, pp. 57–64, 2013.

[22] B. A. Fleming and D. A. Crerar, "Silicic Acid Ionisation and Calculation of Silica Solubility at Elevated Temperature and pH," *Geothermics*, vol. 11, pp. 15–29, 1982.

[23] M. T. Harrison, "The Effect of Composition on short- and long-term durability of UK HLW glass," *Procedia Mater. Sci.*, vol. 7, pp. 186–192, 2014.

[24] O. J. McGann, "The Development of Glass Compositions for the Vitrification of Ion Exchange Resin Wastes from the Nuclear Industry," 2013.

[25] P. A. Bingham, N. C. Hyatt, and R. J. Hand, "Vitrification of UK intermediate level radioactive wastes arising from site decommissioning. Initial laboratory trials," *Glas. Technol Eur. J. Glas. Sci. Technol. A.*, vol. 54, no. 1, pp. 1–19, 2013.

[26] B. P. Spalding, "Volatilisation of caesium-137 from soil with chloride amendments during heating and vitrification," *Environ. Sci. Technol.*, vol. 28, pp. 1116–1123, 1994.

[27] A. J. Connelly, N. C. Hyatt, K. P. Travis, R. J. Hand, M. C. Stennett, A. S. Gandy, A. P. Brown, and D. C. Apperley, "The effect of uranium oxide additions on the structure of alkali borosilicate glasses," *J. Non. Cryst. Solids*, vol. 378, pp. 282–289, 2013.

7. Discussion

The purpose of this PhD thesis was to study the potential of using vitrification to condition three different ILW streams- encapsulated Magnox swarf drums showing evidence of internal corrosion, ion-exchanged clinoptilolite and mixed clinoptilolite / sand waste from SIXEP and BST sludge. The purpose of this chapter is to discuss some of the findings from chapters 4, 5 and 6 and to compare the results to see if the results from one chapter could be used to explain findings from the others or be used to suggest beneficial further work.

There is estimated to be ~12,780 m^3 of encapsulated Magnox swarf at the Sellafield site, of which an unknown proportion of drums may have undergone internal corrosion and may, potentially, need reworking. The clinoptilolite / sand waste and Magnox sludge both have volumes at ~2460 and ~1250 m^3 respectively. For the activity the main sources for encapsulated Magnox swarf are typical fission products including- Ce-144, Sr-90, Cs-137 and Cs-134, as well as Pu-241, which is bred in the reactor. The activity associated with clinoptilolite is mainly from Cs-137, whereas the sludge has high concentrations of Sr-90, Pu-241 and Cs-137 as well as a significant uranium fraction [1]–[4]. All three wastes were conditioned with use of borosilicate glasses. Reworking cemented Magnox swarf (UNBS-46% composition) gave essentially a Na_2O- MgO- CaO- B_2O_3- Al_2O_3- SiO_2 glass (T_g = 590- 610 ^oC). Clinoptilolite vitrification gave essentially a Na_2O- Cs_2O- B_2O_3- Al_2O_3- SiO_2 glass (T_g = 460- 520 ^oC) and vitrification of clinoptilolite / sand waste with BST sludge gave a Li_2O- Na_2O- K_2O- MgO- CaO- U_3O_8- B_2O_3- Al_2O_3- SiO_2 glass (T_g = 540- 570 ^oC).

Secondary phases are a common occurrence in waste glasses and for the conditioned waste streams considered in this study, this is no different. For the repackaged encapsulated Magnox swarf waste the spinel phase was found to occur in most glass compositions and its origin was deduced to be from the corrosion of the stainless steel fraction of the waste. Similarly, spinel phases were identified in the low-melting Cs clinoptilolite glass formulations, but not in as high a concentration as those found in the repackaged cemented waste. The lower concentration is due to two reasons- one is the lower temperatures used for the Cs clinoptilolite vitrification (900-1050 ^oC) compared to 1200-1300^oC; the second reason is the greater surface area of the

stainless steel waste for the repackaged encapsulated Magnox swarf waste, as it had been size reduced. The spinel phase in the reworked cemented waste was found to have an average formula of $(Mg_{0.6}Fe_{0.4})(Cr_{0.9}Al_{0.1})_2O_4$, whereas in the vitrified Cs clinoptilolite the molecular formula was estimated to be $FeCr_2O_4$. Essentially the spinels that form in both cases are iron chromite with a solid solution of Mg and Fe in the A site of those found in the repackaged encapsulated Magnox swarf waste. The reason there is no Mg, in the iron chromite, formed in the vitrified Cs clinoptilolite, is that its concentration is very low (0.4 mol%) versus 19.8 mol% in the repackaged encapsulated Magnox swarf waste. The mechanism for spinel formation is hypothesised to be through the corrosion of the steel by the glass melt, creating a high local concentration of chromium, which precipitates out and partitions Fe and Mg into the A site of the spinel.

Mössbauer spectroscopy was used to calculate iron redox ratios $\frac{Fe^{2+}}{\Sigma Fe}$. For the repackaging of encapsulated Magnox swarf wastes the redox ratios were between 74%-75%, for the clinoptilolite melted in stainless steel crucibles, the redox ratios were between 70-76%, with a trend towards more reducing atmospheres at higher processing temperatures. It is clear that stainless steel imposes a strongly reducing redox environment on the glasses. For the repackaged encapsulated Magnox waste two sites were fitted to account for Fe^{2+}, with one of them assigned to the spinel and one for the glass. Fitting only one site produced very poor fits (reduced $\chi^2 \geq 1.40$). Fitting two sites to account for Fe^{2+} was not possible for the low melting clinoptilolite glass formulations, due to the low concentration of the spinels. For the thermal conditioning of clinoptilolite and co-conditioning of SIXEP clinoptilolite / sand waste, with BST sludge, the area of greatest crucible corrosion was at the melt line. It was estimated 26 ± 3% of the stainless steel crucible had corroded after 12 h at temperatures between 900 and 1050 ^oC, whereas 35 ± 6% of the crucible had corroded at the melt line after 2 h at 1300 ^oC. This highlights the significant amount of corrosion caused to the mullite crucible, even after such as short period at the melt temperature. There was no appreciable iron in the glass formulations for the clinoptilolite / sand with sludge waste, therefore, a measure of redox ratio was not possible. However, as the sludge is likely to contain more corroded (i.e. oxidised) waste compared to the encapsulated Magnox swarf waste, and the melting vessel is ceramic, the melt atmosphere will be

more oxidising. This can be important for uranium solubility in glass melts. Uranium(IV) has a solubility limit in borosilicate glasses of ~9 wt%, where it precipitates out as UO_2, whereas uranium(VI) can be incorporated up to 40 wt% [5]. For the reworked encapsulated Magnox swarf with uranium, the uranium content of the drums will be significantly less than the uranium(IV) solubility limit, similarly, for clinoptilolite / sand and BST sludge glasses the concentration of uranium will be significantly less than the uranium(VI) solubility limit. Therefore, the differences in solubility of uranium, due to different valencies is less of a problem.

At higher waste loadings compositions, for the reworking of encapsulated Magnox swarf drums, other Mg-containing secondary phases were observed- diopside ($MgCaSi_2O_6$), monticellite ($MgCaSiO_4$), periclase (MgO) and, in particular, forsterite (Mg_2SiO_4). Forsterite was also frequently observed in the co-processing of clinoptilolite / sand and BST sludge; at 1300 ^oC, it was found to form when the concentration of MgO in the glass is > 30 mol%, at 1200 ^oC forsterite was observed in all compositions- all that can be surmised is that MgO needs to be significantly less than 27.5 mol%. For the repackaged encapsulated Magnox swarf waste, at 1300 ^oC and 1200 ^oC, forsterite crystallisation did not occur up to 22 mol%. It was estimated that the MgO content of those compositions containing forsterite was 29 mol% at 1300 and 1200 ^oC. Heat treating glassy waste forms produced from clinoptilolite / sand with BST sludge (specifically Mg22.5NL7.5BS-75%) produced some of the phases observed in the higher waste loading reworked encapsulated Magnox swarf waste, specifically forsterite, diopside and periclase, however, no monticellite was observed and a new phase enstatite ($MgSiO_3$) was observed to crystallise from the glass. It is clear that high MgO containing glasses are prone to secondary phase crystallisation. To produce more optimised glass compositions there are two further compositions that could be examined. One is a higher waste loading composition for the reworking of the encapsulated Magnox swarf drums and the second is a composition for the clinoptilolite / sand waste processed with BST sludge that is capable of being produced at 1200 ^oC. At 1300 ^oC, for the encapsulated Magnox waste, it may be possible to increase the MgO content up to 26-28 mol% to produce a glass with low porosity and minimal secondary phases. For the 72% waste loading the repackaged waste forms were monolithic and would have passivated the two main reactants in the

corrosion reactions (i.e. Magnox and uranium), but they contained a large amount of porosity and hadn't fully reacted; there was also a high concentration of forsterite. For the clinoptilolite / sand and BST sludge waste, a composition of approximately 22 mol% MgO should produce an acceptable waste form, at 1200 ^{o}C. A composition of Mg16NL7.5BS-67.5% was calculated to achieve this (i.e. a sludge loading to give 16wt% MgO in the final waste form). The motivation for processing at 1200 ^{o}C, or potentially lower, would be to mitigate the losses of volatile radionuclides such as Cs-137, Cs-134 and Ru-106, and also to minimise corrosion from Cl and SO_3, to extend melter life.

When designing glass formulations it is important to maximise waste loadings to minimise the final total volume of waste. For the encapsulated Magnox swarf drums, waste loadings between 36 and 46 wt% produced vitreous waste forms, with waste loadings of 72 wt% producing a porous, partially sintered waste form. Sand was added to the encapsulated Magnox swarf waste to increase the SiO_2 content to improve glass properties and durability. To increase waste loadings further the addition of sand could be omitted as durability of the waste was high and an increase in waste loading leading to the production of a marginally less durable waste form be justified. For Cs clinoptilolite vitrification, waste loadings of 50-60 wt% were achieved. For the clinoptilolite / sand with BST sludge, at 1300 ^{o}C, waste loadings between 76-84 wt% were achieved. Table 7-1 contains waste volumes produced by thermal conditioning, versus cementation, for the three waste streams studied in this thesis. These values were calculated using the following compositions- UNBS-46% (for reworking encapsulated Magnox cemented waste), N15NBS-53.5% (for low melting Cs clinoptilolite) and UMg34.2NL7.5BS-75% (for co-conditioning of clinoptilolite / sand with BST sludge).

Table 7-1.
Waste volumes of the three waste streams and waste volumes after thermal conditioning and after cementation.

	Reworked Encapsulated Magnox Swarf	Clinoptilolite	Clinoptilolite / Sand and Sludge Waste
Nominal Volume of Waste (m^3)	1	1	1
Volume of Thermal Conditioned Waste	1.2 ± 0.1	0.9 ± 0.1	0.7 ± 0.1
Volume of cemented Waste	1.5 + 0.3	3.8 ± 0.4	4.2 ± 0.4

Reworking encapsulated Magnox swarf waste produces a slight volume increase on the original waste, but a significant decrease in waste volume compared to using cementation as a repair strategy. Both clinoptilolite vitrification, at 900 ºC, and co-conditioning of clinoptilolite / sand with BST sludge offer decreases in the waste volume compared to the original wastes, and offer very large decreases in waste volume compared to cementation. For the clinoptilolite alone (using compositions designed to be processed at a lower temperature) this is a decrease by a factor of 4.2 and for co-conditioning / sand with BST sludge this is a decrease by a factor of 6.

One similarity in the glass compositions in chapters 4 and 5 is the very reducing nature of the glass melts. For chapter 4, this is because of the high fraction of metallic waste associated with the encapsulated Magnox swarf drums and for chapter 5, because of the use of stainless steel as a melting vessel. To quantify the redox conditions,

All three vitrified waste streams were subjected to the PCT-B protocol to determine the short-term durability of the waste forms. Studies were conducted in both deionised water and saturated $Ca(OH)_{2(aq)}$, as it is likely a GDF will contain a high quantity of cement from the ILW packages and backfill material and, therefore, groundwater is likely to contain a high concentration of calcium when it comes into contact with the waste form. Na, B and Si were the three dissolution tracers used for the glasses in this study. Table 7-2 shows normalised mass losses of glasses over 7 days.

Table 7-2. Normalised mass losses (g m^{-2}) for key glass tracer elements over 7 days for the three thermally conditioned waste streams in this study.

Chapter		4	5		6
Glass Composition		UNBS-46%	NBS-56.0%	N15NBS-53.5%	Mg22.5NL7.5BS-75%
90 °C	NL_{Na}	0.23	2.8	2.4	0.06
	NL_{B}	0.07	1.8	1.3	0.08
	NL_{Si}	0.008	0.05	0.33	0.002

The glasses produced from reworking encapsulated Magnox swarf and from co-conditioning of clinoptilolite / sand with sludge all perform better than HLW and ILW glass formulations. On the other hand glasses produced from low melting Cs clinoptilolite formulations perform worse than both HLW and ILW glasses [6]–[8]. Mg is known have a mixed effect on glass dissolution: enhancing durability in the short-term but can cause rate resumption for long-term glass dissolution [9]–[11]. For certain compositions and leachate concentrations it is found to form part of the alteration layer whilst in others it does not. For the reworked encapsulated Magnox swarf waste forms, the UNBS-46% composition has a MgO concentration of ~20 mol%, for the clinoptilolite / sand waste with sludge vitrification the MgO concentration is ~30 mol%, in both cases, it is found to form part of the alteration layer when dissolved in deionised water. However, for UNBS-46% when dissolved in saturated $Ca(OH)_{2(aq)}$, it does not form part of the alteration layer. This corroborates Thien who found that Mg will form part of the alteration layer when Ca is not in solution, however, when in solution the Ca preferentially occupies divalent sites in the alteration layer [11].

7.1 References

[1] NDA, “Waste Stream 2D35/C Encapsulated Retrieved Magnox Cladding,” *2013*. [Online]. Available: http://ukinventory.nda.gov.uk/wp-content/uploads/sites/18/2014/05/2D35_C.pdf. [Accessed: 15-Nov-2014].

[2] NDA, “Waste Stream 2D38/C Encapsulated Magnox Cladding,” *2013*. [Online]. Available: http://ukinventory.nda.gov.uk/wp-content/uploads/sites/18/2014/05/2D38_C.pdf. [Accessed: 15-Nov-2014].

[3] NDA, “Waste Stream 2D26 Ion Exchange Material (Clinoptilolite) and Sand,”

2013. [Online]. Available: http://ukinventory.nda.gov.uk/wp-content/uploads/sites/18/2014/04/2D26.pdf. [Accessed: 15-Nov-2014].

[4] NDA, “Waste Stream 2D34 Sludge from Sand Filters and Transfers,” 2016. [Online]. Available: http://ukinventory.nda.gov.uk/wp-content/uploads/sites/18/2014/04/2D34.pdf. [Accessed: 14-Mar-2017].

[5] H. D. Schreiber and G. B. Balazs, “The Chemistry of Uranium in Borosilicate Glasses. Part 1. Simple Base Compositions Relevant to the Immobilisation of Nuclear Waste,” *Phys. Chem. Glas.*, vol. 23, p. 139, 1982.

[6] H. Zhang, C. L. Corkhill, P. G. Heath, R. J. Hand, M. C. Stennett, and N. C. Hyatt, “Effect of Zn- and Ca- oxides on the structure and chemical durability of simulant alkali borosilicate glasses for immobilisation of UK high level wastes,” *J. Nucl. Mater.*, vol. 462, pp. 321–328, 2015.

[7] M. T. Harrison, “The Effect of Composition on short- and long-term durability of UK HLW glass,” *Procedia Mater. Sci.*, vol. 7, pp. 186–192, 2014.

[8] N. C. Hyatt, R. R. Schwarz, P. A. Bingham, M. C. Stennett, C. L. Corkhill, P. G. Heath, R. J. Hand, M. James, A. Pearson, and S. Morgan, “Thermal Treatment of Simulant Plutonium Contaminated Materials From The Sellafield Site By Vitrification In A Blast-Furnace Slag,” *J. Nucl. Mater.*, vol. 444, pp. 186–199, 2014.

[9] E. Curti, J. L. Crovisier, G. Morvan, and A. M. Karpoff, “Long-term corrosion of two nuclear waste reference glasses (MW and SON68): A kinetic and mineral alteration study,” *Appl. Geochemistry*, vol. 21, pp. 1152–1168, 2006.

[10] H. Aréna, N. Godon, D. Rébiscoul, R. Podor, E. Garcès, M. Cabie, and J. P. Mestre, “Impact of Zn, Mg, Ni and Co elements on glass alteration: Additive effects,” *J. Nucl. Mater.*, vol. 470, pp. 55–67, 2016.

[11] B. M. J. Thien, N. Godon, A. Ballestro, S. Gin, and A. Ayral, “The dual effect of Mg on the long-term alteration rate of AVM nuclear waste glasses,” *J. Nucl. Mater.*, vol. 427, pp. 297–310, 2012.

8 Conclusions

The aim of this body of research was to demonstrate the benefits of thermal conditioning of three, different, intermediate level waste streams, requiring additional treatment. The main advantage of thermal conditioning of ILW is the reduction in waste volume, which directly leads to reductions in cost in terms of GDF size, interim storage space and transport to the final GDF. In addition to this, compared to cementation as a conditioning method, the waste form produced offers increased passive safety and durability.

Vitrification, as a means of reworking problematic cemented waste forms, was shown to produce several advantages over other rework strategies. In particular, passivation of the underlying corrosion reaction in cemented Magnox, through oxidation of the Magnox (which partitions into the glass and secondary phases), and uranium, (which forms part of the glass only). At high waste loading glass formulations (89 and 72%) there is a significant quantity of porosity and crystalline phases present. At lower waste loading formulations (46% and 36%), a more homogeneous waste form is produced, with only spinel phases forming. These spinel phases were found to be rich in chromium, iron and magnesium. The glass composition UNBS-46% was studied, *via* XANES and Mössbauer spectroscopy, indicating that multivalent ions in the glass prefer to adopt the lower oxidation state due to the highly reducing nature of the glass melt. Short-term PCT-B studies demonstrate that a durable glass is produced with NL_{Na} and NL_{B} less than HLW and similar to ILW glass dissolution rates.

Clinoptilolite can be vitrified in low melting (< 1050 ^{o}C), castable glass formulations at waste loadings between 50-60 wt% on a ~80 g scale, with the potential to scale up to larger waste volumes. At these waste loadings the final glass has a volume approximately the same as the original clinoptilolite, but can offer a reduction in waste volume of ~3.8 compared to cementation. The final waste forms are amorphous, with no significant crystalline phases, the small quantity of crystalline phases identified were found to be iron chromite (from corrosion of the metallic crucible) and a small amount of undigested quartz. Crucible corrosion is evident particularly at the melt line. NBS-56.0%, melted at 1050 ^{o}C showed significantly more crucible corrosion compared to those compositions melted at lower temperatures. Melting in stainless

steel produces a very reducing atmosphere with between 70% and 76% of the total iron present as Fe^{2+}. Cs, the main source of activity associated with clinoptilolite, is incorporated into the glass structure. There is no major loss of caesium containing compound on heating (from STA-MS experiments) and chemical analysis of the glass suggests caesium retentions of between 92% and 99%. The R-value (i.e. $\frac{Na_2O}{B_2O_3}$) has a large impact on the structure of glass. Increasing this ratio results in more Si-O-B bonds as assigned from Raman spectra, associated with danburite like-units and a depolymerisation of the glass network. The high boron and sodium content of these glasses results in relatively low durability (1.6 to 2.3 times less durable than waste loaded MW glass frit).

Mixing sand / clinoptilolite waste with BST sludge was demonstrated to have several benefits. The main advantage is the significant decreases in waste volumes available by combining these two waste streams, with a 6-fold decrease in volume, versus cementation. The effect of increasing the ratio of BST sludge to sand / clinoptilolite waste is to increase the concentration of MgO, U_3O_8 and CaO and to decrease the concentration of SiO_2, Al_2O_3 and B_2O_3. Raman spectroscopy was used to study the impact of a higher ratio of BST sludge to clinoptilolite / sand waste on glass structure and it was found to cause a decrease in network polymerisation with Q_3 of 79% and Q_2 of 21% for Mg17.5NL7.5BS-75% and Q_3 of 66% and Q_2 of 34% for Mg25NL7.5BS-75%. The presence of forsterite, and other Mg-containing secondary phases, for a given glass composition, is to significantly increase the waste form durability in the short-term by an order of magnitude. This was determined by PCT-B on two glasses of the same composition, but one 100% amorphous, and the other 62 ±5% amorphous. It was highlighted that re-examining glass compositions that melt at 1200 ^oC, may be beneficial to reduce the loss of Cs at 1300 ^oC and mitigate the attack of volatile species at the melt line.

8.1 Further Work

For the reworking of cemented encapsulated Magnox drums, demonstration on a pilot scale is a priority, to demonstrate this technology can operate at an industrial scale. Glass composition development could be optimised with waste loadings above 46%, but less than 72%, explored, in particular with the knowledge that forsterite

crystallisation improves waste form corrosion performance. Also waste loadings could be increased by omitting some of the additional SiO_2 added.

For the low temperature thermal conditioning of Cs clinoptilolite, promising Cs retentions during glass processing were obtained, it would be beneficial to corroborate this with studies of the off-gas species produced. Melting at 900 ^{o}C (or less) is possible, with less crucible corrosion observed than at high temperatures, however, it would also be worth exploring waste containers that offer higher resistance to high temperature oxidation to improve the process.

For the thermal co-conditioning of clinoptilolite / sand waste, with sludge, demonstration on a pilot scale using ICV would be the next suggested step, in particular, with actual sludge waste. It would also be recommended for longer-term dissolution experiments to be performed on the UMg34.2NL7.5BS-75% composition, and a partially crystallised waste form of similar composition. Determining whether rate resumption is observed for these high MgO containing waste forms, and the dissolution behaviour of uranium in general, over longer time scales, is important, as of the three waste streams studied the BST sludge will contain the highest concentration of longer-lived isotopes. Again waste form composition development could be optimised with a composition melting at 1200 ^{o}C identified and characterised; it was suggested that the Mg16NL7.5BS-67.5% composition should produce a suitable waste form.

In summary all three waste streams conditioned thermally in this study offered decreases in total waste volume, increases in chemical durability, compared to cementation, and produced waste forms with increased passive safety. Some of the technical challenges of conditioning these waste streams thermally were examined and potential routes to improve the current approach were identified. It is hoped that this study provides a strong case of some of the benefits of thermally conditioning of some, of the many, legacy wastes requiring additional treatment in the UK radioactive waste inventory.

Bibliography

Abraitis, P.K. et al., 2000. Single-pass flow-through experiments on a simulated waste glass in alkaline media at 40°C.: I. Experiments conducted at variable solution flow rate to glass surface area ratio. *Journal of Nuclear Materials*, 280, pp.196–205.

Akovali, Y.A., 2004. Nuclear Data Sheets for A=243. *Nuclear Data Sheets*, 103, pp.515–564.

Andriambololona, Z., Godon, N. & Vernaz, E., 1992. Glass Alteration in the Presence of Mortar: Effect of the Cement Grade. *Proc. Mat. Sci. Symp.*, 257, pp.151–158.

Aréna, H. et al., 2016. Impact of Zn, Mg, Ni and Co elements on glass alteration: Additive effects. *Journal of Nuclear Materials*, 470, pp.55–67.

Armbruster, T., 2001. Clinoptilolite-heulandite: applications and basic research. *Studies in Surface Science and Catalysis*, 135, pp.13–27.

Asano, M., Kou, T. & Yasue, Y., 1987. Mass Spectrometric Study Of Vaporisation Of Caesium-Containing Borosilicate Glasses. *Journal of Non-Crystalline Solids*, 92, pp.245–260.

ASTM, 2017. *C1220 - 17. Standard Test Method for Static Leaching of Monolithic Waste Forms for Disposal of Radioactive Waste*, West Conshohocken, PA.

ASTM, 2014. *C1285 - 14. Standard Test Methods for Determining Chemical Durability of Nuclear, Hazardous, and Mixed Waste Glasses and Multiphase Glass Ceramics: The Product Consistency Test (PCT)*, West Conshohocken, PA.

Bancroft, G.M., 1973. *Mössbauer Spectroscopy: an introduction for inorganic chemists and geochemists*, Wiley, pp. 17-47.

Baquerizo, L.G. et al., 2015. Hydration states of AFm cement phases. *Cement and Concrete Research*, 73, pp.143–157.

Baxter, S.G. & Berghauser, D.C., 1986. The selection and performance of the natural zeolite clinoptilolite in British Nuclear Fuels' site ion exchange effluent plant, SIXEP. *Waste management*, 2(86), pp.347–358.

Baxtor, S.G. & Berghauser, D.C., *The Selection and Performance of the Natural Zeolite Clinoptilolite in British Nuclear Fuels' Site Ion Exchange Plant (SIXEP)*,

Bingham, P. et al., 2011. Corrosion of glass contact refractories for the vitrification of radioactive wastes: a review. *International Materials Reviews*, 56(4), pp.226–242.

Bingham, P.A. et al., 2017. Modelling the sulfate capacity of simulated radioactive waste borosilicate glasses. *Journal of Alloys and Compounds*, 695, pp.656–667.

Bingham, P.A. & Hand, R.J., 2008. Sulphate incorporation and glass formation in phosphate systems for nuclear and toxic waste immboilisation. *Mater. Res. Bull.*, 43, pp.1679–1693.

Bingham, P.A., Hand, R.J. & Scales, C.R., 2006. Immobilization of simulated plutonium-contaminated material in phosphate glass: an initial scoping study. *Mater. Res. Soc. Symp. Proc.*, 932, pp.345–352.

Bingham, P.A., Hyatt, N.C. & Hand, R.J., 2012. Vitrification of UK intermediate level radioactive wastes arising from site decommissioning: property modelling and selection of candidate host glass compositions. *Glass. Technol.: Eur. J. Glass Sci. Technol. A*, 53, pp.83–100.

Bingham, P.A., Hyatt, N.C. & Hand, R.J., 2013. Vitrification of UK intermediate level radioactive wastes arising from site decommissioning. Initial laboratory trials. *Glass Technol: Eur. J. Glass Sci. Technol. A.*, 54(1), pp.1–19.

Birle, J.D. et al., 1968. Crystal Structures of Natural Olivines. *The American Mineralogist*, 53, pp.807–823.

Borges, P.H.R. et al., 2010. Carbonation of CH and C-S-H in composite cement pastes containing high amounts of BFS. *Cement and Concrete Research*, 40(2), pp.284–292.

Browne, E., 1997. Nuclear Data Sheets for A=90. *Nuclear Data Sheets*, 82, pp.379–546.

Browne, E. & Tuli, J.K., 2007. Nuclear Data Sheets for A=137. *Nuclear Data Sheets*, 108(10), pp.2173–2318.

Browne, E. & Tuli, J.K., 2015. Nuclear Data Sheets for A=238. *Nuclear Data Sheets*, 127, pp.191–332.

Browne, E. & Tuli, J.K., 2014. Nuclear Data Sheets for A=239. *Nuclear Data Sheets*, 122, pp.293–376.

Browne, E. & Tuli, J.K., 2017. Nuclear Data Sheets for A=99. *Nuclear Data Sheets*, 145, pp.25–340.

Bunker, B.C. et al., 1990. Multinuclear nuclear magnetic resonance and Raman investigation of sodium borosilicate glass structures. *Physics and Chemistry of Glasses*, 31, pp.30–41.

Busey, R.H. & Mesmer, R.E., 1997. Ionisation equilibriums of silicic acid and polysilicate formation in aqueous sodium chloride solutions to 300oC. *Inorganic Chemistry*, 16, pp.2444–2450.

Cable, M. & Chaudry, M.A., 1975. Volatisation from soda-lime-silica melts at one atmosphere and reduced pressures. *Glass Technol*, 16, pp.125–134.

Carpenter, J.H. et al., Caesium Vaporisation Losses from Synroc Mineral Barium-Caesium Hollandite. In G. Wicks & W. Ross, eds. *Nuclear Waste Management, Advances in Ceramics*. Columbus, Ohio: American Ceramic Society.

Casler, D.G. & Hrma, P., 1999. Nonisothermal kinetics of spinel crystallization in a HLW glass. *Mater. Res. Soc. Symp. Proc.*, 556, pp.255–262.

Caurant, D. et al., 2007. Effect of Molybdenum on the structure and on the crystallisation of SiO_2-Na_2O-CaO-B_2O_3 glasses. *J. Am. Ceram. Soc.*, 90, pp.774–783.

Chase, M.W.J., 1998. NIST-JANAF Thermochemical Tables. *J. Phys.Chem. Ref. Data*, Monograph, pp.1–1951.

Chave, T. et al., 2011. Glass-water interphase reactivity with calcium rich solutions. *Geochim. Cosmochim. Acta*, 75, pp.4125–4139.

Collier, N.C. & Milestone, N.B., 2010. The encapsulation of $Mg(OH)_2$ sludge in composite cement. *Cement and Concrete Research*, 40(3), pp.452–459.

Connelly, A.J. et al., 2013. The effect of uranium oxide additions on the structure of alkali borosilicate glasses. *Journal of Non-Crystalline Solids*, 378, pp.282–289.

Corkhill, C.L. et al., 2013. Dissolution of UK High-Level Waste Glass Under Simulated Hyperalkaline Conditions of a Colocated Geological Disposal Facility. *International Journal of Applied Glass Science*, 4, pp.341–356.

Cronin, J. & Collier, N., 2012. Corrosion And Expansion Of Grouted Magnox. *Miner. Mag.*, 76(8), pp.2901–2909.

Curti, E. et al., 2006. Long-term corrosion of two nuclear waste reference glasses (MW and SON68): A kinetic and mineral alteration study. *Applied Geochemistry*, 21, pp.1152–1168.

Deckers, J., 2013. The innovative plasma tilting furnace for treatment of radioactive and problematic chemical waste. In *Thermal treatment of radioactive wastes: research, development and demonstration*. https://www.sheffield.ac.uk/polopoly_fs/1.384714!/file/SymposiumDecember2013.pdf [Accessed November 15, 2015].

Deegan, D. & Scales, C., 2009. The role of Tectronics plasma vitrification technology in the management and conditioning of nuclear waste. *Proceedings of the International Conference on Environmental Remediation and Radioactive Waste Management*, pp.1179–1189.

Dell, W.J., Bray, P.J. & Xiao, S.Z., 1983. ^{11}B NMR Studies and Structural Modelling of Na_2O-B_2O_3-SiO_2 glasses of high soda content. *Journal of Non-Crystalline Solids*, 58, pp.1–16.

Dietzel, A., 1942. Die Kationenfeldstarken und ihre Beziehungen zu Entglasungsvorgangen, zur Verbindungsbildung und zu den Schmelzpunkten von Silikaten. *Z. Elektrochem.*, 48, pp.9–23.

Director-General For Research, E.U., 2004. Geological Disposal of Radioactive Wastes Produced by Nuclear Power... from concept to implementation. pp. 4–43.

Donald, I.W., 2007. Immobilisation Of Radioactive And Non-Radioactive Wastes In Glass-Based Systems: An Overview. *Glass Technol: Eur. J. Glass Sci. Technol.*

A., 48, pp.155–163.

Donald, I.W., 2010. Waste Immobilisation in Glass and Ceramic Based Hosts- Radioactive, Toxic and Hazardous Wastes. In Chichester: Wiley, pp. 1–31, 57–177, 275–334, 465–490.

Doremus, R.H., 1994. Glass Science. In New York: John Wiley & Sons, pp. 113–121.

Du, L.S. & Stebbins, J.F., 2003. Solid-state NMR study of metastable immiscibility in alkali borosilicate glasses. *Journal of Non-Crystalline Solids*, pp.239–255.

Du, W.F. et al., 2000. Study of Al_2O_3 effect on structural change and phase separation in Na_2O-B_2O_3-SiO_2 glass by NMR. *Journal of Materials Science*, 35, pp.4865–4871.

Dyar, M.D. et al., 2006. Mössbauer Spectroscopy of Earth and Planetary Materials. *Annual Review of Earth and Planetary Sciences*, 34, pp.83–125.

Elliot, M.N. et al., 1962. Fixation of radioactive waste in glass. Part I. Pilot-Plant Experience at Harwell. *Treatment and Storage of High-Level Radioactive Wastes*, pp.465–487.

Environment Agency, 2005. *Reworking intermediate level radioactive waste. Science report: SC040047*, Bristol, U.K.

Fairhall, G.A. & Palmer, J.D., 1992. The Encapsulation of Magnox Swarf in Cement in the United Kingdom. *Cement and Concrete Research*, 22, pp.293–298.

Farges, F. et al., 1992. Structural environments of incompatible elements in silicate glass/melt systems: U(IV), U(V), U(VI). *Geochim. Cosmochim. Acta*, 56, pp.4205–4220.

Farges, F. et al., 2004. The effect of redox state on the local structural environment of iron in silicate glasses: a combined XAFS spectroscopy, molecular dynamics and bond valence study. *Journal of non-crystalline solids*, 334, p.176.

Ferraro, J.R. & Nakamoto, K., 1994. *Introductory Raman Spectroscopy*.

Fleming, B.A. & Crerar, D.A., 1982. Silicic Acid Ionisation and Calculation of Silica Solubility at Elevated Temperature and pH. *Geothermics*, 11, pp.15–29.

Fleury, B. et al., 2013. Son68 glass dissolution driven by magnesium silicate precipitation. *Journal of Nuclear Materials*, 442, pp.17–28.

Frugier, P. et al., 2008. SON68 nuclear glass dissolution kinetics: Current state of knowledge and basis of the new GRAAL model. *Journal of Nuclear Materials*, 380, pp.8–21.

Gaisford, S., Kett, V. & Haines, P., 2016. Principles of Thermal Analysis and Calorimetry. In London: Royal Society of Chemistry, pp. 18–43, 67–103, 214–228.

Geisler, T. et al., 2015. The mechanism of borosilicate glass corrosion revisited. *Geochimica et Cosmochimica Acta*, 158, pp.112–129.

Gin, S. & Mestre, J.P., 2001. SON 68 nuclear glass alteration kinetics between pH 7 and pH 11.5. *Journal of Nuclear Materials*, 295, pp.83–96.

Gin, S., Robert, I. & Couillard, M., 2001. Role and properties of the gel formed during nuclear glass alteration: importance of gel formation conditions. *Journal of Nuclear Materials*, 298, pp.1–10.

Godfrey, H.I. & Brogden, M., 2004. *Minimisation of Uranium Corrosion when Treating Hanford KE and KW Basin Wastes using Cementation, NSTS(04) 4993*.

Goles, R.W. & Sevigny, G.J., 1983. *Off-Gas Characteristics of Defence Waste Vitrification Using Liquid-Fed Joule Heated Ceramic Melters, PNNL-4819-UC70, Pacific Northwest National Laboratory, Richland, Washington*, U.S.A.

Goodhew, P.J., Humphreys, J. & Beanland, R., 2001. *Electron Microscopy and Analysis* 3rd ed., London: Taylor and Francis.

Gordon, L., 2008. *Encapsulation of clinoptilolite in cement-based system (PhD Thesis)*. University of Sheffield.

Greaves, G.N. et al., 1989. Glancing Angle X-ray Absorption Spectroscopy of Corroded Borosilicate Glass Surfaces Containing Uranium. *Journal of the American Chemical Society*, 111, p.4313.

Grenthe, I. et al., 2010. *Uranium in The Chemistry of the Actinide and Transactinide*

Elements 3rd ed. L. R. Morss, N. M. Edelstein, & J. Fuger, eds., Dordrecht: Springer.

Harrison, M.T., 2014. The Effect of Composition on short- and long-term durability of UK HLW glass. *Procedia Materials Science*, 7, pp.186–192.

Henry, S.. et al., 1994. Physical Properties. In *ASM Speciality Handbook: Stainless Steels*. p. 489.

Herber, R.H., 1965. Introduction to Mössbauer Spectroscopy. *Journal of Chemical Education*, 42(4), pp.180–188.

Hesketh, K.W., 1996. Power Reactors. In *The Nuclear Fuel Cycle From Ore To Waste*. Oxford: Oxford University Press, pp. 84–96.

Housecroft, C. & Sharpe, A., 2008. Inorganic Chemistry. In *Inorganic Chemistry*. Harlow, pp. 100–102.

Hrma, P. et al., 2006. Chromium phase behaviour in a multi-component borosilicate glass melt. *Journal of non-crystalline solids*, 352, p.2114.

Hrma, P. et al., 1995. Prediction of Processing Properties for Nuclear Waste Glass. *Ceram. Trans.*, p.505.

Hrma, P., Vienna, J.D. & Schweiger, M.J., 1996. Liquidus Temperature Limited Waste Loading Maximisation For Vitrified HLW. *Ceram. Trans.*, 72, pp.449–56.

Hrma, P.R. et al., 2005. *Testing of Large-Scale ICV Glasses with Hanford LAW Simulant*., pp.1-101.

Hyatt, N.C. et al., 2007. Plasma vitrification of waste plutonium contaminated materials. *Materials Research Society Proceedings*, 985, pp.393–398.

Hyatt, N.C. et al., 2014. Thermal Treatment of Simulant Plutonium Contaminated Materials From The Sellafield Site By Vitrification In A Blast-Furnace Slag. *Journal of Nuclear Materials*, 444, pp.186–199.

Hyatt, N.C. & James, M., 2013. Thermal Treatment of ILW. *Nuclear Engineering International*, pp.10–14.

IAEA, 1992. IAEA, Design And Operation Of High Level Waste Vitrification And

Storage Facilities. *Technical Report Series No. 339*.

Iller, R.K., *The Chemistry of Silica. Solubility, Polymerisation, Colloid and Surface Properties and Biochemistry*, Wiley.

INC, S.S.I., 2015. SSI Shredding Systems, Four-Shaft Shredders. Available at: https://www.ssiworld.com/en/products/four_shaft_shredders/ [Accessed November 15, 2015].

Jantzen, C.. & Bibler, N.E., 2009. The Product Consistency Test (PCT): How and Why It Was Developed. In *Environmental Issues and Waste Management Technologies*. John Wiley & Sons, pp. 155–167.

Jantzen, C.M., Smith, M.E. & Peeler, D.K., 2005. Dependency of Sulfate Solubility on Melt Composition and Melt Polymerisation. *Ceram. Trans.*, 168, pp.141–152.

Janz, G.J. & Lorenz, M.R., 1961. Solid-liquid phase equilibriums for mixtures of lithium, sodium, and potassium carbonates. *J. Chem. Eng. Data*, 6(3), pp.321–323.

Jensen, M. & Yue, Y., 2012. Effect of stirring on striae in glass melts. *Journal of Non-Crystalline Solids*, 358(2), pp.349–353.

Kamizono, H. et al., 1989. Volatilisation of ^{137}Cs and ^{106}Ru from Borosilicate Glass Containing Actual High-Level Waste. *Journal of the American Ceramic Society*, 72(8), pp.1438–1441.

Kawamura, K. & Ohuchi, J., 1995. Characterisation of highly waste loaded glass for HLW. *Mater. Res. Soc. Symp. Proc.*, 353, pp.87–93.

Kjeldsen, J. et al., 2013. Mixed alkaline earth effect in sodium aluminosilicate glasses. *Journal of Non-Crystalline Solids*, 369, pp.61–68.

Knowlton, G.D., White, T.R. & Mckague, H.L., 1981. Thermal Study of Types of Water Associated With Clinoptilolite. *Clays and Clay Minerals*, 29(5), pp.403–411.

Kohara, S. et al., 2004. Glass Formation at the Limit of Insufficient Network Formers. *Science*, 303, pp.1649–1652.

Konijnendijk, W.L. & Stevels, J.M., 1976. The Structure of Borosilicate Glasses Studied By Raman Scattering. *Journal of Non-Crystalline Solids*, 20, pp.193–224.

Kroeker, S. & Stebbins, J.F., 2000. Magnesium coordination environments in glasses and minerals: New insight from high-field magnesium-25 MAS NMR. *American Mineralogist*, 85(10), pp.1459–1464.

Kruger, A.A. et al., 2006. *Final Report - Sulfate Solubility in RPP-WTP HLW Glasses, VSL-06R6780-1*,

Li, D., Peng, M. & Murata, T., 1999. Coordination And Local Structure Of Magnesium In Silicate Minerals and Glasses: Mg K-Edge XANES Study. *The Canadian Mineralogist*, 37, pp.199–206.

Lightfoot, P. et al., 2001. The widespread occurrence of negative thermal expansion in zeolites. *Journal of Materials Chemistry*, 11(1), pp.212–216.

Long, D.A., 1977. *Raman Spectroscopy* 1st ed., London: McGraw Hill.

Lu, X.D. et al., 1999. Corrosion of K-3 glass-contact refractory in sodium-rich aluminosilicate melts. *Mater. Res. Soc. Symp. Proc.*, 556, pp.279–286.

Mackay, D.J., 2008. Sustainable Energy- Without The Hot Air. In pp. 161–173.

Maher, Z. et al., 2016. Americium and plutonium association with magnesium hydroxide colloids in alkaline nuclear industry process environments. *Journal of Nuclear Materials*, 468, pp.84–96.

Manara, D., Grandjean, A. & Neuville, D.R., 2009. Advances in Understanding the Structure of Borosilicate Glasses: A Raman Spectroscopy Study. *American Mineralogist*, 94, pp.777–784.

Marsh, G. & Eccles, H., 1996. Fuel Fabrication. In *The Nuclear Fuel Cycle From Ore To Waste*. Oxford: Oxford University Press, p. 43,48-50.

Matlack, K.S. et al., 2010. Sellafield Thermal Treatment Trials Using Advanced Joule Heated Ceramic Melter Technology. *Waste Management*, pp.1–13.

Matson, D.W., Sharma, S.K. & Philpotts, J.A., 1983. The Structure of High-Silica

Alkali-Silicate Glasses. A Raman Spectroscopic Investigation. *Journal of Non-Crystalline Solids*, 58, pp.323–352.

McGann, O.J., 2013. *The Development of Glass Compositions for the Vitrification of Ion Exchange Resin Wastes from the Nuclear Industry (PhD Thesis)*. University of Sheffield

McGann, O.J. et al., 2012. The effects of gamma radiation on model vitreous wasteforms intended for the disposal of intermediate and high level radioactive wastes in the UK. *Journal of Nuclear Materials*, 429, pp.353–367.

McQuarrie, D.A. & Simon, J.D., 1997. Physical Chemistry: A Molecular Approach. In *Physical Chemistry: A Molecular Approach*. San Francisco: University Science Books, pp. 118–124, 257–260, 292–302.

Meera, B.N. & Ramakrishna, J.N., 1993. Raman Spectral Studies of Borate Glasses. *Journal of Non-Crystalline Solids*, 159, pp.1–21.

Micromeritics, AccuPyc II 1340 Pycnometer Gas Displacement Pycnometry System. Available at: http://www.micromeritics.com/Product-Showcase/AccuPyc-II-1340.aspx [Accessed October 2, 2018].

Mika, M. et al., 1997. Liquidus temperature of spinel precipitating high-level waste glasses. *Scientific Basis for Nuclear Waste Management XXX*, p.71.

Morgan , S. , Hand , R. J. , Hyatt , N. C. , and Lee, W.E., 2004. Interactions of simulated high level waste (HLW) calcine with alkali borosilicate glass. *Mater. Res. Soc. Symp. Proc.*, 807, pp.151–156.

Moynihan, C.T. et al., 1976. Dependence of the Fictive Temperature of Glass on Cooling Rate. *Journal of the American Ceramic Society*, 59(1–2), pp.12–16.

Mumpton, F.A., 1999. La Roca Magica: Uses of Natural Zeolites in Agriculture and Industry. *Proceedings of the Natural Academy of Science USA*, 96(7), pp.3463–3470.

NDA/RWMD/013, 2010. *Geological Disposal: Steps Towards Implementation. Nuclear Decommisioning Authority Report*, pp. 1-58.

NDA, 2013a. NDA radioactive waste inventory. Available at: https://www.nda.gov.uk/ukinventory/the-2013-inventory/2013-uk-data/ [Accessed September 10, 2016].

NDA, 2013b. Waste Stream 2D26 Ion Exchange Material (Clinoptilolite) and Sand. Available at: http://ukinventory.nda.gov.uk/wp-content/uploads/sites/18/2014/04/2D26.pdf [Accessed November 15, 2014].

NDA, 2016. Waste Stream 2D34 Sludge from Sand Filters and Transfers. Available at: http://ukinventory.nda.gov.uk/wp-content/uploads/sites/18/2014/04/2D34.pdf [Accessed March 14, 2017].

NDA, Waste Stream 2D35/C Encapsulated Retrieved Magnox Cladding. *2013*. Available at: http://ukinventory.nda.gov.uk/wp-content/uploads/sites/18/2014/05/2D35_C.pdf [Accessed November 15, 2014a].

NDA, Waste Stream 2D38/C Encapsulated Magnox Cladding. *2013*. Available at: http://ukinventory.nda.gov.uk/wp-content/uploads/sites/18/2014/05/2D38_C.pdf [Accessed November 15, 2014b].

Nesaraja, C.D., 2015. Nuclear Data Sheets for A=241. *Nuclear Data Sheets*, 130, pp.183–252.

Nirex Solutions, *Work Package Part 1. The Wastes and cementation processes employed at Sellafield for treatment of ILW*,

Ojovan, M.L. & Lee, W.E., 2005. An Introduction To Nuclear Waste Immobilisation. In Oxford: Elsevier, pp. 81–85, 187, 213–248, 259–268.

Osborne, M.D., Fleet, M.E. & Bancroft, G.M., 1981. Fe(II)-Fe(III) ordering in chromite and Cr-bearing spinels. *Contributions to Mineralogy and Petrology*, 77(3), pp.251–255.

Parkinson, B.G. et al., 2005. The effect of Cs2O additions on HLW wasteform glasses. *Journal of Non-Crystalline Solids*, 351(30), p.2425.

Paul, A., 1990. Chemistry of Glasses. In London: Chapman and Hall, pp. 1–15.

Pedone, A. et al., 2008. Role of magnesium in soda-lime glasses: insight into

structural, transport, and mechanical properties through computer simulations. *Journal of Physical Chemistry C*, 112, pp.11034–11041.

Penner-Hahn, J.E., 2004. X-ray Absorption Spectroscopy. In *Comprehensive Coordination Chemistry*. Oxford: Pergamon, pp. 159–186.

Phillips, M.W., Gibbs, G.V. & Ribbe, P.H., 1974. The Crystal Structure of Danburite: A Comparison with Anorthite, Albite and Reedmergnerite. *American Mineralogist*, 59, pp.79–85.

Rajec, P. et al., 1998. Sorption of caesium and strontium on clinoptilolite- and modernite-containing sedimentary rocks. *Journal of Radioanalytical and Nuclear Chemistry*, 229, pp.49–55.

Raman, S.V., 1998. The Effect of Mixed Modifiers on Nuclear Waste Glass Processing, Leaching and Raman Spectra. *Journal of Materials Research*, 13, pp.8–15.

Randall, J., Rooksby, H. & Cooper, B., 1930. X-ray Diffraction and the Strcuture of Vitreous Solids - I. *Z. Kristallogr*, 75, pp.196–214.

Ravel, B. & Newville, M., 2005. ATHENA, ARTEMIS, HEPHAESTUS: Data analysis for X-ray absorption spectroscopy using IFEFFIT. *Journal of Synchrotron Radiation*, 12(4), pp.537–541.

Reimer, L., 1998. *Scanning Electron Microscopy Physics of Image Formation and Microanalysis* 2nd ed., Berlin: Springer.

Richardson, S., Curd, P. & Kelly, E.J., 1996. Disposal of Fuel or Solid Wastes. In *The Nuclear Fuel Cycle From Ore To Waste*. Oxford, pp. 184–197.

Rockett, T.J. & Foster, W.R., 1981. The High-Silica Liquidus Surface of the System Na_2O-B_2O_3-SiO_2. *Journal of the American Ceramic Society*, 64, pp.148–149.

Rodriguez-Trejo, R., Bosch, P. & Bulbulian, S., 2006. Combustion treatment of Co2+ and Cs+ exchanged zeolites. *Journal of Nuclear Materials*, 354, pp.110–122.

Rolin, M. & Recapet, J., 1964. Contribution Letude Des Proprietes Thermodynamiques Des Carbonates Alcalins 1. Le Diagramme Ternaire Na_2CO_3-

K_2CO_3- Li_2CO_3. *Bulletin De La Societe Chimique De France*, (9), pp.2104–2110.

Rose, P.B. et al., 2011. Crystallisation of a simulated borosilicate high-level waste glass produced on a full-scale vitrification line. *Journal of non-crystalline solids*, 357, pp.2989–3001.

Rosenhain, W., 1927. The Structure and Constitution of Glass. *J. Soc. of Glass Technol. Trans.*, 11, pp.77–97.

Sawatazky, G.A., 1969. Recoiless-fraction ratios for 57Fe in octahedral and terahedral sites of a spinel and a garnet. *Phys. Rev.*, 183, pp.383–386.

Schreiber, H.D. et al., 1982. The Chemistry of Uranium in Borosilicate Glasses. Part 2. Base Compositions Containing Titanium Relevant to the Immobilisation of Nuclear Waste. *Physics and Chemistry of Glasses*, 23, p.147.

Schreiber, H.D. & Balazs, G.B., 1982. The Chemistry of Uranium in Borosilicate Glasses. Part 1. Simple Base Compositions Relevant to the Immobilisation of Nuclear Waste. *Physics and Chemistry of Glasses*, 23, p.139.

Schreiber, H.D., Balazs, G.B. & Solberg, T.N., Chemistry of Uranium in Borosilicate Glasses. Part 6. The Leaching of Uranium from Glass. *Physics and Chemistry of Glasses*, 26, p.35.

Schubert, D.M., 2003. Borates in Industrial Use. In *Group 13 Chemistry III. Industrial Applications*. pp. 25–28.

Sellafield, Information on Sellafield Reprocessing. Available at: http://www.sellafieldsites.com/solution/spent-fuel-management/ [Accessed March 14, 2015a].

Sellafield, Information on Sellafield Storage. Available at: http://www.sellafieldsites.com/solution/risk-hazard-reduction/ [Accessed March 14, 2015b].

Selvaraj, U. & Rao, K.J., 1984. Infrared spectroscopic study of mixed-alkali effect in borate glasses. *Spectrochimica Acta Part A: Molecular Spectroscopy*, 40(11–12), pp.1081–1085.

Sen, S., Maekawa, H. & Papatheodorou, G.N., 2009. Short-Range Structure of Invert Glasses along the Pseudo-Binary Join MgSiO3-MgSiO4: Results from 29Si and 25Mg MAS NMR spectroscopy. *Journal of Physical Chemistry B*, 113, pp.15243–15248.

Shelby, J.E., 2005. Introduction to Glass Science and Technology. In pp. 3–6, 26–48, 93–100, 154–159, 198–200.

Sonzogni, A.A., 2004. Nuclear Data Sheets for A=134. *Nuclear Data Sheets*, 103(1), pp.1–182.

Sonzogni, A.A., 2001. Nuclear Data Sheets for A=144. *Nuclear Data Sheets*, 93(3), pp.599–762.

Spalding, B.P., 1994. Volatilisation of caesium-137 from soil with chloride amendments during heating and vitrification. *Environmental Science and Technology*, 28, pp.1116–1123.

Szczerba, J. et al., 2013. Influence of time and temperature on ageing and phases synthesis in the MgO- SiO_2- H_2O system. *Thermochimica Acta*, 567, pp.57–64.

Tan, S. et al., 2015. MoO3 incorporation in magnesium aluminosilicate glasses. *Journal of Nuclear Materials*, 458, pp.335–342.

Taylor, H.F.W., 1987. A Method for Predicting Alkali Ion Concentrations in Cement Pore Solutions. *Advances in Cement Research*, 1, pp.5–16.

Taylor, H.F.W., 1990. Cement Chemistry. In London: Academic Press, pp. 1–28.

Terai, R. & Kosaka, E., 1976. *Osaka Kogyo Gijutus Shikenjo Kiho 27:150. Volatilisation of Low Temperature Borosilicate Glasses for High-Level Radioactive Wastes at Elevated Temperatures*,

Thien, B.M.J. et al., 2012. The dual effect of Mg on the long-term alteration rate of AVM nuclear waste glasses. *Journal of Nuclear Materials*, 427, pp.297–310.

Timar, J. & Elekes, Z., 2014. Nuclear Data Sheets for A=129. *Nuclear Data Sheets*, 121, pp.143–194.

Toby, B.H., 2006. R factors in Rietveld analysis: How good is good enough? *Powder*

Diffraction, 21(01), pp.67–70.

Utton, C.A. et al., 2013. Dissolution of vitrified wastes in a high-pH calcium-rich solution. *Journal of Nuclear Materials*, 435, pp.112–122.

Utton, C.A. et al., 2013. Formation of alteration products during dissolution of vitrified ILW in a high-pH calcium-rich solution. *Journal of Nuclear Materials*, 442(1–3), pp.33–45. Available at: http://dx.doi.org/10.1016/j.jnucmat.2013.08.026.

Valenkov, N. & Poray-Koshitz, E., 1936. X-Ray Investigation of the Glassy State. *Z. Kristallogr*, 95, pp.195–229.

Vernaz, É. & Bruezière, J., 2014. History of Nuclear Waste Glass in France. *Procedia Materials Science*, 7(December 2014), pp.3–9. Available at: http://linkinghub.elsevier.com/retrieve/pii/S2211812814010451.

Vienna, J.. et al., 2001. *Hanford Immobilised LAW Product Acceptance Testing: Tank Focus Area Results, PNNL-13744, Pacific Northwest National Laboratory, Richland, Washington*,

Vienna, J.D. et al., 2014. Toward Understanding the Effect of Low-Activity Waste Glass Composition on Sulfur Solubility. *Journal of the American Ceramic Society*, 97(10), pp.3135–3142. Available at: http://doi.wiley.com/10.1111/jace.13125.

Vogel, W., 1994. Glass Chemistry. In Berlin: Springer-Verlag, pp. 123–157.

Waclawska, I., 1995. Thermal Decomposition of Borax. *Journal of Thermal Analysis*, 43, pp.261–269.

Warren, B.E., 2003. *X-Ray Diffraction* 1st ed., New York: Dover.

Watts, S.J. et al., 2010. Influence of magnesia on the structure and properties of bioactive glasses. *Journal of Non-Crystalline Solids*, 356(9–10), pp.517–524. Available at: http://dx.doi.org/10.1016/j.jnoncrysol.2009.04.074.

Witwer, K. et al., 2013. GeoMelt ICV Treatment of Sellafield Pond Solids Waste. *Proceedings of the Waste Management Symposia*.

Woodcock, D.A. et al., 1999. Strong negative thermal expansion in-the siliceous zeolites ITQ-1, a ITQ-3 and SSZ-23 3. , 70(c), pp.349–351.

Wright, A.C., 2014. The great crystallite versus random network controversy: A personal perspective. *International Journal of Applied Glass Science*, 5(1), pp.31–56.

Yun, Y.H. & Bray, P.J., 1978. Nuclear Magnetic Resonance Studies of Glasses in the System Na_2O- B_2O_3- SiO_2. *Journal of Non-Crystalline Solids*, 27, pp.363–380.

Yun, Y.H., Feller, S.A. & Bray, P.J., 1979. Correction and Addendum to "Nuclear Magnetic Resonance Studies of the Glasses in the system Na_2O-B_2O_3-SiO_2." *Journal of Non-Crystalline Solids*, 33, pp.273–277.

Zhang, H. et al., 2015. Effect of Zn- and Ca- oxides on the structure and chemical durability of simulant alkali borosilicate glasses for immobilisation of UK high level wastes. *Journal of Nuclear Materials*, 462, pp.321–328.

Zwicky, H.U. et al., 1988. Corrosion behaviour of British Magnox Waste Glass in Pure Water. *MRS Online Proceedings Library*, 127, p.129.

Conditioning of Legacy Radioactive Wastes Requiring Additional Treatment

J. Clarke

Thesis presented for partial fulfilment of the requirement for degree of Doctor of Philosophy

December 2018

Department of Materials Science and Engineering

The University Of Sheffield.